SpeleoDrone - Final Report

AE3200 - Design Synthesis Exercise

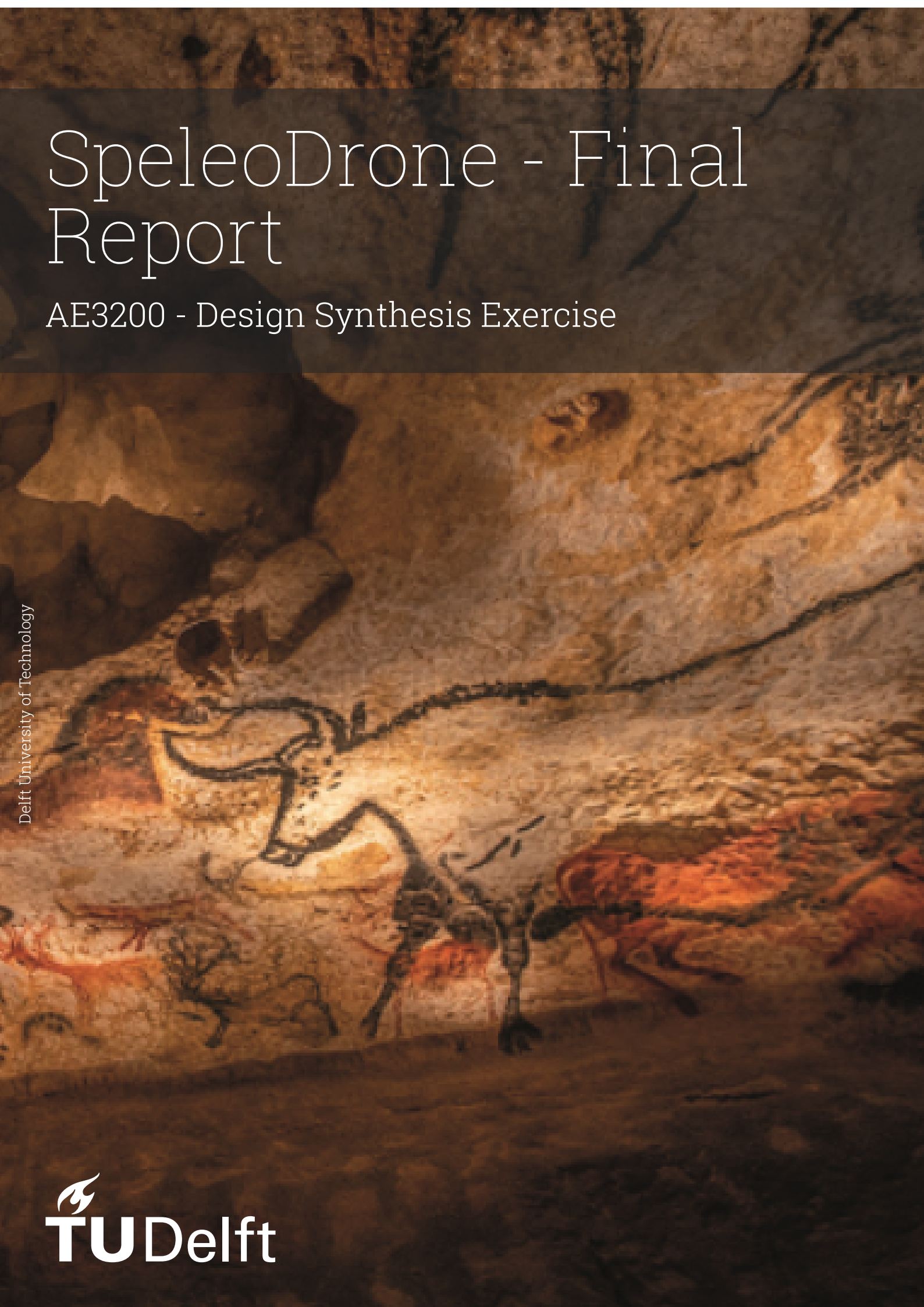

Delft University of Technology

TU Delft

This page is intentionally left blank.

SpeleoDrone - Final Report

by

Maria Beisert	5683459
Max Blankestijn	5825725
Friso Broekhuizen	5487668
Razvan Herscovici	5560217
George Khalko	5553296
Nika Limarenko	5544602
Salma Mohamed	5757053
Jerzy Olszewski	5264464
Lilly Scharfenberg	5572185
Agata Zdanowicz	5449367

Acknowledgments

Group 24 would like to express their sincere gratitude to the team tutor, John-Alan Pascoe, for his dedicated guidance and support throughout the development of the SpeleoDrone project. His insights, feedback, and encouragement were invaluable at every stage of the design process.

The team is also deeply grateful to Paul Gaucher and Amy Morin, whose coaching, experience, thoughtful advice, and mentorship greatly contributed to the success of our work. This design would not have been possible without your unwavering support and expertise.

Course:	AE3200 Design Synthesis Exercise
Primary Tutor:	J. A. Pascoe
Coaches:	P. Gaucher & A. Morin
Course Coordinator:	J. Melkert
Faculty:	Faculty of Aerospace Engineering, Delft

Cover: https://www.britannica.com/art/cave-art Accessed [21/05/2025]

TU Delft

Executive Summary

Human presence in cave systems stretches back thousands of years. These caves have served as vital shelter, protecting people from harsh weather, wild animals, and other threats. Beyond their practical role in survival, caves also offer invaluable cultural insights. The walls of many caves are adorned with paintings that reflect aspects of identity, hunting practices, religious beliefs, and much more, providing a window into the lives and values of early humans.

As such, archaeologists are highly interested in exploring these cave environments. While caves once offered crucial protection, today they can pose significant risks, including hazardous gases, confined spaces, and sudden flooding. To safeguard archaeologists from these dangers, the SpeleoDrone was developed as a means to take on the most dangerous tasks within caves, reducing the need for researchers to enter hazardous areas themselves.

The motivation of this project can be summarized by the following mission need statement:

> ***Allow archaeologists to comprehensively map cave systems whilst preserving site integrity and safety of expedition teams.***

The project objective statement stems from this:

> ***Design a UAS to be remotely operated by an archaeologist, capable of visually mapping a cave system while maintaining site integrity, within 10 weeks by 10 students.***

The primary objective of the mission is to visually map the cave while maintaining site integrity. In addition, secondary and tertiary objectives were derived from the project objective and user requirements. These objectives then determine the functions the system must be able to perform, of which the top-level functions are displayed in the functional flow diagram in Figure 1

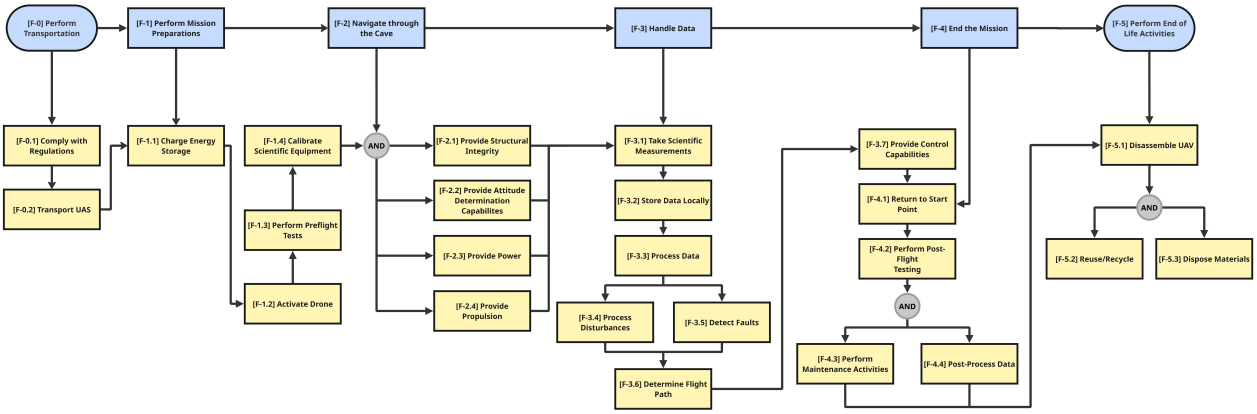

Figure 1: Flow of top-level functions

In order to conform to the needs of groups involved in the project stakeholders were identified, with the key stakeholder being Dr. Hayley Mickleburgh, the local wildlife and regulatory agencies.

Additionally, a market analysis was used to identify other potential stakeholders and explore the competitive edge the drone could hold. A global estimate was made of 50 hypothetical customers. Possible market expansion opportunities were also considered, like mapping other hazardous places with archaeological interest, like structurally unstable buildings and mines. A competitor analysis was conducted, where the competitive edge could be highlighted. The SpeleoDrone would not be wider than already existing drones used for cave exploration, and should have a larger endurance. This design goal did work out, as the estimated endurance of the SpeleoDrone is about 6 minutes more than the main competitor, Elios 3, while having a smaller frontal area and remote operation capability.

After determining that the design was financially viable, the next step was to identify the most important user requirements. The three most important requirements were related to size, cost and emissions:

> ***STK-DRN-04:*** *The system shall be able to pass through any opening an adult human can pass through*
>
> ***STK-OPR-03:*** *The system shall have a purchase cost of no more than €25000.*
>
> ***STK-OPR-06:*** *The system shall not produce any emissions inside the cave system.*

Additionally, for the system end of life, it was also important to design with recyclable materials in mind due to the requirement

> ***STK-OPR-02:*** *The system shall be 75% by weight recyclable, excluding the payload*

The end of life refers to the point when the drone is no longer able to complete missions. Thus instead of disposing of it, the requirement aims to recycle it and avoid as much possible waste and harm to the environment as possible. The entire system is recyclable except for the LiPO battery safety bag, thus fulfilling the requirement.

A focus in the design process is to incorporate sustainability in the project. The main goal of this is to reduce the environmental impact of the product, this to meet stakeholder requirements. In the prior design stages of the project, a sustainability strategy for the design was set up. Four key aspects related to sustainability were chosen to focus on. The first, circularity, ensures an extended lifespan of the system. Different aspect from the R-ladder strategy for circularity are applied: recyclability, repairability, and repurposability. Durability, which is also focused on, aims to reduce critical damages of the system, for example by protection of exposed components. Furthermore, the emissions and energy use of the system will be tracked for all phases of the product and minimized. And lastly, the site disturbance will have to be minimized to respect the flora and fauna that live in the targeted caves - think about bats, frogs, or insects.

Final Design

The final design of the system is a quadcopter which can be seen in Figure 2. The SpeleoDrone is connected to a ground station through a fiber optic cable which transfers information gathered by navigational sensors and the payload. Its location is shown in blue in the visual, at the rear of the SpeleoDrone. The SpeleoDrone is mounted with a LiDAR, flashlight, visible light camera, and a visible to short infrared camera located in the orange module of the visual. These gather topological and visual information of the cave system. For navigation, it uses information from LiDAR, imagery from the cameras, IMUs and additional time-of-flight sensors to decide upon the path of the SpeleoDrone using an AI algorithm to maximize scanned areas of the cave systems whilst minimizing time taken. The SpeleoDrone is stabilized using a controller built on various PIDs. Finally, the entire SpeleoDrone is powered by two batteries shown located in the green module of the visual.

Figure 2: SpeleoDrone Final Design Model

During the mission, the SpeleoDrone operator is outside of the cave system, operating the ground system, which provides an interface for them to view information such as the present topological map of the cave system and visual imagery, as well as adjusting the drone's path. This also comes with a solar-powered charging station providing power in remote areas.

Payload

The most important requirements for the payload were identified as:

> ***STK-DRN-1:*** *The system shall be able to fully map a cave system distance of up to 500 m from the entrance, within 1 week.*
>
> ***STK-DRN-2:*** *The system shall be able to visually map the cave system with a resolution of 1 cm.*
>
> ***STK-DRN-3:*** *The system shall be able to georeference a location on the map with a resolution of 1 cm.*

The drone payload consists of two types of mapping devices, namely a LiDAR and a visible + infra red spectrum camera. The former is used for 3D mapping, while the camera will be used for detecting obstacles and also creating a visual model of the cave. The visible spectrum camera requires a light source in order to capture good images, meaning a flashlight was also added to the payload. All payload has been placed in a box, that has been mounted on a swivel in the front part of the drone.

The characteristics of the lens and the camera chosen for the visible spectrum imagery dictate the maximum speed the drone can achieve in order to avoid motion blur in the images. This value is also dependent on other parameters, such as the distance from the wall and the image resolution. The combination of the chosen parameters resulted in an optimal mapping speed of 0.65 m/s.

Structural Design

The structure of the SpeleoDrone made use of composite beams as the primary structural elements, with magnesium alloy components present to facilitate load transfer. The structure was designed around impact scenarios, as an early-stage stiffness study found that standard operational and handling loads would be able to be handled by a simple frame from a cheap plastic called ABS. The composite beams reinforced this ABS plastic with carbon fibers, and were novel in their use of a thermoplastic polymer as a matrix in contrast to the industry standard of thermoset epoxy. This novel choice of materials allowed the entirety of the SpeleoDrone structure to be recycled. The magnesium alloy AZ31B was used to manufacture connective elements for the composite beams.

The final structural frame of the SpeleoDrone is presented below in Figure 3. It shows the beams, the elbow and T joints used to connect the beams, as well as the motor mounts and landing gears.

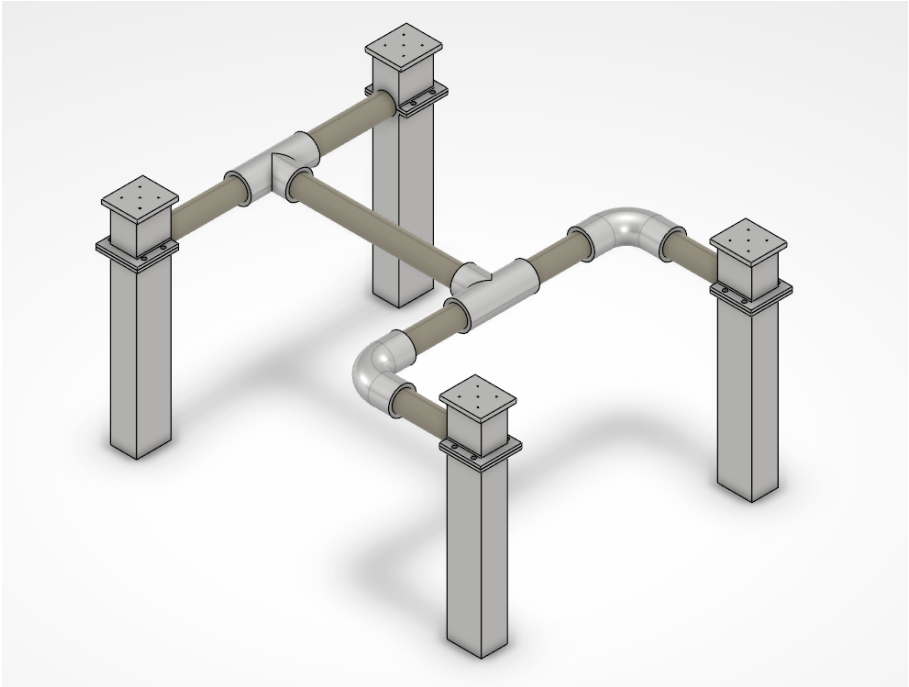

Figure 3: SpeleoDrone Frame Assembly

Flight Performance Analysis

As part of analyzing the flight performance, the motors and rotors were selected, and ducts were designed for these propellers. Through iterations in the drone mass and power consumption, the 'ECOII-2807-1300KV' motors and the 'HQ 7*3.5*3' rotors were selected for their optimal performance.

Through drag and horizontal acceleration calculations, the main focus of the design parameters evaluation was the endurance of the drone. Through the use of Thrust-to-Weight ratio calculations, the flight time in hover condition was calculated to be over 18 minutes, whilst the maximum range of the drone was found to be over 14 km, traveling at a pitch angle of 26.75° and a T/W ratio of 1.12. Further calculations found the desired mapping speed to be 0.65 m/s, flying at a pitch angle of 0.03°, resulting in a maximum range of 821 meters for optimal cave mapping.

The noise analysis for the drone showed operational noise level emissions ranging from 65 dB to 73 dB, being close to a normal conversation and not disturbing the ecosystem. In order to achieve these lower noise emissions during operation, and protect the rotors from potential damage, rotor ducts were designed, which contributed to an overall 10% thrust efficiency increase.

Control design

Next, the control subsystem was designed that will allow for navigating the complex cave environment. For this, a Simulink model was created, which will take a combined input from an AI model, a simulation and sensor readings using Kalman filters to estimate the position and move to a desired position. However, before any simulation and state prediction can be done, the AI model must provide a desired state.

SpeleoDrone features an integrated AI-based control system designed to enable autonomous drone navigation in GPS-denied and visually complex environments such as caves. It leverages multiple AI technologies to facilitate real-time decision-making, obstacle avoidance, and region-of-interest detection during exploration missions. The Autonomous Control System consists of two main components: artificial intelligence (YOLO + LSTM + D3QN) and the path-planning algorithm D* Lite. These components are described in more detail in Table 1.

Table 1: Core components of SpeleoDrone Autonomous Control System and their purpose

Component	Purpose	Usage Phase
YOLO (You Only Look Once)	Real-time object detection from high-resolution images (obstacles & regions of interest)	Continuous during exploration
LSTM (Long Short-Term Memory)	Maintains temporal memory to handle partial observability, noisy data, and plan multi-step actions	Supports both learning and decision-making throughout exploration
D3QN (Deep Double Dueling Q-Network)	Reinforcement learning-based policy for exploring unknown terrain with curiosity-driven strategies	Used during initial exploration phase
D* Lite	Classical path planning algorithm for efficient navigation in mapped environments	Activated after 80% area coverage or during fallback

The autonomous system ensures that even amateur operators can conduct missions safely. The different navigation phases and corresponding control strategies are detailed in Table 2.

Table 2: Autonomous Control System strategy during different navigation phases

Phase	AI Technique	Description
Initial Exploration	D3QN + LSTM + YOLO	Drone learns terrain, detects obstacles/ROIs, and navigates adaptively
Post-Exploration	D* Lite + YOLO	Map-based goal navigation with lightweight computation
Emergency Return (e.g., signal loss)	D* Lite	Autonomous return to base using stored map

The system follows an *Operator-in-the-loop* philosophy: primary functions are performed autonomously, but a human operator retains control over high-level decision-making and may intervene when necessary.

- **Autonomous Navigation:** $\sim$85% of mission time

- **Operator (Pilot) Intervention:** ∼15% (e.g., analysis of regions of interest, overriding complex paths, takeoff/landing)

With the AI model laid out, the controller and plant were designed. The controller sends control signals to the plant, which models the physics of the quadcopter and updates the position, orientation and velocities. The state then feeds back into the controller to determine the error relative to the desired state and repeat the process. This process is visualized in Figure 4.

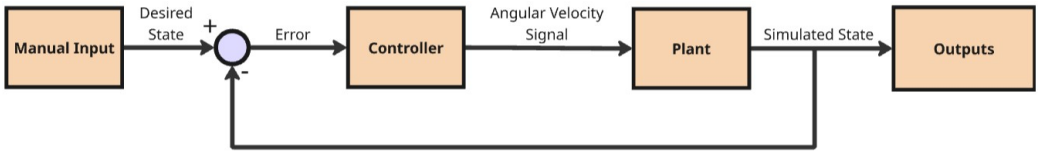

Figure 4: Diagram of the Simulink controller

Avionics design

To power the drone, a battery had to be selected. After evaluating the available options, the 'Spektrum' battery was selected due to its high energy density. To further improve the endurance of the drone, the design includes two of these batteries. The sensors which were selected for the drone include a Inertial Measurement Unit (IMU) sensor, a Time of Flight sensor, a Temperature and Humidity sensor, as well as a buzzer (selected for audio feedback to the user), Remote ID (compliance with regulations) and a GPS sensor.

In addition to the selection of the sensors and their connections to the electrical system, the software and data handling connections were defined throughout the ground station, charging station, and the drone itself. They are presented visually in block diagrams.

Operations and Logistics

The operational design of the drone prioritizes both sustainability and usability for non-technical operators. To enable continuous data transmission, a fiber optic cable was selected as the communication method. To reduce environmental impact in the event that the cable becomes irretrievable, a biodegradable sheath was developed. The cable connects to a laptop-based ground control station via supporting hardware, such as a media converter.

To meet user requirement **STK-OPR-05** - "The system shall be able to operate in a remote location (i.e. no access to grid power or cellular telephone networks)" - a portable solar-powered charging station was developed. This setup enables off-grid charging of both drone batteries and the ground control laptop during operations. The mission operation concept is visualized in Figure 5.

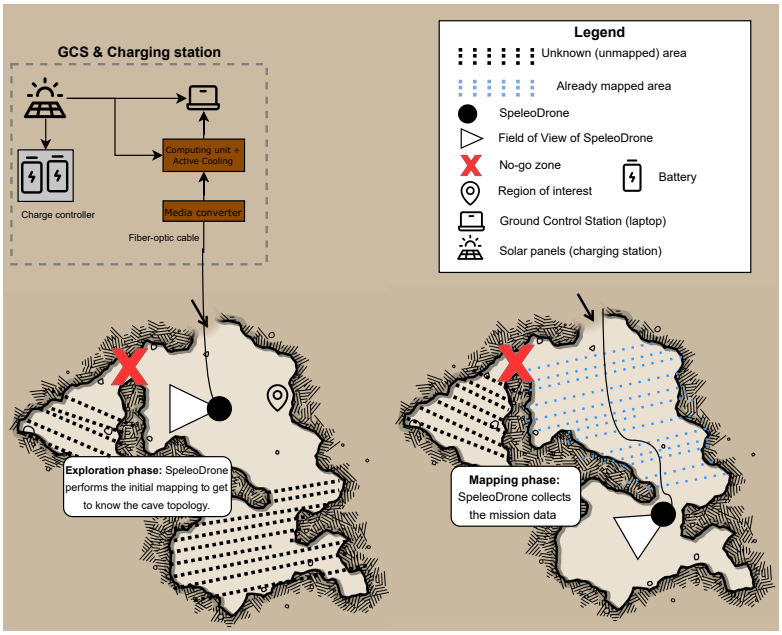

Figure 5: Mission operation concept

Production

A manufacturing plan was defined for the SpeleoDrone structural components. These components would be made in-house, with CNC machining being used to produce all the metal components and filament winding being used for the composite beams. The unidirectional tape used for this filament winding process would also have to be produced in-house using a process called wet impregnation. An assembly plan was also created in order to better illustrate the steps that need to be taken to successfully and accurately assemble all drone components.

Cost analysis

A cost analysis was conducted to assess the financial feasibility of the project. Based on market research, a purchase price of € 45,000 per unit was established. A conservative estimate assumed the sale of eight units, with a production cost of € 40,000 each. Under these conditions, the projected return on investment (ROI) is 20%. The relationship between development cost per unit and the number of units produced is illustrated in Figure 6a, while the corresponding ROI is shown in Figure 6b.

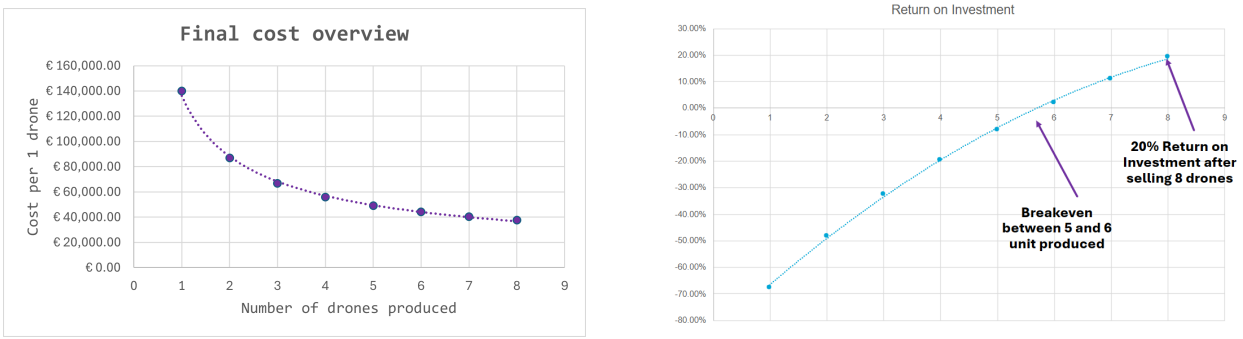

(a) Final cost overview

(b) Return on Investment analysis

Figure 6: Cost analysis overview

Technical Risk Assessment

A risk analysis was carried out in order to identify the biggest threats to the project. For each of the identified risks a prevention and a mitigation strategy were derived, in order to minimise the probability of them occurring or minimse the impact on the mission in case they do occur. These strategies were then implemented in the design.

The most probable risk after mitigation remained: ***RSK-OP-010****: Fiber optic cable getting stuck on a rock*. In case this was to happen the drone would get stuck and possibly get damaged. In order to prevent this from happening, the algorithm choosing the path for the drone should be trained to avoid turns as much as possible- this would also have a beneficial effect on endurance and help avoid looping the fibre optic around a stalagmite or another similar structure. In case it does happen, a recommendation was made to implement a cutting mechanism, that could cut the cable off and trigger a return to home protocol, where the drone would autonomously navigate back to the cave entrance. The probability and severity of this occurring before mitigation were rated as 5 and 5 respectively, meaning the event is almost guaranteed to happen and its impact on the mission would be catastrophic. After mitigation the probability has been lowered to 4 (likely to occur) and the severity to 3 (moderate impact on the project).

There is a number of risks that have an equal severity after mitigation, two of those being ***RSK-PP-008****: Motor failure due to bearing failure* and ***RSK-PP-009****: Motor failure due to overheating*. Both of these pertain to motor failure. Before mitigation their probability was rated as 4 (likely) and 3 (possible) respectively and the severity of both of them was deemed to be 5 (catastrophic). Both risks were assigned a prevention strategy, that decreased the probability of them occurring down to 2 (unlikely), but they both still lack a mitigation strategy. As such, in the future of the project a one motor inoperative flight scenario will have to be assessed, which will require a more detailed analysis of the controllability of the drone and possibly remodeling of the Simulink model.

After the risk analysis the Reliability, Availability, Maintainability and Safety (RAMS) characteristics were assessed. The maintenance of the drone was briefly discussed, resulting in a 25 min downtime between each run in the cave and a 140 min long downtime for the longer, weekly maintenance. Reliability of the drone was also assessed by the means of a Fault Tree Analysis (FTA), which helped identify all possible failure modes. The ones deemed most likely, that being motor failure, communication system failure or failure of the AI navigation were used to complete the risk analysis and will be monitored in the future of the project. Safety aspects were

also discussed and an overview of safety recommendations was given. Personal Protection Equipment (PPE) needed by the team was identified as helmets and the impact of the drone on the bats living in the cave was lowered by implementation of foam around Electronic Speed Controllers (ESCs) and ensuring the flashlight would only be used if no bats were to be present in the area.

Verification and Validation

To guarantee that at the end of the design, the system will meet all customer needs, extensive Verification and Validation procedures were laid out for the most important high-level requirements and all subsystem requirements. These tests are performed either through inspection, analysis, demonstration, or testing of the system.

Additionally, the models used in the design of each subsystem were individually validated through a range of tests, including unit tests, system tests, and sensitivity analysis. This ensures that the data presented is reliable.

Finally, a compliance matrix was constructed that compared the user requirements to the analysis performed throughout the report. The conclusion is that after the renegotiation of the cost from €25000 to €50000, every stakeholder requirement except for the size requirement, which is slightly exceeded by 1.4cm.

Future Development of the Project

Finally, the future steps of the project are outlined visually in a project design and development block diagram. The next step in the design cycle of the SpeleoDrone is thorough simulation and modeling of the design at hand. This is followed by prototyping where prototypes of the drone subsystems are constructed, to check for their functionality. Following this is the software development, as well as the integration and assembly of the individual subsystems. The final step in the design cycle is the testing of the drone system. Since the design is an iterative process, all of these individual steps may be repeated after design alterations, however, the steps followed remain the same for each iterations of the design.

TABLE OF CONTENTS

Nomenclature

Abbreviations

Abbr.	Definition
3D	3-Dimensional
3DM	3-Dimensional Mapping
ABS	Acrylonitrile butadiene
AI	Artificial Intelligence
ALT	Altimeter
ATT	Attitude Sensor
BLOS	Beyond Line of Sight
CAM	Camera Module
CCNTR	Collision Control
CDS	Camera Data Storage
CG	Center of Gravity
COM	Communication Method
COTS	Commercial Off The Shelf
CPI	Consumer Price Index
CRM	Continuous Risk Management
DRL	Deep Reinforcement Learning
DOT	Design Option Tree
DRN	Drone
DRC	Drone Control
EASA	European Union Aviation Safety Agency
ENRG	Energy
ESC	Electronic Speed Controller
EV	Exposure Value
FAA	Federal Aviation Administration
FC	Flight Control
FMAT	Fuselage Material
FMCW	Frequency Modulated Continuous Wave
FoV	Field of View
FVF	Fiber Volume Fraction
FPS	Frames per Second
GPU	Graphical Processing Unit
GR	Georeferencing
GRS	Ground Station
GSD	Ground Sampling Distance
ID	Identifier
IM	Imagery
IMU	Internal Measurement Unit
IR	Infrared
LCA	Life Cycle Analysis
LED	Light Emitting Diode
LIDAR	Light Detection and Ranging
Li-Po	Lithium Polymer
Li-S	Lithium Sulfur
LSTM	Long Short Term Memory
LWIR	Long Wave Infrared
MIS	Mission
MMOI	Mass Moment of Inertia
MNS	Mission Need Statement
NIR	Near Infrared
OP(R)	Operation(al)
PCB	Printed Circuit Board
PL	Payload
PMAT	Propeller Material
POS	Project Object Statement
PP	Power and Propulsion
PPE	Personal Protection Equipemnt
PROP	Propulsion Configuration
RC	Radio Controlled
RDT&E	Research Development Test and Evaluation
REQ	Requirement
RM	Rotor Motion
ROI	Region of Interest
RPM	Rotations per Minute
RSK	Risk
SNH	Sensor Housing
SPL	Soubd Pressure Level
SSB	Solid State Battery
STK	Stakeholder
STR(C)	Structur(al)
SYS	System
TBD	To Be Determined
TRL	Technology Readiness Level
T/W	Thrust-to-Weight ratio
UAS	Unmanned Aerial System
UAV	Unmanned Aerial Vehicle
URL	Uniform Resource Locator
UT	Unit Test
UV	Ultraviolet
UvA	Universiteit van Amsterdam
VLOS	Visual Line of Sight
WBS	Work Breakdown Structure
WFD	Work-Flow Diagram
WSA	Weakness of Survivors Analsysis

Symbols

Symbol	Definition	Unit
a	Acceleration	[m/s^2]
a_h	Horizontal acceleration	[m/s^2]
a_v	Vertical acceleration	[m/s^2]
c	Speed of light	[m/s]
C_D	Drag Coefficient	[-]
E	Young's Modulus	[GPa]
E_b	Battery Energy	[J]
f	Fraction	[-]
g	Acceleration due to gravity	[m/s^2]
h	Planck's constant	[m^2kg/s]
I_{xx}	Mass Moment of Inertia about x-axis	[kg·m^2]
I_{yy}	Mass Moment of Inertia about y-axis	[kg·m^2]
I_{zz}	Mass Moment of Inertia about z-axis	[kg·m^2]
l	Length	[m]
m	Mass	[kg]
S	Surface area	[m^2]
S_{top}	Top surface area	[m^2]
S_{front}	Front surface area	[m^2]
T	Thrust	[N]
v	Velocity	[m/s]
α	Angular acceleration	[rad/s^2]
λ	Wavelength	[mm]
ϵ	Strain	[-]
ω	Rotational velocity	[rad/s]
ϕ	Roll	[rad]
ψ	Yaw	[rad]
ρ	Density	[kg/m^3]
σ	Stress	[MPa]
τ	Torque	[Nm]
θ	Pitch	[rad]

1. Introduction

Human presence in cave systems stretches back thousands of years, offering crucial insights into both our history and human nature itself. Cave exploration has yielded significant archaeological discoveries[1], preserving evidence of early human life, and magnificent cave paintings[2]. Long before and even after the rise of civilizations, caves served as protective shelters, shielding people from predators, harsh weather, and other threats[3].

For a long time, archaeologists have explored cave systems to gain insights into the past. However, these environments pose significant hazards, including narrow passages, toxic gases and substances, as well as the risk of landslides and sudden water surges[4]. Moreover, many archaeologists are not trained speleologists, making them particularly vulnerable to these risks.

These risks could be mitigated with an autonomous system that can remotely explore and map these cave systems, removing the need for humans to enter dangerous spaces. A team of 10 engineers from the TU Delft was assigned to design a specialized vehicle called the 'SpeleoDrone', following a request from Dr. Hayley Mickleburgh of the University of Amsterdam (UvA). Dr Mickleburgh specified that the drone would be used for looking for signs of ancient human activities in caves, in particular the caves of Isla de Mona, Puerto Rico [20]. These caves pose their own dangers, with narrow passages and significant presence of guano[5].

Following the previous phases where the workflow, design options, budgeting, and requirements were set up [7] [11], and an in-depth trade-off analysis of selected configurations and a preliminary design was conducted [6], this report covers the detailed and final design of the SpeleoDrone project.

The report begins with Chapter 2, which is a review based on previous report that mainly extends specific topics covered in those reports, including project objectives, functional assessment, user requirements & constraints, and a trade-off summary. The sustainability approach, which was a very important aspect of the design, is covered in Chapter 3. The final design is then presented in Chapter 4, including the design layout and the budget allocation & breakdown. After presenting the final design, the subsystems are discussed.

Chapter 5 discuses various payloads and their characteristics, including the camera, lens, lighting and LiDAR. Structural and material characteristics can be found in Chapter 6. Chapter 7 covers the flight performance characteristics followed by stability and control characteristics in Chapter 8. Chapter 9 shows the avionic and system characteristics.

These subsystems are followed by Chapter 10 in which the ground station and charging station are presented, alongside the communication through between the drone and user. Chapter 11 explains the manufacturing, assembly and integration of the SpeleoDrone. In Chapter 12, the final stages of the drone where the safe disposal and recycling of the system is presented as well as the life cycle of the drone. In Chapter 13, the costs of the drone are covered, as well as market involvement including return on investment. In Chapter 14, various risks are considered in the risk assessment, and mitigation methods are proposed.

Chapter 15 discussed the verification and validation procedures that were and will be used throughout the design, followed by Chapter 16 talking about post DSE activities to be performed should development continue, and finally a conclusion in Chapter 17.

[1] URL: https://news.wisc.edu/archeologists-uncover-evidence-of-intentional-burial-cave-engravings-by-early-human-ancestor/[Acc
21 May 2025]

[2] URL https://bradshawfoundation.com/lascaux/[Accessed: 24 June 2025]

[3] URL: https://nckri.org/caves/archaeology/ [Accessed: 2 May 2025].

[4] URL: [https://en.wikipedia.org/wiki/Floyd_Collins[Accessed: 20 May]

[5] URL: [https://www.707pestsolutions.com/blog/what-is-bat-guano-is-it-harmful-to-humans-and-pets/ [Accessed: 21 May]

2. Project Background

Project Background chapter introduces all important information needed to follow the rest of the report. In Section 2.1 project objectives are outlined. In Section 2.2 the functional assessment is presented. Section 2.3 provides and explains all user requirements. Section 2.4 discusses the trade-off that was performed in previous design stages in order to obtain current design configuration. Lastly, Section 2.5 provides extensive market analysis.

2.1. Project Objectives

In systems engineering project objectives are divided into primary, secondary and tertiary objectives, based on their relative importance. Primary objectives are the ones critical to the success of the mission, secondary objectives exist to support the primary objective and the tertiary objectives are additional goals that would preferably be achieved, but are not critical to the project itself.

The Project Objective Statement (POS), which encompasses the primary objectives of the project, has remained unchanged since the Baseline Report [5], and is defined as follows:

- *Design a UAS to be remotely operated by an archaeologist, capable of visually mapping a cave system while maintaining site integrity, within 10 weeks by 10 students.*

From the remaining objectives, most were incorporated into the design and fulfilled. Below the lists of secondary and tertiary objects, taken verbatim from the Baseline Report[5], can be found.

Secondary Objectives:

- Design a system that can be operated remotely.
- Design a system that is able to access any passage that an adult human can.
- Design a robust and re-usable system.
- Have a system sale price of 25,000 euros or below.
- Design a system that minimizes disturbance to cave fauna and archaeological sites during operation.
- Ensure that the system can legally operate with expedition members inside of the cave, meeting safety standards.
- Generate 3D geo-referenced maps of cave systems.
- Be able to map cave systems at a rate comparable to expeditions on foot.
- Ensure that the system is portable and can travel on airlines.

Tertiary Objectives

- Be able to bypass water obstacles in the form of flooded cave sections.
- In addition to images in the visual spectrum, produce images of archaeological sites in alternative spectra.
- The product must be 75% recyclable by weight.
- Design the product with alternative markets and modularity in mind.
- Be operable by archaeologists without specialist training.

From these objectives the two not completed are *have a system sale price of 25,000 euros or below* and *be able to bypass water obstacles in the form of flooded cave sections*. Additionally, the secondary objective *design a system that is able to access any passage that an adult human can* has not been irrefutably fulfilled either. The first objective, the one asking for the cost to be under €25,000, was quickly found to be infeasible. The corresponding requirement has been renegotiated at the midterm review phase[1] and the current price of the system is higher, which is discussed in depth in Chapter 13. The objective pertaining to traversing the flooded section was also disregarded early on in the design, as a convertible-submersible configuration was deemed too experimental and too big to be effectively used for cave mapping. Additionally, the caves of Puerto Rico don't suffer from frequent or significant flooding. Finally, the objective detailing that the SpeleoDrone is to fit in a 'human-sized' opening, the exact details of the phrase 'human-sized' were discussed vigorously. Originally, this was interpreted as 25 cm, which was found infeasible. Afterwards, this was reinterpreted to 40 cm.

[1] for more detail please consult the Midterm Report[6]

2.2. Functional Assessment

This section covers the functions the system must be able to execute, which were used to derive requirements. This goes two ways, since the required functionality stems from the user requirements.

2.2.1. Functional Breakdown Structure

The functional breakdown structure (FBS) in Figure 2.1 was used to provide a general overview of the functions the system must be able to perform to operate. The diagram consists of four color-coded levels, where the top-level functions flow down into more detailed sub-functions.

The top level consists of the functions that need to be performed between the operational life and the end of life. First, **F-0** and **F-1** describe the functions required for transportation and the preparation required before the mission can start. Then, **F-2**, **F-3**, and **F-4** detail the functions involved in performing the actual mission, including navigating the cave, processing the onboard data, and concluding the mission. Finally, **F-5** describes the functions detailing the handling of the drone after end of life.

2.2.2. Functional Flow Diagram

To describe the flow of functions performed by the system, a functional flow diagram (FFD) was created, displayed in Figure 2.2 and Figure 2.3. The FFD provides a high-level time-dependent overview of the functions of the system, supporting the FBS. The diagram is divided into three levels, with each lower level describing the higher-level functions in more detail.

The FFD covers the complete life cycle of the quadcopter. This includes the design, production, operational life, and end of life stages. First, preparations must be taken to guarantee required functionality. This includes charging the unmanned aerial vehicle (UAV), performing performance tests, and calibrating the scientific equipment. Next, the UAV must navigate through the archaeological site while processing the data it measures. To achieve this, the subsystems must provide sufficient information for navigation and control over the UAV, and provide the necessary capabilities to carry out the maneuvers, while minimizing site disturbance. Once the mission is over, the UAV must be capable of returning to the entrance of the cave, and additional testing and maintenance have to be performed in between missions. Finally, at the end of life, the components of the UAV are recycled and reused as much as possible.

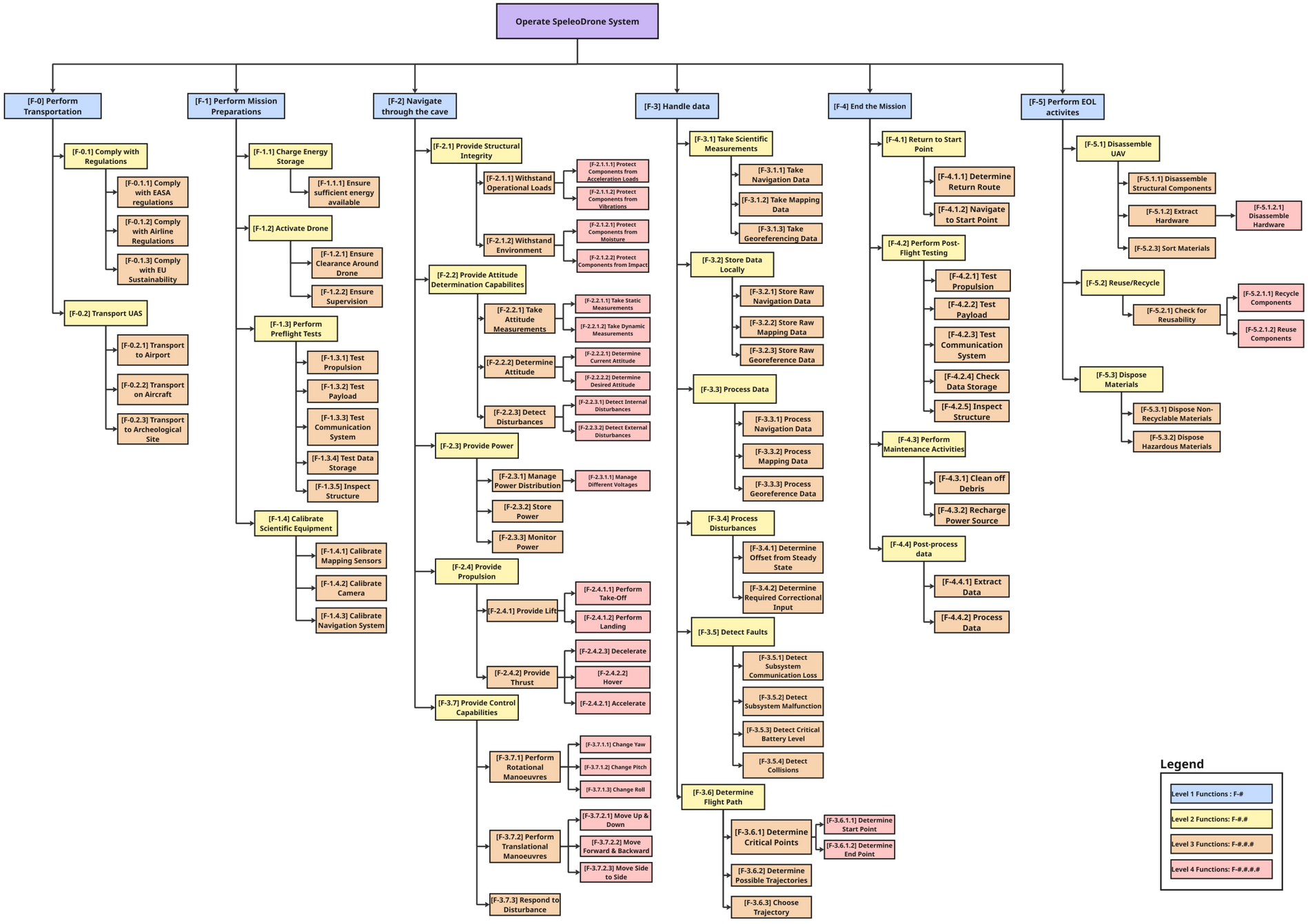

Figure 2.1: Functional Breakdown Diagram

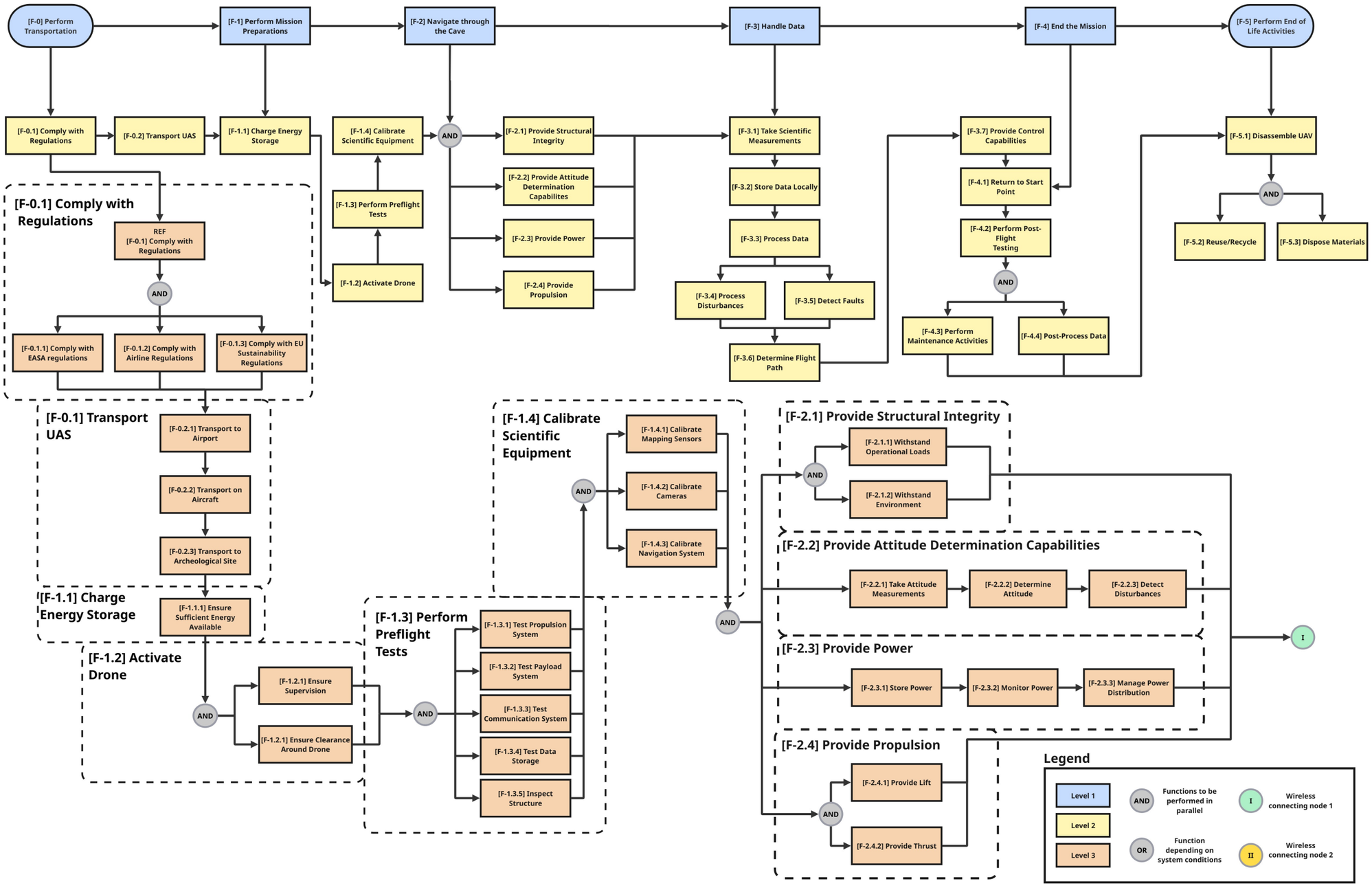

Figure 2.2: Functional Flow Diagram (First Half)

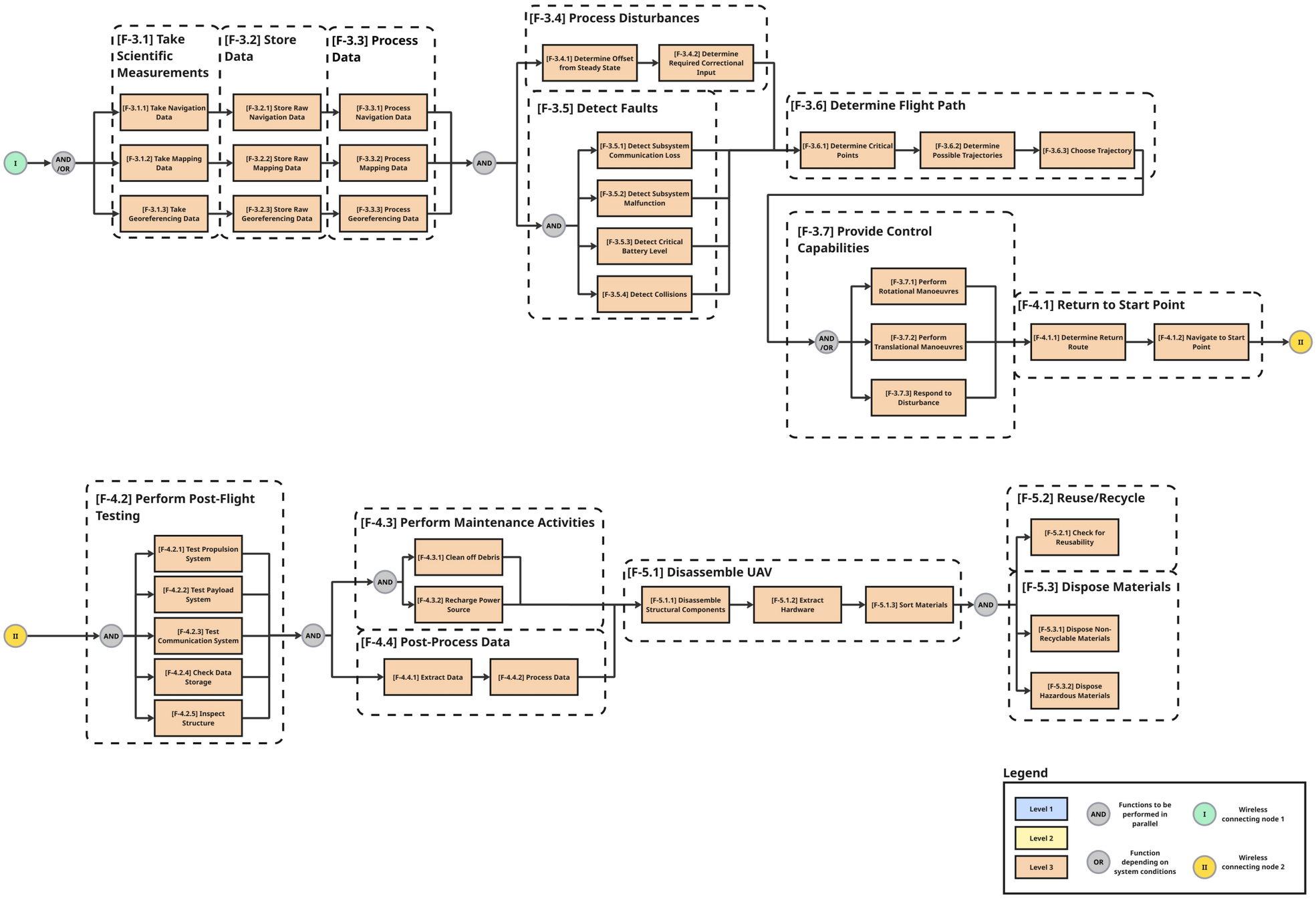

Figure 2.3: Functional Flow Diagram (Second Half)

2.3. User Requirements and Constraints

This section outlines the essential expectations and limitations defined by stakeholders for the development of the system. These requirements represent the functional and non-functional capabilities the final product must deliver, while the constraints define the boundaries within which the system must operate (e.g., regulatory, environmental, or budgetary limits).

These requirements and constraints define the expectations of stakeholders for the final product. As such, all efforts should be directed toward meeting them to ensure client satisfaction. The requirements have been categorized into three groups:

- ***Key*:** Of primary importance to the customer and define the mission objectives.
- ***Driving:*** Heavily influence the overall design of the mission.
- ***Killer:*** Initially drove the design to an unacceptable level and required renegotiation.

Table 2.1: User requirements

ID	Description	Definition
STK-DRN-1	The system shall be able to fully map a cave system distance of up to 500 m from the entrance, within 1 week	Key
STK-DRN-2	The system shall be able to visually map the cave system with a resolution of 1 cm.	Key
STK-DRN-3	The system shall be able to georeference a location on the map with a resolution of 1 cm.	Key
STK-DRN-4	The system shall be able to pass through any opening an adult human can pass through	Driving
STK-OPR-01	The system shall comply with EASA requirements for safe operation of drones.	Key
STK-OPR-02	The system shall be 75% by weight recyclable, excluding the payload	Key
STK-OPR-03	The system shall have a purchase cost of no more than €25,000	Driving/Killer
STK-OPR-04	The system shall be suitable for transportation as air cargo	
STK-OPR-05	The system shall be able to operate in a remote location (i.e. no access to grid power or cellular telephone networks)	Driving
STK-OPR-06	The system shall not produce any emissions inside the cave system.	Driving
STK-OPR-07	The system shall minimize disturbance to the site being investigated	Key
STK-OPR-08	The system shall be designed to be operable with minimal training	Key

Out of the initial set of eight requirements, several required further specification:.

1. **STK-DRN-1**: ”One week” was defined as 56 operational hours (7 days × 8 hours). Mapping is limited to areas accessible as per **STK-DRN-4**—i.e., through openings large enough to pass through safely.
2. **STK-DRN-2** and **STK-DRN-3**: Both visual mapping and georeferencing are limited to accessible areas.
3. **STK-DRN-4**: The minimum passable opening was defined as having a width of 40 cm.
4. **STK-OPR-01**: Key operational constraints include integration of a remote identification system, a mass below 25 kg, avoidance of flight over uninvolved people, and a maximum flight altitude of 120 m.
5. **STK-OPR-03**: After market analysis and budget assessment, the original €25,000 cost ceiling was found to be unfeasible and was renegotiated to €50,000.
6. **STK-OPR-04**: The system’s batteries must comply with commercial airline regulations, meaning each battery should have a capacity below 160 Wh to be eligible for air transport. Packaging should prioritize compliance with airline size and weight limits, while also ensuring portability—each component should be light enough (ideally under 16 kg) and ergonomically designed for manual carriage across difficult terrain.
7. **STK-OPR-08**: ”Minimal training” implies the system must be operable by amateur users with limited experience.

A summary of how these requirements were addressed is provided in Section 15.3.

2.4. Trade-off Summary

In the Midterm Report [6], the trade-off for the design of the SpeleoDrone was conducted. It started off by looking at the viable options from the Design Option Tree (DOT) from the baseline report [5]. Then, a Weakness of Survivors Analysis (WSA) was performed, from which the final design options for our trade-off analysis could be chosen. These were then assembled to form four design configuration, presented in Table 2.2.

Table 2.2: Proposed four configurations

Design Segment/Configuration Option	Configuration 1	Configuration 2	Configuration 3	Configuration 4
[PROP] Propulsion configuration	Helicopter	Submersible drone	Helicopter	Quad-copter
[RM] Rotor Motion	Fixed Arm, Variable Pitch	Variable Arm, Variable pitch	Fixed Arm, Variable Pitch	Fixed Arm, Variable Pitch
[ENRG] Energy Source	Rapid Recharge Battery	Switchable Battery	Hydrogen	Switchable Battery
[DRC] Drone Control	Hand-held Control	Major AI Control with Forced User Input	AI Safety Features	Operator-in-the-loop

It was decided that because the payload doesn't have impact on the other aspects of the drone, it would be traded-off separately. The payload trade-off took place before the system trade-off and was there to identify the optimal instruments to be used in the SpeleoDrone.

In order to simplify the payload trade-off even more, it was split into two separate trade-offs, one regarding the 3D mapping instrument and one for the imagery payload. The winners of both trade-offs were then combined into one winning payload configuration. For the 3D mapping payload, the criteria used were the resolution, the mass and the cost. The trade-off was done between a LiDAR and a single-chip radar. The LiDAR won the trade-off. For the imagery payload, the criteria used were cost, mass, resolution, application and light exposure. Two cameras came out favorable in the payload, a VIS + NIR camera and a UV camera, so both were chosen as payload.

System trade-off was then conducted. The criteria chosen for the system trade-off are as follows:

- **Endurance (5/5):** The maximum time the drone can spend flying. In this criterion the propulsion configuration had the biggest impact on the final score.
- **Navigation & Control (5/5):** The determining factor for this criterion was the maneuverability of the drone and its precision
- **Size (2/5):** Maximum dimension was considered, with smaller configurations being preferable
- **Cost (2/5):** the cost of producing the drone, including the estimated cost of manufacturing and the cost of developing an autonomous navigation model
- **Environmental Impact (3/5):** Encompassing the production and operations, assessed the amount of emission generated during the life cycle of a drone as well as site disturbance or impact on local wildlife
- **Technology Readiness Level (3/5):** Standardized scale for technology maturity

For each of the six criteria, each configuration was assigned one of the four possible scores- *excellent*, *good*, *acceptable deficiencies* or *unacceptable*. The scores, multiplied by the weight of each criteria, then summed up to a final results, presented in Table 2.3.

Table 2.3: System Trade-Off Results

Configuration	Score	Corresponding Score
Configuration 1	2.65	Acceptable with Deficiencies
Configuration 2	1.85	Unacceptable
Configuration 3	2.35	Unacceptable
Configuration 4	2.8	Good

Configuration 4 has clearly won the trade-off. Afterwards, the decision was made to remove the drone cage due to maneuvering constraints, and the winning payload was integrated into the design. The overview of the final conflagration can be found in Table 2.4. Additionally, to ensure the winning configuration is indeed the most optimal one, a sensitivity analysis was carried out, in which the weights of different criteria were changed around to confirm the chosen configuration would loose if the team prioritized different aspects a bit more. The conclusion of the sensitivity analysis was that configuration four is indeed the best one.

Table 2.4: Winning Configuration Overview

Design Segment	Solution Chosen
Propulsion Configuration	Quadcopter
Rotor Motion	Fixed Arm
Energy Source	Switchable Battery
3D Mapping Payload	LiDAR
Imaging Payload	UV Camera & VIS+NIR Camera

2.5. Market Analysis

In order to gain a competitive edge, and to evaluate the commercial potential of the SpeleoDrone, a comprehensive market analysis was conducted to assess its potential value, identify key competitors, and define target sectors where the system's unique capabilities could offer a clear advantage. As the drone itself is a custom product developed at request, the product is quite niche. Although at first sight this could be seen as a negative, it can also be seen as a positive, due to competition also being very small.
These existing competitors were also considered in the market characterization, after which the market expansion opportunities were considered, followed by the identification of a wide range of stakeholders, and finally the product analysis, which consisted of a 'SWOT'-analysis and a 'Product life cycle'-analysis.

2.5.1. Market Characterization

The first thing considered was the market size. The market size of SpeleoDrone consists of the total number of potential customers within the archaeological cave exploration industry. As can be imagined, this market is very niche. Potential customers primarily include archaeological research institutes and archaeologists specializing in cave exploration. The potential to increase the market size is notable, as will be discussed in Subsection 2.5.2. To give an indication of the growth of the drone industry in general, the drone market was 14.1 billion dollars in 2018, and had the prospect of threefold growth by 2024 [30]. This highlights the significant growth potential within the drone industry, and consequently, the potential niche that SpeleoDrone occupies within it. More recent estimations on the drone market indicated an even higher evaluation, where the market size in 2024 was estimated to be 58.5 billion [2]. As of 2025, recent military developments, particularly highlighted by the Russia-Ukraine conflict, have driven rapid innovation in drone technology. One example is the growing use of fiber optic communication in military drones[3] , which may transition into civilian and commercial applications in the near future, potentially benefiting systems like the SpeleoDrone. [4] [5] Estimating the number of caves with archaeological significance is challenging due to limited global data. However, in England, one of the few regions where systematic cave recording has been conducted, over 4,000 caves are known and studies suggest that approximately 10–20% of these may contain archaeological deposits [33]. This rough estimation could give an idea of the potential usefulness of SpeleoDrone. The number of unexplored cave systems worldwide is difficult to estimate. However, cave databases highlight the vast global presence of large cave systems, many of which remain only partially explored.[6]. With this vast amount of cave systems globally, and the high amount of archaeological deposits in them, there is strong potential demand for autonomous cave exploration tools. The research institutes listed in Table 2.5 represent just a small sample of the global organizations involved in cave archaeology or speleology. Many countries have national archaeological bodies or speleological societies, and major universities with anthropology or archaeology departments often conduct fieldwork in caves.

Based on this broader global landscape, it is estimated that there are approximately 50 institutions worldwide with both the interest and financial capacity to acquire a system like the SpeleoDrone. This estimate includes national research centers, large academic institutions, and private foundations that conduct or fund archaeological expeditions.

[2] URL: https://www.zionmarketresearch.com/report/drone-market-size?, [Accessed: 24 June 2025]
[3] URL: https://www.economist.com/europe/2025/05/05/how-new-drones-are-sneaking-past-jammers-on-ukraines-front-lines, [Accessed: 13 June 2025]
[4] URL: https://www.nato.int/cps/fr/natohq/declassified_215371.htm?msg_pos=1, [Accessed: 13 June 2025]
[5] URL: https://kyivindependent.com/what-to-expect-from-ukraines-defense-innovation-in-2025/, [Accessed: 13 June 2025]
[6] URL: https://www-sop.inria.fr/agos-sophia/sis/DB/database.html, [Accessed: 13 June 2025]

Table 2.5: Prominent research institutes interested in cave exploration.

Institute/Organization	Location
National Cave and Karst Research Institute (NCKRI)	Carlsbad, New Mexico, USA [7]
Cueva de Nerja Research Institute (IICN)	Nerja, Spain [8]
Office of the State Archaeologist (OSA), University of Iowa	Iowa, USA [9]
Chauvet-Pont d'Arc Cave Research Team	Ardèche, France [10]
Cave Research Foundation (CRF)	United States (national)[11]
Union Internationale de Spéléologie (UIS) – International Union of Speleology	Global (headquarters in Postojna, Slovenia) [12]
Foundation for the Preservation and Exploration of Caves (FPEC)	Kyrgyzstan [13]
National Speleological Society (NSS)	United States (national)[14]

The competition is also very important to consider. The amount of competition determines the pace of innovation, pricing strategies, market entry barriers, and how quickly a dominant design may emerge. The competition for (commercially) automated cave exploration is almost non-existent. Due to specific conditions, unique to the environment the drone will operate in, it is not possible to just buy a Commercial-Off-The-Shelf (COTS) drone, meant for other purposes and fly it around the cave. Primary concerns would be the ability to communicate with the drone. Most commercial drones require some degree of human control, but contact with such a drone would be lost in the cave without significant modifications being made. Additionally, most commercial drones would have only part of the requested payload, not all required elements to identify archaeological finds and map the cave extensively.

A competitor analysis was conducted based on drones previously used for cave exploration[15]. Due to the limited number of drones specifically designed for this application, the analysis was broadened to include general 3D mapping drones[16], as they share similar payload and operational characteristics with those used in cave environments. Table 2.6 below shows these drones, and their respective size, cost and endurance.

Table 2.6: Competitor analysis table

Drone	Type	Used in caves	Size [cm]	Cost [€]	Endurance [min]
Elios 3 [17]	Quad	✓	48.0 x 48.0 x 38.0	45,000	12.5
Elios 2 [18]	Quad	✓	38.0 x 38.0 x 38.0	35,000	9
DJI Matrice 300 RTK [19]	Quad	✓	81.0 × 67.0 × 43.0	30,572	55
Acecore Zoe [20]	Quad	✓	114.2 x 113.8 x 56.5	19,900	47
Ziyan Ranger P2X UAV [21]	Heli	X	169.0 x 24.7 x 49.5	N.P.A	120
Velos V3 [22]	Heli	X	172.0 x 62.0 x 73.0	N.P.A.	80
INF Galaxy [23]	Heli	X	180.0 x 55.0 x 58.0	N.P.A.	45
UAVOS UVH-25EL [24]	Heli	X	267.0 x 67.0 x 260.0	250,000	90
Parrot Anafi USA [25]	Quad	X	28.2 x 37.3 x 8.2	1200	25
DJI Mavic 3 [26]	Quad	X	26.6 × 32.5 × 10.6	1,400	45
DJI Air 3S [27]	Quad	X	21.4 × 10.1 × 8.9	1,530	41
Autel EVO 2 Pro RTK V3 [28]	Quad	X	56.3 × 65.7 × 14.7	5,599	42
Autel EVO Max 4T XE [29]	Quad	X	57.6 x 66.0 x 14.9	9,000	42

[7] URL: https://www.nckri.org/ [accessed: 16 June 2025]
[8] URL: https://www.cuevadenerja.es/en/research-institute/ [accessed: 16 June 2025]
[9] URL: https://archaeology.uiowa.edu/annual-report [accessed: 16 June 2025]
[10] URL: https://archeologie.culture.gouv.fr/chauvet/en [accessed: 16 June 2025]
[11] URL: https://www.cave-research.org/ [accessed: 16 June 2025]
[12] URL: https://www.uis-speleo.org/ [accessed: 16 June 2025]
[13] URL: https://www.fpec.kg/ [accessed: 16 June 2025]
[14] URL: https://caves.org/ [accessed: 16 June 2025]
[15] URL:https://dronesdeli.com/blogs/blog-posts/the-best-drones-for-exploring-caves-and-underground-areas, [Accessed: 12 May 2025]
[16] URL: https://surveytransfer.net/51-best-drones-for-3d-mapping-in-2024/ [accessed: 14 May 2025]
[17] URL: https://www.flyability.com/blog/elios-3-vs-elios-2, [Accessed: 13 June 2025]
[18] URL:https://e38surveysolutions.com/collections/dji-matrice-300-350-rtk?srsltid=AfmBOor5GMIG_GIqcL8rDgtTGVPHPfp3IBh7yKTa5810wDk6j2yUCPU3,[Accessed: 13 June 2025]
[19] URL: https://store.dji.com/nl/product/matrice-300-rtk-and-dji-care-plus?vid=111261,[Accessed: 13 June 2025]
[20] URL: https://acecoretechnologies.com/models/,[Accessed: 13 June 2025]
[21] URL: https://www.ziyanuas.com/products/FlightPlatforms/xiazai [accessed: 13 May 2025]
[22] URL: https://velos-rotors.com/home/products/velos-v3/ [accessed: 13 May 2025]
[23] URL: https://www.unmannedsystemstechnology.com/company/innoflight-technology/galaxy/ [accessed: 12 May 2025]
[24] URL: https://www.uavos.com/uavos-introduces-uvh-25el-lidar-mapping-uav/ [accessed: 13 May 2025]
[25] URL: https://www.parrot.com/en/drones/anafi-usa/technical-specifications [accessed: 15 May 2025]
[26] URL: https://store.dji.com/nl/product/dji-mavic-3 [accessed: 15 May 2025]
[27] URL: https://www.dji.com/nl/air-3s/specs [accessed: 14 May 2025]
[28] URL: https://www.autelrobotics.com/productdetail/evo-max-series/#jsgg [accessed: 15 May 2025]
[29] URL: http://autelrobotics.com/productdetail/evo-max-series/#jsgg [accessed: 15 May 2025]

One of the drones mainly used in cave exploration is the DJI Matrice 300. The DJI can provide a centimeter-level accuracy and has a very good endurance with an operating time of roughly 55 minutes. Unfortunately, the drone is quite sizable, with a width of 810 mm and can thus not fit trough narrow areas in the caves. Similar issues exist with Acecore Zoe.

The most likely competitor of the SpeleoDrone is the Flyability Elios drone series. Elios 2 has been used in cave inspections and its successor, Elios 3, is used for inspections of mines and nuclear reactors. Its also equipped in a LIDAR, one of the possible payloads considered for the SpeleoDrone. Additionally, it has a cage surrounding it, which protects it from possible damage.

Fortunately, an opportunity for the SpeleoDrone to outcompete Elios 3 was identified. According to technical documentation of the product[30], its endurance is limited to around 12.5 minutes, depending on the payload and conditions. That translates into a maximum range of 450 m, below the endurance SpeleoDrone could provide, which is roughly 18.5 minutes. As such, if the endurance can be improved, SpeleoDrone could replace Elios 3 in a lot of its use cases. Additionally, the size of almost 50 cm would limit the accessibility of the narrower passages to the Elios 3 drone. SpeleoDrone has a width slightly smaller than 40 cm,further improving its standing in the market. The Elios 3 and 2 have prices starting from 35,000 euros, one sale of the SpeleoDrone would cost about 41,000 euros, and when more drones would be produced, the cost could go down to around 30,000 euros. This lower production price would make it possible for the SpeleoDrone to capture a significant portion of the Elios market, thanks to its comparable cost and an endurance that is approximately 33% longer.Additionally, a major advantage is that the SpeleoDrone does not rely on grid energy—it can be charged off-grid thanks to its integrated solar panels.

Other options for automated cave exploration currently consist of terrestrial and aquatic vehicles, which are largely unavailable commercially and function more as proof-of-concept technologies than market-ready products. [31]. This absence of competition serves as an opportunity to develop a product that can commercially serve this niche. The proof of concept has been demonstrated by mapping archaeological finds within a cave environment and by general mapping of a cave system [4] [57]. Translating this capabilities into a drone small enough to fit through openings no previous drone could explore, could boost the efficiency of archaeological studies around the world.

Comparing the supply and the demand, it can be noted that both are very small. The supply is almost non-existent and the demand is low due to the product fulfilling a specific niche. Once the product is introduced, it could fill up the niche market and the demand within this niche would be able to grow. If the product is made modular in a sense that it can also serve multiple purposes, as discussed in Subsection 2.5.2, the demand for SpeleoDrone can be considerably increased. A significant weakness of SpeleoDrone sales lies in the customer's heavy reliance on funding from academic grants and university research budgets, which are inherently unstable. This type of funding is highly susceptible to fluctuations driven by global economic conditions, shifting governmental priorities, and changes in national or institutional research policies. As a result, there is a substantial risk of funding cuts or delays, which would directly impact sales opportunities and demand.

2.5.2. Market Expansion Opportunities

The possibility of expanding into different markets was considered, which could be possible with relatively low effort. One such example would be to advertise the drone for general archaeological work in other potentially hazardous regions, such as old structures that might collapse or that should be kept as uninterrupted as possible. Another possible market that could be reached, but would require more significant design changes, is working in more extreme conditions, for example near volcanoes or in radiation zones. The drone would have to be modified more, to ensure all components are radiation / extreme heat resistant, but it is a possibility that could be considered.

In addition to archaeologists, the drone can also appeal to other groups interested in cave exploration, such as geologists and amateur speleologists, by serving as a valuable tool for mapping cave systems. A broader, more large-scale application of this technology could be its use in underground mine inspection and mapping, offering similar functionality in a more industrial context. The mining application is regarded as one of the most promising areas for demand growth [30].

Of course, some modifications would have to be done in order to allow for this application of the drone, but it should be possible. The previously mentioned Flyability Elios drone, Elios 3 in particular, is used for inspecting mines when a hazard is suspected. SpeleoDrone, retrofitted with a different payload, could possibly pose competition to this drone, as Elios 3 only has a total flight time of 12.5 minutes [32]. SpeleoDrone has a longer

[30] See Table 17

[31] URL: `https://www.sciencefocus.com/news/to-boldly-go-meet-the-extreme-robot-explorers` [Accessed: 1 May 2025]

[32] URL: `https://www.flyability.com/blog/mine-drone` [Accessed: 16 June 2025]

endurance, meaning if the project is successful, SpeleoDrone could undermine Elios 3 and enter the mining market as well. A similar argument can be made for inspections of nuclear power plants, which are also sometimes carried out by a configuration of the Elios 3 drone [33].

2.5.3. Stakeholders

Next, the stakeholders had to be identified. All parties that have some ties to the project were considered. Next their connection to the project was evaluated on two axes; interest and impact. This led to creation of the stakeholder map, seen in Figure 2.4.

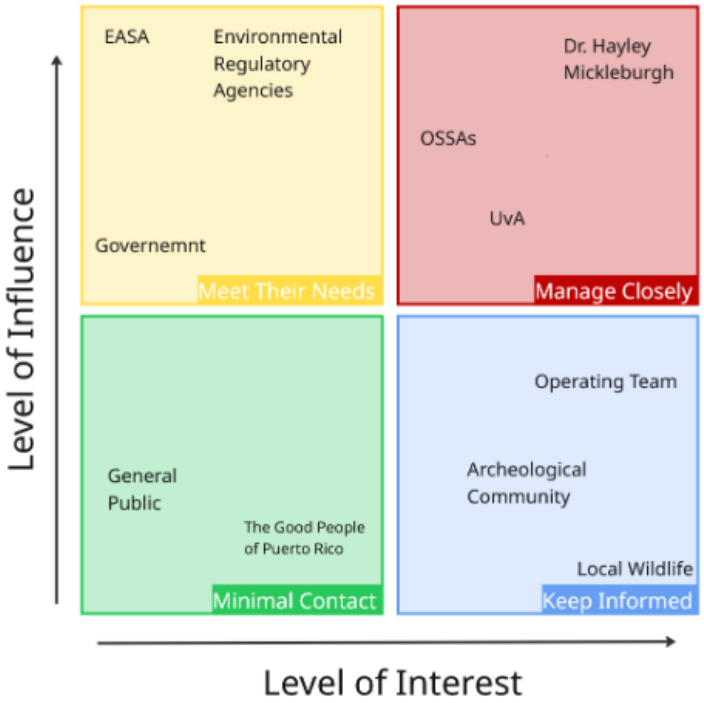

Figure 2.4: Stakeholder Map

The stakeholder map is a tool used to evaluate the most important stakeholders (also known as key stakeholders), and to plan an approach to each stakeholder. For example, for stakeholders that have a low interest in the project but have a high level of influence, such as regulatory agencies, there is no need for constant contact. The team has to, however, monitor them to make sure their needs are met (such as drone regulations imposed by EASA).

The key stakeholders identified by the means of inspecting the stakeholder map are Dr. Hayley Mickleburgh, as the main client, EASA, as the main regulatory body the project will be constrained by and the local wildlife. The last stakeholder was determined to be a key one due to its specific situation- it will be massively impacted by the project, but it has no way of influencing it. As such, it was decided that the needs of the local wildlife will be considered with higher scrutiny. This also ties into the sustainable policy of the project.

The reason why EASA in particular is mentioned here, despite the focus of the operations being Puerto Rico, is that the drone will be purchased and used by the University of Amsterdam, meaning it will have to be certified in Europe. Also requirements imposed by the Federal Aviation Administration (FAA) and by EASA are incredibly similar, so it should not be a problem.

2.5.4. Product Analysis

SWOT Analysis

In order to clearly assess the product and highlight its impact on or from the market, a SWOT analysis was done. This study describes the **S**trengths, **W**eaknesses, **O**pportunities, and **T**hreats the product might experience and illustrates them in a 2 x 2 matrix, Figure 2.5.

[33] URL: `https://www.flyability.com/nuclear-inspection-drones` [Accessed: 16 June 2025]

	Positive	Negative
	Strengths	Weaknesses
Internal	• High quality. • Easily modifiable. • One confirmed customer. • Focused design team. • Targets a niche.	• Nicheness makes it difficult to research and find statistical analyses. • Reliability is unexplored. • Difficult to operate.
	Opportunities	Threats
External	• No established competition. • New cave/archaeological discoveries. • Increase in public interest in archaeology.	• Removal of grants/funding. • Introduction of new environmental regulations. • Introduction to new competition.

Figure 2.5: Product SWOT Analysis

The strengths and weaknesses are considered to internally address the business and its individuals, while the opportunities and threats are external effects on the business.

Product Life Cycle

Considering the four product life cycle phases, shown in Figure 2.6[2], the drone market is transitioning from the introduction/launch phase to the growth phase, marked by increasing consumer adoption and the emergence of more standardized product designs. Although many segments of the market remain in early development, growing investment, improved product usability, and broader applications signal a shift toward growth. This phase involves increasing competition, expanding customer bases, and greater market consolidation, although innovation and uncertainty remain significant[33]. Significant innovation continues to take place in the military sector, with many of these advancements gradually making their way into commercial applications.

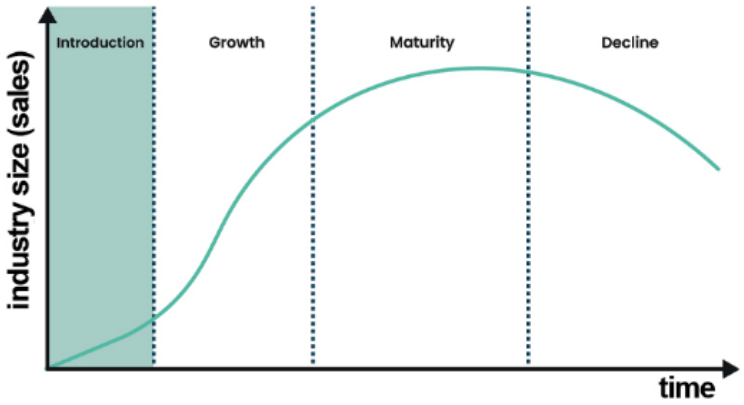

Figure 2.6: Product Life Cycle Phases.

The cave exploration drone market is highly niche, with no company yet having launched a dedicated product specifically for this purpose. As such, it remains firmly in the early stages of the introduction phase. This stage would be identified specifically as the incubation phase, until the market entry of SpeleoDrone marks the first targeted offering in this segment.

Dangers in failing during the launch phase include major technical problems, poor market research, an over-priced product, late development and other new products outperforming SpeleoDrone. Having a good understanding of these common pitfalls is crucial in succeeding in the market.

Further along in the product life cycle of SpeleoDrone, should sales volume increase, a drop in production costs would be expected. The holistic modularity of the drone, with slight adaptions for specific modules, would allow the product to be utilized for other (niche) purposes like exploring hazardous structures, surveying factory equipment or other difficult to access areas.

[33]URL: `https://www.open.edu/openlearn/mod/oucontent/view.php?id=144886&section=3.1` [Accessed: 2 May 2025].

3. Sustainable Development Strategy

A Sustainable Development Strategy for the design process was established at the beginning of the project. This strategy identifies four main sustainability aspects to guide the design: circularity, emissions and energy use, durability, and site disturbance. For each of these aspects, requirements were formulated to clearly define sustainability goals that the design process should aim at. Also, these requirements serve as indicators for tracking progress.

3.1. Key Sustainability Aspects

Circularity was selected as one of the key aspects to ensure an extended system lifetime. For this, the R-ladder, a tool summarizing various strategies that can be applied for the improvement of the circularity[1], was used as inspiration to increase the level of circularity. The main approaches that were selected are recyclability, repairability, and repurposability.

Emissions and energy use over the full life cycle of the product – including material preparation, manufacturing, transportation, use, and disposal – will serve as a quantitative method to measure sustainability. The aim is to minimize emissions and energy consumption throughout this life cycle, and to compare the values to other UAVs on the market. Additionally, stakeholder requirements specified that no emissions shall be produced inside the cave environment, which necessitates the choice of an emission-free propulsion system. A further requirement ensuring that the system will be chargeable on-site by a renewable energy source was introduced.

For durability, the focus lies on expanding the system's operational life by minimizing the risk of damage or malfunctions. This was translated into specific requirements related to the protection of exposed components, implementing obstacle identification and avoidance systems, and incorporating a Return-to-Home function. Also, the need for guidelines on pre- and post-flight operations to further increase the system's reliability was incorporated.

Site disturbance is important given that the target cave locations for missions are the habitat of a rich variety of flora and fauna, such as frogs, goats, insects, and bats [49]. The encountered species when investigating cave sites should be handled with care, and disturbance and harm should be minimized. This was translated into requirements concerning noise levels, light intensity, and the wavelengths of emitted light.

3.2. Implementation During the Prior Design Stages

In the initial design stage, sustainability requirements were formulated based on the strategy described in Section 3.1 as a baseline to guide the design in a sustainable direction. The requirements ensured that the strategy was incorporated into the performed system configuration trade-off. For the payload trade-off, the impact of different types of imagery was looked into. And in the system trade-off, sustainability was present as a trade-off criterion by its own. To cover all aspects of the sustainability strategy in this criterion of environmental impact, the following sub-criteria were used: site disturbance, emissions, durability, repairability, and recyclability.

3.3. Integration of Sustainability Key Aspects in Final Design

How sustainability is integrated into the final design is summarized here based on the four key aspects from the sustainability approach.

Circularity

The propellers and landing gear are designed to be easily replaceable in case of damage, ensuring the system can be quickly repaired on site. Also, materials for the main structure of the drone were chosen in order to allow recyclability of the drone of at least 75% by weight.

Durability

Ducts were added around the propeller for noise reduction reasons, but these will also serve as protection of the propellers in case of collision, making the design more durable. Also, maintenance checks were incorporated to ensure on-time fault discovery.

[1] URL `https://www.rvo.nl/onderwerpen/r-ladder` [cited 2 May 2025].

Site Disturbance

For communication with the ground station, a fiber optic cable is needed. A novel biodegradable sleeve was designed around the fiber optic cable that will allow for retrieval of the cable, which decreases the site disturbance compared to leaving a fiber optic cable in the cave.

The noise levels for the selected configuration were estimated using a semi-empirical method. This resulted in levels between 65-73 dB. To further reduce the noise, ducts were added around the propellers. The ducts result in reduced relative noise, due to decreasing tonal components and increasing broadband noise. This will make the noise perceived as less disturbing due to the relevant noise level of the tonal components being lower with respect to the broadband noise.

Emissions

Emissions inside of the cave are zero during operations because of the choice of battery as a power providing system. Therefore, compliance with requirement STK-OPR-06 has been achieved. To additionally keep the emissions to zero on site outside of the cave, a solar panel charging station was designed that will charge the various batteries used and computers needed for the ground station.

Lastly, a life cycle assessment (LCA) of the design system was performed using the Eco Audit Tool of the material database software Granta EduPack [3]. This provided a value for the emissions related to the design's full life cycle. The LCA results are presented and analyzed in Section 12.2 and recommendations for the future design stages are formulated.

4. Design Configuration

4.1. Design Layout

This section presents an overview of the final design, shown in Figure 4.1. For actual dimensions, the technical drawing can be seen in Appendix B. The colors in the figure are not representative of the actual drone but are intended to clearly indicate the location of each component. The drone's operation is described in detail in Chapter 10. In brief, the drone is powered by two batteries and connected to a ground station outside the cave via a fiber optic cable for data transmission. It autonomously navigates into the cave and begins scanning the environment. To capture "hidden areas" out of the drone's direct line of sight, the payload module rotates independently rather than reorienting the drone itself. The entire system is powered by solar panels located at the external ground station.

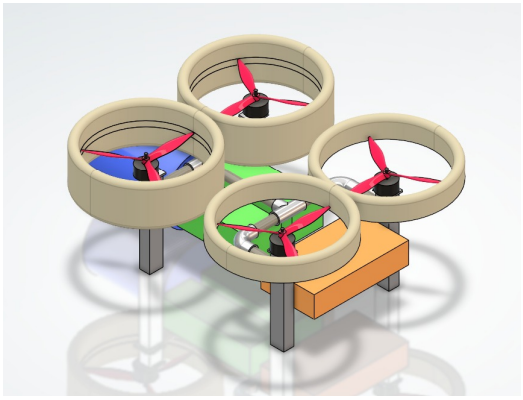

(a) Drone Representation

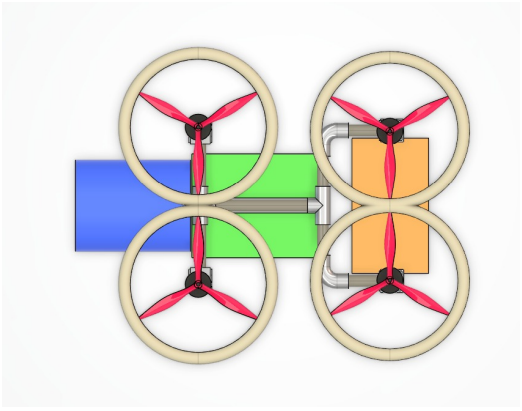

(b) Top View

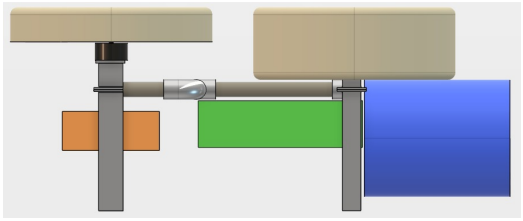

(c) Side View

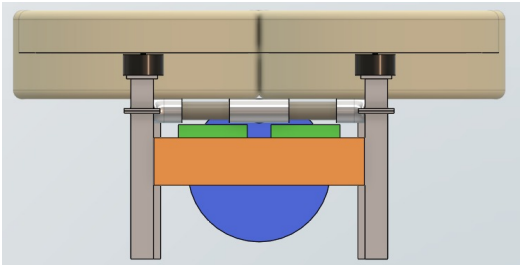

(d) Front View

Figure 4.1: The drone visualized from various angles

The propellers in red are surrounded by foam ducts in beige to increase thrust efficiency and reduce noise. The front ducts are smaller compared to the back ones in order to provide the required field of view for the payload. The motors are attached to the main body in gray, alongside the legs/landing gears of the drone. The characteristics of the propellers, foam ducts, and the motors are presented in detail in Chapter 7. The landing gears are further explained in Chapter 6, as well as the structural characteristics of the entire frame. The payload module, shown in orange, is positioned at the front of the drone. The payload module is connected to the front landing gear via a pivot point, allowing it to rotate freely. Within this module, a visible light camera, lens, flashlight, and a visible to short wave infrared camera are present. This is presented thoroughly in Chapter 5, and the layout of the payload can be seen in Figure 4.3. The drone's two batteries are visualized in green. Finally, the housing for the drone's fiber optic cable connection to the ground station is visualized in blue. The entire electrical block diagram is visualized in Figure 4.2.

The hardware components, such as electronic wiring, are distributed across the modules but are not shown in the images to maintain clarity and provide an unobstructed overview. More details are provided in Chapter 9. The ESC, IMU, flight controller, GPS module, and remote ID sensor are mounted together as a single subassembly attached to the main frame, positioned centrally above the batteries. The temperature and humidity sensors are placed just outside this electronics cluster but remain close to it. One of the two time-of-flight (ToF) sensors is mounted nearby, while the other is located beneath the battery pack.

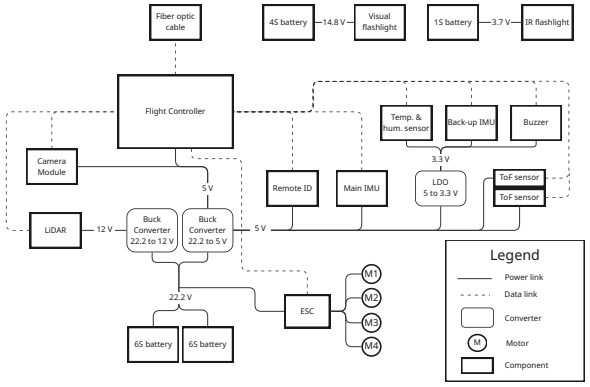

Figure 4.2: Electrical Block Diagram

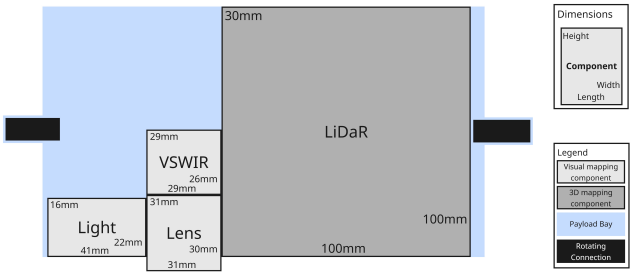

Figure 4.3: Top view of the payload bay, pointing downwards towards the front of the drone.

4.2. Budget Allocation & Breakdown

In order to obtain first order sizing estimates, rough estimates of values such as mass and power consumption had to have been calculated. In the Baseline report, a detailed outline of the predicted mass and power budgets was presented, alongside the power and mass predictions for each subsystem. These predictions were obtained using parameters such as mass fractions of existing drone systems similar in size as well as from literature. After a number of design iterations, both the mass as well as power consumption values converged to more accurate values. The mass of the drone was calculated by gathering manufacturer's specifications on each component and/or possibly calculating them, such as for structural mass. The cables, IMU, and buck converters within were not calculated but are assumed to be within the contingency. The mass budget is presented in Table 4.1. In similar manner, the power usage of all the components at nominal operation were cataloged and/or possibly calculated them through the specifications given by the manufacturers. Cable losses and other such factors that were not directly power consumed by the components were ignored and assumed to be within the contingency. Additionally, the pointing mechanism is considered negligible since the small magnitudes of the inertia and dimensions of the payload module leads to a power in a magnitude of micro-Watts to rotate it to 1 RPM in 5 seconds. Additionally, the power required to keep it in place, assisted by friction, would thus be smaller. As such, all powers in magnitude of micro-Watts are less are considered negligible. The power budget is presented in Table 4.2.

Table 4.1: Final Design Mass Budget

Components	Mass (grams)
Camera	40
Lens	55
LiDAR	360
Flashlight	91
Hygrometer + Thermometer	48
Payload + Sensors	**594**
4 Motors	190
4 Propellers	32
4 Propeller noise foam ducts	80.5
FCU	15
Propulsion and Control	**317.5**
Fiber optic reel and housing	235
Fiber optic snake skin	35
Fiber optic decoder	30
Communication	**300**
ESC	17.5
ESC foam cover	10
2 Batteries	1440
Power	**1467.5**
Structural Mass	**350.9**
Total Power	**3029.9**
Payload + Battery Contingency	2%
Contingency	10%
Total Power + Contingency	**1073.07**

Table 4.2: Final Design Power Budget

Components	Power (W)
Camera	2.6
LiDAR	8
Visual light	8
IR light	2.1
Pointing mechanism	Negligible
Payload	**20.7**
Main IMU	0.36
Red. IMU (with board)	0.041
ToF x 2	0.7
Tem. Hum. Sensor	Negligible
Sensors	**1.1**
Remote ID	0.21
GPS	0.015
Buzzer	Negligible
Misc	**0.23**
Motors @ 35 deg, max range	1030
Propulsion	**1030**
Total Power	**1052.03**
Contingency	2%
Total Power + Contingency	**1073.07**

5. Payload Characteristics

The first subsystem analysis concerns the payload elements, their specifications, and their limitations to the drone's performance. Prior to this phase in the design, the payload needed to fulfill the user requirements set at the beginning of the design phase was selected. This came to a final choice of one Visible to Short-Wave Infrared (VSWIR) camera used to visually map the cave's walls and interiors, and a Light Detection and Ranging (LiDAR) module to map the topography of the cave. All components of the payload are explained in more detail in Section 5.2

5.1. Sub-system Requirements

Before deciding on specific payload elements, some sub-system requirements need to be set in order to carry out the mission successfully. These requirements stem from mission and system requirements previously appointed and restated in Appendix A. Of the following requirements, the most limiting were those restricting the physical size and mass of the payload bay.

Table 5.1: Payload Requirements

Identifier	Description	Upstream Requirement ID
PL-DRN-01	The maximum speed of the drone when visually mapping shall be below 0.7 m/s.	MIS-DRN-1.2
PL-DRN-02	The maximum speed of the drone when 3D Mapping shall be below 0.7 m/s.	MIS-DRN-1.2
PL-DRN-03	The payload components shall be fully operable in temperatures up to 37 degrees Celsius.	MIS-DRN-1.5
PL-DRN-04	The resolution of the camera shall be finer than 1 cm.	MIS-DRN-2.1 and 2.2 and 3.1
PL-OPR-01	All payload components shall be retrievable within 1 week from the beginning of the mission.	MIS-OPR-7.3
PL-OPR-02	The payload shall be fully operable in light conditions under 6000 lux	MIS-OPR-7.4
PL-OPR-03	The light emission of the payload shall be below 10000 lux.	MIS-OPR-7.6 and 7.8
PL-OPR-04	The payload shall require no more than 30 Wh per mission.	MIS-OPR-11.2
PL-DRN-05	The payload shall have a minimum data rate of 9000 bit/s to ensure complete cave mapping within total mission time	SYS-DRN-1.3.2
PL-DRN-06	The payload shall have a maximum data rate of 9000 bit/s to ensure complete data transfer.	SYS-DRN-1.3.2
PL-OPR-05	The combined size of the payload shall be below 18 x 10 x 4 cm^3	SYS-OPR-5.1.1
PL-OPR-06	The combined mass of the payload shall be below 750 g.	SYS-OPR-5.1.2
PL-OPR-07	The noise emission of the payload shall be below 85 dB.	MIS-OPR-7.1

5.2. Detailed Design

The payload consists of any components that are not essential for drone flight, but for mission completion, all found in the payload bay visualized in Figure 5.1. For this mission, requirements (see Table 5.1) state that a cave shall not only be visually mapped, but also 3D mapped and georeferenced, fulfilled via the choice of using a multi-spectral camera as well as Light Detection and Ranging (LiDAR), respectively.

The payload bay shown below is a closed box, customized and fitted to allow visual clearance at the front of the drone. It has dimensions of 18 cm x 10 cm x 4 cm (L x W x H), attached by rotating connectors on either side, both measuring to be 1 cm in diameter, and 2 cm in width, 0.5 cm of which sticks into the payload bay box. This attachment decision was motivated by the need for camera and LiDAR rotation in order to capture the full interior of any cave, without the need for drone maneuvers or variable pitch arms.

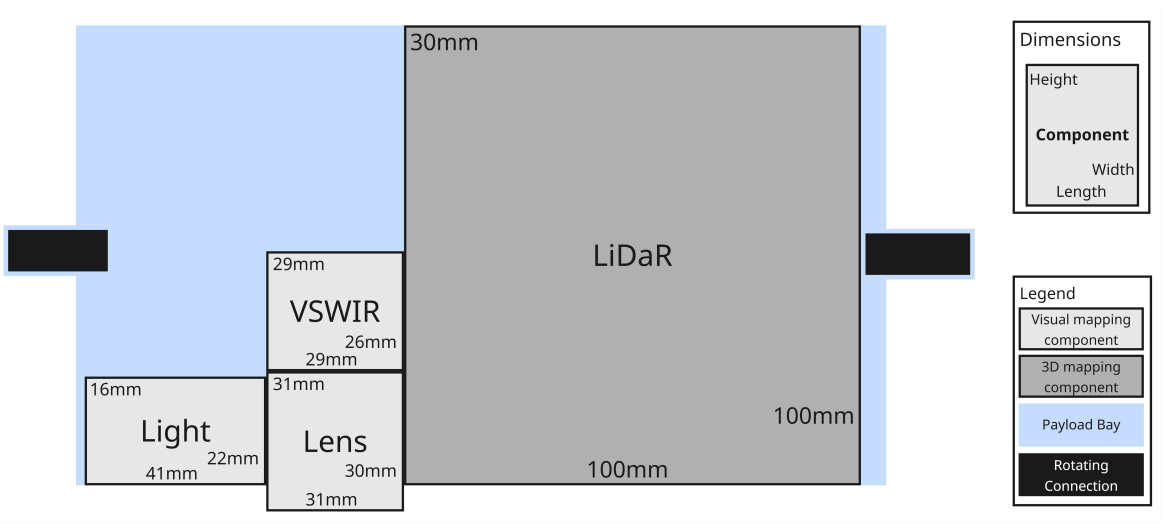

Figure 5.1: Top view visualization of payload bay, pointing downwards towards the front of the drone.

5.2.1. Camera

The camera chosen is a high-performance, multi-spectral module which covers the spectral range of Visible light (VIS), Near Infrared (NIR), and Short-Wave Infrared (SWIR) to allow for an initial 'night vision' sweep of the cave. This keeps fauna disturbance to a minimum and helps the autonomous system map cave interiors for future mission objectives. Contradictory to previous decisions, the UltraViolet-A (UVA) spectrum imaging was omitted from this mission to prioritize the minimization of site disturbance and harmful light emissions. The Alvium 1800 C-320 VSWIR camera[1], stands out for its miniature size, low mass, high resolution, and quick frame rate, all found in Table 5.2. Several more significant specifications like its mass and image pixel size can also be found below.

Table 5.2: Camera specifications [2].

Specification	Value
Spectral Response [nm]	400 - 1700
Size [mm x mm x mm]	26 (L) x 29 (W) x 29 (H)
Mass [g]	40
Power Draw [W]	2.6
Pixel Size [μm x μm]	3.45 x 3.45
Resolution [px x px]	2080 (H) x 1544 (v)
Max. Frame Rate [fps]	131
Sensor	Sony IMX993
Sensor Type	InGaAs
Sensor Size	1/1.8"
Lens Mount	C/CS

The Sony IMX993 Sensor [3] is integrated into the camera and does not have to be assembled manually. A sensor's main function is to capture light and convert it into an electrical system, which can then be processed and turned into a digital image. The type of sensor used determines the camera's data rate, light sensitivity, and image size.

A higher bit ADC (Analog-to-Digital Converter) provides a more precise digital representation of the analog input. The maximum frame rate corresponding to different ADC resolutions, as well as the sensor sensitivity and maximum Quantum Efficiency (QE) of the integrated sensor are all shown in the table below.

Table 5.3: Sensor specifications [4].

Specification		Value
Max Frame Rate [fps]	ADC 8 bit	173
	ADC 10 bit	158
	ADC 12 bit	93

[1]URL: https://www.alliedvision.com/en/products/alvium-configurator/alvium-1800-c/320-vswir/ [Accessed: 11 June 2025]
[2]URL: https://cdn.alliedvision.com/fileadmin/pdf/en/Alvium_1800_C-320_VSWIR_DataSheet_en.pdf [Accessed: 11 June 2025]
[3]URL: https://www.sony-semicon.com/en/products/is/industry/swir/imx992-993.html [Accessed: 14 June 2025]

Table 5.3: Sensor specifications [4].

Specification	Value
Sensitivity [mV]	291
Max Quantum Efficiency [%]	75

Quantum efficiency (QE) is a measure of how efficiently a device converts incoming photons into a usable output, such as electrons. This differs at different wavelengths of light and can help determine the power of light needed for a camera sensor to capture a desired image, explored further in Subsection 5.2.3. The figure below illustrates the fluctuation of the QE with wavelength; however, this is measured relatively to the maximum QE of 75 %, found at 1200 nm.

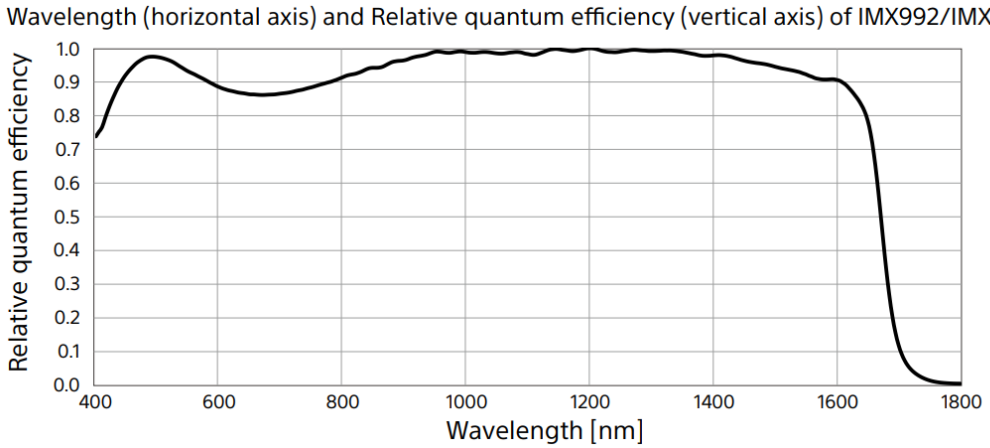

Figure 5.2: Relative Quantum Efficiency of the Sony IMX993 Sensor [5].

5.2.2. Lens

After a camera is acquired, a lens is needed to direct light into the camera sensor and form a clear image. Using the sensor specifications previously mentioned in Table 5.2, mainly its size, and the mounting needed for the selected camera (C/CS) the KOWA LM5NCL lens[6] was chosen.

Table 5.4: Lens specifications [7].

Specification	Value
Size [mm x mm]	31 (⌀) x 30(L)
Mass [g]	55
Sensor Size	1/1.8”
Lens Mount	C
Vertical FOV [°]	66.9
Horizontal FOV [°]	88.8
Diagonal FOV [°]	110.2
Focal Length [mm]	4.5
Picture Size [mm x mm]	5.4 (H) x 7.2 (W)
Distortion [%]	17.5

The most noteworthy value to take from this table is the lens’ field of view (FOV). With a higher FOV, the drone can map the cave at a higher speed to ensure complete coverage. However, the size of the captured surface also depends on the distance from the drone to that surface. Using basic trigonometry, these dimensions were calculated for key distances determined by typical cave sizes, namely: 1.5 m, 2.5 m, and 5 m; the maximum according to the following requirement.

> ***MIS-DRN-2.4:*** *The system shall be capable of photographing the cave walls from a maximum distance of 5 meters.*

This condition also makes it possible to verify that the camera resolution complies with its requirement set by the stakeholder.

[4] URL: `https://www.sony-semicon.com/files/62/flyer_industry/IMX990_991_992_993_Flyer_en.pdf` [Accessed: 14 June 2025]
[5] See Footnote 4
[6] URL: `https://cdn.alliedvision.com/fileadmin/content/documents/products/accessories/lenses/Kowa/Data_sheet/LM5NCL.pdf` [Accessed: 11 June 2025]
[7] See Footnote 6

PL-DRN-04: *The resolution of the camera shall be at least 1 cm or finer.*

This depends on two variables: the surface dimensions and the pixel resolution of the camera. The multitude of dimension definitions can start to get confusing at this stage, so they are summarized in Table 5.5. Here, the surface dimensions are calculated on the basis of the distance from the surface, d, using the following equation.

$$l = 2 \cdot d \cdot tan\left(\frac{FOV}{2}\right) \tag{5.1}$$

Table 5.5: Definitions of dimensions.

Symbol	Definition	Value (W x H)	Unit
l_p	Number of pixels; depends on camera resolution.	2080 x 1544	px
l_i	Physical dimension of image captured; depends on sensor.	7.2 x 5.4	mm
l	Real-life dimension of surface captured; depends on d.	9.8 x 6.6	m

Finally, the resolution, R, can be calculated using these dimensions in order to check whether the requirement is fulfilled.

$$R = 100\frac{l}{l_p} \tag{5.2}$$

This equation can be applied to both the horizontal and vertical aspects of the image, so the applicable FOV, l, and l_p should be chosen.

The horizontal image resolution then comes out to be 0.471 cm, while the vertical image resolution is 0.389 cm at the maximum distance from the surface, fulfilling our 1 cm resolution requirement.

$$R_h = \frac{2 \cdot 500 \cdot \tan\left(\frac{88.8^\circ}{2}\right)}{2080} = 0.471\,\text{cm/px}, \qquad R_v = \frac{2 \cdot 500 \cdot \tan\left(\frac{66.9^\circ}{2}\right)}{1544} = 0.389\,\text{cm/px}. \tag{5.3}$$

5.2.3. Lighting

One final main component needed for successful operation of the camera is the light source. As the drone is set to operate in a dark cave, it is assumed that absolutely no external light can reach the areas being mapped, so a light with sufficient luminous flux to maintain the resolution of images taken needs to be selected. In order to calculate this number, an analysis of photon energy is carried out, explained below.

By measuring the energy needed per photon, E, using the Planck relation (Equation 5.4), an estimate of the energy per pixel can be extracted. This is dependent on the desired image quality and the sensor's QE, as mentioned before in Subsection 5.2.1.

$$E = \frac{hc}{\lambda} \tag{5.4}$$

where h is Planck's constant, c is the speed of light, and λ is the wavelength of light.

Next, the power is calculated using the smallest exposure time possible to ensure that the highest power needed throughout the mission is calculated, and from that, the irradiance, I is extracted according to the image's pixel size. Finally, the illuminance, E_v, is calculated by considering the luminous efficacy, K, at different wavelengths: a measure of how well a light source converts electrical power into visible light.

$$E_v = I \cdot K \tag{5.5}$$

The luminous efficacy is dependent on the wavelength, this value is represented by the luminous efficiency (or photopic response), $V(\lambda)$, represented by the graph in Figure 5.3. This value is given in relation to the maximum efficacy, 683, found at a wavelength of 555 nm [8].

$$K = 683V(\lambda) \tag{5.6}$$

[8] URL: `http://hyperphysics.phy-astr.gsu.edu/hbase/vision/efficacy.html` [Accessed: 16 June 2025]

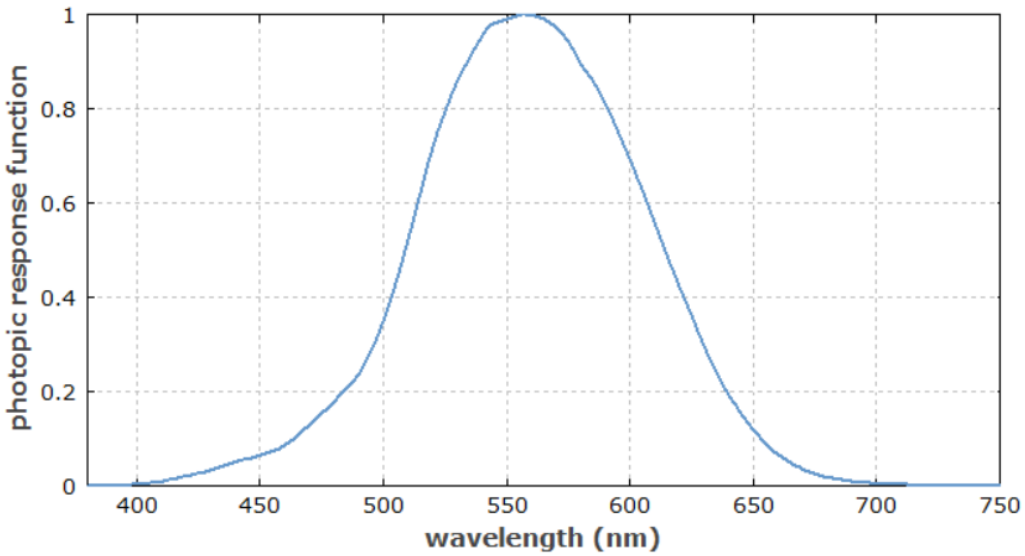

Figure 5.3: Photopic response of different wavelength of light[9].

In order to use this value to find a specific product which can meet the desired ligth power required, the luminous flux is calculated using the maximum surface area possible, which is at a distance of 5 m from the surface mapped.

$$\Phi_v = E_v A \tag{5.7}$$

where Φ_v is luminous flux in lm and A is surface area of desired surface.

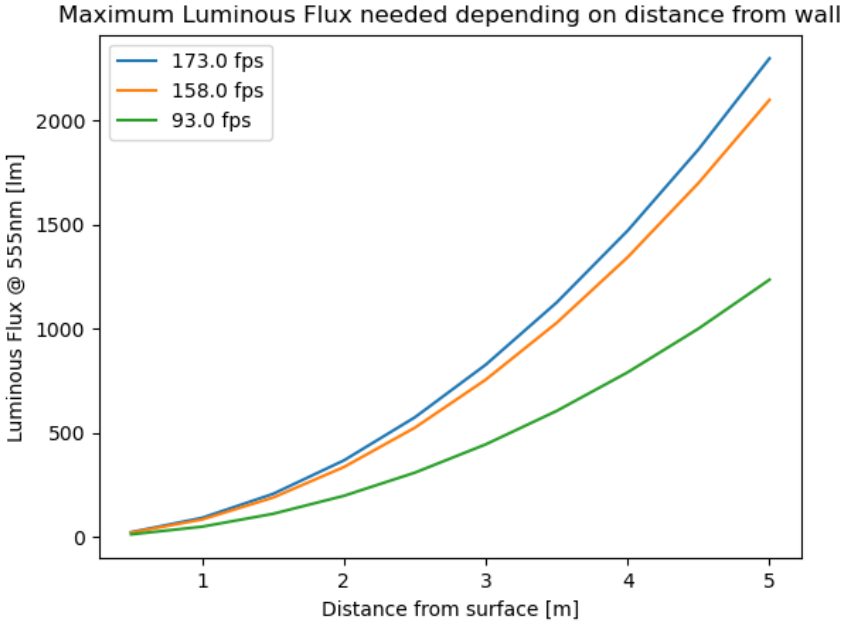

Figure 5.4: Maximum flashlight specs needed at different distances from the surface captured

The maximum value obtained at the highest frame rate can then be extracted from the previous graph as 2300 lm. So, the visible flashlight chosen was that Mini 5 / Avata & Avata 2 Tactical Light [10]. This will be fitted with a microchip, the dafruit Controller Board for DRV2605L for Haptic Motor[11], to ensure control over turning the light on and off. Finally, an Infrared light, the D3060 IR Light[12], was also chosen to ensure night vision photography is possible. This does not harm the cave fauna so no further calculations were needed.

[9]URL: https://www.rp-photonics.com/scotopic_and_photopic_vision.html [Accessed: 16 June 2025]
[10]URL: https://tundradrone.com/product/tundra-drone-mini-5/?c=f37ec89cf952 [Accessed: 16 June 2025]
[11]URL: https://www.adafruit.com/product/2305?srsltid=AfmBOorJca67sBMu3aHwkipfkUuTYsL_kj2xrHYshaBnlVtLOVmlCIL8 [Accessed: 16 June 2025]
[12]URL: https://www.foxfury.com/product/d3060-ir-light/?srsltid=AfmBOoqclgIp0jsztCwabZLtS4bY1Xr13KWdHkGY77rypvSPRHdydtCs [Accessed: 16 June 2025]

With all essential values now obtained, it is time to tackle the concept of motion blur. This is introduced due to the fact that the camera is moving. So, a maximum velocity, v, should be calculated to ensure that the images are still of desired resolution. This is done by defining a pixel blur threshold, p, defined as 0.8 for this case. This was chosen according to general values used in the past, where 1 is used for general imagery and 0.5 for very detailed mapping.

$$v = \frac{p}{t}R \tag{5.8}$$

From this equation, the graph below is plotted to visualize maximum velocities for different mapping distances, as well as frame rates, with a global maximum mapping velocity of 0.652 m/s. A more detailed analysis of the mapping time takes place in Section 10.3.

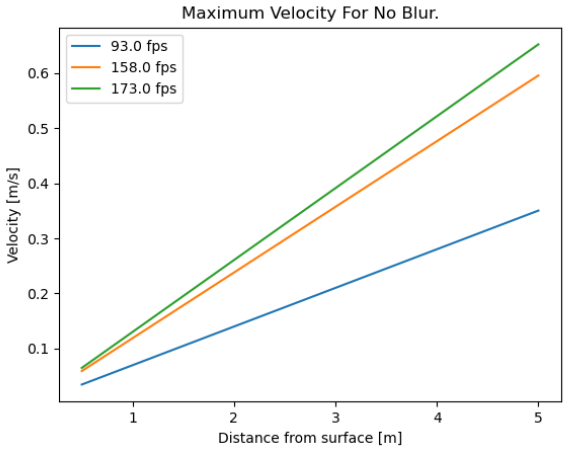

Figure 5.5: Maximum velocity for acceptable motion blur depending on frame rate.

5.2.4. Light Detection and Ranging (LiDAR)

The LiDAR that will be used in the payload bay was already discussed in the Midterm Report [6]. The Hesai ATX specifications are repeated in the table below[13].

Table 5.6: LiDAR Specifications [6]

Characteristic	Mass	Size	Resolution	FOV	Power Use
Value	360 g	100x100x30 mm^3	0.1° x 0.1°	120°x 20°	8 W

5.3. Sensitivity Analysis

This chapter discussed the properties and characteristics of the payload chosen for the SpeleoDrone. As the specifications that properties were calculated from are inherent to the camera, LiDAR and flashlights, these components define the fundamental limits and capabilities of the payload system. All calculations regarding the specifications were performed with the minimum and maximum values provided in the datasheets of the components. For all further analyses, whenever a range of values in the specifications existed, the most restricting and therefore conservative value was used to ensure robustness in the design. As a result, the payload analysis can be concluded with high confidence.

[13]URL: `https://www.hesaitech.com/product/atx/`[Accessed: 4 June 2025]

6. Structural and Material Characteristics

This chapter explores the process of designing the SpeleoDrone structure for a variety of loading scenarios. When designing a structure for aerial applications, a low mass is critical as it ensures longer mission endurance. This need for a lightweight structure must be balanced against a need for structural rigidity, damage-tolerance, manufacture cost constraints and sustainability.

6.1. Material Selection

Before proceeding with the structural design, a list of potential materials for the structure was compiled. Several property indices were included in the list, to help in comparing material choices. These indices were specific stiffness, $\frac{E}{\rho}$, specific bending stiffness, $\frac{E^{1/3}}{\rho}$ and specific yield strength, $\frac{\sigma_y}{\rho}$. In this list, three families of materials that are often used in lightweight aerospace structures were investigated: polymers, fiber-reinforced polymers, and metal alloys. As fiber-reinforced polymer properties depend largely on the layup used, they were investigated later on in the section.

From the polymer family, thermoplastics were of interest due to their recyclability. The metals investigated were lightweight aluminium and magnesium alloys such as Aluminium 6061-T6 and AZ31B. Data was gathered from MatWeb[1], apart from for PPS, where manufacturer datasheets were used[2][3]. The results are presented below in Table 6.1.

Table 6.1: Thermoplastic & Metal Alloy Mechanical Properties

Material	E [GPa]	ρ [g/cm^3]	$\frac{E}{\rho}$ [$\frac{N \cdot m}{kg}$]	$\frac{E^{1/3}}{\rho}$ [$\frac{N^{1/3} \cdot m^{7/3}}{kg}$]	σ_y [MPa]	$\frac{\sigma_f}{\rho}$ [$\frac{N \cdot m}{kg}$]	S_{izod} [J/m]
Nylon 66 (PA)	2.41	1.14	$2.11 \cdot 10^6$	1.18	85	74561	60
ABS	2.35	1.07	$2.24 \cdot 10^6$	1.24	34	31776	300
Polycarbonate	2.39	1.20	$1.99 \cdot 10^6$	1.11	60	50000	700
PEEK	3.88	1.34	$2.90 \cdot 10^6$	1.17	95	70896	58
PPS	5.77	1.35	$4.24 \cdot 10^6$	1.32	94.5	70000.0	32
Aluminium 6061-T6	68.9	2.70	$25.52 \cdot 10^6$	1.52	255	94444	150
AZ31B	45	1.77	$25.42 \cdot 10^6$	2.09	200	112994	430

When looking at impact strengths for thermoplastics, specifically izod impact strength S_{izod}, ABS, Nylon 66 and polycarbonate perform best. However, Nylon 66 absorbs up to 8% of its weight in water over long-term absorption, while significantly degrading in mechanical performance. ABS was chosen as the thermoplastic to be used in SpeleoDrone due to its very low cost, low density, and relatively high specific bending stiffness $\frac{E^{1/3}}{\rho}$, making it most suitable for both structural and cosmetic parts alike. It offers superior specific stiffness and specific bending stiffness than polycarbonate.

The reinforcement of these thermoplastic polymers with fiber elements allows mechanical properties to be aligned with the dominant loading directions. Two potential fibers, carbon fiber and aramid, specifically Kevlar, were investigated. Out of Kevlar fibers, Kevlar 49 is used in aerospace-grade applications and offers increased stiffness. Carbon fiber provides the greatest stiffness to weight ratio, at the expense of brittleness and impact-tolerance. Kevlar offers far improved toughness at a cost of stiffness, making it a strong competitor in airframe parts that are expected to experience impacts. Their mechanical properties are represented below in Table 6.2, with subscripts *1* and *LT* corresponding to the longitudinal direction and *2* and *TT* the transverse direction.

Table 6.2: Composite Fiber Mechanical Properties

Reinforcement Fiber	E_1 [GPa]	E_2 [GPa]	ρ [kg/m^3]	G_{LT} [GPa]	G_{TT} [GPa]	σ_t [MPa]	σ_c [MPa]
Carbon Fiber [27]	230	14	1780	24	5.4	3530	661.8
Kevlar 49 [64]	112.4	4.14	1440	2.90	1.1	2757.9	517.1

It must be noted that the tensile strength, σ_t, varies greatly with fiber grade and manufacturer. For example, T700 and T800 carbon fibers commonly exceed a tensile strength of 5000 MPa, while a tensile strength of 3530 MPa is given in the table. This was done as a conservative measure. Compressive strength is difficult to measure empirically for isolated fibers, with manufacturer data only found for Kevlar 49. The compressive strength of carbon fiber is found by using the ratio σ_t/σ_c for Kevlar 49, as Kevlar is known to have significantly

[1] URL: `https://www.matweb.com` [accessed: 19 May 2025]

[2] URL: `https://www.bearingworks.com/uploaded-assets/pdfs/retainers/pps-datasheet.pdf` [accessed: 19 May 2025]

[3] URL: `https://www.ensingerplastics.com/en-us/shapes/products/tecatron-natural` [Accessed: 20 May 2025]

worse performance in compression than carbon fiber[4]. Assuming this ratio of compressive and tensile strengths, a σ_c of 661.8 MPa was found for carbon fiber. This value is likely to be overly conservative, especially when safety factors will be used in the structural design, necessitating further investigation.

When these fibers are present in a composite laminate, mechanical properties can be found for unidirectional laminates These are found for an fiber-volume-fraction (FVF) of 0.5. This FVF was assumed to provide a contingency factor as composites typically lose mechanical performance when an FVF of 0.6 is exceeded [54], which can occur in sheared areas during the fiber draping process. It must be noted that most empirical data gathered uses epoxy as the matrix rather than the thermoplastics being investigated. However, this should be of little consequence for preliminary data-gathering as the mechanical properties of interest are primarily fiber-dominated.

Table 6.3: Lamina Mechanical Properties

Material	E_1 [GPa]	E_2 [GPa]	ρ [kg/m^3]	E_1/ρ [$\frac{N \cdot m}{kg}$]	σ_t [MPa]	σ_c [MPa]	σ_c/ρ [$\frac{N \cdot m}{kg}$]
Carbon Fiber Unidirectional	130	10	1600	$81.3 \cdot 10^6$	1800	1200	750000
Kevlar 49 Unidirectional	73	5	1400	$52.1 \cdot 10^6$	1400	300	214000

It can be observed that the composite lamina have far superior specific stiffness and specific strength than any of the materials investigated in Table 6.1. Composite parts and any polymer parts will share a thermoplastic in order to reduce costs in the design.

6.2. Structural Requirements

A list of structural requirements were set for the structure. These requirements were assigned identification codes in the form of **DRN-STRC-XX** and relate to everything from stiffness to material properties. Not all requirements were met or assessed at this stage of the design, but they were kept in consideration. The requirements are displayed below in Table 6.4:

Table 6.4: Structural Requirements Definition

Requirement ID	**Description**	**Parent Requirement**
DRN-STRC-01	The structure of SpeleoDrone shall have a mass of less than 0.9 kg.	–
DRN-STRC-02	The direction of the thrust vector shall not vary more than 2° during flight.	–
DRN-STRC-03	During operation, deformation of the structure shall not offset the payload orientation by more than 0.1°.	–
DRN-STRC-04	The structure shall not yield or permanently deform during operation or handling.	–
DRN-STRC-05	The drone structure shall withstand a fall from 1 meters, onto the cave floor.	–
DRN-STRC-06	The structure shall have a fatigue lifespan of 560 operational cycles.	STK-DRN-1
DRN-STRC-07	Oscillations of the structure shall not hinder the function of the payload.	STK-DRN-2
DRN-STRC-08	The structure must not lose more than 10% mechanical performance over its lifespan.	–
DRN-STRC-09	All frame and fastener materials shall be corrosion-resistant and non-reactive in high-humidity environments.	–
DRN-STRC-10	All structural elements shall be 100% recyclable.	STK-OPR-02
DRN-STRC-11	The structural elements & fasteners must be easily switched out or assembled within 10 minutes in the field.	–
DRN-STRC-12	The structure of the SpeleoDrone must provide access to switch out the battery.	STK-OPR-08
DRN-STRC-13	All structural interfaces housing electronics or other water-sensitive components shall support sealing against particulate and moisture ingress.	STK-DRN-2

The fatigue requirement DRN-STRC-06 defined a single operational cycle as take-off and landing after flying in a cave for as long as the battery can allow. Assuming eight missions per day for a week-long mission, as will be discussed in Section 10.4, a total of 56 flights can be carried out during the mission. It was decided that the ability to perform 10 such missions before end-of-life is desired for the drone, bringing the fatigue lifespan requirement to 560 cycles.

[4] URL: `https://compositeenvisions.com/document/composite-fiber-characteristics/` [Accessed: 20 May 2025]

6.3. Configuration & Layout

Prior to defining load cases, the configuration and layout of SpeleoDrone components must be known. Three quadcopter arm-frame configurations are explored: ”Plus-Frame”, ”X-Frame”, and ”H-frame”. These frames are depicted below in Figure 6.1, with black sections depicting the arms that house the motors, and gray depicting the center plate that houses electronics and payload.

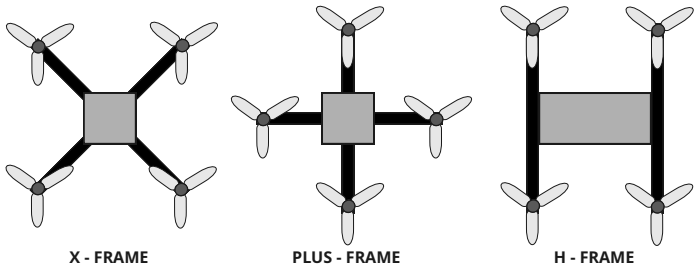

Figure 6.1: SpeleoDrone Frame Design Options

Assuming a head-on impact from collision, X-shaped frames have the benefit of absorbing impact by two rotor ”arms”, while the plus-shaped configuration has a singular arm absorb all the impact. An H-frame behaves similarly to an X-frame but has more spacing between rotor arms on the front for housing payload, and has the shortest rotor arms. As the payload will need a pitch-able turret due to its limited vertical FOV of $20°$, the H-frame is the preferred solution.

This frame layout was modified in several ways to better fit the mission, as can be seen in Figure 6.2 below, where the yellow arrow represents the direction in which the drone flights forwards. First, a separate payload bay was added to the front of the drone to house the LiDAR and cameras, depicted in gray in the figure. This was done to allow the payload bay to pitch vertically. Then, it made most sense to position the housing for the fiber optic reel centrally, towards the back of the drone. This was depicted in blue. It was decided to use this housing as a beam element to support the rear-mounted motors, which forms an idealized ”T” shape at the rear of the SpeleoDrone. The original central bay was then dedicated to housing the avionics and battery, depicted in red. A 3-dimensional view of the frame can be seen in Figure 6.3 below:

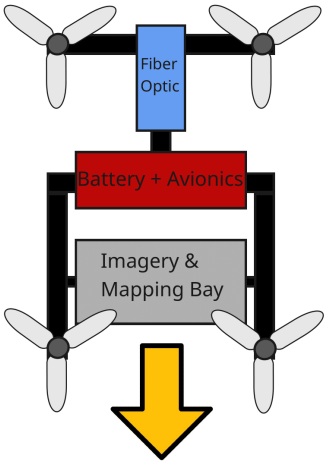

Figure 6.2: SpeleoDrone Top-Down Layout

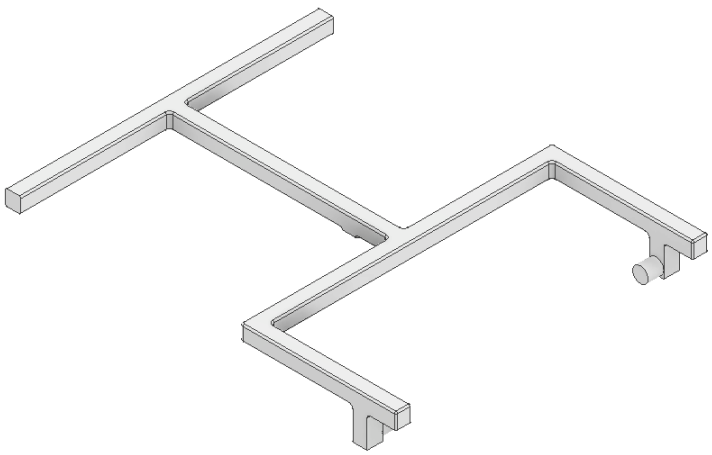

Figure 6.3: SpeleoDrone Frame 3D View

6.4. Defining the Load Cases

A safety factor of 1.5 is used for the structural design, as is standard practice according to NASA [32]. This meant that when defining loads, the maximum expected loads were multiplied by a factor of 1.5.

Three common load cases to be experienced during the lifespan of the SpeoleoDrone were defined, and drawn in Figures 6.3-6.5. Thrust and reaction forces were labeled in green, while all other forces were represented in with red arrows. A yellow and black circle represents the center of gravity, through which all remaining unlabeled weight acts through.

6.4.1. Load Case 1.1:

The first static load case that was analyzed corresponds to the drone maneuvering, for example during climb, at the maximum thrust-to-weight (TW) ratio of 1.5. No external loads act on the drone, and all motors generate

equal thrust, assuming a center of gravity that is aligned with the geometric center of the drone.

The load of 7.7 N downwards represents the force exerted on the frame by the weight of the payload bay, 1.1 N the weight of the motors, 5.2 N the weight of the fiber-optic system, and 24.3 N the weight of the batteries.

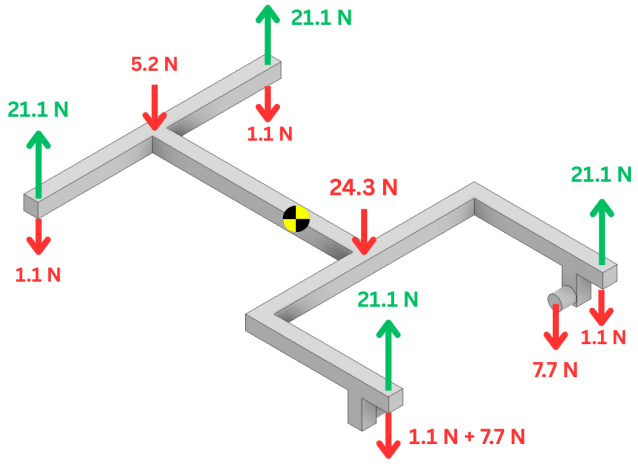

Figure 6.4: Load Case 1.1

6.4.2. Load Case 1.2:

The second static load case corresponds to manual handing of the SpeleoDrone, for example, during transport. During this handling, the drone is carried on its side by the front and rear motor arms. Both arms are loaded equally, assuming a center of gravity that is aligned with the geometric center of the drone. In order to remain conservative, it is assumed that the entire weight of the payload bay is acting on a singular arm, represented by a force of 15.4 Newtons. A vertical acceleration of 1.5 g is assumed, attributed to for example being picked up during a bumpy car ride [21].

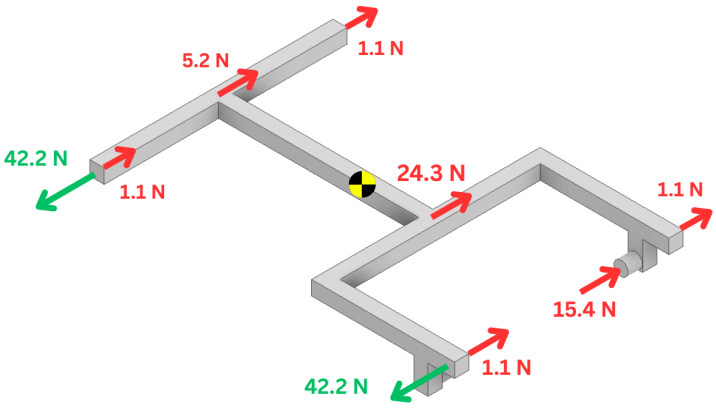

Figure 6.5: Load Case 1.2

6.4.3. Load Case 1.3:

The third static load case also corresponds to manual handling of the SpeleoDrone. In this case, the SpeleoDrone is picked up off the ground by opposing front and rear motor arms. Both arms are loaded equally, assuming a center of gravity that is aligned with the geometric center of the drone. A vertical acceleration of 1.5 g is assumed, roughly equivalent to being picked up during a bumpy car ride [21].

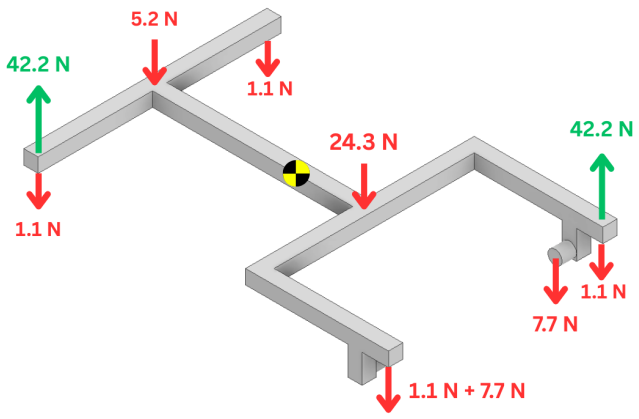

Figure 6.6: Load Case 1.3

6.5. Static Analysis

It is important to understand how a structure responds to operational loads. Hence, the simplified frame structure of SpeleoDrone was modeled and subjected to the three load cases defined earlier in a Finite-Element-Analysis (FEA) simulation using Autodesk Inventor[5].

For this simulation, a section and material assignment had to be defined. For the material, it was chosen to use pure ABS as this allows the cheapest solution to be assessed. The section of each beam was defined to be a solid square of 1 cm sides. This selection of solid cross-section provides a greatly reduced section moment of inertia compared to hollow shapes of equal mass, making the structure especially susceptible to deflection. In the analysis, loads were defined as point loads, and the modeling mesh was refined until a convergence of 2% was reached in the resulting Von Mises stress. Tetrahedral elements were used.

6.5.1. Load Case 1.1 Analysis

In Load Case 1.1, the structure did not experience any yielding or significant deformations. Yielding occurs in a structure when the Von Mises stress exceeds the yield stress of the material, which is 34 MPa for ABS. The maximum yield stress present in Load Case 1.1 is around 10 MPa. Figure 6.7 shows the FEM results.

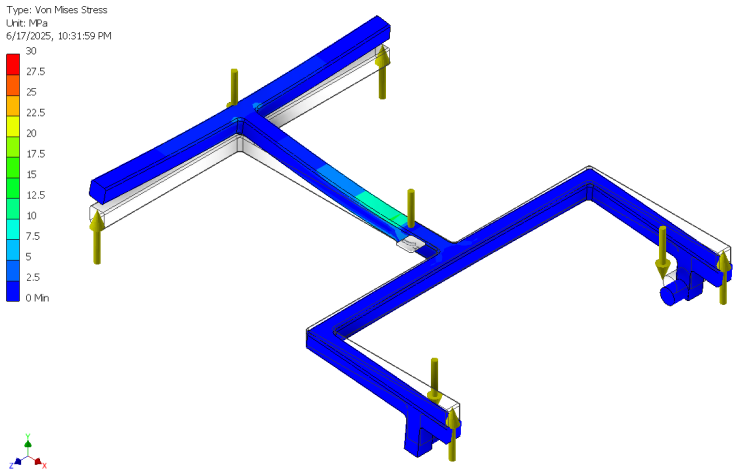

Figure 6.7: Load Case 1.1 Normal View

[5]URL: `https://www.autodesk.com/eu/products/inventor/overview` [Accessed: 12 June 2025]

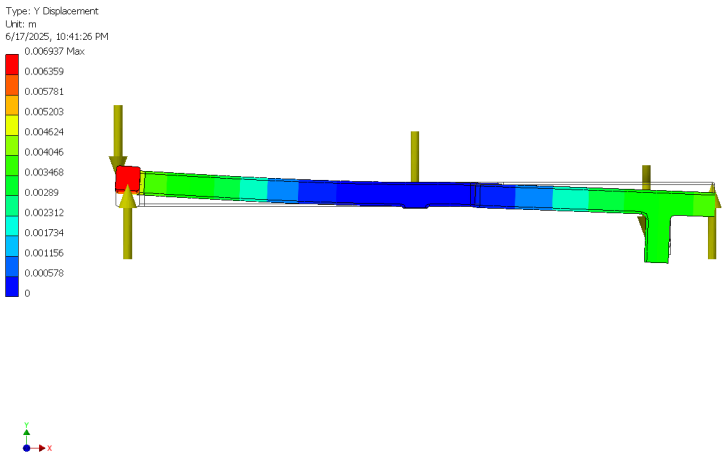

Figure 6.8: Load Case 1.1 Vertical Displacement Side View

6.5.2. Load Case 1.2 Analysis

In Load Case 1.2, the structure did not experience any yielding or significant deformations. This was because the Von Mises stress remained below the ABS yield stress of 34 MPa. The FEA results are depicted in Figure 6.9 and Figure 6.10 below:

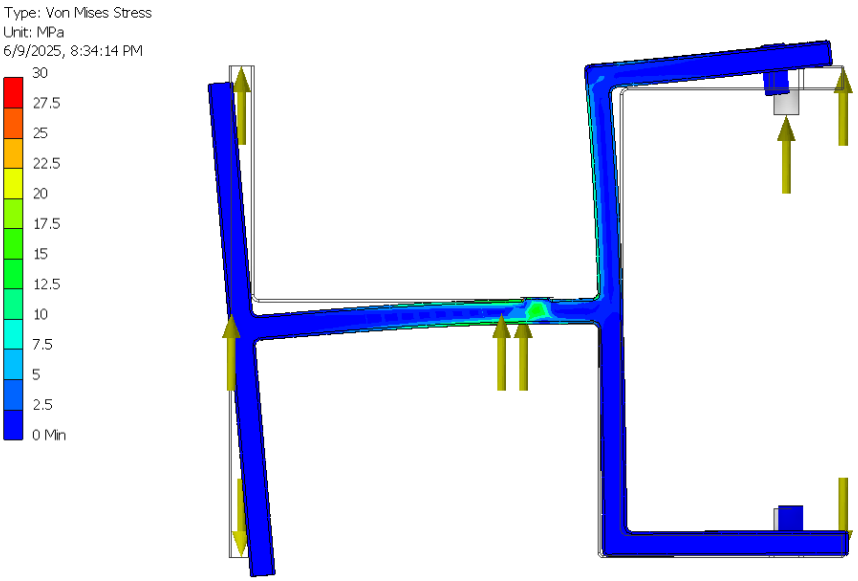

Figure 6.9: Load Case 1.2 Top View

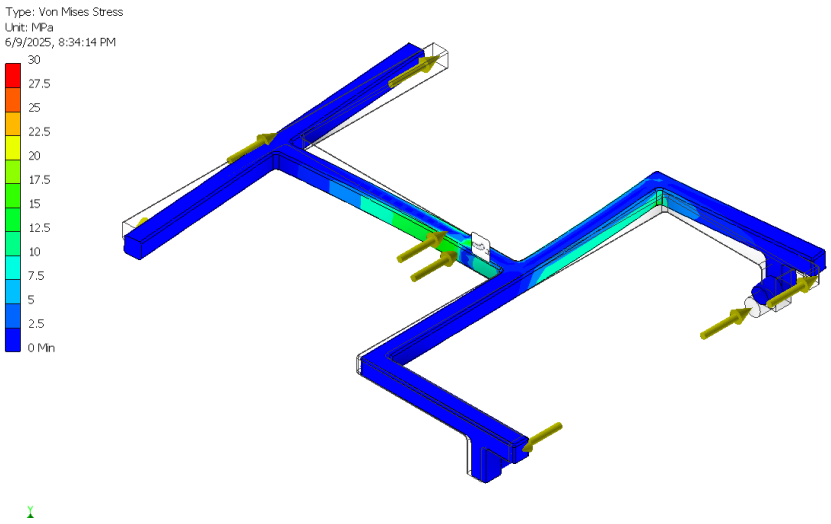

Figure 6.10: Load Case 1.2 Normal View

6.5.3. Load Case 1.3 Analysis

The third load case proved critical, where Figure 6.11 and Figure 6.12 show the FEM results. Here, the resulting Von Mises stress exceeded 40 MPa in multiple parts of the SpeleoDrone frame, higher than the ABS yield stress of 34 MPa. This stress would result in **yielding** and hence **permanent deformation** of the drone structure, making it necessary to reassess the material and cross-section used in the frame. The central beam was most severely loaded, primarily in torsion.

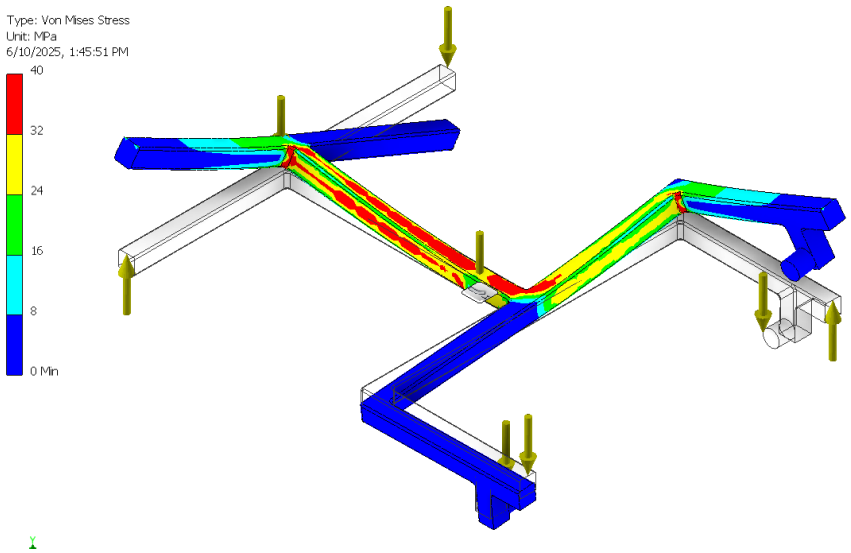

Figure 6.11: Load Case 1.3 Normal View Von Mises Stress

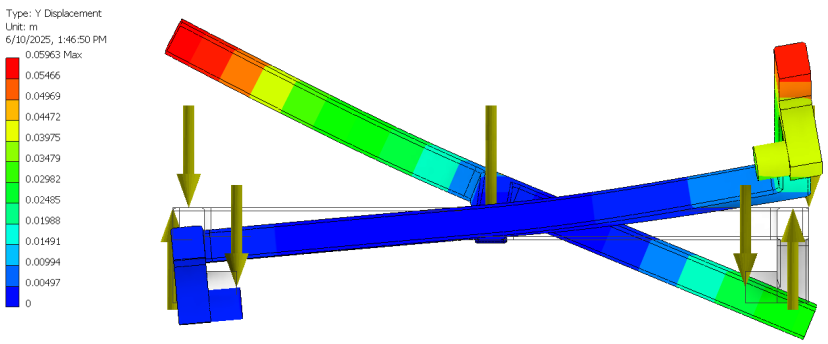

Figure 6.12: Load Case 1.3 Front View Vertical Displacement

6.5.4. Simulation Limitations

The ABS frame used in the simulation has a mass of 73 grams, assuming a constant cross section of 1 x 1 cm. Meanwhile, previous mass budget assumed a structural mass fraction of 0.29, equivalent to 964 grams. The thrust and handling loads defined reflected this structural mass of 964g, leaving just under 891 grams of weight unaccounted for in the FEA simulations. A fixed constraint was added at the centroid of the frame. Through this fixed constraint, the unaccounted for weight acts as a reaction force. This somewhat unrealistic way of modeling the load cases was chosen as it does not affect the deformations and stresses experienced by the limbs of the frame in a non-conservative way, which are the points of interest.

Additionally, this solution caused problems with mesh convergence. This is because of the need to model a slight extrusion at the frame centroid in order to place the fixed constraint, leading to local stress concentrations. These concentrations remain even after adding fillets to the edges of this extrusion. Refining the mesh causes spikes in the modeled stress as the mesh shrinks. Such spikes can be seen in Figure 6.13, which was taken from the finite-element-analysis simulation for Load Case 2. Here, a Von Mises stress peak of 196.8 MPa is present near the boundary condition as a numerical artifact, while the stress in the rest of the structure does not exceed 15 MPa.

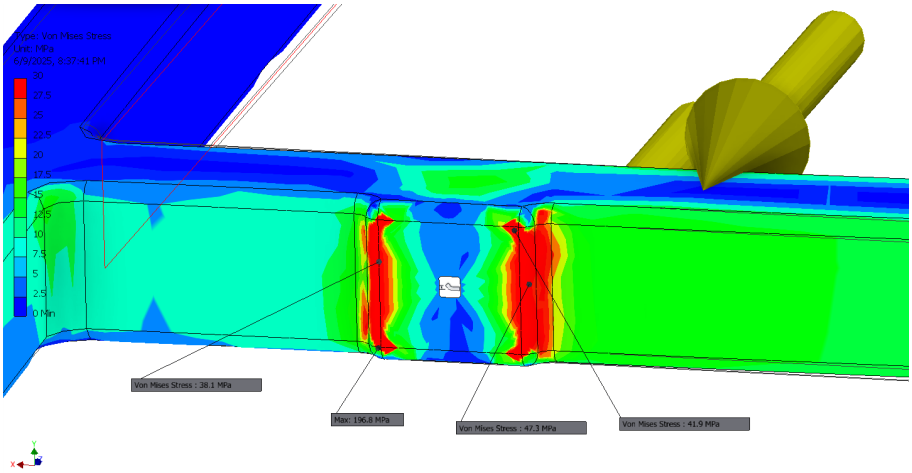

Figure 6.13: Local Stress Concentrations at Extrusion

6.6. Design for Impact

The results from the static analysis were relatively mild for choosing such a suboptimal beam cross section made out of a weak material such as ABS, despite structural yield occurring in **Load Case 3**. However, during impact, loads of far higher magnitude can be expected to act upon the structure than those modeled in the three load cases. During impact, stiffness proves to be of secondary importance, as mapping operations would already be interrupted, while material strength is critical as it ensures the drone can be recovered in a state that is repairable in the field. Finally, the structural design must fail in a controlled manner, with failure occurring first in parts that are easy to replace.

6.6.1. Load Definition

In line with requirement **DRN-STRC-05**, the drone must be able to withstand a fall from 1 meter. This corresponds to a velocity of **4.43 m/s** according to Equation 6.1 below where g is the acceleration of gravity and h is the height of the fall. In order to find the maximum force that would act upon the drone during collisions with the cave environment at this velocity, literature was consulted. A study on impact between a human head and quadcopters was found [52], featuring an impact velocity of **5.3 m/s**. This is roughly comparable to the velocity achieved during 1 meter of freefall, which at 4.43 m/s is 0.84 times as fast.

$$v = \sqrt{2 \cdot g \cdot h} = \sqrt{2 \cdot 9.81 \cdot 1} = 4.43 m/s \tag{6.1}$$

The human head being impacted is significantly less stiff than the rocky walls of a cave, however, this lesser rigidity is assumed to roughly represent how the drone would tumble during falls and collisions, rather than coming to an immediate stop. The study provides the accelerations experienced by the human head during impact, using a Hybrid III human body dummy. This allows for the maximum force acting on the human head to be calculated, which must then be equal to the equivalent force acting on the quadcopter being investigated.

In the study, the human head experienced a peak acceleration of on average 40g over multiple trials [52]. The quadcopter in the study had a weight of 1.051 kg [52], while the SpeleoDrone has a mass budget of 3.455 kg

at an updated iteration of the mass budget, 3.29 times heavier than the drone investigated in the study.

Using the formula for the force needed to change the momentum of an object, given below in Equation 6.2, it was deduced that an object 3.29 times heavier would need 3.29 times the force to decelerate, assuming the same deceleration time t and initial and final velocities v_1 and v_2. This relation holds for initial velocity v_1, where a higher initial velocity would take more force to decelerate.

$$F = \frac{m \cdot v_1 - m \cdot v_2}{t} \tag{6.2}$$

Hence, the human head would experience a maximum acceleration of 40g * 3.29 * 0.84 = 110g upon collision with the SpeleoDrone at a velocity of 5.3 m/s. Using a Hybrid III head mass of 4.54 kg[6], a peak force of **4900** N was calculated to act on the human dummy, in the event of a collision with the SpeleoDrone at 5.3 m/s. According to Newton's third law, an equivalent peak impact force of 4900 N would therefore also act on the SpeleoDrone structure.

As discussed in Section 6.3, the H-frame adjacent configuration was chosen as ahead-on impact would be absorbed by two structural elements, specifically the drone "arms" rather than a single one. Hence, this force will be assumed to be equally split into two loads of **2450 N**.

This peak impact load was then applied to the outer ends of the drone limbs in a subsequent quasi-static analysis. Applying the impact load here would result in the highest bending moments, and therefore stresses, forming a conservative analysis. No safety factor was included for the impact analysis, as the calculation is already **conservative** through its quasi-static nature because of how in reality the maximum accelerations are only sustained for around a millisecond [52].

6.6.2. Iterated Material Characteristics

With a need for stronger and possibly stiffer beams to be used in the SpeleoDrone frame when designing for impact tolerance, an alternative material to ABS was chosen. Lightweight metal alloys from Section 6.1, such as AZ31B were compared against composite lamina involving **Carbon Fiber** or **Kevlar 49**. The composite lamina, specifically those using carbon fiber, were chosen to be used in the SpeleoDrone frame because of their better specific strength and specific stiffness compared to metal alloys. This allows for **greater weight reduction**.

In composite structural design, the Chamis model for unidirectional composites was be used to derive the mechanical properties of unidirectional laminates, allowing layups that have not been empirically tested to be analyzed later on. This unidirectional model was chosen for its simplicity and sufficient modeling accuracy [25].

In the laminate, carbon fiber was used with ABS as the matrix. An FVF of 0.5 was used for the reasoning given in Section 6.1. It was assumed that during the manufacture of the beams, the fibers remain unsheared and the FVF of 0.5 is conserved. The mechanical properties of the carbon fiber and ABS are compiled in Table 6.5 below:

Table 6.5: Fiber and Matrix Properties

Material	E_1 [GPa]	E_2 [GPa]	ρ [kg/m^3]	G_{11} [GPa]	G_{22} [GPa]	σ_t [MPa]	σ_c [MPa]
Carbon Fiber [7] [8]	240	10	1600	24	5.4	4900	2886
ABS [9]	2.35	2.35	1070	2	2	34	34

Relations between the compressive and tensile strength of carbon fibers were found in literature [14]. The book lists a compressive to tensile strength ratio of 58.9% for PAN-based Toray T300 fibers, which are similar in stiffness and type to the PAN-based Toray TR50S fibers used in the carbon fiber cloth selected. Using this ratio of 58.9% and the value of σ_t taken from the data sheet[7], a compressive strength of σ_c was found for carbon fiber.

In the following equations, the subscript 11 refers to the longitudinal direction and 22 refers to the transverse direction. The subscript f refers to the fibers, while m refers to the matrix used. First, the longitudinal and transverse Young's moduli E_{11} and E_{22} were calculated using the rule of mixtures in Equation 6.3 and the Chamis model in Equation 6.4:

[6] URL: https://www.humaneticsgroup.com/sites/default/files/2020-11/hybiii50-tps.pdf [Accessed: 11 June 2025]

[7] Dmitry Ivanov. AENGM0091 Composites Design, Manufacture and Product Development – Coursework Assignment. Bristol Composites Institute, University of Bristol. 2025

[9] URL: https://www.clm-pro.com/store-detail/composite-material/carbon-fiber/ud-carbon-fabric-80-g-m-unidirectional-fabric-det
[Accessed: 18 June 2025]

[9] URL: https://protoxyz.com/materials/plastic/ABS [Accessed: 18 June 2025]

[7] URL: https://www.clm-pro.com/store-detail/composite-material/carbon-fiber/ud-carbon-fabric-80-g-m-unidirectional-fabric-det
[Accessed: 13 June 2025]

$$E_{11} = E_{f_{11}} \cdot FVF + E_m \cdot (1 - FVF) \quad (6.3) \qquad E_{22} = E_m \cdot ((1 - \sqrt{FVF}) + \frac{\sqrt{FVF}}{1 - \sqrt{FVF} \cdot (1 - \frac{E^m}{E^f_{11}})}) \quad (6.4)$$

These result in E_{11} = 121 GPa and E_{22} = 6.23 GPa. Then, the shear moduli G_{12} and G_{21} were calculated using the Chamis model in Equation 6.5 and Equation 6.6:

$$G_{12} = G^m \cdot ((1 - \sqrt{FVF}) + \frac{\sqrt{FVF}}{1 - \sqrt{FVF} \cdot (1 - \frac{G^m}{G^f_{11}})}) \quad (6.5)$$

$$G_{21} = G^m \cdot ((1 - \sqrt{FVF}) + \frac{\sqrt{FVF}}{1 - \sqrt{FVF} \cdot (1 - \frac{G^m}{G^f_{22}})}) \quad (6.6)$$

G_{11} = 4.61 GPa and G_{22} = 3.13 GPa. Then, Poisson's ratio for the unidirectional laminate was found using Equation 6.7 and Equation 6.8:

$$\nu_{12} = \nu^f_{12} \cdot FVF + \nu^m \cdot (1 - FVF) \quad (6.7) \qquad \nu_{21} = \frac{\nu_{12} \cdot E_{22}}{E_{11}} \quad (6.8)$$

This gave values of 0.325 and 0.017 for v_{12} and v_{12}, respectively. Next, the the unidirectional strength parameters were calculated. Only longitudinal strength S_{11} undergoes significant change with fiber volume fraction, as shown by Equation 6.9, while transverse strength S_{22} remains relatively insensitive. Equation 6.9 is traditionally only applied for tensile strength, but research suggests a roughly linear relationship also holds for compressive strength [15], leading to Equation 6.10.

$$S_{\text{tensile}_{11}} = FVF \cdot S_{f_{\text{tensile}}} \quad (6.9) \qquad S_{\text{compressive}_{11}} = FVF \cdot S_{f_{\text{compressive}}} \quad (6.10)$$

These relations give values of **2450 MPa** and **1443 MPa** for $S_{tensile_{11}}$ and $S_{compressive_{11}}$, respectively. This is similar to the previously found laminate compressive strength of 1200 MPa, displayed previously in Table 6.3. Transverse tensile strength 64 MPa [62], transverse compressive strength 100 MPa [62] and shear strength 74 MPa [27].

The longitudinal thermal expansion coefficient a_{11} was also defined, set to a value of 0, which is in line with that of carbon fibers. This was done because carbon fibers dominate the longitudinal properties of a laminate. Meanwhile, the transverse thermal expansion coefficient a_{22} was defined to equal that of the matrix. Hence, a_{22} was defined as $8.2 \cdot 10^{-5}\ 1/°C$. Finally, the density of the laminate was be found using the rule of mixtures, calculated using Equation 6.11 below:

$$\rho_{composite} = FVF \cdot \rho_{fiber} + (1 - FVF) \cdot \rho_{matrix} = 1335 kg/m^3 \quad (6.11)$$

6.6.3. Composite Layup Characteristics

A composite layup that is both balanced and symmetric was preferred as it reduces coupling between tensile/shear/bending modes. This would prove to be highly beneficial during the manufacturing process, where thermoplastics have to be heated to high temperatures before being used as the matrix. During the cooling process, residual thermal stresses might be present, warping the product as it cools.

Symmetry in a layup refers to the stacking sequence of plies being mirrored around the mid-plane of the laminate, while being "balanced" refers to having an equal number of positive and negative oriented plies above and below the mid-plane of the laminate.

The selected layup can be described by the notation **[+45/-45/0/-45/+45]**, from bottom to top. The numbers refer to the orientation of the plies in degrees, relative to the longitudinal direction of the laminate, which will be defined in alignment with the lengthwise direction of the frame beams. For the sake of analysis, these will be treated as five individual unidirectional plies, while in reality the +45/-45 plies will be a single ply of woven orthogonal carbon fiber [8] at an areal density of 100 g/m^2. The 0° ply will be a unidirectional carbon fiber sheet[9] of an areal density of 100 g/m^2. Three such 0° plies will be used in the laminate. The thickness of each 100 g/m^2 ply can be found using Equation 6.12 [27] and Equation 6.13[10] below, where W is density of the fiber,

[8] URL: https://www.castrocompositesshop.com/en/72-unidirectional-ud [Accessed: 12 June 2025]

[9] URL: https://www.carbonwinkel.nl/carbon-fiber/carbon-vezel/carbon-100-gm-ncf-ud-50-cm-breed [Accessed: 12 June 2025]

[10] URL: https://www.epoxyworks.com/calculating-laminate-thickness/ [Accessed: 12 June 2025]

ρ density and X is the mass fraction. The subscript f refers to the fibers, while m refers to the matrix used:

$$t_{\text{ply}} = \frac{W_f}{\rho_f \cdot X_f} = 0.11 \text{ mm} \quad (6.12) \qquad t_{\text{ply}} = \frac{W_f}{\rho_f} + \frac{\left(\frac{W_f}{X_f} \cdot X_m\right)}{\rho_m} = 0.15 \text{ mm} \quad (6.13)$$

Upon closer inspection, Equation 6.13 was chosen to be used as it gave a ply thickness most similar to a ply thickness calculator[11] found on the **Toray Advanced Composites** website, a leading manufacturer for carbon fiber. This calculator gave a single-ply thickness of 0.14 mm.

The [+45/-45/0/-45/+45] stacking of plies was then visualized using Abaqus CAE[12], as seen in Figure 6.14. Thicknesses are represented as t, and are given in mm, while the red striped lines represent the orientation of the carbon fibers. The layup has a total thickness of 0.75 mm.

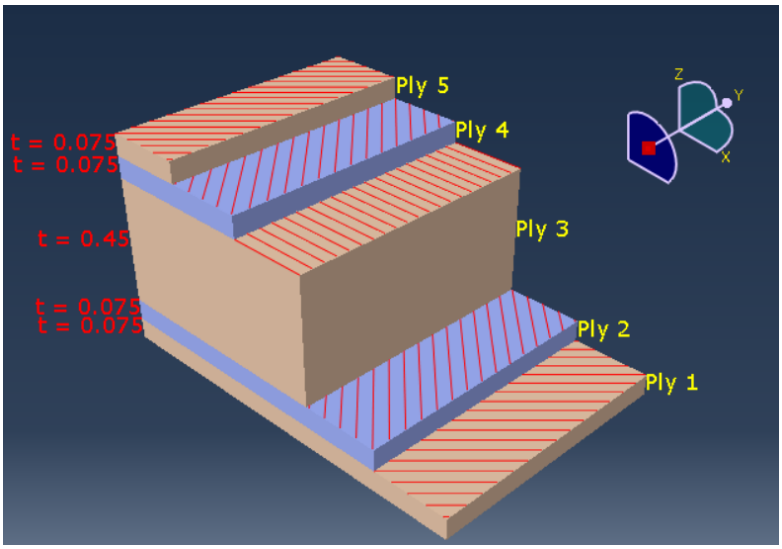

Figure 6.14: Laminate Layup Visualized

With the ply stacking sequence defined, **Classical Laminate Theory** [45] was used to build something called an **ABD Matrix**. This is a form of a stiffness matrix that links loads to strains in the laminate, as explained in Figure 6.15 below. The ABD matrix of the laminate was derived using software called eLamX[13], and is displayed in Figure 6.16 below:

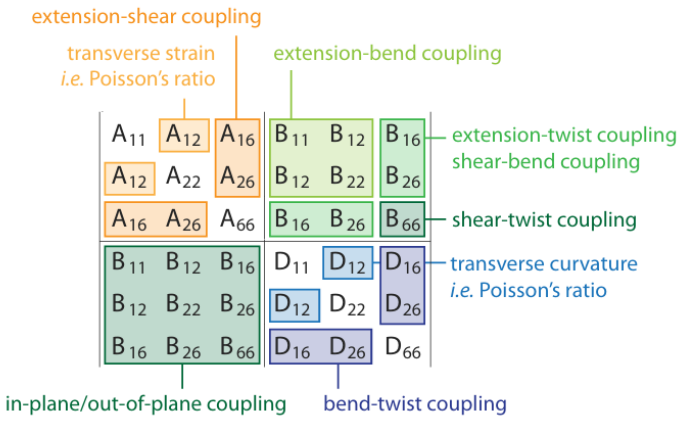

Figure 6.15: ABD Matrix Labeled[27]

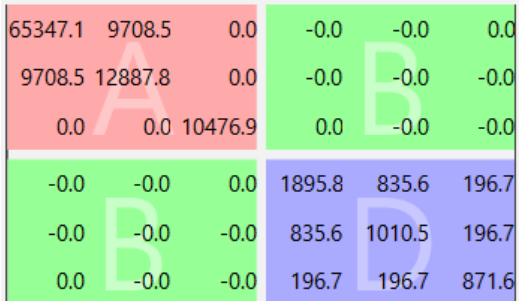

Figure 6.16: Laminate ABD Matrix

This ABD matrix was used to obtain laminate stiffness properties such as E_{xx} and G_{xy}. These properties were chosen as loading in the drone frame during impact primarily occurs through compression, bending and torsion, as will be discussed in Section 6.7. E_{xx} was derived using Equation 6.14:

$$E_{xx} = \frac{1}{h} \cdot \left(\frac{A_{11} \cdot A_{22} - A_{12}^2}{A_{22}}\right) \quad (6.14)$$

[11] URL: `https://www.toraytac.com/resources/Calculators/CPT` [Accessed: 11 June 2025]
[12] URL: `https://www.3ds.com/products/simulia/abaqus/cae` [Accessed: 11 June 2025]
[13] URL: `https://tu-dresden.de/ing/maschinenwesen/ilr/lft/elamx2/elamx?set_language=en` [Accessed: 11 June 2025]

This returned a value of **77.4 GPa** for E_{xx}. This value is in line with what is expected for the given laminate, as **121 GPa** is the longitudinal stiffness of a single 0° unidirectional ply, while the given laminate also features thinner plies oriented at +/- 45°. Shear modulus G_{xy} was calculated using compliance matrix **a**. It was calculated using the sub-matrices of the ABD matrix, as shown in Equation 6.15:

$$\mathbf{a} = A^{-1} - (-A^{-1}B)(D - BA^{-1}B)^{-1}(BA^{-1}) \tag{6.15}$$

The entry a_{66} of compliance matrix a was then used in Equation 6.16:

$$G_{xy} = \frac{1}{\mathbf{a}_{66}h} \tag{6.16}$$

This returned a value of **13.97 GPa**. As expected, this value lies between the shear moduli of ABS and carbon fiber.

6.6.4. Iterated Beam Profile

The cross-section of the beam was updated to a thin-walled hollow circular profile. A circular profile was chosen as it reduces stress concentrations that would otherwise be present in the sharp or filleted corners of a square cross-section, and also as a circular section supports easier clamping. Clamping allows for waterproofing of the drone structure, and a fast method of switching out components, important for modularity. A circular cross-section also provides benefits regarding ease of manufacture, as a process called filament winding can be used for lay-up of the laminate. Filament winding is beneficial by allowing continuous fiber placement, without discontinuities that reduce load-carrying capacity.

The diameter of this iterated cross-section was chosen to be 1.5 cm, in contrast to the square profile with sides of 1 cm used in Section 6.5. This was done to reduce bending stresses, which are given by Equation 6.17:

$$\sigma = \frac{M \cdot y}{I_{xx}} \tag{6.17}$$

While y increases linearly with dimension d, I_{xx} increases exponentially with outer diameter d_o, and decreases with inner diameter d_i as given by Equation 6.18:

$$I_{xx} = \frac{\pi \cdot d_o^4}{64} - \frac{\pi \cdot d_i^4}{64} \tag{6.18}$$

As a result, a linear increase in the cross-sectional profile diameter d decreases bending stresses in the beam cubically. The chosen circular cross-section returned a moment area of inertia I_{xx} of $2.85 \cdot 10^{-10}\ m^4$, and a maximum value for y of 0.75 cm.

6.7. Impact Analysis

For the first iteration of the impact analysis, only a frontal impact was analyzed as this scenario was deemed most likely. In order to make it easier to refer to specific sections of the SpeleoDrone frame easier, sections named **BEAM 1**, **BEAM 2** and **BEAM 3** were defined as seen in Figure 6.17 below:

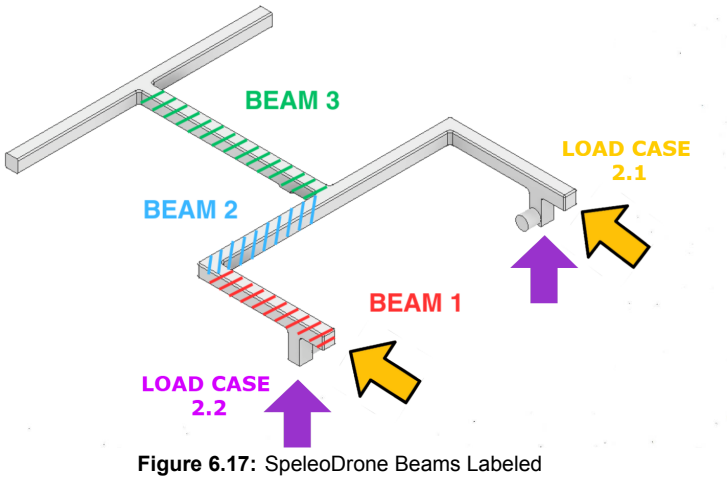

Figure 6.17: SpeleoDrone Beams Labeled

Two collision scenarios are also presented in the figure above, **Load Case 2.1** and **Load Case 2.2**. Load Case 2.1 represents a head-on impact while Load Case 2.2 represents a frontal impact from below. In these load cases, all forces acting on the frame, such as thrust or gravitational forces, were ignored, with the exception of the impact force. This was done because the impact force is more than 2 orders of magnitude larger than any of the operational forces defined in the load cases presented in Section 6.4.

After defining the load cases, the laminate properties E_{xx}, G_{xy} and ν_{12}, previously calculated in Subsection 6.6.3, were used to define a homogeneous isotropic material with a stiffness equivalent to the longitudinal stiffness of the laminate being analyzed. This material was then used in an FEA analysis modeling Load Cases 2.1 and 2.2, where deformations of the circular beam were obtained. These deformations were then used to assess the structure for failure in the laminate plies. This process was presented in the next two subsections.

6.7.1. Load Case 2.1 Analysis

In the event of a head-on collision, where the force of the impact is in-line with the axial direction of BEAM 1, BEAM 1 is subjected to compressive load of 2450 N and BEAM 2 is subjected to a bending moment of:

$$M_{yy} = F \cdot d = 2450N \cdot 0.1m = 245Nm \tag{6.19}$$

Only the compressive performance of BEAM 1 was inspected, as Load Case 2.2 subjects BEAM 2 to an equal bending load, with the addition of other loading modes, making it a more critical load case for BEAM 2. To calculate the compressive loading per unit width acting on BEAM 1, Equation 6.20 was used, which makes use of the circumference of the circular cross-section:

$$n_{xx} = \frac{F}{2 \cdot \pi \cdot r} \tag{6.20}$$

This returned an axial load of **-52 N/mm**. This loading was used as input in eLamX, where Tsai-Hill first ply failure criteria were used to assess whether the laminate fails. A reserve factor RF_{min} of over 11.5 was achieved, concluding that BEAM 1 survived head-on impact. The reserve factor represents how many times stronger a structure is than is required to sustain a load. This result can be seen below in Figure 6.18.

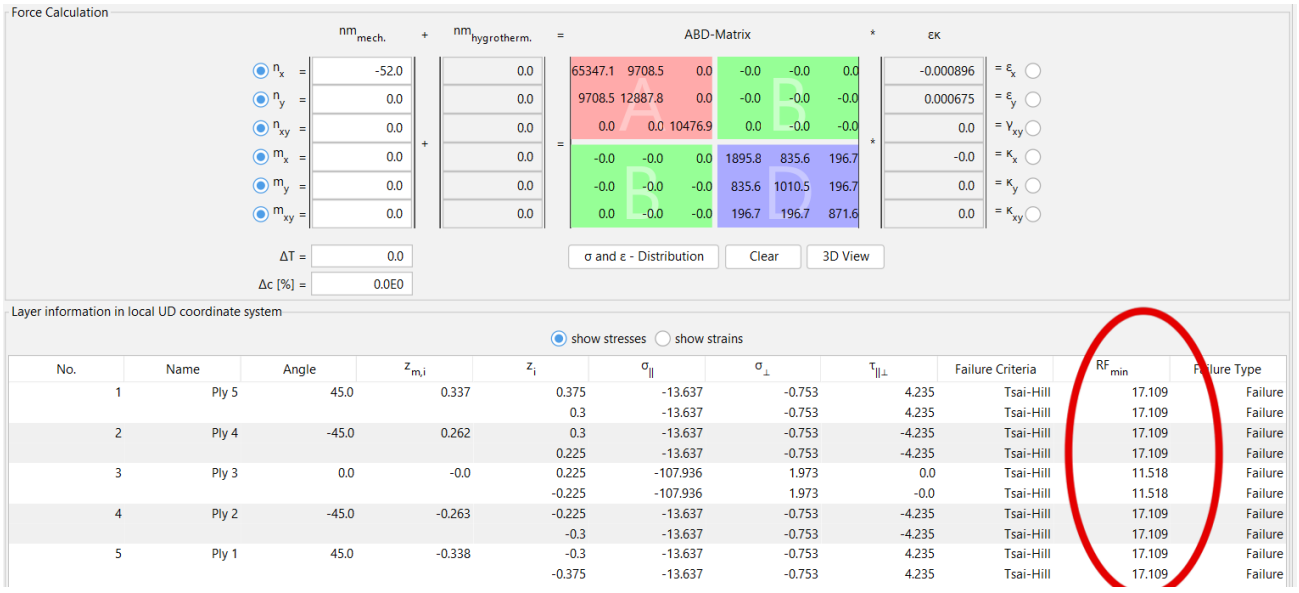

No.	Name	Angle	$z_{m,i}$	z_i	$\sigma_{\parallel}$	$\sigma_{\perp}$	$\tau_{\parallel\perp}$	Failure Criteria	RF_{min}	Failure Type
1	Ply 5	45.0	0.337	0.375	-13.637	-0.753	4.235	Tsai-Hill	17.109	Failure
				0.3	-13.637	-0.753	4.235	Tsai-Hill	17.109	Failure
2	Ply 4	-45.0	0.262	0.3	-13.637	-0.753	-4.235	Tsai-Hill	17.109	Failure
				0.225	-13.637	-0.753	-4.235	Tsai-Hill	17.109	Failure
3	Ply 3	0.0	-0.0	0.225	-107.936	1.973	0.0	Tsai-Hill	11.518	Failure
				-0.225	-107.936	1.973	-0.0	Tsai-Hill	11.518	Failure
4	Ply 2	-45.0	-0.263	-0.225	-13.637	-0.753	-4.235	Tsai-Hill	17.109	Failure
				-0.3	-13.637	-0.753	-4.235	Tsai-Hill	17.109	Failure
5	Ply 1	45.0	-0.338	-0.3	-13.637	-0.753	4.235	Tsai-Hill	17.109	Failure
				-0.375	-13.637	-0.753	4.235	Tsai-Hill	17.109	Failure

Figure 6.18: BEAM 1 Load Case 2.1 eLamX Analysis

6.7.2. Load Case 2.2 Analysis

In the event of a head-on collision from below, BEAM 2 would be subject to both bending and torsional loading. The bending and torsional loads, M_{yy} and T_{xx} acting on BEAM 2 are:

$$M_{yy} = F \cdot d = 2450 \text{ N} \cdot 0.1 \text{ m} = 245 \text{ Nm} \tag{6.21}$$

$$T_{xx} = F \cdot d = 2450 \text{ N} \cdot 0.1 \text{ m} = 245 \text{ Nm} \tag{6.22}$$

Such loading of BEAM 2 is represented in Figure 6.19 below, where one end is modeled as a fixed constraint. The figure also presents a mesh that was refined until a convergence rate greater than 2% was achieved for the Von Mises stress. Meanwhile, Figure 6.20 presents 8 distinct points that were defined along BEAM 2. At these

8 points, strains were analyzed in an FEA simulation involving an isotropic material modeled using previously found laminate values of E_{xx}, G_{xy} and ν_{12}. Tetrahedral elements were used.

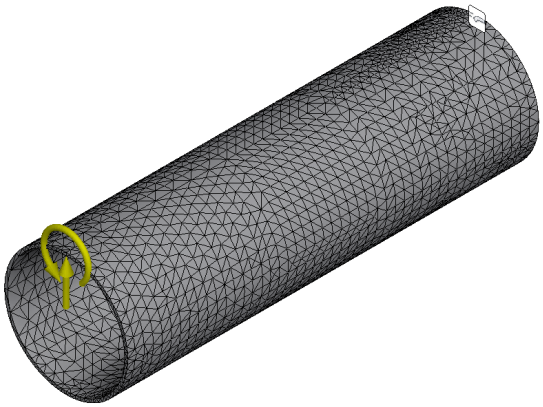

Figure 6.19: BEAM 2 Loading Model and Mesh

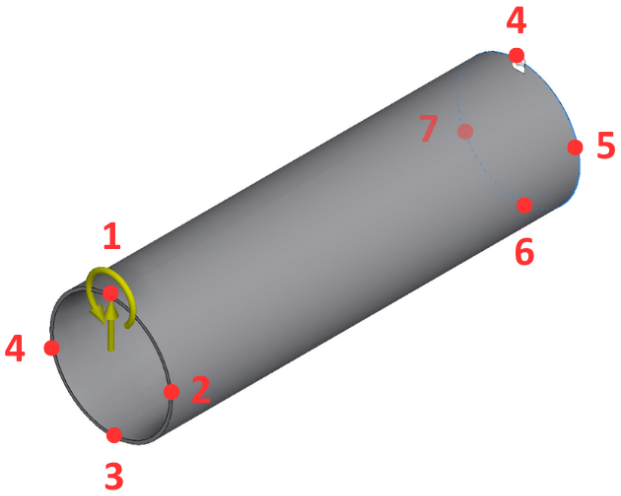

Figure 6.20: BEAM 2 Points Definition

With the points to be analyzed defined, an FEA simulation was carried out on the isotropic simplified model of BEAM 2. The figures below display the results obtained, starting with the axial and hoop strains ϵ_{xx} and ϵ_{zz}.

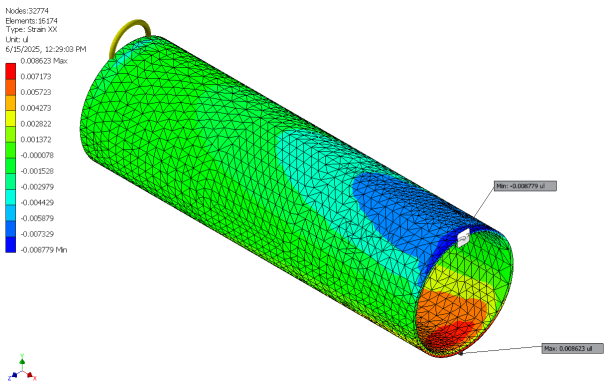

Figure 6.21: BEAM 2 strain ϵ_{xx} distribution

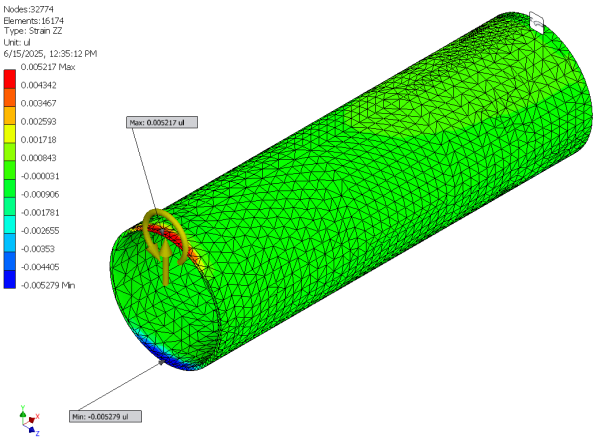

Figure 6.22: BEAM 2 hoop strain ϵ_{zz} distribution

As can be seen in Figure 6.22, hoop stresses, and hence hoop strains ϵ_{zz}, were present through the action of the Poisson ratio ν_{12} in response to the tensile and compressive stresses. These stresses were present at the top and bottom surfaces of the beam, as a result of the bending load acting on the beam. Next, the shear strains ϵ_{xy} and ϵ_{xz} are displayed in Figure 6.23 and Figure 6.24:

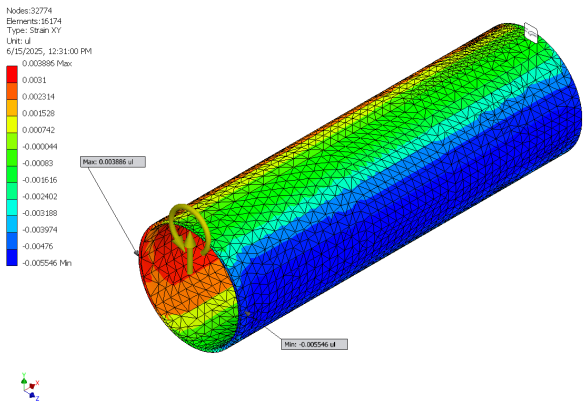

Figure 6.23: BEAM 2 shear strain ϵ_{xy} distribution

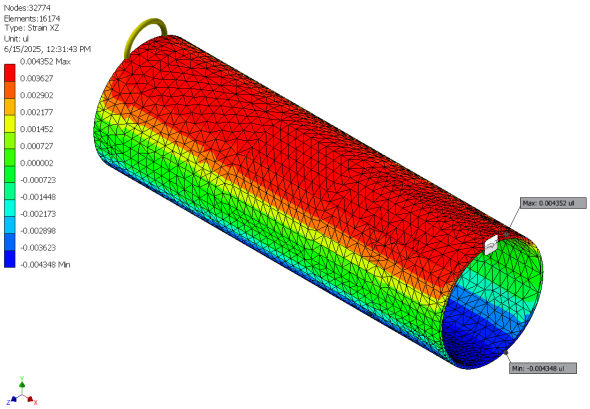

Figure 6.24: BEAM 2 shear strain ϵ_{xz} distribution

The results of the simulation, in the form of a point-wise strain distribution, are presented in Table 6.6.

Table 6.6: Load Case 2.2 Beam Point-Wise Strain Distributions

Point	ϵ_{xx}	ϵ_{xy}	ϵ_{xz}	ϵ_{zz}
1	-0.002	0	0.0041	0.0052
2	0	-0.0055	0	0
3	0.002	0	-0.0041	-0.0052
4	0	0.0039	0	0
5	-0.0088	0	0.0044	0
6	0	-0.0049	0	0
7	0.0086	0	-0.0044	0
8	0	0.0031	0	0

The strains obtained at each point were used as input for the ABD matrix in eLamX, where Tsai-Hill first ply failure was used as a failure criteria. Point 7 proved most critical, where the outer plies had a reserve factor RF_{min} of 1.152 during impact Load Case 2.2, as seen in Figure 6.25 below:

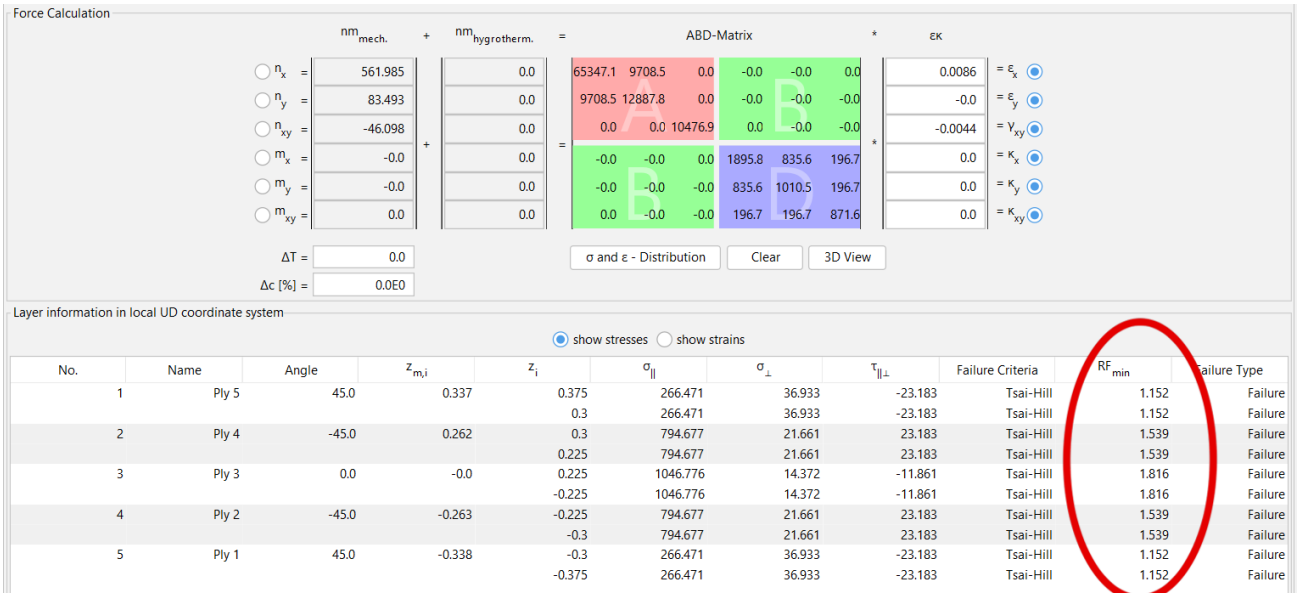

Figure 6.25: BEAM 2 Load Case 2.2 Point 7 eLamX Analysis

As a result, it was concluded that the composite layup selected for the beams would be able to survive in the event of impact and would not need replacement in the field. This concluded that requirement **DRN-STRC-05** was met by the beams.

6.7.3. Connective Elements

As the composite beams cannot be manufactured as a continuous structure due to the 90 degree bends present, connective elements are required to facilitate load transfer between beams. T-shaped and elbow-shaped connective elements, manufactured using AZ31B magnesium alloy, connect the composite beams. These connections feature lower thicknesses at their outer ends, facilitating clamping to the beam with an external circular clamp. This clamping protects against water and particulate ingress and ensures a tight fit. When designing these connections, it was decided that in the event of impact or severe loads, the connections must fail before the composite beams, due to their ease of replacement. They are hence treated as a sacrificial element that ensures the survival of the harder to manufacture composite beams.

Additional mounting elements connect other SpeleoDrone components to the composite beams. Three types of such elements are present in the form of hollow structures made out of AZ31B: motor mounts and two types of landing gears. One type of landing gear has a pin connection for the payload bay, while the other does not. These mounting elements feature a design philosophy similar to the sacrificial philosophy used in the T-shaped and elbow-shaped connections. The structural frame assembly for the SpeleoDrone is displayed below in Figure 6.26:

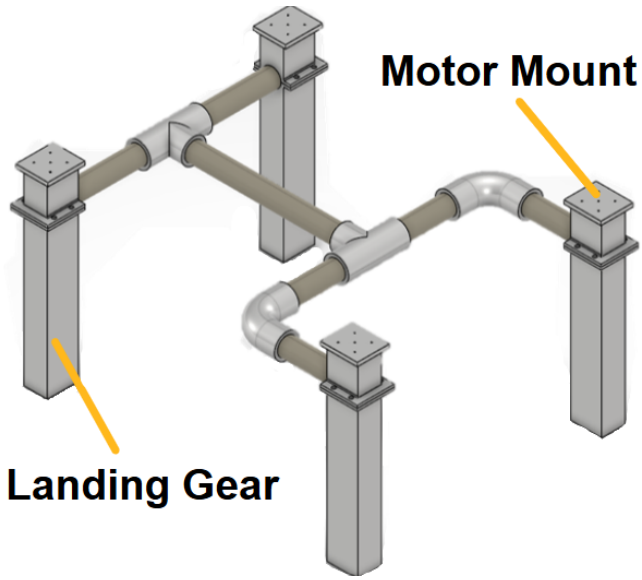

Figure 6.26: SpeleoDrone Frame Assembly

6.7.4. Impact Analysis Limitations

A number of limitations were present in the approach used for the impact-tolerant design. Using an FEA model of an isotropic beam, with axial and shear stiffness properties equivalent to those of the laminate, provides a close approximation for axial strains under the axial loads investigated. However, this approach fails to correctly model for example hoop stresses, as composites have separate Poisson ratios ν_{12} and ν_{21}, while the isotropic beams uses ν_{12} in all directions.

Furthermore, when assessing Tsai-Hill failure criteria for the composite laminate, thermal loads experienced during manufacture were ignored. As ABS has a melt temperature of 260°C [14], and cave temperatures are around 20°C [60], a ΔT of 240°C can be expected during the operation cycle of the SpeleoDrone. This temperature difference would likely lead to transverse matrix failure as a result of thermal stresses, a common occurrence which on its own should not be of concern[15] as the beams are loaded primarily in the axial direction, and not the transverse one. An improved approach would be to model the expected ΔT in eLamX, and investigate whether the thermal load induces ply failure in the longitudinal or matrix directions by inspecting the longitudinal and transverse stresses per ply.

Finally, the methodology used when assessing impact loads on the SpeleoDrone structure could be improved. The methodology included multiple assumptions, and extrapolation of experimental results. The approach used likely overestimated impact loads, especially as a quasi-static analysis based on peak collision loads was used.

More insight would be offered by using an elastic energy model, where in a conservative analysis all of the kinetic energy of the SpeleoDrone during collision would be transformed into elastic energy as the drone structure deforms. The equations used for kinetic and elastic energy $U_{kinetic}$ and U_E are shown below in Equation 6.23 and Equation 6.24:

$$U_{\text{kinetic}} = \frac{1}{2} \cdot m \cdot v^2 \tag{6.23}$$

$$U_E = \sum_{i=1}^{k} \frac{1}{2} \cdot \epsilon_i \cdot \sigma_i \cdot \text{volume}_i \tag{6.24}$$

These equations could be reverse-engineered, as for a specific load case, a ply stress distribution for the laminate could be obtained using an FEA model to obtain strains, similar to what was done in Section 6.7, which is then fed into eLamX to assess laminate failure. This stress distribution could be used to build U_E, which would then be equal to the maximum amount of kinetic energy $U_{kinetic}$ that the drone structure can withstand. From $U_{kinetic}$, the maximum survivable collision velocity could be obtained. Furthermore, $U_{kinetic}$ = U_E assumes that all of the kinetic energy of the SpeleoDrone before collision is used to deform the structure, which is a conservative assumption.

6.7.5. Future Steps

The beam profile should be updated by increasing the diameter of the beams to for example 2.5 cm. This would increase the area moment of inertia of the beam profile, reducing bending stresses and allowing for the use of fewer/thinner 0° plies. Currently, the 0° plies are not critically loaded and are significantly thicker than the +-45

[14] URL:`https://protoxyz.com/materials/plastic/ABS` [Accessed: 18 June 2025]
[15] Private conversation with Prof. Clemens Dransfeld on 17 June 2025.

degree plies. However, their reserve factor RF_{min} is around 1.3 during Load Case 2.2, which does not show significant overdesign.

This change is not expected result in significant weight savings, as the composite beams are already very lightweight at 30g. However, this would reduce the laminate thickness, could translate to less carbon fiber needing to be used in the manufacturing process, leading to cost reduction for manufacturing. A larger cross-section diameter would also make it easier to fit more wiring into the composite beams.

In their current state, the connective elements shown in Subsection 6.7.3 make up the majority of the structural mass at 289 grams, compared to 30 grams mass of the composite beams. When subjected to a quick FEA analysis, it was revealed that they begin yielding only right before the composite beams would fail in an impact scenario. It makes more sense to either reduce the thickness and size of the connections, ensuring that they fail before the composite beams due to their easier to replace nature, or use a weaker, albeit easier and cheaper to manufacture, material for them such as PEEK. This will be discussed further in Section 11.1, however it should be noted that PEEK has a lower specific strength and bending stiffness than AZ31B, meaning that changing the material of the connective structures would lead to an increase in mass.

Finally, manufacturing the ABS and carbon-fiber laminate could prove prohibitively expensive as it is a somewhat novel material and not readily available. In such a case, an alternative thermoplastic, with mechanical properties no weaker than ABS, such as PVC, should be used. The specific choice of matrix is subject to availability, as pre-impregnated unidirectional tape would have to be bought from a third-party provider.

6.8. Sensitivity Analysis

A sensitivity analysis for a drone structure assesses how the structure would be affected by uncertainty in the design values. This uncertainty could be in, for example, the masses of drone components, or in the mechanical properties of the materials used in the drone structure.

As the main structural elements used in the drone were designed to withstand an impact load of 2450 N, almost two orders of magnitude higher than any handling or operational loads defined in Section 6.4, the drone structure was comfortably assumed to be insensitive to any variation in the masses of other drone components, from a rigidity and strength point of view.

Furthermore, when defining impact loads, these were scaled linearly from literature by a factor that corresponded to a ratio of the SpeleoDrone mass to a commercial drone weighing just above 1 kg. When these loads were defined, SpeleoDrone had a mass budget of 3.455 kg, while the final CAD model had a mass of 3.174 kg, albeit with a few missing elements such as wiring. This, paired with the conservative nature of the quasi-static analysis, translated to significantly overestimated impact loads. These overestimated loads, when paired with a resulting reserve factor of 1.15 obtained during the impact analysis, ensure that the SpeleoDrone structure is insensitive to variation in mechanical properties of the composite laminate. This variation could result from for example carbon fibers with a lower compressive or tensile strength, or an ABS matrix with a lower yield strength, or local imperfections in the laminate. The mechanical properties of the fibers or matrix are unlikely to vary more than 10% from technical specifications, which is still well below the safety factor. Regarding local structural imperfections, a study of the variability in the mechanical properties of composite tubes due to local manufacturing defects showed a standard deviation in tensile strength of 6.4% [51]. Assuming a similar distribution in compressive strength, the study implies that the composite beams present in the SpeleoDrone should not lose more than 6.4% mechanical strength, due to manufacturing variations, with a 95% confidence interval for each beam.

7. Flight Performance

The flight performance characteristics of the drone are dictated by its propulsion capabilities, coupled with its aerodynamic parameters. As specified in the design configuration description, Section 2.4, the drone design uses a quadcopter configuration, featuring 4 rotors providing thrust. The rotors may provide varying thrust, causing a thrust differential. Since the drone does not feature any wings or airfoils, the drone itself does not generate any lift forces due to pressure differentials. The flight performance chapter covers flight performance requirements in Section 7.1, all the design details related to the propulsion capabilities of the drone are discussed in Section 7.2, together with more detailed parameters such as drag, accelerations, maximum flight time and maximum range, mapping speed and turn rates. With the propulsion system in mind, the noise identification and mitigation measures are discussed in Section 7.3, together with a duct design. A sensitivity analysis is conducted in Section 7.4, and finally Section 7.5 covers the verification and validation of the flight performance.

7.1. Flight Performance Requirements

The aerodynamic design of the drone is driven by the requirements set out in the Baseline report [11]. However, since the requirements relate to the general scope of the capabilities of the drone, more detailed subsystem requirements need to be set out to make sure that the drone design successfully completes the mission. The subsystem requirements stem from parent requirements, which can be found in Appendix A, and serve as a more accurate way of checking that each mission need is satisfied.

Table 7.1: Flight Performance Requirements Definition

Requirement ID	Description	Parent Requirement
DRN-FP-01	The propulsion system shall have a mass of no more than 0.25 kg.	**MIS-OPR-9.1**
DRN-FP-02	The propellers' diameter shall not exceed 18 cm	**STK-DRN-4**
DRN-FP-03	The minimum total thrust provided by the propellers shall be at least 40 N.	**SYS-DRN-4.2.2**
DRN-FP-04	Maximum cost of the propellers and motors shall be below 100 EUR.	**STK-OPR-03**
DRN-FP-05	The clearance between propellers shall be at least 1 cm.	**MIS-DRN-4.2**
DRN-FP-06	The propulsion system shall use less than 5000 W of power at all times.	**MIS-OPR-11.2**
DRN-FP-07	The drone shall have at least 15 minutes of flight time in hovering flight.	**SYS-OPR-1.2.1**
DRN-FP-08	The combined noise emitted by the propellers shall be less than 85 dB.	**MIS-OPR-7.1**
DRN-FP-09	The propulsion system shall allow the drone to cover a distance of at least 1000 meters on one battery charge	**STK-DRN-1**
DRN-FP-10	The propulsion system shall not produce any emissions during operation	**STK-OPR-06**

7.2. Detailed Design

Once the flight performance requirements were established, the selection of a suitable propulsion subsystem could be conducted. After choosing the most appropriate configuration, a performance analysis was conducted to evaluate how well it met the design objectives under the expected operating conditions.

7.2.1. Propulsion subsystems selection

The propulsion system of a quadcopter drone relies on four motors, each attached to a propeller and controlled by an ESC, which can be 1 for all motors, or 1 for each motor. The ESC receives signals from the flight controller, and adjusts the motor speed. That motor spins the propeller that generates the thrust. All four work together so the drone can lift, move, and turn by varying the power to each motor respectively.

In order to choose a suitable combination, an iterative approach was needed, due to a continuously changing mass in each design stage. Ideally speaking, the propeller's thrust should be as efficient as possible around the thrust needed for the drone to hover and cruise, which would be around a Thrust-to-Weight ratio of around 1-1.1, considering some margin.

In order to consider as many commercially tested combinations as possible, the following sub system requirements were mainly considered to already filter out unsuitable propellers.

DNR-FP-03: The propellers' diameter shall not exceed 18 cm.

DRN-FP-03: The minimum total thrust provided by the propellers shall be at least 40 N.

With still a lot of combinations left, a custom database was constructed using various propeller-motor data commercially available, based on experimental data[1] [2] [3]. This custom database included thrust settings of each propeller-motor combination, together with its power consumption, rotations per minute (RPM), and torque values. To maximize the endurance, a new propeller-motor combination was picked after each design phase with the lowest power consumption for the thrust needed to make the drone hover. For the mass in the final design stage, together with considering appropriate contingencies, there were two contestants for the best performing motor-propeller combinations. The '**ECOII-2807-1300KV**' & '**HQ 7*3.5*3**' have been chosen for the motor and propeller respectively, due to a lower RPM needed to sustain hovering compared to the other contestant which had a similar power consumption. A lower RPM results in lower noise emissions during hovering [46]. With the power and RPM data available for various thrust settings, the root means squared thrust coefficient k_f and torque coefficient k_m could be calculated with the following equations.[63]

$$T_i = k_f \cdot \omega^2 \quad \tau_i = k_m \cdot \omega^2 \tag{7.1}$$

Where T_i is the propeller thrust, τ_i the torque of the propeller and ω is the rotational velocity in rad/s. The propeller-motor data [4] included values for thrust, power and RPM. The ω could be found by multiplying the RPM by $2\pi/60$, the torque in Nm could be found by the equation below, linking the power to the rotational velocity.

$$\tau = \frac{P[W]}{\omega[rad/s]} \tag{7.2}$$

Using the root-mean-square of the data available, the thrust coefficient $k_f = 4.82 \cdot 10^{-6}$ and the torque coefficient $k_m = 8.07 \cdot 10^{-8}$. These values will be used for the controller of the drone.

The ESC could be chosen after a motor-propeller combination was selected. The ESC was selected, based on its continuous current rating which should be higher than the maximum current the propeller-motor combination would draw, preferably with margin around 10 %. [5] The chosen 'ECOII-2807-1300KV[6]' & 'HQ7*3.5*3 [7]' combination has a maximum current of 47.1 A, so to comfortably meet this current, the '**T-Motor F45A V2 4in1 ESC (3-6S)**' was selected, which can support a maximum current of 55 A.

The power required to keep the drone in the air is effortlessly provided by two Spektrum Smart G2 30C LiPos' batteries [8]. The battery selection is covered in Subsection 9.2.1. The actual performance calculations will be covered in the next subsection.

7.2.2. Performance Analysis

The performance of a drone can be evaluated based on various metrics. These metrics can be categorized into two main categories: performance in hovering, steady flight and performance in non-hovering, non-steady flight. The two main performance parameters used to calculate performance metrics in these two categories, were the Thrust-To-Weight (T/W) ratio and Drag.

Hovering, steady flight

During hovering flight, the drone does not move horizontally and maintains its altitude. For this reason, both the horizontal acceleration a_h and vertical acceleration a_v of the drone are equal to zero (i.e. $a_h = 0$, $a_v = 0$). As the drone is stationary, it experiences no drag. Using simple force equilibrium, Equation 7.3 could be obtained.

$$W = 4T = 3.4572[kg] \times 9.81[m/s^2] = 33.92[N] \tag{7.3}$$

As can be seen from the equation, in hovering the total thrust is equal to the weight. This implies a Thrust-to-Weight ratio of 1, during hover.

Since the energy source does not dispose of any emissions, it is assumed that the mass is fully conserved throughout the hovering, and the weight of the drone remains constant. This calculation was also used in the propulsion selection Subsection 7.2.1 to identify the preferred propeller and motor combination.

[1] URL: https://database.tytorobotics.com/,[Accessed: 5 June, 2025]

[2] URL:https://www.mepsking.shop/drone-parts/motors,[Accessed: 5 June, 2025]

[3] URL: https://www.unmannedtechshop.co.uk/product/emax-eco-ii-series-2807-motor-1300kv-1500kv-2700kv/, [Accessed: 6 June, 2025]

[4] See Footnote 3

[5] URL:https://www.mepsking.shop/blog/what-is-esc-comprehensive-guide-for-electronic-speed-controller.html,[Accessed: 12 June 2025]

[6] URL:https://www.unmannedtechshop.co.uk/product/emax-eco-ii-series-2807-motor-1300kv-1500kv-2700kv/,[Accessed: 10 June 2025]

[7] URL:https://droneshop.nl/hqprop-7x3-5x3-propellers#:~:text=Deze%20HQprop%207x3.5x3%20propellers%20zijn%20gemaakt%20van%20polycarbonaat%20(PC,een%20hoge%20flexibiliteit%20en%20duurzaamheid.&text=Deze%20propellers%20zijn%20uitgevoerd%20in%20de%20kleur%20grijs.&text=HQProp%20is%20een%20specialist%20in,werd%20HQProp%20opgericht%20in%20China,[Accessed: 10 June 2025]

[8] URL:https://www.spektrumrc.com/product/22.2v-7000mah-6s-30c-smart-g2-lipo-battery-ic5/SPMX76S30.html,[Accessed: 9 June 2025]

Non-hovering, non-steady flight

In order to accurately quantify the flight parameters and performance capabilities of the drone in non-hovering, non-steady flight, the two most important parameters which have to be accurately quantified are the Thrust-to-weight (T/W) ratio and the drag experienced by the drone. As the T/W ratio is a relation which depends only on the weight and thrust capabilities of the drone, it is a rather simple relation. However, drag is a more complicated calculation which has to be quantified accurately before any performance analysis can be performed.

The drag force experienced by the drone during horizontal flight can be obtained using Equation 7.4 [9].

$$D = \frac{1}{2} \cdot C_D \cdot \rho \cdot v^2 \cdot S \tag{7.4}$$

As can be seen, the equation has a number of variables which have to be taken into account simultaneously. The variables include the drag coefficient, air density, velocity of the drone and the reference surface area experiencing drag, which in turn varies with the pitch angle of the drone.

The incoming velocity V was assumed to be equal to the drone velocity, whilst for the sake of simplicity, it was assumed that the air density was equal to sea level air density $\rho = 1.225 kg/m^3$ (this can be assumed due to the negligible variations in cave air density throughout the day [10]). Since the drone was assumed to approximate a flat plate, the drag coefficient was taken to be 1.28 [11].

The next step involved calculating the reference drone surface area, S_{ref}. This area is defined as the vertical component of the surface area of the drone in the direction of motion. As horizontal drag is the primary focus, assuming that the effective area of the drone varies only with the pitch angle, the equation for the effective drone area (the vertical component of the drone area) could be calculated with Equation 7.5:

$$S_{ref} = (S_{top})sin(\theta) + (S_{front})cos(\theta) \tag{7.5}$$
$$S_{ref} = (0.164)sin(\theta) + (0.04988)cos(\theta) \tag{7.6}$$

The values for the top and frontal areas are calculated by summing the frontal areas of the components of the drone. A diagram describing the definition of the pitch angle θ, reference drone surface area, S_{ref} as well as the top and front areas, S_{top} and S_{front} respectively, is provided below:

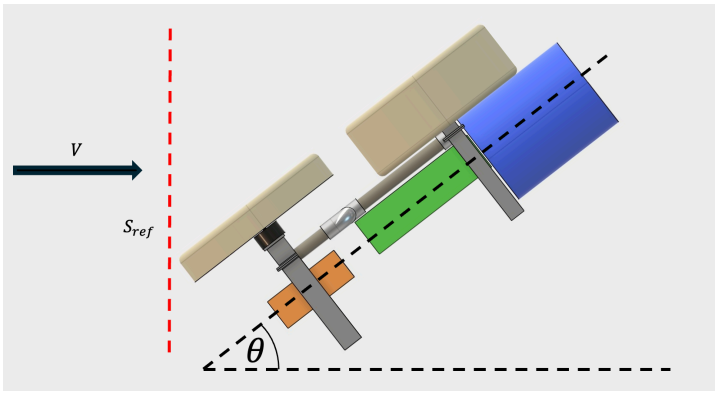

Figure 7.1: Pitch angle of the drone

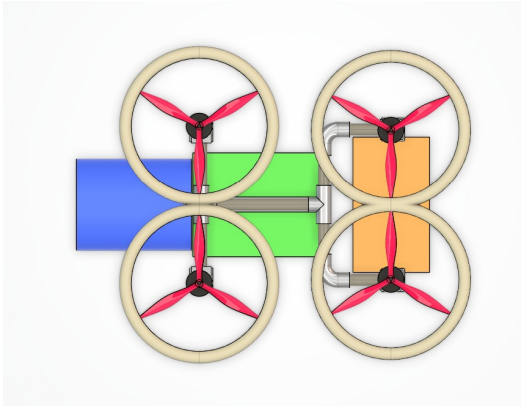

Figure 7.2: Geometrical definition of the top area of the drone (S_{top})

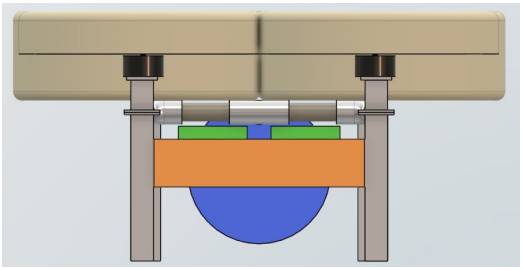

Figure 7.3: Geometrical definition of the frontal area of the drone (S_{front})

[9] URL: https://www.grc.nasa.gov/WWW/k-12/VirtualAero/BottleRocket/airplane/shaped3.html [accessed 19 May 2025]
[10] URL: https://shorturl.at/tbKeW, (https://www.researchgate.net/) [accessed 20 May 2025]
[11] URL: https://www.grc.nasa.gov/WWW/k-12/VirtualAero/BottleRocket/airplane/shaped3.html [accessed 19 May 2025]

Using the area equation as well as the values and the drag equation defined earlier, the relationship of the drag with pitch angle was plotted for velocities ranging from 0.5 m/s to 10 m/s in increments of 0.5 m/s. The results are displayed in figure 7.4:

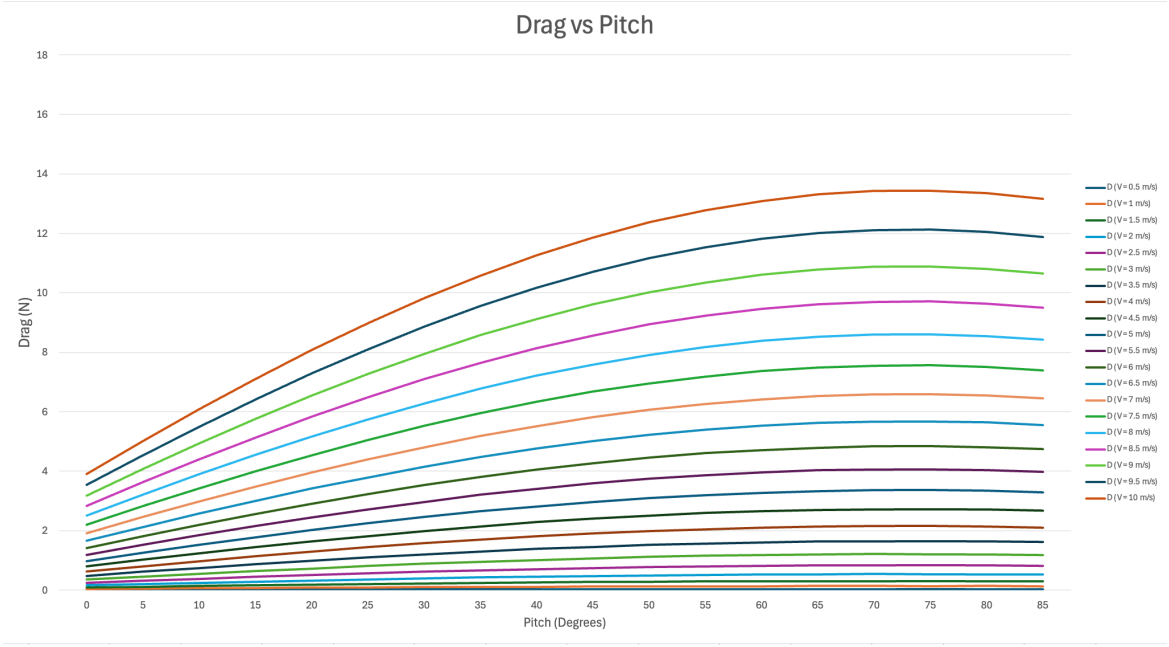

Figure 7.4: Drag vs. Pitch angle

Maximum horizontal acceleration

Another parameter analyzed is the maximum horizontal acceleration of the drone. For this analysis, the equations of motion presented in Equation 7.7,Equation 7.8 were established:

$$ma_h = 4T\sin(\theta) - D \quad ma_h = 4T\sin(\theta) - C_D\tfrac{1}{2}\rho v^2 S_{ref} \tag{7.7}$$

$$ma_v = 4T\cos(\theta) - W \tag{7.8}$$

The equation including the term a_h (horizontal acceleration) corresponds to horizontal motion, whilst the equation featuring the term a_v (vertical acceleration) corresponds to vertical motion. In order for the motion to be purely horizontal, the vertical acceleration must remain zero, leading to the following relation:

$$ma_v = 4T\cos(\theta) - W = 0 \quad W = 4T\cos(\theta) \qquad T_{a_v=0} = \frac{W}{4\cos(\theta)} \tag{7.9}$$

In order to calculate the maximum pitch angle for purely horizontal flight, the term $T_{a_v=0}$ is replaced by $T_{max} = 25.3N$. This gives a maximum pitch angle $\theta = 72.09°$. Using the equations of motion above, the graph of maximum acceleration in horizontal flight vs pitch angle could be plotted as can be seen in Figure 7.5.

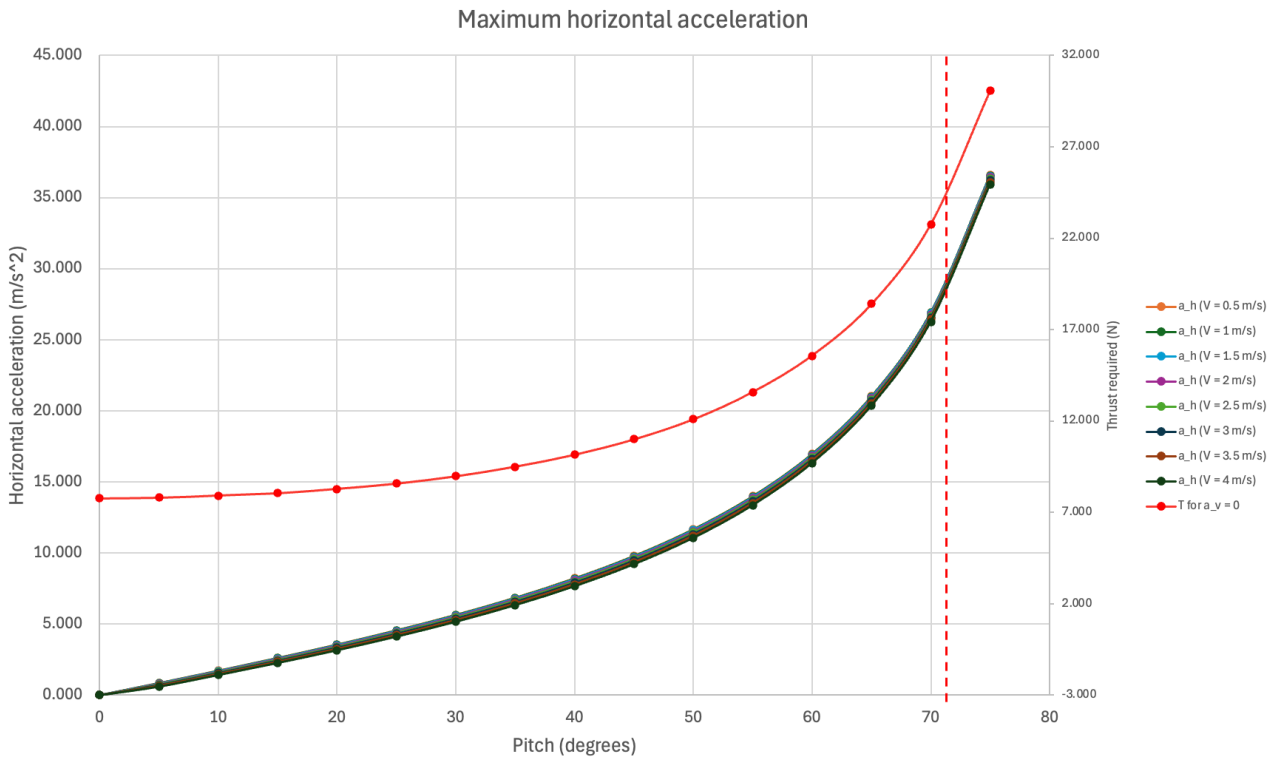

Figure 7.5: Maximum horizontal acceleration vs Pitch angle

The graph also features the thrust required at each pitch angle (red parabolic line) using a secondary y-axis on the right-hand side, as well as a dotted vertical red line, placed at $\theta = 72.09°$. This line marks the limit on the maximum pitch angle the drone can fly at with purely horizontal motion, as mentioned before. Flying with a pitch angle higher than $\theta = 72.09°$ would not be possible for purely horizontal flight due to constraints on thrust.

Endurance

For the mission at hand, the most important aspect to consider was the endurance of the drone. The endurance determines how long the drone can operate in air before it needs to be recharged, and how far in the cave the drone could go, therefore affecting the rate at which the cave can be mapped. To quantify these for a number of potential scenarios the drone can encounter in operation, various maneuvers were considered through the use of the drone's T/W ratio, and the corresponding power consumption. Since the layout of the cave is unknown, the difficulty and pace of the maneuvers which the drone will have to perform is not known. However, the complexity of these maneuvers can be roughly quantified through the use of the drone's T/W ratio in a given situation. Sharp and sudden maneuvers require a high accelerations, which comes from larger thrust, and therefore can be characterized to a higher T/W ratio, whilst longer, slower maneuvers can be performed with lower accelerations and less thrust, leading to a smaller T/W ratio.

For a given T/W ratio, the required thrust per propeller was calculated. Using the specifications sheet of the selected propeller and motor, the power required to achieve this thrust was then calculated and multiplied by 4 in order to obtain the complete power consumption of the propellers for a given Thrust-to-Weight ratio. Using the battery energy capacity, and the given power consumption, the operating time was calculated. The following values have been obtained:

As can be seen in the table, the values rise with an increment of 0.1 until a T/W ratio of 2, and then increase with increments of 0.2, ending at a T/W ratio of 3.25 which is the maximum achievable Thrust-to-Weight ratio using the drone's maximum thrust capabilities. During operation, maneuvers requiring a T/W ratio higher than 1.8 are regarded as extreme maneuvers and are therefore preferably avoided. The data was plotted in order to obtain a regression relation between the T/W ratio and flight time, which will be used in future calculations.

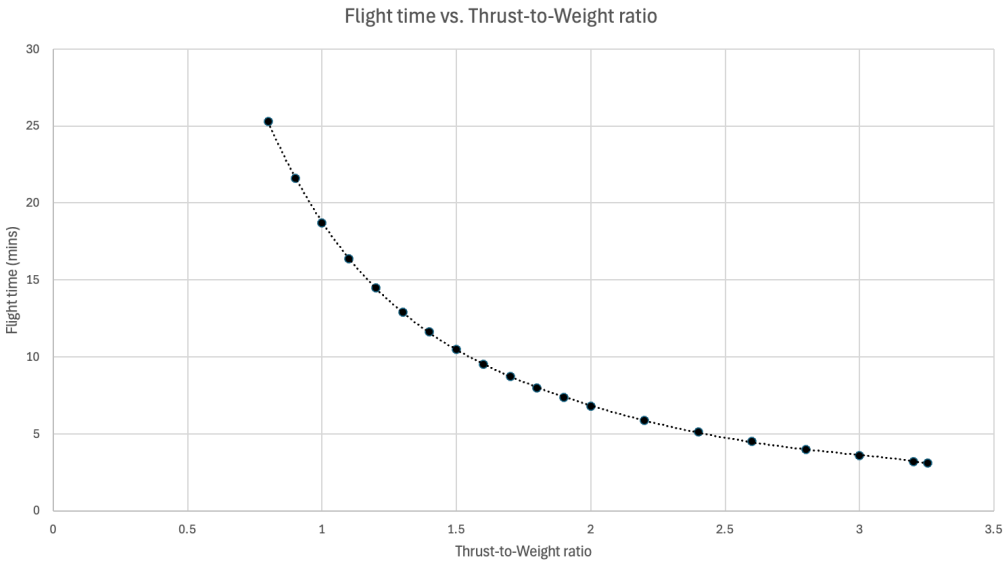

Figure 7.6: Flight time vs Thrust-to-Weight ratio

The graph produced the following regression relation:

$$t(T/W) = -0.9704(T/W)^5 + 11.455(T/W)^4 - 54.077(T/W)^3 + 129.78(T/W)^2 - 164.46(T/W) + 97.038 \tag{7.10}$$

Maximum velocity and range

In order to quantify the maximum distance which the drone can travel (range) for a range of T/W ratios, a simple kinematic estimate is used, utilizing the calculated flight times.

First, the maximum flight velocity of the drone was calculated for given pitch angles, ranging from $0°$ to $72.09°$, the maximum pitch angle in horizontal flight. The maximum velocity is obtained when the horizontal drag experienced by the drone is equal to the horizontal thrust force, resulting in a horizontal acceleration of 0, as can be seen through the equations of motion in Equation 7.7. For a given pitch angle, using the thrust required for no vertical flight ($T_{a_v=0}$, obtained through Equation 7.9) and the equation of motion for horizontal flight (Equation 7.8), the drag required for $a_h = 0$ is calculated. Finally, the calculated drag value, as well as the reference drone area at the given pitch angle are used in Equation 7.4, and the equivalent maximum flight velocity is calculated. After the maximum velocities have been calculated, the flight time for at each pitch angle was obtained. By dividing the values of $T_{a_v=0}$ by weight, the T / W ratio can be obtained for purely horizontal flight at a given pitch angle. Next, using Equation 7.10, an equation linking T/W and flight time established earlier through regression methods, the flight time at each pitch angle can be found. Using the simple kinematic relation of velocity = distance/time, the distance covered flying at each pitch angle can be found. The results of this calculation can be found in the table below:

Table 7.2: Maximum velocity and range of the drone

Pitch angle [°]	$T_{a_v=0}$ [N]	Max. velocity [m/s]	T/W	Flight time [min]	Range [m]
0	7.782	0.000	1.000	18.74	0
5	7.812	8.336	1.003	18.64	9325
10	7.902	10.745	1.015	18.35	11829
15	8.056	12.257	1.035	17.85	13131
20	8.281	13.403	1.064	17.17	13809
25	8.586	14.385	1.103	16.31	14077
30	8.986	15.308	1.154	15.28	14036
35	9.500	16.239	1.220	14.10	13743
40	10.158	17.230	1.305	12.80	13237
45	11.005	18.331	1.414	11.41	12546
50	12.106	19.597	1.555	9.94	11685
55	13.567	21.104	1.743	8.40	10642
60	15.564	22.960	1.999	6.79	9359
65	18.413	25.340	2.365	5.16	7847
70	22.753	28.560	2.923	3.70	6347
72.09	25.310	30.293	3.251	2.24	4067

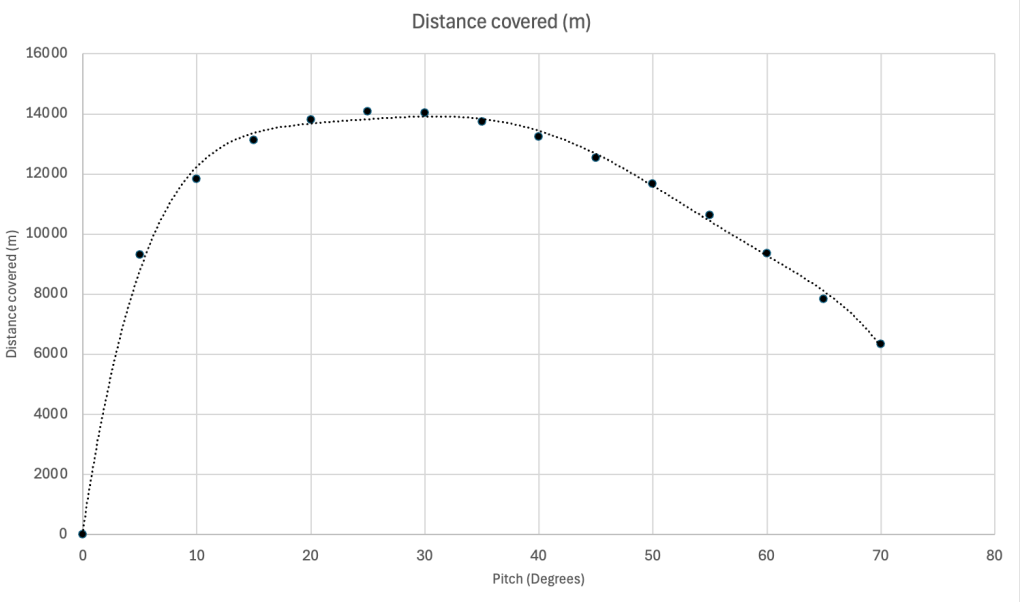

Figure 7.7: Range vs Pitch angle

Using regression methods, a relation linking the pitch angle with the maximum range can be established:

$$\begin{aligned} R(\theta) = & -0.0000072(\theta)^6 + 0.0017397(\theta)^5 - 0.1643011(\theta)^4 \\ & + 7.7374229(\theta)^3 - 194.2609378(\theta)^2 + 2525.7272818(\theta) + 154.4581254 \end{aligned} \tag{7.11}$$

The calculation shows that the minimum flight distance of 500 meters is met at each pitch angle. Furthermore, by evaluating the local maximum of the graph and utilizing the regression relation presented in Equation 7.11, it is found that the drone can fly with a maximum range of **14,094 meters** at a pitch angle $\theta = 26.75°$. This is an important finding, highlighting which pitch angle setting the drone should aim to fly at in order to achieve the highest range in horizontal flight. Utilizing the equations of motion for vertical flight (Equation 7.8), it was found that the T/W ratio for purely horizontal flight corresponding to a pitch angle of **26.75** degrees is **1.12**.

Mapping Speed

As can be seen in Figure 5.5, the maximum mapping speed for the mapping with the camera was established to be 0.65 m/s. This speed will ideally be used extensively in drone missions, in order to cover as much space as possible in a given time frame, so its power consumption should be considered. The pitch angle needed for reaching and maintaining that speed in vertical equilibrium could be estimated, together with its power consumption.

First, the 2 back propellers spin more, generating more thrust than the front ones to create pitch, after that, the propellers do spin approximately equally to have a moment equilibrium at a certain pitch angle such that there is a resultant thrust component in the forward direction, called $T_x = T_{tot} \cdot sin(\theta)$.

Similar to the explanations about the maximum velocities, the mapping speed, as the maximum speed when drag is equal to horizontal thrust for a certain pitch angle, could be linked to the power consumption to sustain that Thrust-to-Weight ratio for that pitch angle. Using the drag formulas mentioned above, and by considering vertical force equilibrium, the pitch angle could straight forwardly be linked to the maximum reachable velocity, as can be seen in Figure 7.8 with the use of the following equation.

$$V = \sqrt{\frac{mg \cdot \tan(\theta)}{\rho C_D \cdot (S_{top} sin(\theta) + S_{front} cos(\theta))}} \tag{7.12}$$

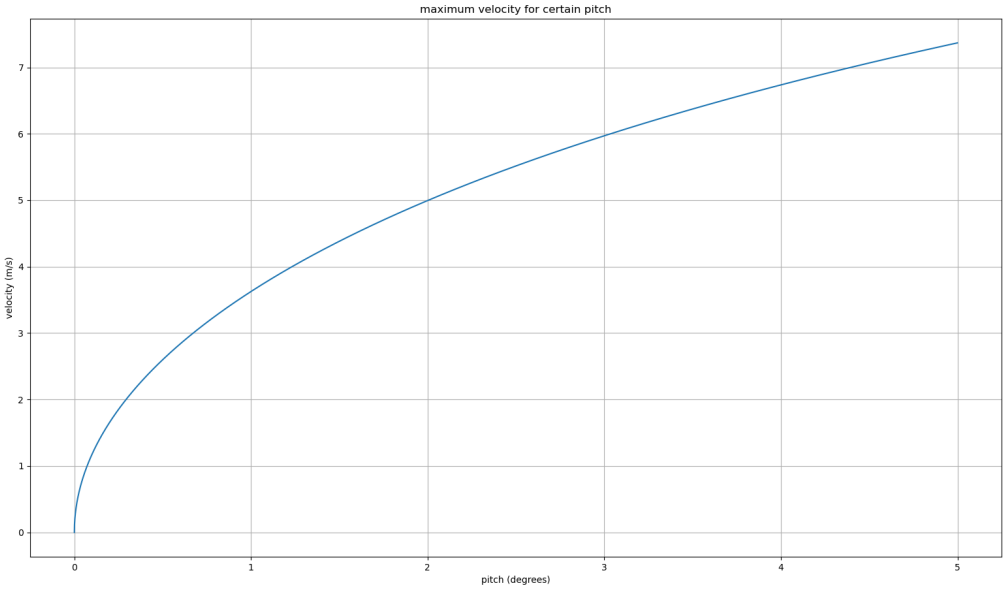

Figure 7.8: Maximum velocity vs Pitch angle

The pitch angle was calculated to be 0.03 °in order to sustain the mapping speed of 0.65 m/s. This angle can be sustained with a $T/W = 1/cos(\theta) \approx 1$, meaning that the mapping speed will require almost exactly the hover power due to the incredible small pitch angle needed. If the drone was to map the cave during its entire flight, it would be able to fly for 18.7 minutes as calculated in the endurance part, covering 821 meters. As specified in requirement DRN-FP-09, the drone shall cover a distance of 1000 meters on one battery charge. Flying purely at the mapping speed, the drone would not meet the requirement. However, this does not mean the drone is incapable of mapping the cave accurately and meeting the 1000 meters range requirement. In practice, the drone will map the cave for distance of 500 meters from the entrance, and then return to the ground station at a greater velocity (returning to ground station at 14 m/s, for example, would give the drone the highest range capabilities), covering the required 1000 meters.

Yaw Turning

When the drone would need to perform a horizontal turn during mapping, it would have to create a certain yaw motion. This yaw motion, in vertical equilibrium, is conducted by creating a resultant torque. Since the drone's propellers spin in the same direction diagonally, increasing the RPM of one diagonal pair while decreasing the RPM of the other creates a net torque. This torque is what enables the drone to perform a yaw turn. This yaw turn does not create any vertical or horizontal displacement if the resultant thrust from the four propellers is still equal to the weight. [12] Using Equation 8.8 derived later in Section 8.2 and ignoring non-linear terms, the yaw angle $\Psi = 1/2 \cdot \iota \cdot t^2$, where ι is the yaw acceleration $\iota = \frac{\tau_{resultant}}{I_{zz}}$, where $\tau_{resultant}$ is the resultant torque, and I_{zz} is the inertia of the drone around the yaw axis. With this in mind, the rotation time t for a 90°turn can be seen in Equation 7.13.

$$t = \sqrt{\frac{\pi \cdot I_{zz}}{\tau_{resultant}}} \tag{7.13}$$

The fastest time to turn would be when the 2 diagonal propellers are not turning, while the other ones provide a T/W of 2, this would provide vertical equilibrium, while creating a resulting torque of 0.52 Nm in total. Knowing, from the CAD, that the $I_{zz} = 0.051\ kg/m^2$, the fastest time to horizontally turn 90°could be estimated to be 0.56 seconds. The increased power consumption for such a maneuver would be for a very small time, and would thus not decrease the endurance significantly.

7.3. Noise

Noise is an important performance metric for the SpeleoDrone. One of the key mission requirements of the drone is not to disturb the ecosystems and wildlife in the caves it is exploring. This made noise an important consideration in the design process, as high noise levels could have a negative effect on the wildlife present in the cave. In this section, the design considerations related to noise levels are outlined in detail.

[12] URL: `https://www.nasa.gov/wp-content/uploads/2020/05/aam-science-behind-quadcopters-reader-student-guide_0.pdf`, [Accessed: 17 June 2025]

7.3.1. Noise Quantification

Aerodynamic noise is generated due to the relative velocity between a solid body, such as a rotor or propeller, and its surrounding medium. For a propeller, this noise can be split up into two components. The vortex component, also described as broadband noise, is produced due to turbulence effects and the occurrence of vortices. The rotational component is noise produced at discrete frequencies that are a multiple of the fundamental blade passage frequency (BPF). This is the frequency at which propeller blades pass the same location. The pressure field changes generated by the rotating blade, which cause the noise, oscillate at this frequency. The BPF corresponds to the first harmonic, and its multiples to the second, third, and higher-order harmonics [31].

Noise level quantification is performed to understand how well the design performs with respect to minimizing the disturbance of fauna present in the cave during operation. Ideally, this disturbance is kept to a minimal level. First-order estimates of the noise levels produced by the design were derived to get an indication of their magnitude and to verify if the relevant noise requirements are met (DRN-FP-08).

Since modeling the aero-acoustics of the propellers in detail was not feasible within the scope of this project and its time limitations, a semi-empirical method established by Lowson was used instead, for estimating the noise output of the current design [31]. With this method, the rotational noise of one rotor in steady flight was quantified based on key parameters such as angular velocity, rotor radius, and observer position. It was decided to focus on the rotational noise component since this is the tonal aspect of the rotor noise, which is typically perceived as the most disturbing. The noise emissions are quantified using sound pressure levels, expressed in decibels relative to a normal human hearing threshold of 0.0002 dynes/cm^2 [31]. In Table 7.3, the computed noise levels for two different mission situations, flyby and hover, are summarized. For both cases, the observer location was set at 5 m away in x, y and z direction, resulting in an observer distance of approximately 9 m.

Since fauna in the cave may be located above the drone, for example bats, an attempt was made to mimic this situation when calculating the SPL. However, the method seemed not to be designed for using negative observer location, which would place the observer above the drone. To still approximate this, the incidence angle was set to 70°, which is the maximum angle for which the method's graphs provide results. The SPL calculated for this scenario can be found in Table 7.3 under 'SPL above'. In the hovering case with the observer below the drone, the incidence angle was set at zero. For the flyby with the same observer location, it was set at 25° to assume an extreme and therefore conservative situation.

The blade passage frequency, at which the noise peaks will occur, is also computed and included in Table 7.3 together with its harmonics. It is calculated with the following formula:

$$BPF = \frac{nB}{2\pi}, \tag{7.14}$$

where n is the rotational speed in rad/s and B the number of blades. The number of blades is 3 and the rotational speed is set at 13611 and 13003 RPM for flyby and hovering, respectively.

Table 7.3: Sound pressure levels (SPL) at the fundamental (1st harmonic) and its multiples of the blade passage frequency for different flight conditions.

	Harmonic	1st	2nd	4th	10th	20th
Flyby	Frequency [Hz]	680.55	1361.1	2722.2	6805.5	13611
	SPL under [dB]	65	56	44	< 34	< 24
	SPL above [dB]	60	50	40	< 34	< 24
Hover	Frequency [Hz]	650.15	1300.3	2600.6	6501.5	13003
	SPL under [dB]	67	56	46	35	25
	SPL above [dB]	59	48	39	< 33	< 23

The method used for the computation makes use of formulas together with graphs showing the SPL for different rotational Mach numbers and angles between the propeller plane and the observer direction. The velocity of the drone had little effect on the calculations, because of its small value. It was therefore approximated to be zero to simplify the calculations.

Since the applied model estimates the noise output from one propeller, but the designed system has 4 rotors, the effect on the SPL due to the interference between the four propellers was examined. From literature, it was found that in the field of acoustics, one cannot simply double the decibel levels when multiple sources are present. For 4 equally strong, but uncorrelated sources, the following formula can be used [61]:

$$L_{p_{tot}} = L_{p_1} + 10 \cdot \log(4) \tag{7.15}$$

where $L_{p_{tot}}$ is the total SPL and L_{p_1} is the SPL of one source, in this case 1 propeller. Using this formula would lead to an increase of + 6 dB when comparing the single propeller case to having 4 of them. This would raise the highest noise level from Table 7.3, which is 67 dB, related to the case of hovering with the observer underneath the drone, to 73 dB. With this adjustment, the noise levels of the drone fall into the range of **65 to 73 dB**. The computed values comply with the noise requirement of an SPL below 85 dB, which was based on the level for which long or repeated exposure can cause hearing loss[13].

7.3.2. Noise Mitigation

When evaluating noise emissions, the primary sources on the drone are the propellers, motors, and ESCs. The propellers and motors predominantly emit lower-frequency noise, while the ESCs generate high-frequency signals, typically around 40 kHz. Although this frequency is beyond the range of human hearing, it can potentially interfere with the echolocation systems of certain bat species inhabiting cave environments [41]. It is important to note that while high-frequency sounds like these propagate easily through materials, they also dissipate rapidly with distance. Therefore, as long as bats remain a few meters away from the drone, significant disturbance is unlikely [34]. To further mitigate potential impact, it is recommended to enclose the ESC and motor housing in high-density, sound-dampening foam. However, foam materials specifically engineered to absorb such high-frequency (ultrasonic) noise do not currently exist and would need to be developed for this purpose.

The lower frequency motor and propeller noise could be partially mitigated as well by that same foam in the future, but for now, other approaches were considered to decrease the noise emissions. First and most importantly, an emphasis was made on trying to keep the drone as light as possible, this would increase endurance, but also require the propeller and motor to produce less thrust needed to hover. Needing less thrust also results in a lower rpm needed, and thus less noise, as discussed in Subsection 7.2.1. The maximum propeller size possible to fit the bounding box was also chosen with this RPM consideration in mind.

Considering this lower RPM needed to hover, and to block the noise itself, a duct was examined below.

Duct Consideration

In an attempt to reduce the noise emissions of the propulsion system, adding ducts around the 4 propellers of the drone was considered. A duct is a cylindrical structure that surrounds a propellers or propeller. According to a study by Malgoezar et al. [40] on the effect of ducted propellers on noise radiation, the addition of ducts was shown to be beneficial against noise emissions, depending on the operating conditions. The study analyzed a propeller with and without ducts under two conditions: no incoming airflow and incoming airflow of 10 m/s, using an experimental acoustic measurement setup.

They found that the two components of propeller noise, broadband noise and tonal noise, are affected differently by the addition of a duct. In case of no airflow, overall noise levels increased for most frequencies in the presence of a duct. This is mainly due to additional broadband noise caused by the interaction between the propeller blades and the duct boundary layer. With airflow present, a slight increase in broadband noise was observed, while tonal noise decreased. This reduction occurs because the airflow moves the turbulence created by the propeller out of the duct, preventing it from interacting with the duct walls and causing acoustic resonances in the duct.

The study was performed on a 30 cm diameter 3-bladed propeller with a simple duct at an angular velocity of 7500 RPM, which is different in size and rotational rate from the 3-bladed propeller chosen for the design, as mentioned in Subsection 7.2.1. However, it was assumed that the conclusions from the study also hold for the drone under design. For the mission of this drone, the propellers will experience minimal incoming airflow due to the propellers being pointed mostly up or under small pitch angles; they will not be directly pointed into the airflow direction. Also, the flight speeds will be lower than the 10 m/s considered in the study, but the airflow would still be non-zero. Therefore, it was assumed that for the drone under design, a combination of the study cases with and without airflow is applicable.

In both cases covered by the study, the sound pressure level differences between the tonal peaks and broadband noise were reduced when ducts were added to the design, due to the increase in broadband noise. As a result, the prominence ratio of the tonal components, which is their relative noise level compared to the surrounding broadband noise, decreased. The tonal components of noise are normally experienced as the disturbing part of noise. According to literature, a lower prominence ratio of tones leads to them being perceived as less annoying [35]. In the case of airflow present, the prominence ratio is even smaller due to the additional reduction in tonal noise, which amplifies this effect of less perceived disturbance.

Furthermore, the propeller efficiency will be increased by the addition of ducts, due to an increased mass flow rate and more streamlined flow past the propeller. Therefore, less power will be needed to produce the same

[13] URL: `https://www.nidcd.nih.gov/health/noise-induced-hearing-loss`[Accessed 24 June 2026]

amount of thrust. This will allow the angular velocity of the propellers to be lower for the same amount of thrust, which in itself reduces the noise emissions [40]. Another additional benefit of ducts is that they serve as propeller protection in case of collision, thereby making the drone more durable.

To conclude, the addition of ducts has various benefits for the drone design in relation to noise. Next to increased efficiency, the propeller noise would be perceived as less annoying due to the relative, and sometimes absolute, decrease in tonal noise levels under certain airflow conditions. Therefore, the design is made including ducts, but their precise effect should be tested in the future design stages when a prototype of the drone is made. Also, the design of the ducts is kept modular to allow removal in case the tests show adverse or little effect. The details of the duct design are discussed in the next subsection.

Duct Design

The ducts around the propellers were designed carefully to make the drone more efficient. They were made to fit closely around the propellers to improve the thrust efficiency[1], kept lightweight so the extra weight would not cancel out the efficiency gain, and shaped so they would not get in the way of other parts of the drone, like the payload or the fiber optic cable.

The dimensions of the duct were scaled according to a design tested by Frank Simon [56], which used a larger propeller diameter, and considered two duct heights, out of which the lower one was scaled due to obstruction of subsystem considerations, and added weight.

With a scaled duct height of 6 cm, the duct would still obstruct the required field of view of the LiDAR and camera, so it was decided that for the two front ducts, the heights would be 3 cm, with the other dimensions still being the same, and not go below the propellers such that the payload could map in all desired directions. A visualization of the front and back ducts can be seen in Figure 7.9. Another option, where the front ducts would have simple cut-outs for the payload field of view, was first considered, but not chosen due to the unpredictable flow that would form around these cut-outs.

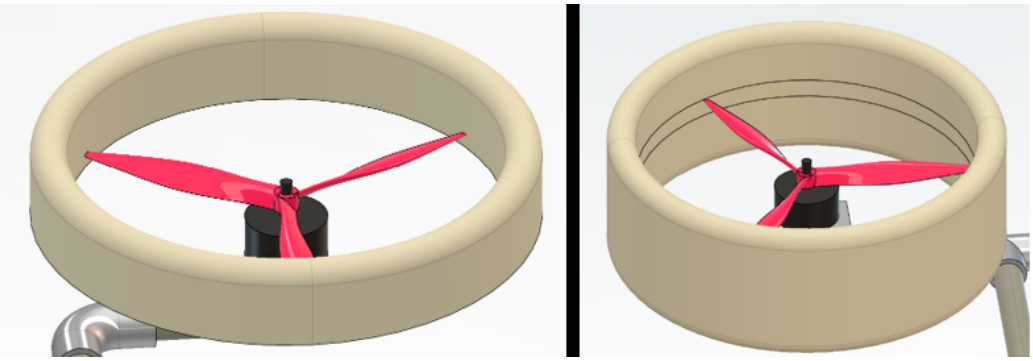

Figure 7.9: Front ducts (left) & Back ducts (right)

Concerning the weight, the light weight foam 'Styrodur' was chosen as the material for the duct. It is a stiff foam commonly used in drone applications[14]. This styrofoam is very stiff and light to protect the drone, is water resistant which is beneficial in a humid cave environment and has noise reducing capabilities as well[15]. It has to be noted that the paper by Frank Simon [56] used a much higher density, hard acrylate-based plastic which has different noise reducing properties. The foam does still aid with noise reduction, but the extent can not be straightforwardly quantified based on this report and it should be experimentally tested in the future.

For in the case that a single drone would be made, the design as discussed above would be used. In the case where more drones would be ordered, manufacturing costs would go down and there would be more room for a more complicated duct and propulsion design, thus even more noise reducing recommendations are covered below.

The first recommendation is to apply a sound reducing foam like Akotherm [16] closely to the propellers. This foam would be placed between the black lines on the right of Figure 7.9, Palleja-Cabre [47] shows that placing noise reducing material, or obstructions only close to the rotors already can have a significant impact on the noise reduction. This paper does only use metal obstructions and not noise reducing foams, so such an application would need to be tested experimentally as well.

Another recommendation would be to optimize the duct design for aerodynamic efficiency. The duct cross

[14] URL: https://defense-update.com/20140818_skate.html, [Accessed: 18 June 2025]
[15] URL:https://epsole.com/styrofoam-soundproof/, [Accessed: 18 June 2025]
[16] URL: https://akoterm.com/en/products/shumoizolyaciya-akoterm, [Accessed: 18 June 2025]

section could have a more airfoil shaped design to further increase the aerodynamic efficiency [44] and the area ration of the duct could also be tuned to optimize the aerodynamic efficiency. This increased efficiency would require a lower RPM and again lower noise emissions.

A better propeller design could also increase the aerodynamic efficiency of the drone. The off-the-shelf propeller has a narrow blade tip, this makes sense in a open rotor drone, where a narrow blade tip decreases vortex drag. Only when considering a ducted propeller, the duct already minimizes the formation of tip vortices, so a narrow tip is not needed and the wider tip could increase aerodynamic performance. Designing such a custom propeller would only make economical sense when the amount of orders would increase significantly.

7.4. Sensitivity Analysis

As can be seen, the evaluation of the flight performance of the drone is a very mathematically intense process, which relies on a number of calculations, with changes in individual values affecting subsequent results. The evaluation and subsequent analysis of the performance metrics of the drone uses accurate calculations of the mass and surface dimensions of the drone.

During production, some of these values may change. The mass of the drone is calculated to be 3.1741 kg, whilst the frontal area of the drone is calculated to be 0.04988 m^2 and the top area 0.164 m^2. These values are obtained from extremely precise calculations, and the real-life final values could very easily be different post-production, due to potentially flawed products or simply human error during manufacturing. For this reason, it is very important to consider how sensitive the performance metrics of the drone are to potential differences in the physical dimensions of the drone.

As was found in Subsection 7.2.2, the desired mapping speed is achieved at a pitch angle of 0.03 degrees, flying at a T/W ratio of 1, which gives a flight range of 821 meters. In order to check the sensitivity of these values to potential differences in physical dimensions, a calculation was performed where the mass of the drone was adjusted between 90% and 110% of the original value, in increments of 2%, and subsequent changes in results were analyzed. The same process was performed for the sensitivity to the surface area of the drone at a pitch angle of 0.03 degrees. The results are presented in the table below.

Table 7.4: Sensitivity analysis for mass deviations at pitch angle = 0.03 degrees

Mass [kg]	$T_{a_{v=0}}$ [N]	$D_{a_{h=0}}$ [N]	Frontal area [m^2]	Max. velocity [m/s]	T/W	Flight time [min]	Range [m]
2.86	7.00	0.0147	0.0500	0.692	1.000	18.7	779
2.92	7.16	0.0150	0.0500	0.700	1.000	18.7	787
2.98	7.31	0.0153	0.0500	0.708	1.000	18.7	796
3.05	7.47	0.0156	0.0500	0.715	1.000	18.7	804
3.11	7.63	0.0160	0.0500	0.722	1.000	18.7	812
3.17	7.78	0.0163	0.0500	0.730	1.000	18.7	821
3.24	7.94	0.0166	0.0500	0.737	1.000	18.7	829
3.30	8.09	0.0170	0.0500	0.744	1.000	18.7	837
3.36	8.25	0.0173	0.0500	0.751	1.000	18.7	845
3.43	8.40	0.0176	0.0500	0.758	1.000	18.7	853
3.49	8.56	0.0179	0.0500	0.765	1.000	18.7	861

Table 7.5: Sensitivity analysis for area deviations at pitch angle = 0.03 degrees

Frontal area [m^2]	Mass [kg]	$T_{a_{v=0}}$ [N]	$D_{a_{h=0}}$ [N]	Max. velocity [m/s]	T/W	Flight time [min]	Range [m]
0.0450	3.17	7.78	0.0163	0.769	1.000	18.7	865
0.0460	3.17	7.78	0.0163	0.761	1.000	18.7	856
0.0470	3.17	7.78	0.0163	0.753	1.000	18.7	847
0.0480	3.17	7.78	0.0163	0.745	1.000	18.7	838
0.0490	3.17	7.78	0.0163	0.737	1.000	18.7	829
0.0500	3.17	7.78	0.0163	0.730	1.000	18.7	821
0.0510	3.17	7.78	0.0163	0.723	1.000	18.7	813
0.0520	3.17	7.78	0.0163	0.716	1.000	18.7	805
0.0530	3.17	7.78	0.0163	0.709	1.000	18.7	797
0.0540	3.17	7.78	0.0163	0.702	1.000	18.7	790
0.0550	3.17	7.78	0.0163	0.696	1.000	18.7	783

As can be seen in Table 7.4, a 10% change in the drone mass can cause the maximum range to change by 40 meters when flying at the mapping speed. A change of 40 meters is equivalent to a change of around 5% of the range at the optimum mass, a substantial amount. As explained in the Mapping Speed section of Subsection 7.2.2, even though the drone has a range of less than the required 1000 meters at the mapping velocity, this does not mean the drone is incapable of complying with the 1000 meter range requirements. This simply means that the drone is incapable of completing an entire 1000 meter round trip whilst only mapping the cave. If the mass were to increase, it would cause the drone to map a smaller distance of the cave on one battery charge, prolonging the time taken to map the whole cave, potentially risking requirement MIS-DRN-1.2, as presented in Appendix A. For this reason, it is of utmost importance that the final post-production mass of the drone does not increase significantly beyond the 3.174 kg mark.

In Table 7.5 it can be seen that a change in the physical dimensions of the drone also has a significant influence on the range. A 10% change in the drone area causes the maximum range to change by 40 meters, similar to the mass parameter. As is the case with the mass sensitivity, this change would cause the drone to map a smaller distance of the cave on one battery charge, prolonging the time taken to map the whole cave. However, a more pressing issue which has to be kept in consideration is that the physical dimensions of the drone not only impact the range but also the general size of the drone. This is arguably a bigger issue, as it could potentially cause the drone to not meet the size requirements MIS-DRN-4.3, also presented in Appendix A. For this reason, the physical dimensions of the drone are the more important parameters which have to be kept accurate compared to the design specifications.

7.5. Validation

One way to validate the endurance estimate of the SpeleoDrone was to compare its calculated endurance with that of similarly-sized drones that have also been used in cave environments, such as the Elios 2 and 3, as discussed in the market analysis, Section 2.5. In Table 7.6 below, the mass, dimensions, and endurance of these competitor drones are compared with those of the SpeleoDrone.

Table 7.6: Endurance validation table, competitor comparison

Drone	Mass [kg	Size [cm]	Endurance [min]
Elios 3	2.35	48.0 x 48.0 x 38.0	12.5
Elios 2	1.45	38.0 x 38.0 x 38.0	9
SpeleoDrone	3.18	40.4 x 51.5 x 21.0	18.7

Several important conclusions can be drawn from the comparison of these drones. First, the SpeleoDrone has a similar overall size to the Elios 2 and 3, with its width falling between the two. It features a lower and more elongated shape compared to both Elios models. Despite its smaller size, the SpeleoDrone offers significantly greater endurance, highlighting a clear competitive advantage and indicating strong aerodynamic efficiency. It is important to note, however, that the SpeleoDrone achieves this performance with a substantially heavier battery setup, using two batteries. As a result, it is heavier than both Elios drones. The battery mass fraction of the SpeleoDrone is also considerably higher,48% compared to 38% for the Elios 2 and 26% for the Elios 3 [6]. This higher battery mass fraction explains the increased endurance, albeit at the cost of added weight.

8. Stability and Control Characteristics

This chapter covers the stability and control of the quadcopter, primarily focusing on simulating the dynamics using Simulink. First, subsystem requirements are defined in Section 8.1. Next, for modeling purposes, the equations of motion are derived in Section 8.2. After that, a brief description of how the time stepping is performed in the Simulink model is given in Section 8.3. Following that, the autonomous control system is discussed that will provide the desired position to the flight controller in Section 8.4. Then, the actual Simulink model is discussed in detail in Section 8.5. Next, the performance of the quadcopter is assessed in Section 8.6. Finally, the model is verified and validated in Section 8.7.

8.1. Sub-system Requirements

The control design of the SpeleoDrone was driven by the requirements set out in the Baseline report[5]. For completeness, several others were added in order to ensure that all factors were accounted for.

Table 8.1: Stability & Control Subsystem Requirements

ID	Requirement	Parent
MIS-DRN-1.4	The system shall detect and localize physical collision risks with at least 95% accuracy from a minimum distance of 1 meter.	STK-DRN-1
MIS-DRN-4.2	The system shall be capable of safely navigating through horizontal and vertical openings of 45cm x15cm dimensions with a minimum clearance of 2 cm during flight, without contact with surrounding surfaces.	STK-DRN-4
SYS-DRN-1.2.1	The system shall maintain an attitude positioning accuracy of less than 2 degrees on each of the three principal axes (roll, pitch, and yaw) during nominal flight conditions.	MIS-DRN-1.2
SYS-DRN-4.2.1	The system shall maintain its position with an accuracy of less than 15 cm per axis during hover or groundspeeds lower than 25 m/s, under nominal conditions	MIS-DRN-4.2
SYS-DRN-4.2.2	The system shall be capable of providing translation acceleration along X and Y axis up to 1.5g m/s^2 during nominal flight conditions.	MIS-DRN-4.2
CTRL-DRN-01	The system shall allow for angular acceleration of 380 rad/s^2 or less in each axis during nominal flight conditions	MIS-DRN-4.2
CTRL-DRN-02	The system shall limit the overshoot of each state variable to less than 10% of the commanded value during step-response tests, measured under nominal flight conditions	MIS-DRN-4.2
CTRL-DRN-03	The system shall autonomously reduce speed when nearing physical boundaries within 50 cm, based on onboard sensors	MIS-DRN-4.2
CTRL-DRN-04	The control system shall support soft constraints to limit roll and pitch angles to less than 70 degrees during tight maneuvering	SYS-DRN-1.2.1
CTRL-DRN-05	The system shall compensate for minor disturbances (<30 N impact force) without catastrophic loss of stability	MIS-DRN-4.2
CTRL-OPR-06	The system shall include a Return-to-Home function that automatically activates upon signal loss, battery levels below 30%, or user instruction.	MIS-OPR-7.3

8.2. Equations of motion

To determine the position of the quadcopter, two frames are established: the earth fixed frame E_I, or flat Earth frame, and the body fixed frame E_B, visualized relative to each other in Figure 8.1. The Earth fixed frame does not translate or rotate and its origin and orientation are set at the start of the mission. The body fixed frame has 6 degrees of freedom (DOF) and its axis system is defined in Figure 8.2, with the positive roll, pitch and yaw directions defined in Figure 8.3.

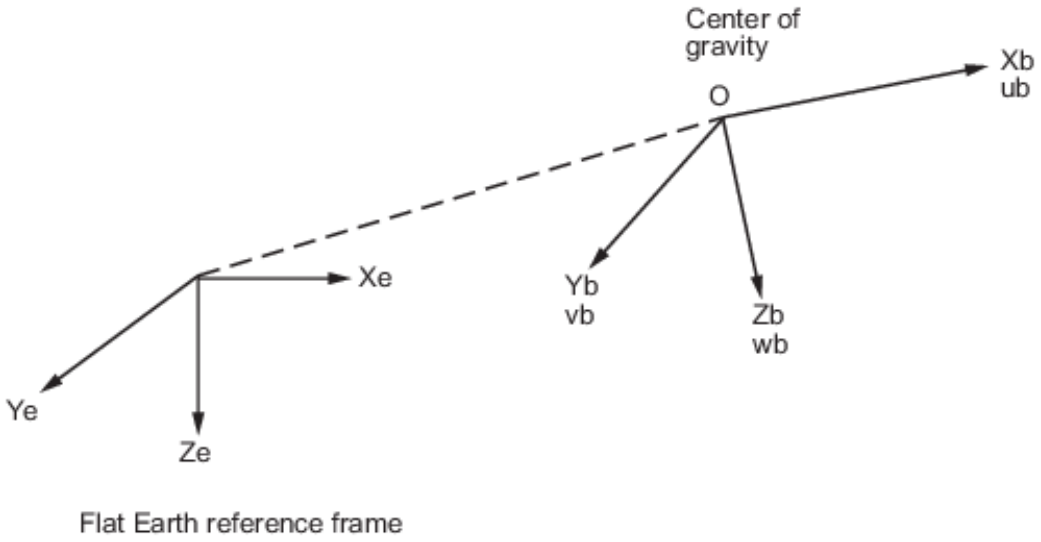

Figure 8.1: Relation between earth fixed and body reference frames[1]

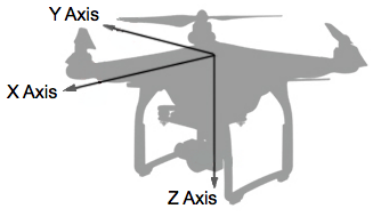

Figure 8.2: Quadcopter body fixed frame axis definitions. [1]

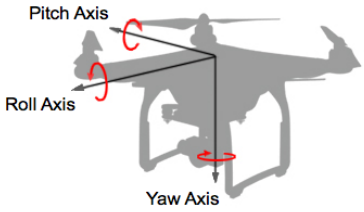

Figure 8.3: Quadcopter body fixed frame angle definitions. [1]

Let the position vector be defined as $\mathbf{x} = [x \quad y \quad z]^T \in E_I$, and the angular orientation vector be described by $\eta = [\phi \quad \theta \quad \psi]^T \in E_I$, where the angles represent roll, pitch and yaw respectively. Then, the linear and angular velocity vectors in the body frame are $\mathbf{V} = [u \quad v \quad w]^T \in E_b$ and $\mathbf{\Omega} = [p \quad q \quad r]^T \in E_b$ [38, 63]. The position and velocity in the earth fixed frame are related by

$$\begin{aligned} \dot{\mathbf{x}} &= \mathbb{T}_{Ib}\mathbf{V} \\ \dot{\eta} &= \mathbf{\Omega}_{Ib} \end{aligned} \tag{8.1}$$

Where $\mathbb{T}_{Ib}$ is the transformation matrix from body to earth fixed frame and $\mathbf{\Omega_{Ib}}$ is the rotational velocity vector in the inertial frame, described using the body rotational velocity vector:

$$\mathbb{T}_{Ib} = \mathbb{T}_z(\psi)\mathbb{T}_y(\theta)\mathbb{T}_x(\phi) \tag{8.2}$$

$$\mathbf{\Omega_{Ib}} = \mathbf{\Omega_{IE'}} + \mathbf{\Omega_{E'E}} + \mathbf{\Omega_{Eb}} = p\mathbf{x}_b + q\mathbf{y}_{E'} + r\mathbf{z}_E = p\mathbf{x}_b + q\mathbb{T}_x(\phi)\mathbf{y}_b + r\mathbb{T}_x(\phi)\mathbb{T}_y(\theta)\mathbf{z}_b \tag{8.3}$$

Here, $\mathbb{T}_x$, $\mathbb{T}_y$ and $\mathbb{T}_z$ are the unit-axis transformation matrices. To make the equations more concise, the cosine and sine functions are abbreviated as c and s. This leads to the following transformation matrix and rotational vector:

$$\mathbb{T}_{Ib} = \begin{pmatrix} \mathrm{c}\theta\mathrm{c}\psi & \mathrm{s}\phi\mathrm{s}\theta\mathrm{c}\psi - \mathrm{c}\phi\mathrm{s}\psi & \mathrm{c}\phi\mathrm{s}\theta\mathrm{c}\psi + \mathrm{s}\phi\mathrm{s}\psi \\ \mathrm{c}\theta\mathrm{s}\psi & \mathrm{c}\phi\mathrm{c}\psi + \mathrm{s}\phi\mathrm{s}\theta\mathrm{s}\psi & \mathrm{c}\phi\mathrm{s}\theta\mathrm{s}\psi - \mathrm{c}\psi\mathrm{s}\phi \\ -\mathrm{s}\theta & \mathrm{s}\phi\mathrm{c}\theta & \mathrm{c}\phi\mathrm{c}\theta \end{pmatrix} \qquad \mathbf{\Omega}_{Ib} = \begin{pmatrix} 1 & 0 & -\mathrm{s}\theta \\ 0 & \mathrm{c}\phi & \mathrm{s}\phi\mathrm{c}\theta \\ 0 & -\mathrm{s}\phi & \mathrm{c}\phi\mathrm{c}\theta \end{pmatrix} \mathbf{\Omega} \tag{8.4}$$

With this, the quadcopter dynamics can be described by assuming the quadcopter is rigid. This makes it possible to apply Newton-Euler equations that describe the linear and angular motion in the inertial frame [63, 26]:

[1] URL: https://nl.mathworks.com/help/aeroblks/6dofeulerangles.html [Accessed: 16 June 2025]
[2] URL: https://tinyurl.com/mvxvnmas,(https://developer.dji.com/) [Accessed: 17 June 2025]

$$\begin{bmatrix} \mathbf{F_g} + \mathbb{T}_{Ib}\mathbf{F_b} \\ \tau \end{bmatrix} = \begin{bmatrix} mI & 0_{3\times3} \\ 0_{3\times3} & J \end{bmatrix} \begin{bmatrix} \ddot{\mathbf{x}} \\ \ddot{\eta} \end{bmatrix} + \begin{bmatrix} 0 \\ \dot{\eta} \times (J\dot{\eta}) \end{bmatrix} \tag{8.5}$$

Where $\mathbf{F_g}$ is the force due to gravity in the inertial frame and $\mathbf{F_b}$ are the forces acting in the body frame, described in Equation 8.6; I is the 3×3 identity matrix and J is the 3×3 matrix of mass moment of inertia, which were obtained from CAD model:

$$\mathbf{F_g} = \begin{pmatrix} 0 \\ 0 \\ mg \end{pmatrix} \qquad \mathbf{F_b} = \begin{pmatrix} -D \\ 0 \\ -T \end{pmatrix} \qquad J = \begin{pmatrix} I_{xx} & 0 & 0 \\ 0 & I_{yy} & 0 \\ 0 & 0 & I_{zz} \end{pmatrix} \tag{8.6}$$

The contribution of the asymmetric inertia is assumed to be negligible with respect to the symmetric inertia, since their contributions are small due to quadcopters being mostly symmetrical, which is also the case for the primary mass contributions of the SpeleoDrone [38]. Consequently, the following three linear equations of motion are obtained:

$$\begin{aligned} \ddot{\mathbf{x}} &= -\frac{T}{m}(\mathsf{s}\phi\mathsf{s}\psi + \mathsf{c}\phi\mathsf{s}\theta\mathsf{c}\psi) - \frac{D}{m}(\mathsf{c}\theta\mathsf{c}\psi) \\ \ddot{\mathbf{y}} &= -\frac{T}{m}(\mathsf{c}\phi\mathsf{s}\theta\mathsf{s}\psi - \mathsf{s}\phi\mathsf{c}\psi) - \frac{D}{m}(\mathsf{c}\theta\mathsf{s}\psi) \\ \ddot{\mathbf{z}} &= g - \frac{T}{m}(\mathsf{c}\phi\mathsf{c}\theta) + \frac{D}{m}(\mathsf{s}\theta) \end{aligned} \tag{8.7}$$

With the corresponding three rotational equations of motion:

$$\begin{aligned} \ddot{\phi} &= \frac{\tau_\phi}{I_{xx}} + \frac{I_{yy} - Izz}{I_{xx}}\dot{\theta}\dot{\psi} \\ \ddot{\theta} &= \frac{\tau_\theta}{I_{yy}} + \frac{I_{zz} - I_{xx}}{I_{yy}}\dot{\phi}\dot{\psi} \\ \ddot{\psi} &= \frac{\tau_\psi}{I_{zz}} + \frac{I_{xx} - I_{yy}}{I_{zz}}\dot{\phi}\dot{\theta} \end{aligned} \tag{8.8}$$

The thrust and torque generated at each propeller are linearly related to the square angular velocity [63, 38]

$$\begin{aligned} T_i &= k_f\omega_i^2 \\ \tau_i &= k_m\omega_i^2 \end{aligned} \tag{8.9}$$

Where the coefficients k_m and k_f are properties of the motor, found in Subsection 7.2.1. With this, the thrust and torque acting around each axis can be described as

$$\begin{aligned} T &= k_f(\omega_1^2 + \omega_2^2 + \omega_3^2 + \omega_4^2) \\ \tau_\phi &= l_y k_f((\omega_1^2 + \omega_4^2) - (\omega_2^2 + \omega_3^2)) \\ \tau_\theta &= l_x k_f((\omega_1^2 + \omega_2^2) - (\omega_3^2 + \omega_4^2)) \\ \tau_\psi &= k_m((\omega_2^2 + \omega_4^2) - (\omega_1^2 + \omega_3^2)) \end{aligned} \tag{8.10}$$

Here, the angular velocities are defined according to Figure 8.4, and l_x and l_y are the distances to the motors along the x and y axes, respectively.

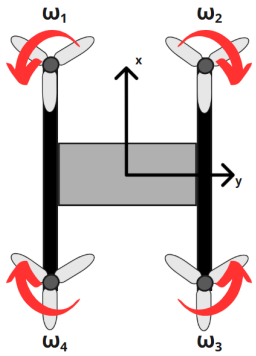

Figure 8.4: Angular velocities with respect to fixed body reference frame

8.3. Time integration

Due to the complexity of non-linear dynamics and controllers, systems are typically modeled in a Linear Time Invariant (LTI) manner, with linear Partial Integral Derivative (PID) controllers [63]. However, since the dynamics described by the equations of motion are highly nonlinear, this introduces a large amount of error, especially when there are large deviations from the hover condition. Thus, the 6 DOF (Euler Angles) block was used from the Aerospace Blockset[3]. The Aerospace Blockset is a group of blocks with built-in functionality for modeling aerospace systems.

The 6 DOF (Euler Angles) block solves the equations of motion from Equation 8.7 and Equation 8.8 in a non-linear manner by numerically integrating them. While the linear PID controllers can be tuned for non-linear systems, the settling time and convergence are slower [43]. Consequently, to minimize non-linearity, the drag terms were neglected. This assumption makes it easier to tune the controller and does not significantly impact the quality of results, as at the low operating velocities, drag values are small relative to the thrust. Furthermore, the controller is tuned to be able to handle disturbances, such as the drag.

8.4. Autonomous Control System

As illustrated in Figure 9.3, the drone supports two distinct control modes: Autonomous and Assisted User Control. Both modes incorporate varying degrees of autonomy. In Autonomous mode, the drone navigates primarily via artificial intelligence, enabling fully independent operation. By contrast, Assisted User Control blends manual operator input with embedded autonomous functions, ensuring safety during amateur operation. This section describes in details the autonomous control system.

8.4.1. Artificial Intelligence model

Artificial Intelligence (AI) plays a crucial role in exploring unknown regions by identifying regions of interest and detecting obstacles in real time. The system integrates data from multiple sensors, including LiDAR and cameras, processed through advanced neural networks for efficient analysis. The proposed model architecture is presented in Figure 8.5. The different blocks shown in the figure will be discussed in more detail in the following text.

[3]URL: `https://nl.mathworks.com/help/aeroblks/6dofeulerangles.html` [accessed: 17 June 2025]

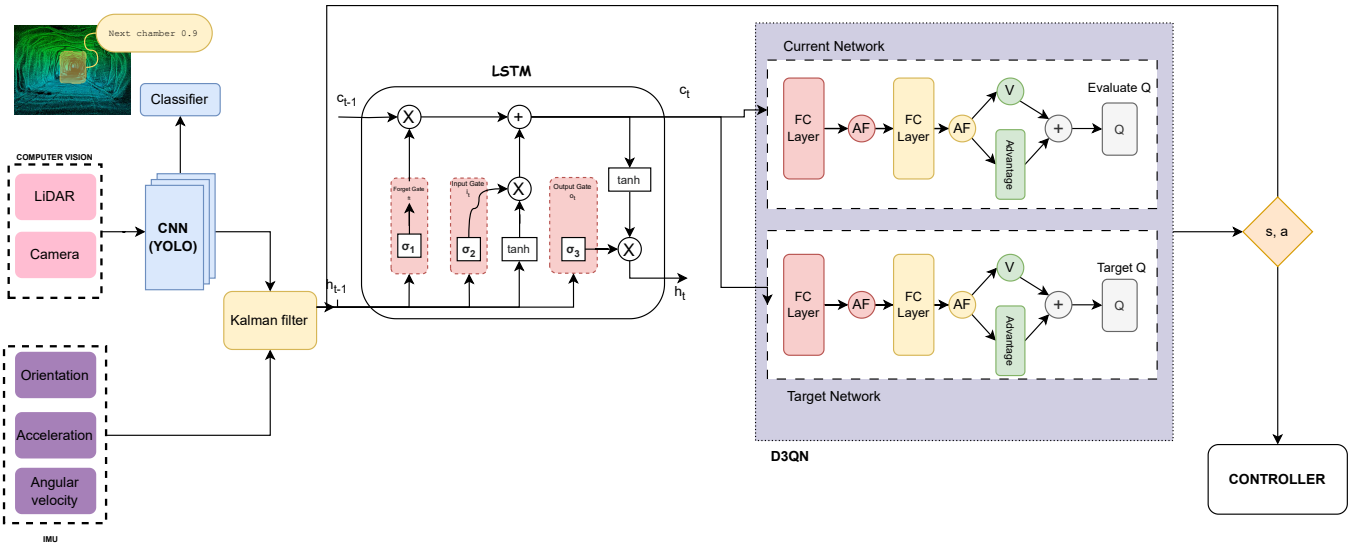

Figure 8.5: Autonomous control model architecture

Convolutional Neural Network

The AI model processes high-dimensional visual input from the LiDAR and onboard camera, which captures RGB images at a resolution of 2592 by 1944 pixels, as detailed in Chapter 5. This results in over 15 million input variables for the image data alone. To handle this computational complexity, a Convolutional Neural Network (CNN) preprocesses the visual data, applying edge-detection kernels and feature extraction to reduce dimensionality while preserving critical spatial information. For real-time object detection, the system employs **You Only Look Once (YOLO)**[28], a state-of-the-art model that localizes and classifies objects within the drone's field of view. YOLO identifies two key categories:

1. **Obstacles** (e.g., bats, stalactites) - critical for collision avoidance.
2. **Regions of Interest (ROI)** – potential archaeological artifacts or areas requiring further inspection.

YOLO processes images in a single forward pass of a neural network. Unlike traditional detectors that analyze different image regions separately, YOLO divides the input image into a grid where each cell predicts multiple bounding boxes. For each box, the system estimates the object's location (coordinates and dimensions), a confidence score reflecting detection certainty, and class probabilities identifying what the object is. These predictions are generated simultaneously across the entire grid, allowing YOLO to efficiently detect all objects in the image at once. After prediction, a post-processing step called non-maximum suppression removes redundant or overlapping boxes, keeping only the most confident and accurate detections. This streamlined approach enables YOLO to achieve remarkable speed while maintaining strong accuracy, making it ideal for applications like drone navigation where real-time processing is critical. By analyzing each frame for obstacles and regions of interest in one swift operation, YOLO provides the rapid, reliable object detection needed for autonomous exploration.

Regions of Interest (ROIs) are flagged and transmitted to the ground station for operator evaluation. Confirmed ROIs are logged in the system's mapping database, enabling targeted return missions for further inspection or data collection as needed.

To improve navigation accuracy, the system uses a Kalman filter to combine data from the drone's IMU and the visual information processed by the CNN. The IMU gives fast, continuous updates about the drone's movement, but its readings can become unreliable over time due to noise and small errors. On the other hand, the CNN provides more stable and spatially grounded information, though at a lower rate. The Kalman filter blends these two sources: it predicts the drone's position using the IMU and then corrects it whenever new visual data is available. This smart combination helps the drone stay aware of its location and movement, even in challenging environments without GPS -like caves - ensuring smooth and reliable navigation.

Long-Short Term Memory (LSTM)

An LSTM (Long Short-Term Memory) network is a type of recurrent neural network (RNN) designed to work with sequential data. Unlike traditional feedforward networks, which treat each input in isolation, LSTMs are built to remember information over time. They maintain internal hidden states and cell states that are updated at every time step, allowing them to retain important past information while discarding what's no longer relevant.

LSTMs achieve this through a series of gates:

- **Forget gate:** decides what information to discard from the cell state
- **Input gate:** determines what new information to add to the cell state
- **Output gate:** Controls what information to pass to the next time step

This makes LSTMs particularly useful in scenarios like drone navigation, where the environment is only partially observable. The drone doesn't always have full access to its current state, especially in cluttered or unpredictable environments. Instead, the LSTM's hidden state acts as a compact summary of all past observations up to the current moment, giving the system a richer understanding of the situation.

LSTMs help the system cope with real-world challenges. In situations with limited visibility, such as dark or cluttered environments, LSTMs allow the drone to retain important past observations that are no longer visible but still relevant. They also excel at learning temporal patterns - for instance, recognizing the movement of a bat colony over time. When sensor inputs are noisy or inconsistent, the LSTM can use context from earlier time steps to smooth out the data and maintain stable perception. Additionally, LSTMs support more complex decision-making by enabling the system to plan multi-step actions, such as choosing the best path to safely detour around an obstacle.

Reinforcement Learning

Reinforcement learning (RL) is a learning framework where an agent learns to make decisions by interacting with an environment, receiving rewards for good actions and penalties for poor ones. Over time, the agent aims to maximize the total reward it accumulates by learning which actions are most beneficial in different situations. In this context, the *Q-value* represents the expected total reward the agent can earn by taking a specific action a in a given state s, and then following the optimal policy. In simpler terms, it quantifies how useful a particular action is in a given moment.

Traditional **Deep Q-Networks (DQN)** use neural networks to estimate Q-values. However, they tend to overestimate these values due to the use of the `max` operator, which always selects the highest predicted Q-value for the next state, even when it's not accurate. This overestimation can lead to unstable training and poor decision-making, such as a drone misjudging tight passages and repeatedly crashing into obstacles.[4]

To address this, the drone uses a **Deep Double Q-Network (D3QN)**, which incorporates improvements from **Double DQN**, **Dueling DQN**, and the original DQN architecture [59]. Double DQN reduces overestimation by separating action selection and evaluation: the online network selects the action, while a target network—updated less frequently—estimates its value. Dueling DQN further refines this by splitting the Q-value output into two streams: a *value function*, which measures how good the current state is, and an *advantage function*, which assesses how much better or worse a specific action is compared to others. This separation is especially useful in scenarios where the exact action matters less than reaching a valuable state.

The D3QN agent is trained in a simulated cave environment using **domain randomization**, exposing it to diverse conditions (e.g., different lighting, textures, and obstacles) to improve its robustness in the real world. Since the drone operates in a partially observable environment, the agent also includes an **LSTM**, which helps it interpret raw sensor inputs (LiDAR, camera, IMU, etc.) over time by remembering past observations. During training, the emphasis is on *exploration*—gradually learning the layout, building internal maps (such as occupancy grids or topological graphs), and developing policies focused on curiosity, coverage, and safe autonomous navigation.

8.4.2. Algorithm-based navigation

Once the SpeleoDrone has sufficiently explored the unknown environment, the system transitions from a learning-based approach (D3QN) to a classical path planning algorithm, namely **D* Lite**.

Deep Reinforcement Learning methods such as D3QN are well-suited for exploration in unknown or partially observable environments due to their ability to learn complex policies. However, DRL is both computationally intensive and energy-consuming, making it less suitable for extended missions in power- and hardware-constrained systems like autonomous drones.

To balance performance with resource efficiency, the control architecture is designed to switch from DRL to classical planning once the environment has been mapped to arbitrary chosen coverage threshold - 80% of the environment explored. At this point, adaptive exploration is no longer required, and a transition is made to a deterministic and computationally lightweight planning algorithm: D* Lite [19]. The transition is triggered automatically by the control system when the coverage threshold is reached. The explored environment is converted into a grid-based map representation, which serves as input to D* Lite. D* Lite is an incremental heuristic path planner, designed to operate efficiently in dynamic or partially known environments. It builds upon

[4] URL: `https://www.baeldung.com/cs/q-learning-vs-deep-q-learning-vs-deep-q-network` [Accessed: 3 June 2025]

the A* algorithm by using a priority queue to expand nodes based on an estimated cost-to-go function, typically computed using Euclidean or Manhattan distance [39]. Crucially, D* Lite supports incremental replanning: when new obstacles are detected, it avoids recalculating the entire path from scratch. Instead, it selectively updates only the affected portions of the existing plan using previously computed data, thereby significantly reducing computational overhead [39]. This makes D* Lite especially suitable for structured yet evolving environments such as caves, where changes to the map are typically localized rather than global.

Within the SpeleoDrone architecture, D* Lite is utilized in the following scenarios:

- **Exploration phase:** D* Lite is used for navigating back to the base point during the exploration phase
- **Post-exploration tasks:** D* Lite ensures efficient goal-directed navigation once the environment is known
- **Return-to-home fail-safe:** In case of communication loss (e.g., due to a fiber-optic cable rupture), the AI system –which runs on a Jetson platform located outside the cave (see Section 10.5) – becomes unreachable. In such cases, D* Lite enables the drone to autonomously navigate back to the ground control station, ensuring mission safety and system recovery.

8.5. Simulink Model

The next step in the design of the controller was constructing a Simulink model of the quadcopter's controller. Simulink is a graphical programming language based on MATLAB. It is commonly used for controller design and simulation.

8.5.1. System Overview

The system was broken into four main components: the plant, the controller, the reference, and the sensor readings, connected as in Figure 8.6. The plant models the physical behavior of the system and is used to predict the response of the system to a control input. The job of the controller is to drive the plant to some desired position by adjusting the input appropriately. The desired state is dictated by the reference, which would be input from the AI system in the final flight controller as described in Section 8.4.

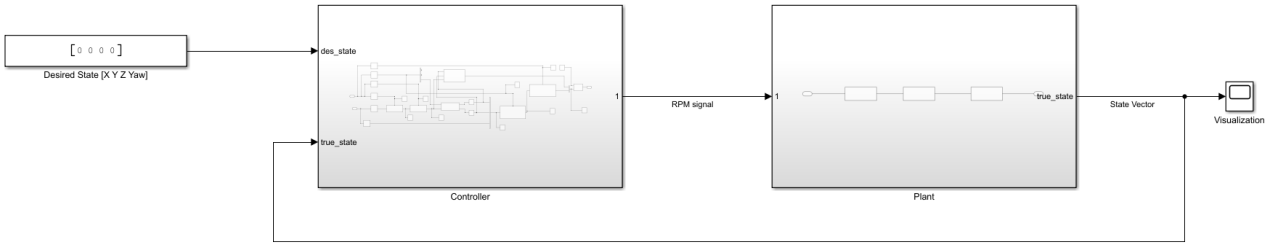

Figure 8.6: Simulink system overview

The desired position consists of the x, y, z positions and the yaw angle ψ. Due to time constraints, the AI has not actually been constructed yet, but time has been reserved for it in the future plan (see Chapter 16). For testing and debugging of the model, a constant input was used instead. The input was adjusted based on what was being tested.

That information then flows into the controller, described in detail in Subsection 8.5.3, which processes the information and determines what square angular velocity signal is fed into the plant to reach the desired state.

The plant, described in Subsection 8.5.2, assesses the physical response of the quadcopter to the input provided by the controller. The plant takes into consideration additional dynamics, such as actuator delay that the equations of motion do not capture, and then numerically integrates through time to update the state. The updated state is then fed back into the controller.

However, since the plant makes simplifications and is thus not a true representation of the physics, data from the IMU, camera, and LiDaR are combined with the simulation output to obtain a better prediction of the true state. This is commonly done through the use of Kalman filters, which would be added to the feedback loop [58]. Since this requires sensor data, it was not implemented in the simulation. However, in future development, this should be integrated.

8.5.2. Plant

The plant describes the physics of the quadcopter and consists of three primary subsystems: The motor dynamics subsystem, the conversion subsystem that converts the output of the controller to the control variables, and

the time integration subsystem that numerically integrates the equations of motion. The input to the plant is the vector of square angular velocities of each propeller, and the output is the estimated state vector.

The motor dynamics subsystem, displayed in Figure 8.7, has the function of introducing a delay between input and output to simulate the real actuator delay. As an input, it takes the squared angular velocities and outputs them with a time delay. It was modeled as a feedback loop with a gain and an integrator, where the gain describes the response time [10]. The gain was chosen to be 0.1, which leads to a conservative response time of around 0.6 seconds to a step input [65].

The conversion subsystem is visualized in Figure 8.8. It takes the delayed vector of square angular velocities, separates the components, and adds them together according to Equation 8.10. Finally, a gain is applied that represents the factor by which the linear combination of square angular velocities is multiplied to obtain the control variables. This is then combined into a single vector and sent to the time integration subsystem.

The time integration system receives the vector of control inputs, which are used to update the state of the quadcopter as shown in Figure 8.9. The thrust is converted to the body reference frame and fed into the 6DOF block together with the torques. From this, an updated state is obtained, including the transformation matrix for the updated angles. Simulink inherently uses adaptive time steps while time stepping, which vary the size of the time step based on what is locally required for convergence.

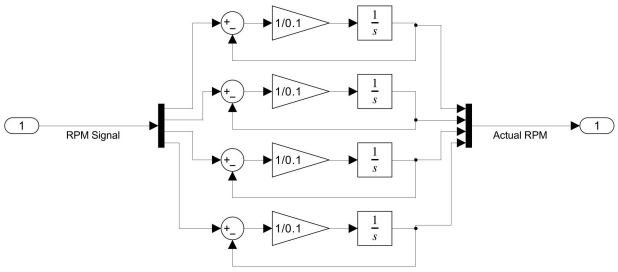

Figure 8.7: Actuator Dynamics

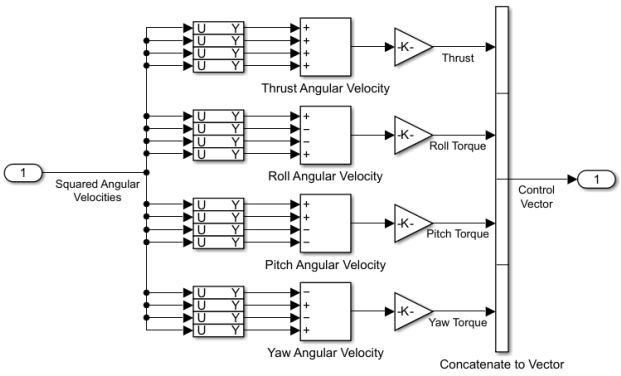

Figure 8.8: Simulink conversion subsystem diagram

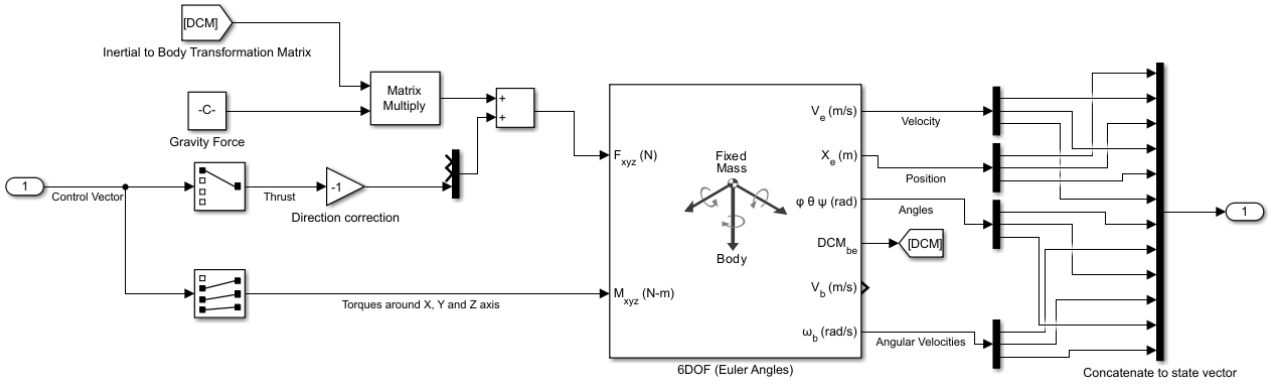

Figure 8.9: Simulink state-space subsystem diagram

8.5.3. Controller

The control architecture of SpeleoDrone implements a cascaded multiloop controller. The inner loops are responsible for the stabilization of the aircraft, and the outer loops are responsible for tracking a desired trajectory.

The first controller is responsible for tracking the position of the UAV. It receives the desired position from autonomous module or user input, and actual position from the state model. It computes the desired velocity vector V_{des} using a PID controller to reduce position error. The desired velocity is kept within a range of $\langle -32.98, 32.98 \rangle$ m/s, which are maximum achievable speeds, as calculated in Chapter 7. Then, the desired velocity is fed into the velocity controller, which outputs the desired acceleration, within the range of $\langle 1.5g, -1.5g \rangle$ for x and y axes, as calculated in Chapter 6, and $\langle 0.95g, -1.5g \rangle$ for z axis. As the z-axis is pointing down, the first number indicates the maximum downward acceleration, which has to be lower than gravity in order to keep the thrust positive.

The calculated accelerations are used in the calculation of the desired attitude, using the Equation 8.11.

$$\theta_{des} = -atan2((a_x \cdot \cos(\psi) + a_y \cdot \sin(\psi)), (-a_z + g)), \text{ and}$$
$$\phi_{des} = -atan2((a_x \cdot \sin(\psi) - a_y \cdot \cos(\psi) \cdot \cos(\theta_{des})), (-a_z + g)) \tag{8.11}$$

The calculated angles were again saturated to the range $\langle -0.785, 0.785 \rangle$ radians, as found in Chapter 7. Combining the desired accelerations with desired pitch and roll angles, the necessary thrust in the body z-axis is calculated using Equation 8.12.

$$T_z = \frac{m \cdot (g - a_z)}{\cos(\theta_{des}) \cdot \cos(\phi_{des})} \tag{8.12}$$

Following that, the desired roll, pitch and yaw, along with the actual Euler angles are passed to the attitude controller. It computes the angular velocity needed to reach the desired orientation. Finally, the rate controller forms the innermost control loop. It compares the desired angular rates to the actual ones and generates control torques. Using relation described in Equation 8.10, thrust and torques are converted into desired RPMs, which are passed to actuator dynamics.

The whole controller architecture is presented in Figure 8.10. Additionally, in Figure 8.11 the Position Controller is presented as an example of the controller - rest of the blocks follow the same logic. The PID controllers were tuned via combination of PID Tuner App[5] and manual manipulation.

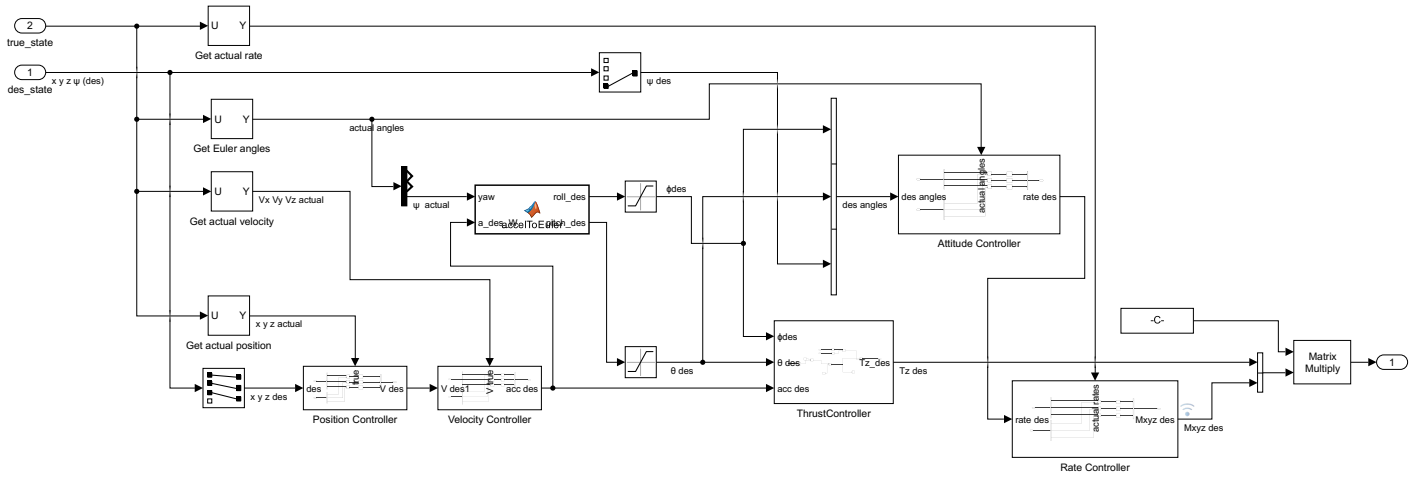

Figure 8.10: Controller Architecture Diagram of the SpeleoDrone

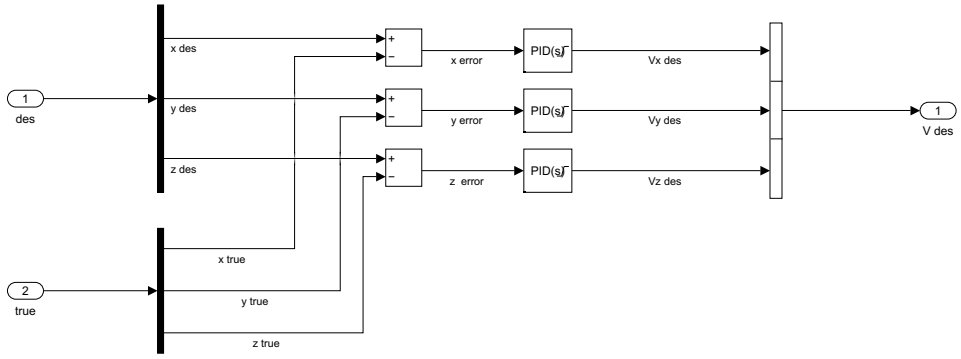

Figure 8.11: Example of Controller: Position Controller

8.6. Performance Analysis

To assess the performance of the quadcopter during different maneuvers, several desired states were input into the model. From this, the position, angles, velocities, and angular rate were obtained as a function of time.

[5]URL: `https://nl.mathworks.com/help/control/ref/pidtuner-app.html` [Accessed: 17 June 2025]

Then, this was used to obtain the settling time, overshoot, and power draw of the motors which were used as criteria to determine the performance.

The settling time is the value where the output deviates no more than 1% from the steady state. This indicates how fast the quadcopter stabilizes at the desired position. Meanwhile, the overshoot describes how far the system goes beyond the desired value, which is an important parameter when the desired position is close to obstacles or walls. Last but not least, the power draw of the motors provides a more accurate indication of the power usage during different maneuvers. The power can be estimated as $P = \tau\omega$ and since the following holds based on Equation 8.9, $\tau \propto \omega^2$, the power is related to the angular velocity as

$$P = c_P \omega^3 \tag{8.13}$$

Where c_P is the linear correlation coefficient between the power and cubed angular velocity, with the value of $8.75 \cdot 10^{-8}$, derived from the motor specifications. The individual power of each motor is summed and divided by four to obtain the mean power used per motor, which can be compared to the specifications.

Figure 8.12 and Figure 8.14 show that the controller is capable of tracking the desired position for both x and y position step inputs by appropriately adjusting the drone's velocity and orientation. Figure 8.13 also shows the power consumption during the x maneuver, according to Equation 8.13, providing an indication of the power use during the maneuver. This spikes up to 210 W per motor, but is also lower than the hover condition for a short period of time, leading to only slight increases in the overall power used. The maximum power usage corresponds to a thrust-to-weight ratio of 1.1, indicating the low thrust-to-weight ratios necessary for maneuvers.

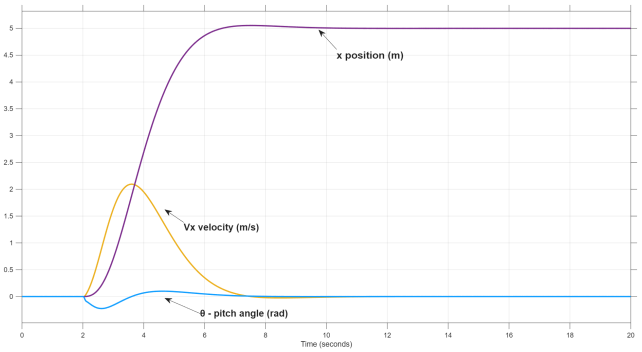

Figure 8.12: System response to a step input of magnitude 5 m in the x direction at time $t = 2$ s

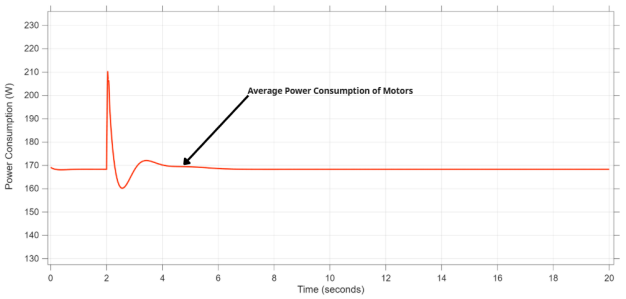

Figure 8.13: Power usage during system response to a step input of magnitude 5 m in x direction at time $t = 2$

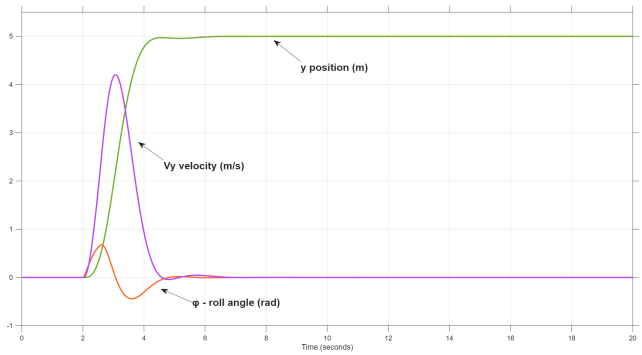

Figure 8.14: System response to a step input of magnitude 5 m in the y direction at time $t = 2$ s

Figure 8.15 presents the system's combined response to simultaneous step inputs in the x (magnitude 3 m), y (magnitude 2 m), z (magnitude −1 m) directions and for ψ - yaw angle (magnitude 0.3 rad). The resulting changes in position, velocity, and orientation demonstrate that the controller is able to respond appropriately even under mixed-input conditions.

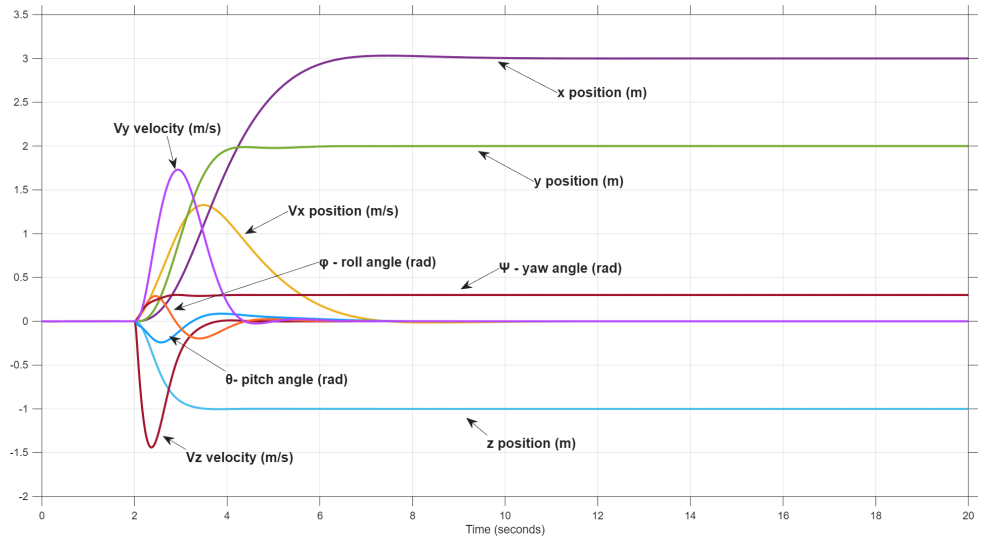

Figure 8.15: Combined system response to step inputs: $x = 3$ m, $y = 2$ m, $z = -1$ m, $\psi = 0.3$ rad at time $t = 2$ s. The corresponding velocity and orientation responses are also shown.

8.7. Verification and Validation

The Simulink model was verified and validated extensively to guarantee that the results are accurate. Since Simulink is a graphical programming environment, tests were performed by analyzing the response of blocks, subsystems, or the complete model to different inputs and outputs in line with the procedures outlined in Chapter 15. Since the experimental data integration and Kalman filters can not be integrated yet, they are not tested either. However, in the post-DSE phase, they would be tested in a similar manner.

8.7.1. Unit Tests

The unit tests that were carried out are summarized in Table 8.2. To visualize the data, built-in scope and display blocks were used in addition to the signal data inspector app. This allows for extracting values at fixed time steps and plotting and comparing individual signals as a function of time.

Table 8.2: Simulink model unit tests overview

Test Case ID	Description	Input	Expected Output	Status
CT-UT-01	Verifies that the conversion subsystem computes torques and thrust correctly	Fixed set of angular velocities	Control vector according to Equation 8.10	PASS
CT-UT-02	Confirms that the 6DOF block results in single-axis accelerations in the expected direction and frame in response to deviations in a single control variable	Altering each control value individually	Positive accelerations in exclusively z, roll, pitch or yaw direction depending on the input	PASS
CT-UT-03	Verifies that the transformation matrix output by the 6DOF block matches the expected matrix	Non-zero desired X, Y and yaw value	Matrix elements that correspond with the inverse of the left-hand side of Equation 8.4	PASS
CT-UT-04	Tests if the 6-DOF block produces results that match the equations of motion	Control input to 6DOF block and linearized state-space system[63].	Error below <1% for first time steps	PASS

CT-UT-05	Checks whether the gravity vector is assembled correctly	Zero vector as control input	Gravity vector in body frame in the form $\mathbf{F_g}\|_b = (\mathbb{T}_{Ib})^{-1}\mathbf{F_g}\|_I$	PASS
CT-UT-06	Verifies that the actuator dynamics are delaying the signal as expected	Step input going from 0 to 1 after 1 second	Delayed response before converging to step value	PASS
CT-UT-07	Tests if the controller outputs are constrained to realistic values	Desired positions in X, Y and Z	Controller outputs within limits specified in saturation blocks	PASS
CT-UT-08	Checks that all PID controllers are tuned to a stable value	Step inputs to controllers	Each PID controller is stable in the Simulink tuning app	PASS
CT-UT-09	Verifies that the sign of the controller outputs are correct	Positive errors	RPM signals that would result in reduction of error	PASS
CT-UT-10	Tests whether the matrix multiplication with the transformation matrix is being carried out correctly	Constant matrix and vector	Correct vector elements	PASS
CT-UT-11	Checks that controllers output zero responses when the error is zero	Zero desired state	Zero output out of all of the controllers	PASS

8.7.2. System Tests

Similarly, Table 8.3 summarizes the system tests that were executed on the model. The combination of unit tests and system tests indicates the model performs as expected.

Table 8.3: Simulink model system tests overview

Test Case ID	Description	Input	Expected Output	Status
CT-ST-01	Determines whether the system is deterministic by running the simulation multiple times for identical inputs	Varying desired states	Identical responses for each desired state	PASS
CT-ST-02	Verifies that the model still stabilizes without excessive overshoot with extreme desired states	Varying desired states up to 100m and 360 degrees	A stable response	PASS
CT-ST-03	Tests if the complete model has no response when there is zero error	Zero desired state	All states being zero at all times	PASS

CT-ST-04	Checks whether the model converges for a number of desired states common in operation	Varying low distance desired states	Convergence to desired state	PASS
CT-ST-05	Verifies the unit tests cover every block of the model	Unit tests from Table 8.2	Involvement of each block of the model	PASS

8.7.3. Sensitivity Analysis

Additionally, a sensitivity analysis was carried out to see how sensitive the model is to variations in key parameters, without retuning the controllers. This is to account for the imperfections during manufacturing and to compensate for deviations from ideal conditions, since the controller must still be able to operate under these conditions. For the purpose of analysis, the overshoot and settling time mentioned are for desired states at distances of 10m in x, y and z direction. The key parameters that may be influenced are the thrust and moment coefficients, mass, and inertia.

Increases to the thrust and moment coefficients make the model slightly more sensitive to inputs, leading to minor increases in overshoot and settling time. However, this effect is small and using extreme values between $9 \cdot 10^{-5}$ and 10^{-6} for the thrust coefficient and between $9 \cdot 10^{-7}$ and 10^{-8} for the moment coefficient, based on commonly used values [29, 16, 53], still leads to stable behaviour, with an overshoot of 4% compared to 1% initially and settling times 15% longer than the initial settling time.

Since the mass and size are heavily constrained by the requirements, and most uncertain components are close to the center of gravity, the inertia is relatively certain. As such, the behaviour was investigated up to deviations of 30%, which should encompass the possible variations due to small changes in structure. This directly affects the angular accelerations, which indirectly affects the linear accelerations. However, within the 30% range the effect is hardly noticeable and will not be of influence on the design, exhibiting negligible increases in settling time with negligible increases and decreases in overshoot for higher and lower inertia, respectively.

Increasing the mass leads to increased overshoot and minor increases in the settling time. Using 4 kg instead of 3.17 kg leads to an overshoot of around 3% relative to the desired position, compared to 1%. Meanwhile, the settling time increases by roughly 10%. All of this would still be acceptable, though, in reality, since most components are commercial off-the-shelf, the increase in mass will likely not exceed 300 grams, which shows practically no difference in response.

Experiments were also run with a combination of varied parameters, showing amplification of the previously described behaviour. However, since each individual effect was already practically negligible within the ranges considered, this still resulted in minimal change, increasing overshoot up to 5% of the reference and settling time by a maximum of 20% compared to the initial value. These results are promising, barely meeting the requirements. Furthermore, after production, each controller will be fine-tuned to accommodate the adjusted parameters, which should lead to correction for any deviations and bring the overshoot and settling time down even further.

8.7.4. Validation

Due to the different control methods used in literature, which typically set the desired z position and Euler angles rather than the position and yaw, it is difficult to compare outputs directly. So, instead, the simulation procedure, position response, and values commonly used in literature were compared.

First, the thrust and moment coefficients were compared to those commonly used in literature. Typically the thrust coefficients are in the order 10^{-6} and the moment coefficient in the range 10^{-7} to 10^{-8} [29, 16, 53]. Since the values obtained in Chapter 7 fall into this range, they can be assumed to be realistic.

Additionally, the methodology in each of the papers [29, 16, 53] is identical to what was used, up to deriving the equations of motion and control variables. After that, each of the models diverges into different methods for time integration and controlling the system. Since similar equations and matrices were obtained, it indicates that the equations behind the model are applicable to simulating this design's dynamics as well.

Finally, a comparison was performed with another simulation that allows for setting the desired x, y, and z positions. With the desired positions set to 0.7m in each direction, the model output as a function of time is displayed in Figure 8.16, while their response is visualized in Figure 8.17 [37].

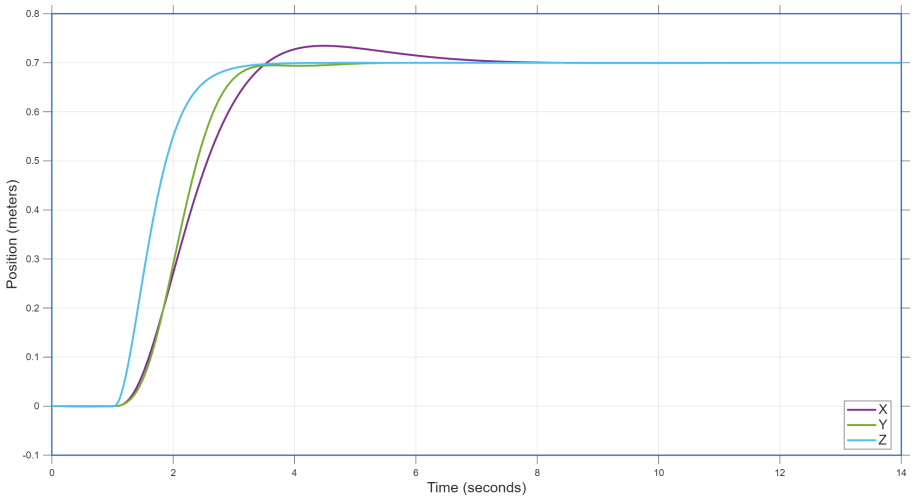

Figure 8.16: Simulink model response to desired states [x, y, z] = [0.7, 0.7, 0.7]

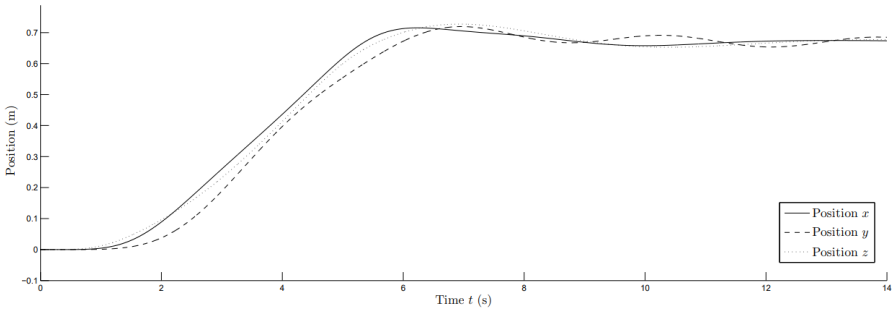

Figure 8.17: Model response to desired states by Luukkonen [x, y, z] = [0.7, 0.7, 0.7] [37]

Comparing the responses, the Luukkonen model stabilizes more slowly in Y and Z direction, with similar times in X direction and less overshoot in X direction. This shows that the faster response time in each direction comes at the cost of additional overshoot in a specific direction. Besides this, the slight oscillatory behaviour in the Luukkonen model was also observed during tuning but faded away after properly tuning the model. The similar methodologies and behaviour shown improve confidence in the methodology and validate that our results are applicable.

9. Avionics Subsystem

In this chapter talks about the avionics subsystem of the drone design. The battery and sensor selection is covered in Section 9.2, where also the electrical interfacing of all components is visualized with the use of an electrical block diagram. Furthermore, the software and data handling approaches are presented in Section 9.3. The chapter is concluded with a sensitivity analysis in Section 9.4

9.1. Sub-system Requirements

The avionics subsystem consists of the batteries and sensors selected for the design. Table 9.1 shows the subsystem requirements that need to be complied with. Also shown is each requirement's parent from the mission, system, or stakeholder requirements, or risk analysis.

Table 9.1: Avionics Requirements Definition

ID	Requirement	Parent
DRN-AVIO-01	The batteries shall not have a capacity larger than 160 Wh	STK-OPR-04
DRN-AVIO-02	The batteries shall be possible to separate from the drone in less than ten minutes	MIS-DRN-1.2
DRN-AVIO-03	The batteries shall be rechargeable	MIS-OPR-10.3
DRN-AVIO-04	The batteries shall have a minimum voltage of 22.2 V	SYS-DRN-1.11.2
DRN-AVIO-05	The batteries shall be able to provide a minimum total current of 50 A	SYS-DRN-1.11.1
DRN-AVIO-06	The batteries shall have a total capacity large enough to power the drone in hovering conditions for at least 15 minutes	SYS-OPR-1.2.1 & RSK-PP-005
DRN-AVIO-07	Voltage converters shall be included in the electronic circuit for components that draw less than 22.2 V	MIS-DRN-1.11
DRN-AVIO-08	The system shall be supplied with a total of 10 batteries: 4 batteries designated for the flight and charging loop, and 6 additional spare batteries	MIS-OPR-8.3
DRN-AVIO-09	Sensors used for control shall have a main and redundant variant	RSK-FC-005
DRN-AVIO-10	The avionics subsystem shall be able to measure acceleration with 0.05 mg resolution	MIS-DRN-3.1
DRN-AVIO-11	The avionics subsystem shall be able to measure rotational rate with 0.003°/sec resolution	SYS-DRN-1.2.1
DRN-AVIO-12	The avionics subsystem shall be able to measure the distance between the drone and the ceiling of the cave with an accuracy of 1% of the distance	MIS-DRN-1.4 & RSK-OP-001
DRN-AVIO-13	The avionics subsystem shall be able to measure the distance between the drone and the floor of the cave with with an accuracy of 1% of the distance	MIS-DRN-1.4 & RSK-OP-001
DRN-AVIO-14	The avionics subsystem shall be able to measure the relative humidity in the vicinity of the drone with 0.5%RH accuracy	MIS-DRN-1.1
DRN-AVIO-15	The avionics subsystem shall be able to measure the ambient temperature in the vicinity of the drone with 0.1°C accuracy	MIS-DRN-1.1
DRN-AVIO-16	The avionics subsystem shall be equipped with a remote identification transmitter	MIS-OPR-1.2

9.2. Detailed Design

In this section, it will be discussed how the avionics subsystem was designed. This includes the choice of battery and sensors. Furthermore, all powered systems and components will be integrated into an electrical block diagram, showing how all systems interact on an electrical level.

9.2.1. Battery Selection

The battery, as the primary power source, is one of the most critical components of the design that directly affects its flight duration on site per mission and, indirectly, the amount of mapping that can be done in a certain time period. It is important that the chosen battery type provides sufficient power for all power-requiring components, e.g., payload, motors, and sensors, to work effectively. Also, the power source should make it feasible for the drone to reach the range of 500 m specified by STK-DRN-1. For the selection method of the battery, a stepwise procedure was set up as follows.

1. Compile electronics specifications of all subsystems
2. Choose voltage rating for the battery
3. Calculate peak total current and average power
4. Enforce limitation of capacity (DRN-AVIO-01)
5. Compile a battery database
6. Select most suitable option based on energy density

In earlier design stages, it was already decided to use a lithium-polymer (LiPo), and not, for example, a lithium-ion (Li-ion) battery. Both batteries are commonly used in drone design. The choice for a LiPo battery was mainly based on its higher power density and discharge rate compared to Li-ion. Since current draws in the maximum power setting of the drone can lie above 50 A, the typical C-rate specifications, a measure for how quickly a battery can discharge its power, of Li-ion batteries were generally not high enough. LiPo batteries allow the battery to be lighter while providing enough current and power needed for power-heavy take-off or quick maneuvering of the drone. These aspects are judged to be of higher advantages than the downsides of the lower cycle life and lower energy density than Li-ion batteries [9, 24]. An electronics specification overview was compiled, as shown in Table 9.2, to get an indication of what battery capacity and C-rate would be needed to provide a sufficient endurance of at least 10 minutes and preferably higher.

Table 9.2: Electronic specifications of all subsystems

Components	Count	Voltage [V]	Current [A]	Power [W]
Propulsion				
Motor (T/W =1.5)	4	25.2	15.9	400
Payload				
Lidar	1	5	0.67	8
Camera	1	12	0.52	2.6
Total / max		25.2	64.8	1610.6

The motor data was compiled for a 1.5 thrust/weight ratio, because the battery would need to provide enough burst current to also fly in that configuration. The average thrust/weight ratio is lower than 1.5. The electronic specifications in Table 9.2 are estimates based on datasheets from the selected components, but their exact values could slightly change in different flight configurations. The compiled data yields that a battery with a capacity of 5000 mAh, would need a C-rate of 13. A higher capacity battery would need a slightly lower C-rate to meet the burst current required. Since most components will be connected in parallel, the battery voltage needed was determined by the component that requires the highest voltage: motors. The chosen motors draw about 25.2 V, which requires a 6S battery. These batteries provide 25.2 V when fully charged. Sensors were not included in this table, as their power consumption is normally small compared to the payload and propulsion subsystems. A final power breakdown of all components incorporated in the design is compiled in Section 4.2.

Because the system has to be transportable by air, the capacity cannot exceed 160 Wh (DRN-AVIO-01). To find a battery that provides as much endurance as possible, batteries with a capacity close to 160 Wh were looked at. The specifics of the 4 most promising 6S LiPo batteries found with a sufficient C-rate are summarized in Table 9.3. All these batteries have a nominal voltage of 22.2 V.

Table 9.3: Technical Specifications of Evaluated LiPo Battery Options

Manufacturer	Capacity [mAh]	C-rate	Mass [g]	Energy Density [Wh/kg]	Size (cm)
Spektrum[1]	7000	30	720	215.8	16.9 x 5.8 x 4.6
SLS XTRON[2]	7000	25	793	196.0	13.9 x 4.2 x 6.4
Tattu[3]	7000	25	812	191.4	13.8 x 4.3 x 6.3
GNB[4]	7200	70	845	189.2	14.2 x 6.9 x 4.4

The specifications of the different battery options from Table 9.3 are relatively similar. The Spektrum battery was selected for the design due to its high energy density, which directly translates into increased endurance. To ensure sufficient flight time, the design includes two of these batteries. During each mission, the batteries will be discharged to a maximum of 80% to perserve battery life and prevent damage. The final endurance estimates are summarized in Subsection 7.2.2.

9.2.2. Sensor Selection

Various types of sensors are needed to ensure the drone has enough input data to maintain stable flight, estimate its proximity to objects, and monitor environmental conditions. For the selection method of the sensors, a stepwise procedure was set up as follows.

1. Identify needed sensor types
2. Enforce restrictions on weight and power
3. Compile data from 3-4 sensors of each type
4. Select most suitable option based on performance relative to weight, power and cost

This procedure was followed, and the selected sensors and their relevant specifics are discussed below. Lightweight, low power, and affordability were the main selection points, next to accuracy.

Inertial Measurement Unit

An inertial measurement unit (IMU) calculates the drone's linear and angular acceleration and helps measure its attitude angles in roll, pitch and yaw maneuvers. The flight control system highly relies on the data gathered on the drone's motion and orientation by the IMU to operate accurately. An IMU generally consists of an accelerometer, a gyroscope, and sometimes a magnetometer [55]. For drone operations in caves, a magnetometer will be unreliable due to magnetic interference from rock and minerals [22]. Therefore, a potentially present magnetometer in an IMU will be inactivated in this design. Often, an IMU is combined with a GPS sensor to correct for drift; however, in a cave, no GPS signal can be received. For that reason, the IMU will be combined with the LiDAR from the payload module to improve this drift. Also, a lighter redundant IMU sensor is added to the design as a backup for safety in case the main IMU encounters problems. It will ensure navigation is still possible in such a situation. The IMUs selected and their specifications are summarized in Table 9.4.

Table 9.4: Specifications of selected Inertial Measurement Units

Components	Bias stability	Bandwidth	Mass	Cost	Voltage	Power
Main: MicroStrain 3DM-CV5-IMU[11]			11 g	€445	3.2 - 5.2 V	0.36 W
Acceleramетor	0.08 mg	225 Hz				
Gyroscope	8 deg/hr	500 Hz				
Redun.: BNO055[12]			3 g	€ 31	2.4 - 3.6 V	0.04 W
Acceleramетor	-	8-100 [Hz]				
Gyroscope	-	12 - 523 [Hz]				

Time of Flight Sensor

A common type of drone altimeter, a sensor that provides height information, is a barometer, which measures altitude based on air pressure. However, this sensor type would not suffice for operation in a cave, due to irregular pressure differences and insufficient precision for detecting the relatively small height differences in a cave environment.

Therefore, a Time of Flight sensor (ToF) was selected as altimeter that provides height information by emitting laser pulses. A ToF is placed both on the top and bottom of the drone, to detect the distances to the ceiling and ground. Its data will be used for collision detection, together with the LiDAR from the payload subsystem. The ToF selected and its specifications are summarized in Table 9.5.

[1] URL: https://www.spektrumrc.com/product/22.2v-7000mah-6s-30c-smart-g2-lipo-battery-ic5/SPMX76S30.html [Accessed: 10 June 2025]

[2] URL: https://www.stefansliposhop.de/en/batteries/sls-multirotor-uav/sls-xtron/sls-xtron-7000mah-6s1p-22-2v-25c-50c::2193.html [Accessed: 10 June 2025]

[3] URL: https://gensace.de/collections/industrial-drone/products/tattu-lipo-6s-7000mah-22-2v-25c-battery-pack-with-xt90 [Accessed: 10 June 2025]

[4] URL: https://rcdrone.top/nl/products/gnb-6s-22-2v-7200mah-70c-drone-batterij [Accessed: 10 June 2025]

[5] URL: https://www.microstrain.com/inertial-sensors/3dm-cv5-10 [Accessed: 10 June 2025]

[6] URL: https://www.adafruit.com/product/2472 [Accessed: 10 June 2025]

Table 9.5: Specifications of selected Time of Flight sensor

Component	FoV	Range	Accuracy	Mass	Cost	Voltage	Power
101990620[5]	2 deg	0.1 - 12 m	1%	12 g	€39	5 V	0.7 W

Temperature and Humidity Sensor

Temperature and humidity sensors, also referred to as hygrometers, are not mission-critical, but could be used for archeological research purposes and were therefore added to the design. When selecting an exact component, it was looked at sensors with a detectable humidity range of 0 - 100 % humidity since cave environments can be very humid. Also, the sensor's temperature range should cover temperatures between 0 and 60 °C, to increase its versatility for usage in various cave environments. In the selection process, accuracy was prioritized over response time, because the system does not directly rely on the sensor data.

Table 9.6: Specifications of selected Temperature and Humidity Sensor

Component	Accuracy	Range	Mass	Cost	Voltage	Power
HDC3022DEJR[6]			1.6 g	€2	3.3 V	< 0.01 W
Temperature part	±0.1°C	–40°C - 125°C				
Humidity part	±0.5%RH	0-100%RH				

Miscellaneous

Some additional components were integrated into the design. Specific types, added as footnotes to the function description, were selected to serve as a reference for size, power draw, and mass indications.

1. **Buzzer**[9] - Emits a sound when the drone is turned on as a status indication for the ground crew.
2. **Remote ID**[10] - Ensures compliance with regulations when (test) flying the drone system outside the cave environments. It sends out information about the drone's location and specifications.
3. **GPS sensor**[11] - Required for functioning of the Remote ID as it supplies data about the drone's position.

9.2.3. Electrical Block Diagram

In this section, the components of the drone are integrated electrically in an block diagram. This is shown in Figure 9.1.

The diagram only shows electrical interfaces between components, their supplied voltage and data links. The physical layout of the components in the diagram is only for illustration purposes.

As the components require different input voltages, converters had to be used. The components were grouped based on voltages such that one converter would serve multiple components requiring the same voltage. 3 converters were in total needed for the different voltage levels of 12, 5 and 3.3 V. For smaller voltage differences, a Low Dropout Regulator was used as converter. This is converter is normally used for small voltage differences as it dissipates the excess voltage as heat. For higher conversion efficiency, the higher voltage gaps were bridged with buck converters, which are converters with low heat dissipation that use switching principle to lower voltage[12]. The three converters are visible in Figure 9.1.

One of the main components of the electrical interfacing of the system is the flight controller, which will collect data from all components, such as sensor data, and run the software described in Chapter 8 to navigate, maintain stability and controllability, and collect data. The flight controller will be a custom-made design, tailored for the application of this drone, and put on a printed circuit board (PCB).

Other components that can be seen in Figure 9.1, are four different batteries. Two 6S batteries power most of the components. The two flashlights use their own integrated batteries. Also, between the flight controller and all other components, data links are present to connect these. The flight controller processes all received data and transmits it to the ground station via the fiber optic cable. Since the flight controller will be custom-made, an off-the-shelf flight controller was used as reference for the diagram.

[7] URL:https://www.digikey.nl/en/products/detail/seeed-technology-co-ltd/101990620/11506470 [Accessed:10 June 2025]
[8] URL: https://www.digikey.nl/en/products/detail/texas-instruments/HDC3022DEJR/17748469 [Accessed: 10 June 2025]
[9] URL: https://www.digikey.nl/en/products/detail/pui-audio-inc/AT-2440-TWT-R/1464842[Accessed: 10 June 2025]
[10] URL: https://droneshop.nl/bluemark-db152fpv-remote-id-module[Accessed: 10 June 2025]
[11] URL: https://flywoo.net/products/goku-gm10-nano-v3.1-gps[Accessed: 10 June 2025]
[12] URL: https://tinyurl.com/mr48chm4 (www.utmel.com) [Accessed: 10 June 2025]

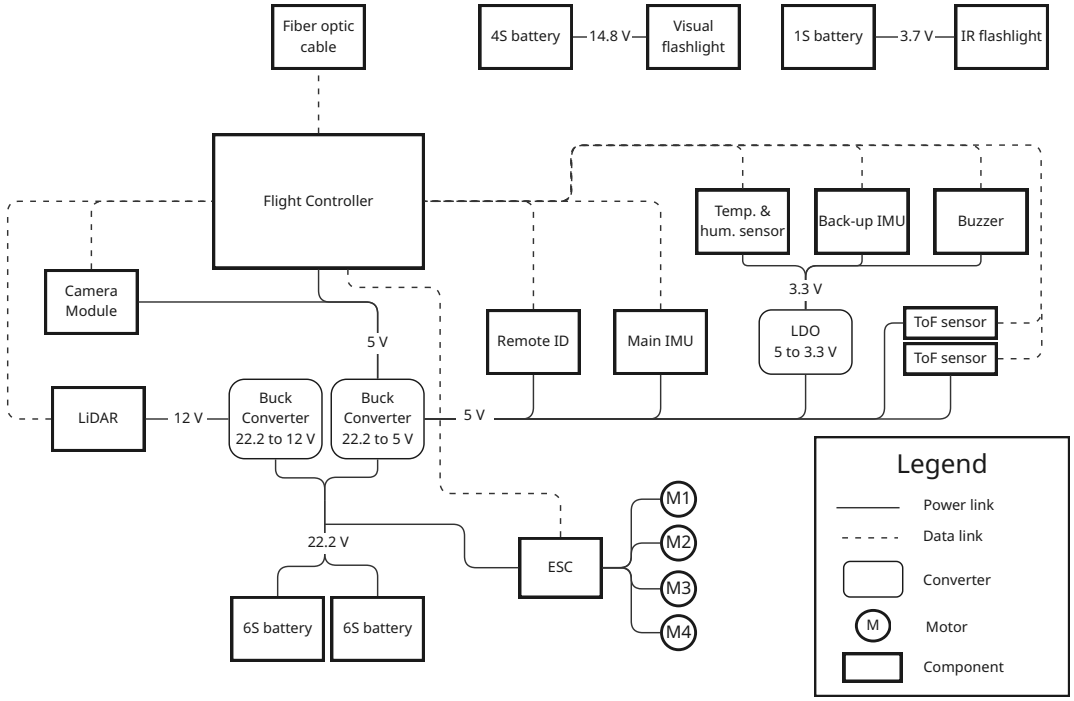

Figure 9.1: Electrical Block Diagram

9.3. Software and Data Handling

Having the components selected and connected, the interaction between the user and each component must be defined, as well as the software structure and logic throughout the system.

The software incorporated within the system must encompass the transmission and receiving of data, the storage, fault detection and rebooting, as well as all the mission specific requirements such as stability and control, propulsion, and data gathering. In Figure 9.2, the software and data handling are presented within one diagram.

The ground station presents the user the data of interest as explained in section Section 10.5, however all data is logged. As such, all data is sent from the flight controller to the ground station via the fiber optic cable, processed and stored, and showcased for the user alongside the option to access any other data of the system through the settings of the interface. Most importantly, the data is processed for the AI algorithm and sent to the drone via fiber optic cable. Additionally, the ground station receives data from the charging station regarding the batteries and solar panels. Regarding the data storage of the ground station, it's required to have 12 terrabytes for 800 minutes of operation at a bitrate of 994 megabytes per second, explained in Section 10.3.

To ensure the ground station and drone function correctly, the ground station contains a watchdog. The watchdog in the ground station uses a AI algorithm to predict future crashes in the software and the time until they happen [13], a pretrained fine-tuned for caves to be done post-DSE. This watchdogs doesn't instantly reboot the systems but sends a signal to the ground station to land and then reboot to avoid crashing, if there is not enough time to return to the ground station. The landing location is either picked by the user or picked by a separate region-based AI algorithm on the ground station that identifies safe landing locations based on sensor data [14], pretrained fine-tuned for caves to be done post-DSE.

The software/hardware on the drone controls the power distribution to the sensors, payload, and propulsion by communicating back and forth with the user from the ground station to ensure that all modules and specific components are functioning as expected. Additionally, it has an onboard flight control system which consists of the controller presented in Chapter 8. At first glance, it may seem that the Payload control system and the power distribution control system are different hardware components, but they have been split from the processing unit within the module for better representation of the intended software.

The charging station measures the power generated, alongside the temperatures of both the solar panels and batteries to avoid potential hazards and sends it to the ground station for optional monitoring. To make sure

[13] URL:https://www.sciencedirect.com/science/article/pii/S0951832004000857[Accessed: 6 June 2025]
[14] URL:https://www.sciencedirect.com/org/science/article/pii/S2564493924000195[Accessed: 6 June 2025]

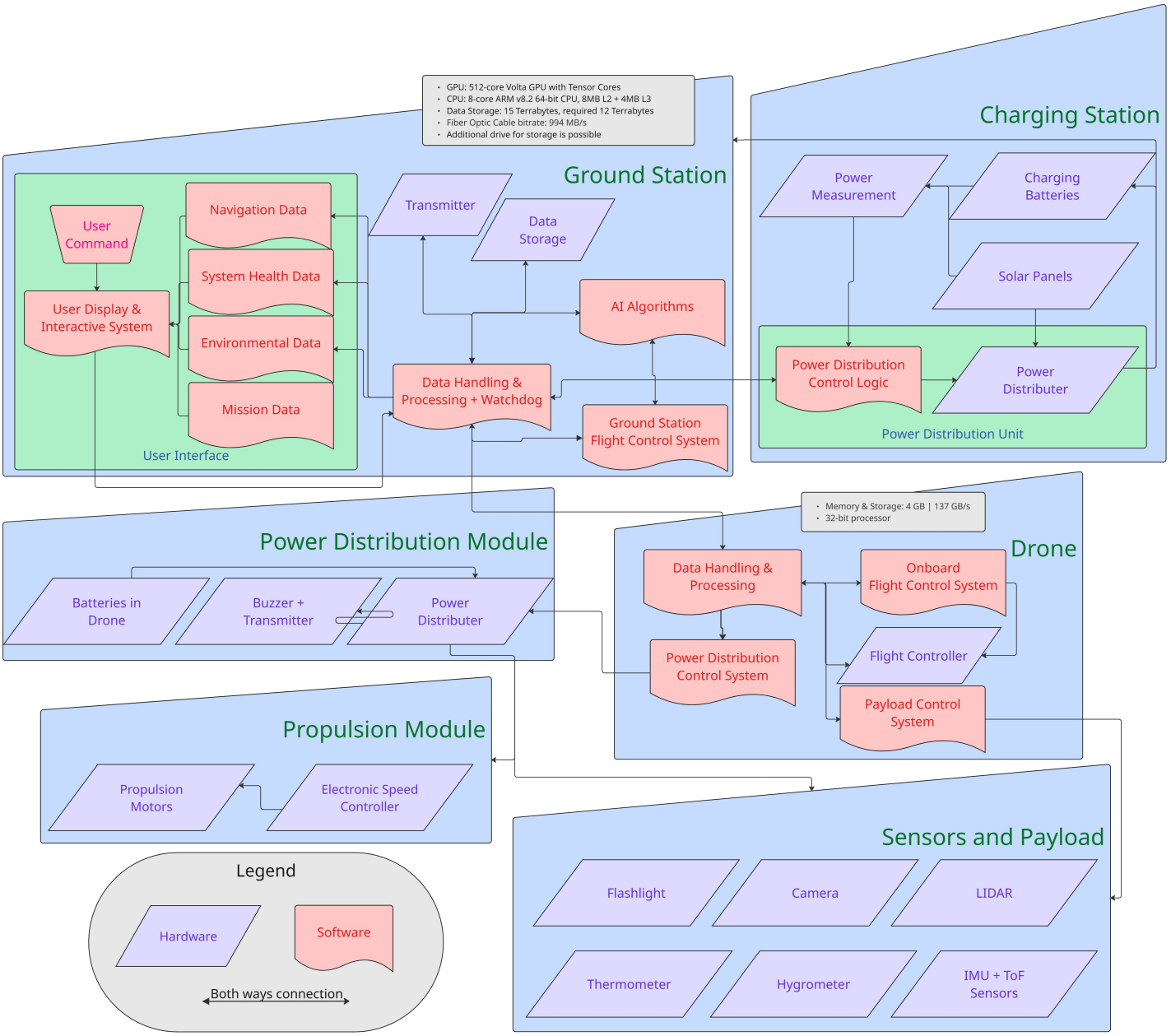

Figure 9.2: Software and Data Handling Block Diagram

the ground station has enough power, data regarding itself is sent to the charging station, from which the power distribution control logic takes into account the data from the solar panels, batteries, and ground station to send the “intended distribution” signals to the power distribution unit.

9.3.1. State Machine

The final piece of software architecture to be discussed is the planned layout of the state machine for the flight controller. it is directly related to the flight modes of the quadcopter, those being assisted user controlled and autonomous flight. Additionally, a return to base mode was added, which will be activated in case of low battery or if a return command it sent to the flight controller. That command can be sent by the user or triggered automatically by a fault detection system, for example in the case of loss of contact with the ground station.

The state machine diagram found in Figure 9.3 shows those modes, the activities taken as a part of them and triggers that cause them to move between different states. The diagram follows the UML conventions, meaning the rounded rectangles represent activities, the bigger rectangles specific states and the dots an entry and exit points for the software. The flag looking element represents an external signal being received, in this case the return to base command.

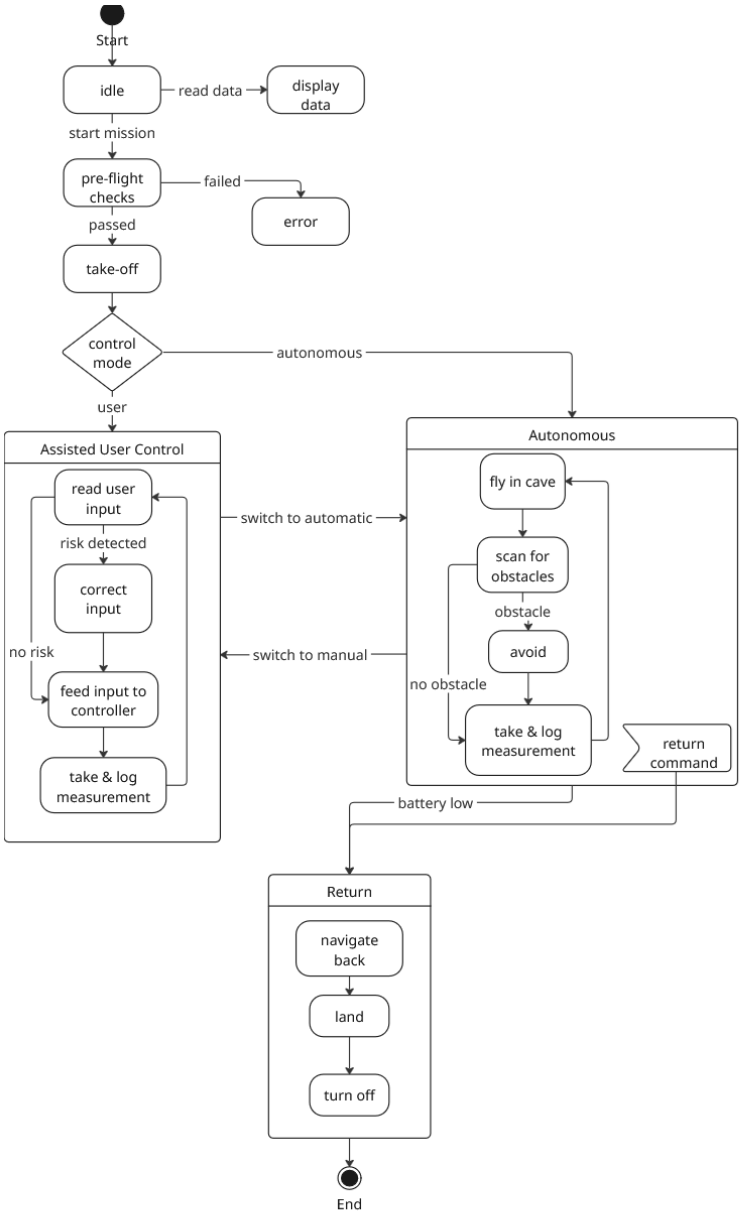

Figure 9.3: State Machine

In terms of the exact architecture, the state machine will be implemented over the reference of the controller,

discussed in Section 8.5. Depending on the state active at the moment, either the position determined by the AI will be given as input into the flight controller or the input of the user, corrected by the AI to avoid collision or hard landings. The exact implementation of the state machine might differ in the future, as only parts of the software have been defined at the moment, but it should still follow a similar layout.

9.4. Sensitivity Analysis

No software modules or programming were used for the computations except for Microsoft Excel. The Excel-based calculations were verified with manual unit testing by performing the calculations simultaneously by hand and comparing the results. It was checked that all formulas were correctly implemented by systematically changing input values and checking that the output values changed as expected. The verification of the actual components is for a future project stage, when a prototype of the electrical system can be made, and in this way, it can be checked if the battery, sensors, and electrical interfaces work together as expected.

The avionics subsystem mainly consists of off-the-shelf components. These were selected based on a comparison between multiple commercially available options found online. For battery selection, approximately 20 batteries with a capacity of around 7000 mAh were compared. The sensor selection was, on average, based on comparing 4 to 10 similar components.

Not all available components on the market could be compared due to the time constraint of this project. Therefore, the possibility exists that a better alternative sensor or battery is available in terms of performance, weight, size or cost. However, it is assumed that since multiple components were compared, sufficiently adequate parts were selected. If, in further design stages, it turns out that a better option exists for a component, adjusting the choice of component will be possible with minimal impact on the overall design, due to their small size and mass. These adjustments would be limited to, for example, wiring or type of connector.

With regards to the battery selection, it was also analyzed how much their performance will degrade over time. According to literature, lithium-polymer batteries typically have a cycle life of 300-500 cycles, after which their capacity reduces to approximately 80% of the total capacity[15]. For one mission duration of 7 days with 8 flights a day, one battery goes through approximately 12 charge-discharge cycles, when 10 batteries are brought along on the mission. A battery capacity in the range of 100% to 80% will be sufficient to provide the drone with enough power to execute a mission and provide an endurance between roughly 12 to 18 minutes. When looking at the lower limit of a cycle life of 300 cycles, this would mean the batteries suffice for 25 mission periods as defined above. The drone is designed for 10 mission periods, but from the perspective of battery degradation, this lifespan could be more than doubled.

[15] URL: `https://www.lipolbattery.com/lithium-polymer-battery-life.html` [Accessed: 24 June 2025]

10. Operations and Logistics

In this chapter, the operations and logistics of the drone mission will be discussed It startws ith high-level overview in Section 10.1. Section 10.2 discusses the communication, Section 10.3 discusses the payload, Section 10.4 describes the power generation, Section 10.5 describes the Ground Control Station, Section 10.6 describes the transport logistics, Section 10.7 discusses repairability and finally Section 10.8 gives an outline for the User Manual.

10.1. Operations and Logistics Concept

This section presents a high-level overview of the operations and logistics concept behind the SpeleoDrone system, covering all mission phases from preparation to post-flight procedures.

As illustrated in Figure 10.1, operations begin before the mission departure. The drone must be registered with the appropriate regulatory authorities, in accordance with aviation guidelines. All necessary components should be carefully packed using the provided casing system, as described in Section 10.6, to ensure safe transportation. Before deployment, the mission's feasibility is assessed based on current weather conditions and the operational status of all system components. Should any part exhibit signs of malfunction or damage, or if environmental conditions—such as heavy rain, strong winds, or insufficient sunlight for charging—pose a risk to safe operation, the mission must be postponed or canceled. Upon arrival at the mission site, the ground control and charging stations are set up. The drone undergoes initial diagnostics immediately after powering on to identify any faults. Clear safe zones are then established and marked to alert the crew of potential interaction areas with the drone, in line with the safety procedures outlined in Section 14.2.

To comply with legal requirements for outdoor flight testing, the drone must be equipped with a Remote Identification module. This is mandated by EASA regulations to ensure visibility of unmanned aerial systems to external stakeholders, such as air traffic management. Once the drone enters the cave environment, the remote ID module can be safely removed, as it is no longer required for subterranean operations.

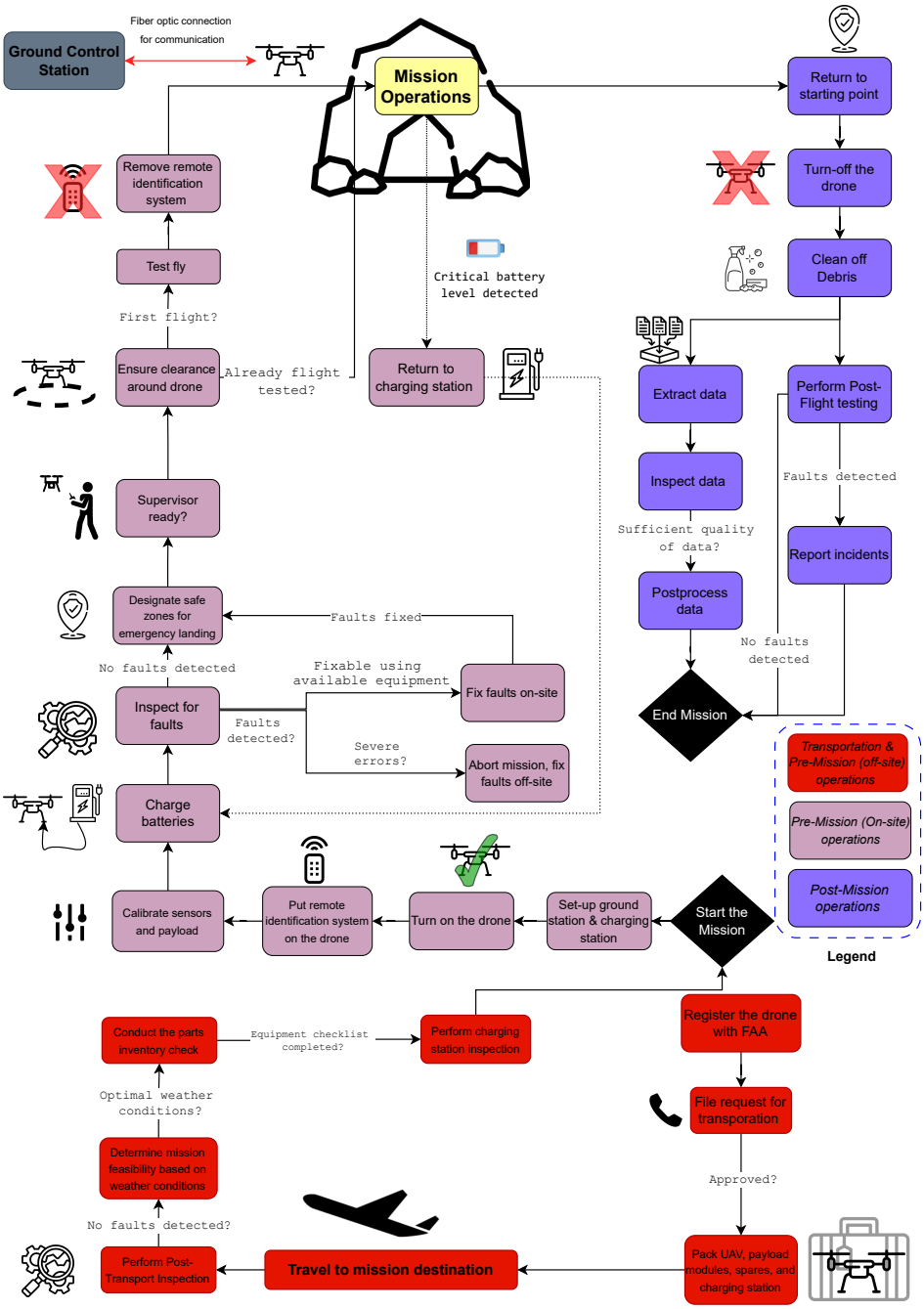

Figure 10.1: Pre- and post-mission operations

The operational mission - visualized in diagram presented in Figure 10.2 begins with the Exploration phase. During this stage, the drone performs an initial mapping of the cave topology using only infrared light to avoid disturbing sensitive cave-dwelling fauna. If a bat colony or similar biological feature is detected, its location is logged and excluded from further visible light exposure in subsequent mission stages. Navigation at this point is handled by the onboard AI model, detailed in Section 8.4, which identifies “no-go zones” where the drone physically cannot pass due to size limitations. The AI also conducts preliminary detection of potential regions of archaeological interest, assigning confidence scores to flagged areas. These are then reviewed by the operator, who evaluates the relevance of each location for further investigation.

After the initial exploration, the system transitions to the Mapping phase. In this mode, control shifts from the AI model to a path-planning algorithm—specifically D* Lite—which guides the drone through the environment to collect mission-critical data, following the payload operation logic outlined in Section 10.3. As the mission progresses, previously mapped areas are bypassed efficiently to conserve energy, allowing the drone to focus on unmapped chambers. This approach enhances both operational speed and mission range by maximizing flight endurance.

The mission concludes with a set of standardized post-operation procedures. The drone is powered down, cleaned of any dust or debris accumulated during flight, and subjected to post-flight testing to ensure continued system integrity for future deployments.

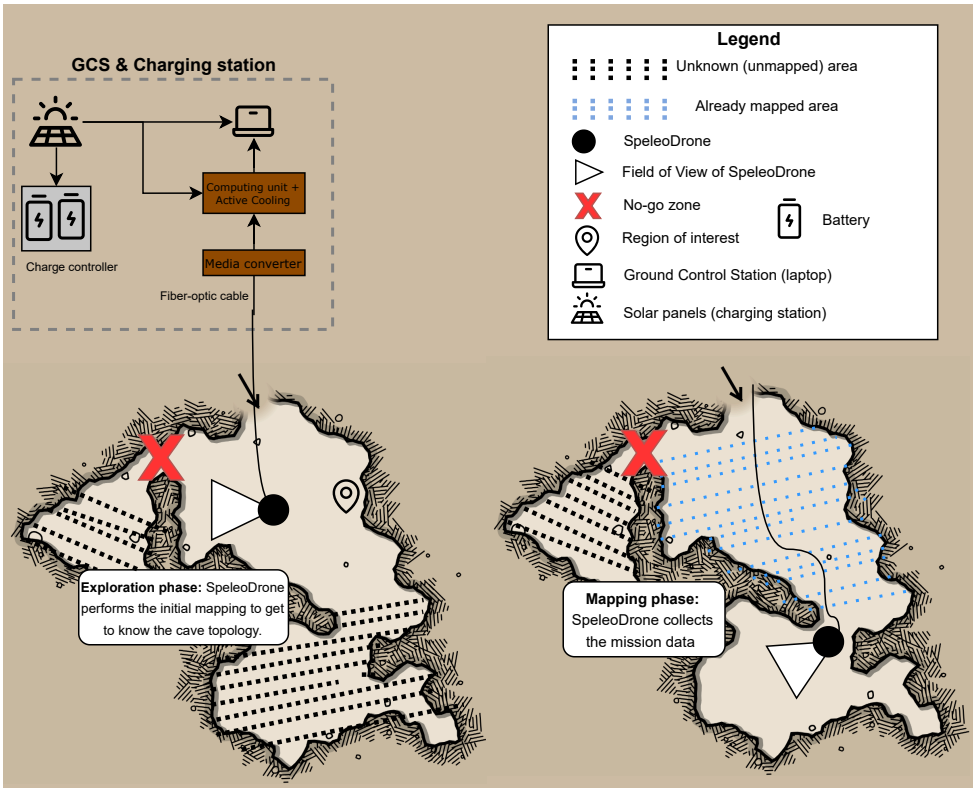

Figure 10.2: Mission operations

10.2. Communication

Communication with a UAV can come in many forms. For the SpeleoDrone, the decision was made to connect the drone to the ground station via a fiber optic cable (FOC). With the cable connection, the requirement STK-OPR-13: 'The drone shall be capable of both autonomous operation and human-controlled modes' can be fulfilled. This was preliminarily outlined and documented in the Midterm Report [6].

The implementation is as follows: The thin fiber optic cable will be tightly wound on a reel with machine precision. The reel is stored in a casing that can be attached to the drone, and the cable will unwind itself from the reel during flight. The other end of the cable is attached to the ground station. The cable provides a two-way connection from drone to ground station, allowing for data and command transfer. After the mission ends, the drone will return back to the base. In Figure 10.3, an example of a spool with FOC on a drone is shown.

Although a fiber optic connection has multiple benefits, designing it also comes with several problems. For example, the cable could break or tear, the cable could get stuck on the reel, or it could get tangled. To ensure proper communication and data transfer at all times, the FOC should have a length of at least 1000 m.

Figure 10.3: A spool with fiber optic cable, attached to a drone[1].

It has to be ensured that the cable will not hold the drone back if stuck, that it can resist the environment, and most importantly, a solution had to be found for the retrieval of the FOC.

The first problem was already discussed in the Midterm Report [6]: the UAV itself will contain the reel to dispense the cable. The FOC will experience low tension as it is reeling off. If stuck, the tension will temporarily increase, and the reel will roll off more cable until equilibrium is restored.

To resist the environment in the cave, the fiber optic cable consists of a silica glass core and an acrylate outer layer, as explained in the Midterm Report [6].

Finally, the procedure following each operation of the drone in the cave regarding the fiber optic cable is discussed below. When a mission is completed, the drone will fly back out of the cave and land. Then, the reel with the FOC can be detached from the drone, and the FOC can be detached from the ground station. Thus, the two loose ends of the cable will be outside of the cave. The following options were discussed for the procedure after this, found through brainstorming or research.

1. Leave the fiber optic cable in the cave after each mission.
2. Pull the fiber optic cable out of the cave.
3. Retrieve the fiber optic cable by hand.
4. Reel the fiber optic cable back onto the drone after each mission.
5. Shatter the fiber optic cable core into tiny glass pieces.
6. Place the fiber optic cable in a thin, biodegradable tube that it can be pulled out of after each mission, and leave the tube in the cave.

The first option is the least favorable out of the six, as it violates MIS-OPR-7.3: 'All components of the system shall be retrievable from the environment after operation within 1 week since the beginning of the mission'. Pulling the fiber optic cable out of the cave is also problematic, as the tension due to the surface friction could rip the cable, part of the cable could be left behind. Moreover, the potentially complex and irregular cave interior as shown in Figure 10.4 might cause the cable to get tangled or stuck.

Retrieving the FOC by hand is something that will not be evaluated in the design, as the system shall be operable without intervention from humans in the cave. If (part of) the cave is accessible to humans, then it is easiest to retrieve the fiber optic cable by hand; however, this will not be assumed. Therefore, this option will not be considered and it is up to the team during mission operations to judge the cave's accessibility and determine whether to proceed with entry.

As the drone uses a pathfinding algorithm that optimizes as the drone flies as was explained in Subsection 8.4.2, the drone's exit path will differ from its path into the cave. Reeling the FOC back would require the drone to follow the original path, flying slow enough to reel the cable up, effectively cutting mission time in half. It could also introduce problems for drone stability, drone size and power draw.

(a) Stalagmites found, in sizes comparable to that of humans[2].

(b) Stalagmites and stalactites with rough surfaces[3].

Figure 10.4: Isla de Mona cave interiors.

[1]URL: https://www.forbes.com/sites/davidhambling/2024/08/02/german-jam-proof-fiber-optic-drone-testing-in-ukraine/ [Accessed: 18 June 2025]

[2]URL: https://brill.com/view/journals/nwig/89/1-2/article-p30_2.xml [Accessed: 11 June 2025]

[3]URL: https://www.nytimes.com/2024/03/20/magazine/mona-island-puerto-rico.html [Accessed: 11 June 2025]

Option 5 relies on the principle that tiny glass shards are in essence sand[4]. The fiber optic cable would consist of a very thin glass inner core, covered by a biodegradable protection layer. After the mission, the inner core can be shattered to minimize the FOC's negative impact on the environment. The procedure is further explained by Hawkes et al. [23]. It must however be noted that requirement MIS-OPR-7.3 will still be violated.

The last option requires further explanation. A sketch is shown in Figure 10.5. The fiber optic cable will be manufactured as usual. The thin, biodegradable tube is a loose sleeve around the cable. The fiber optic cable is depicted in blue, and the sleeve is shown in dark gray in the sketch. The depicted dimensions are justified in Subsection 10.2.1.

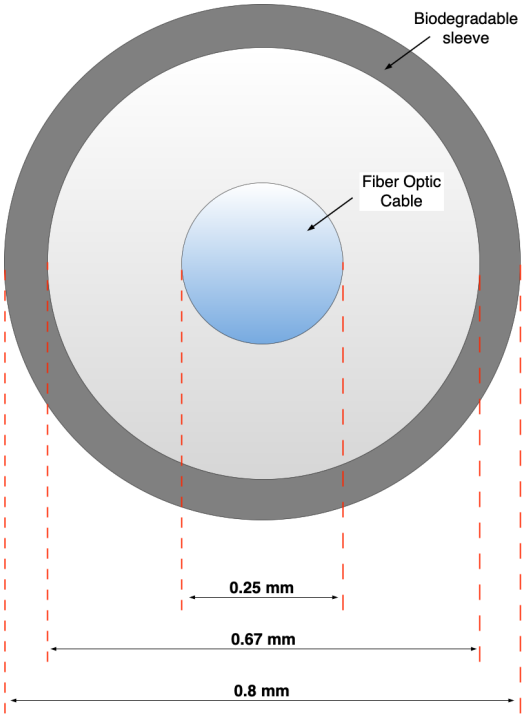

Figure 10.5: Sketch of the Fiber Optic Cable inside the biodegradable sleeve, with dimensions.

The sleeve with the FOC inside is wound around the spool. The mission procedure in the cave is then the same as for a spool with only the FOC: the spool is attached to the drone, and while it flies, the cable, in this case including the sleeve, is gradually released. When the drone is back at the ground station, the spool is detached from the drone. To then retrieve the fiber optic cable that is inside the sleeve, this outer sleeve will be held in place, while the inner glass cable is wound upon a spare spool. After the inner glass wire has been pulled out, only the biodegradable tube is left in the cave. Even though this would still violate MIS-OPR-7.3, this approach was seen as a good trade-off between site disturbance, the other requirements, and practicality. Therefore, option 6 was chosen as the main option for the retrieval of the fiber optic cable. Its design was further worked out and is documented below.

10.2.1. Fiber Optic Cable with Sleeve

To determine a suitable material and structure for the sleeve, the following things were taken into consideration.

1. The sleeve should degrade in a to be determined timeframe, to ensure that the environmental impact is as small as possible.
2. The sleeve should be able to withstand relevant point loads, to protect the cable against the cave environment.
3. The material should be solid in the operational temperature range.
4. The material of the sleeve should be flexible enough to be spooled around the reel.
5. The sleeve should be strong enough to withstand the force created by the friction of pulling the cable out.
6. The sleeve should not be thinned out too much due to elongation, to maintain structural integrity.

First, the required diameter and skin thickness of the sleeve had to be found. Currently, this was based on available resources on the market. A short market analysis was conducted to find the minimum dimensions of polymer tubing, as the diameter of the fiber optic cable itself is only 0.25 mm [6].

[4]URL: `https://andelaproducts.com` [Accessed: 18 June 2025]

The minimum non-custom flexible polymer tubing diameter that is on the market is 1/32" [5] [6], in combination with a minimum skin thickness of 0.005"[5]. The following calculations are based on these dimensions for the outer sleeve. All dimensions are summed in Table 10.1 below. A visual representation of the fiber optic cable with dimensions was previously presented in Figure 10.5.

Table 10.1: Fiber optic cable dimensions

Description	Variable	Value [mm]
Silica core diameter	d_{glass}	0.125
Acrylate cover outer diameter	d_{shell}	0.25
Sleeve inner diameter	$d_{skin,in}$	0.67
Sleeve outer diameter	$d_{skin,out}$	0.8

To find a suitable material, first the desired properties were compared to non-biodegradable plastic polymers that are used in industrial tubing, sleeving and wiring applications. The mechanical, thermal and chemical properties of these materials were then compared to various biodegradable materials [8].

The properties that were considered were based on the considerations shown at the beginning of this subsection. Table 10.2 below shows the three most promising materials from this analysis and their relevant properties: Polybutylene Succinate Adipate (PBSA), Polybutylene Succinate (PBS) and Polycaprolactone (PCL).

Table 10.2: Mechanical and thermal properties of candidate biodegradable materials [8]

Material	Yield Strength [MPa]	Tensile Strength [MPa]	Flexural Strength [MPa]	Elongation at Break [%]	Hardness Shore D	Glass Transition Temp. [°C]	Melting Temp. [°C]
PBSA	17.4	29.5	16.3	405	53.5	-47	92
PBS	35.9	42.2	35	275	65.1	-30	118
PCL	18.1	30.9	22.4	1247	54.6	-62	70

In further development, these material properties will be cross-referenced with other sources. Next to these properties, it was important to consider the biodegradability of these materials. PBSA is a biodegradable material, but only under industrial composting conditions[7]. If not disposed of correctly, it can cause harm to the environment. Therefore, this material will not be used. PBS is more promising[8], but it will need to be tested in the operational environment for actual degradation rates. And finally, although PCL degrades relatively slowly[9], it is biodegradable in various environments like soil, compost, and water[10]. Therefore, this material scores best in relation to biodegradability.

These last two materials will thus be further assessed in the testing stage of design, to test the material properties in relevant environments.

To approximate the mass of the fiber optic cable including the sleeve, the following equation was used:

$$l_{\text{skin}} = \pi \cdot \frac{d^2_{\text{glass}}}{4} \cdot \rho_{\text{glass}} + \pi \cdot \frac{d^2_{\text{shell}} - d^2_{\text{glass}}}{4} \cdot \rho_{\text{shell}} + \pi \cdot \frac{d^2_{\text{skin, out}} - d^2_{\text{skin, in}}}{4} \cdot \rho_{\text{skin}} \tag{10.1}$$

with l_{skin} the mass in grams per meter, and the values for the constants repeated in Table 10.3 below. As PCL has an approximate density of 1.2 g/cm^3 [11] and PBS has an approximate density of 1.25 g/cm^3 [8], the mass and size analysis was continued with the highest value for the density, to avoid underestimating the final mass.

[5] URL: https://www.ace-extrusions.com/custom-plastic-pipe-tubing.html [Accessed: 18 June 2025]
[6] URL: https://www.siliconeproducts.eu/products/silicone-hoses [Accessed: 18 June 2025]
[7] URL: https://www.chembroad.com/pbsa-plastic-a-sustainable-and-biodegradable-alternative-to-traditional-plastics/ [Accessed: 18 June 2025]
[8] URL: https://pmc.ncbi.nlm.nih.gov/articles/PMC8963078/#sec6-polymers-14-00844 [Accessed: 18 June 2025]
[9] URL: https://www.degruyterbrill.com/document/doi/10.1515/psr-2020-0074/html [Accessed: 18 June 2025]
[10] URL: https://www.sciencedirect.com/science/article/pii/S0014305725003210 [Accessed: 18 June 2025]
[11] URL: https://www.polyfluor.nl/assets/files/datasheet-pcl-filament-uk.pdf [Accessed: 24 June 2025]

Table 10.3: Densities of materials

Description	Symbol	Value
Density of silica glass core	ρ_{glass}	2.2 g/cm^3 [11]
Density of acrylate shell coating	ρ_{shell}	1.18 g/cm^3 [11]
Density of outer sleeve material	ρ_{skin}	1.25 g/cm^3

As mentioned before, the length of the cable must be at least 1000 m. Therefore, the mass of the fiber optic cable including the sleeve is approximately 260 grams. The spool mass is taken from the Midterm Report [6] and is approximately 165 grams. Thus, the total mass of the reel is 425 grams.

To find the dimensions of the spool, again the starting values from the Midterm Report [6] were used, where the length and the outer diameter of the spool were cited to be 64 mm and 84 mm, respectively[13]. The inner diameter was estimated to be two centimeters smaller, therefore being 64 mm. A code was written to approximate the number of times the cable could be wound on the spool per length of the spool, to find the new spool diameter including the wound sleeve. Then, the initial length and inner diameter could be adjusted to fit the drone's dimensions, the height from the ground, and the clearance with the propellers, according to Chapter 7. Finally, the two centimeter clearance from inner to outer diameter was added again, and the final dimensions of the spool were found to be 0.15 m and 0.12 m for length and outer diameter, respectively.

To confirm the functionality of the sleeve, various experiments and tests have to be performed to ensure that the 1000 m of cable can be pulled out of the cave reliably. As explained before, the biodegradability of the two materials will have to be tested in an operational environment, where the temperature, humidity, and the microbiome of the cave will be mimicked [8].

Furthermore, the feasibility of the solution will be tested by creating a prototype and replicating the cave environment. For the first prototype, a FOC of at least 20 m should be tubed in a polymer with dimensions as specified above. For this first experiment, the polymer does not have to be biodegradable: this test serves solely as a proof-of-concept. The properties of the material used should however be similar to the biodegradable candidates. The prototype will be routed around obstacles like pillars at varying heights, to simulate the cave environment as shown previously in Figure 10.4. When both ends meet at the starting point, the FOC will be pulled out of the sleeve to evaluate the concept.

Below, the properties that should at least be measured in this experiment are listed:

1. Required pulling force to extract the cable
2. Maximum point load the sleeve can withstand without sustaining damage
3. Minimum achievable bending/turn radius of the sleeve
4. Elongation/strain of the sleeve
5. Twist in the sleeve

After the experiment, the cable as well as the sleeve should be inspected for damage. The sleeve should then be separately evaluated in tension, twisting, heating and point load tests, against an identical cable that was not subjected to the experiment, to ensure that its integrity has not been compromised.

The above tests should be conducted multiple times, to increase the confidence in the results. If the first sets of experiments are successful, the FOC length can be increased to 100 m, 500 m, and ultimately to the target of length 1000 m.

To retrieve the cable, it will be manually rewound to a spool outside of the cave. To speed up the reeling process, this spool will have a larger diameter than the spool that can be attached to the drone. The exact dimensions have to be determined at a later stage in the design. Since the cable needs to be wound upon the reel with machine precision, it cannot be wrapped on site and it can therefore not be re-used for the same mission once it is reeled off the spool. Thus, it is necessary to use a new, pre-manufactured reel for each drone operation inside the cave. However, if wound up correctly after each operation, stored safely and inspected for damage, the FOC could be re-sleeved and re-used for future missions. The production process of the fiber optic reel is discussed in Chapter 11.

Finally, recommendations for future are as follows. As mentioned before, the dimensions used for the sleeve of the fiber optic cable are restricted by market availability. However, if custom made solutions are available, the outer diameter and skin thickness could be decreased, decreasing size and mass of the reel. Additionally,

[12] URL: `https://www.matweb.com/search/datasheet.aspx?bassnum=01303&ckck=1` [Accessed: 18 June 2025]

[13] URL:`https://rb.gy/iqd275` [Accessed: 18 June 2025]

adding a sensor that checks the rate of reeling of the cable during operations could prove useful, in case of jamming of the cable. Moreover, to increase sustainability, options for the fiber optic cable retrieval can be combined. For example, for the FOC-in-sleeve, after retrieval of the inner cable, it can be attempted to pull out as much of the outer biodegradable sleeve as possible as well, so that site disturbance is even lower. The used sleeve can then be temporarily be stored and later composted in regulated conditions. Last but not least, it is recommended to investigate the other options to dispose of the fiber optic cable in the later stages of design. In case the experiments and tests with the FOC surrounded by a biodegradable sleeve fail, one should look into the shattering of the inner core of the FOC, or the drone itself retrieving the cable after each operation.

10.3. Payload

This section describes any logistics related to the payload during a mission. This includes physical constraints from gathering images needed to reconstruct the cave map, as well as mission logistics explaining how these images will be assembled post mission.

10.3.1. Cave Size Estimation

The total drone mapping time was calculated on the basis of small flank-margin caves [20] in the Caribbean area, as they are the most prominent, and from that research showed that typical cave sizes are as follows:

- Entrance height range: 0.5 to 2 m.
- Interior height range: 1 to 3 m.
- Interior width range: 3 to 10 m.
- Internal cave pockets can rise slightly but rarely exceed 3 m unless they are part of a larger cluster.

Since this type of cave forms on thin margins of a fresh-water lens, they tend to be larger in width rather than height [42]. Since we only have a requirement on distance from the entrance, we can ignore the horizontal extensity and focus on the vertical restriction.

On top of that, caves closer to the cliff face or with narrow development tend to have lower ceilings, so these values are on the higher end of what could be encountered. For example, smaller caves on the eastern and southern coastal terraces often feature an entrance with heights of 0.5 - 2 m and interiors with heights of 1.5 - 2.5 m. Figure 10.6 shows a top view of Cueva del Aleman, as well as some cross sections throughout the cave to illustrate typical cave sizes in the area of interest.

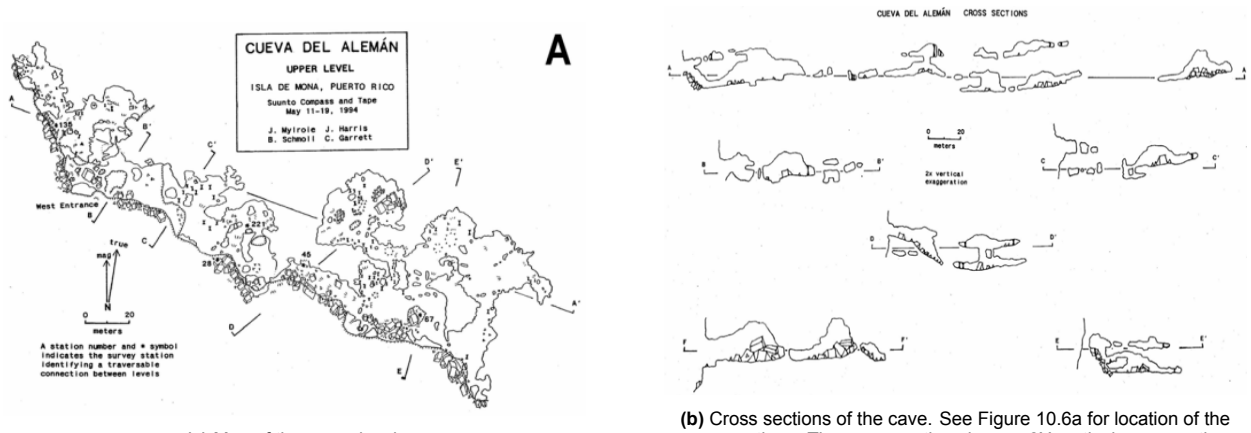

(a) Map of the upper level.

(b) Cross sections of the cave. See Figure 10.6a for location of the cross sections. The cross sections have a 2X vertical exaggeration.

Figure 10.6: Dimensions of Cueva Aleman, Isla de Mona, Puerto Rico [42].

With this analysis, and the primary stakeholder requirement:

> ***STK-DRN-1:*** *The system shall be able to fully map a cave system distance of up to 500 m from the entrance, within 1 week,*

it is safe to assume that the following areas need to be mapped:

Table 10.4: Cave surface areas to be mapped.

Surface	Area [m^2]
Walls x 2	500 x 3
Interior x 2	500 x 3
Ceiling	500 x 10
Ground	500 x 10

To cover all surfaces mentioned, a preliminary drone path visualization is illustrated below in Figure 10.7. In order to cover the whole surface, the drone flies back and forth, while changing its flight altitude (in case of wall mapping) or its position (in case of ceiling and ground). The exact numbers and calculations for these logistics are given in Subsection 10.3.2.

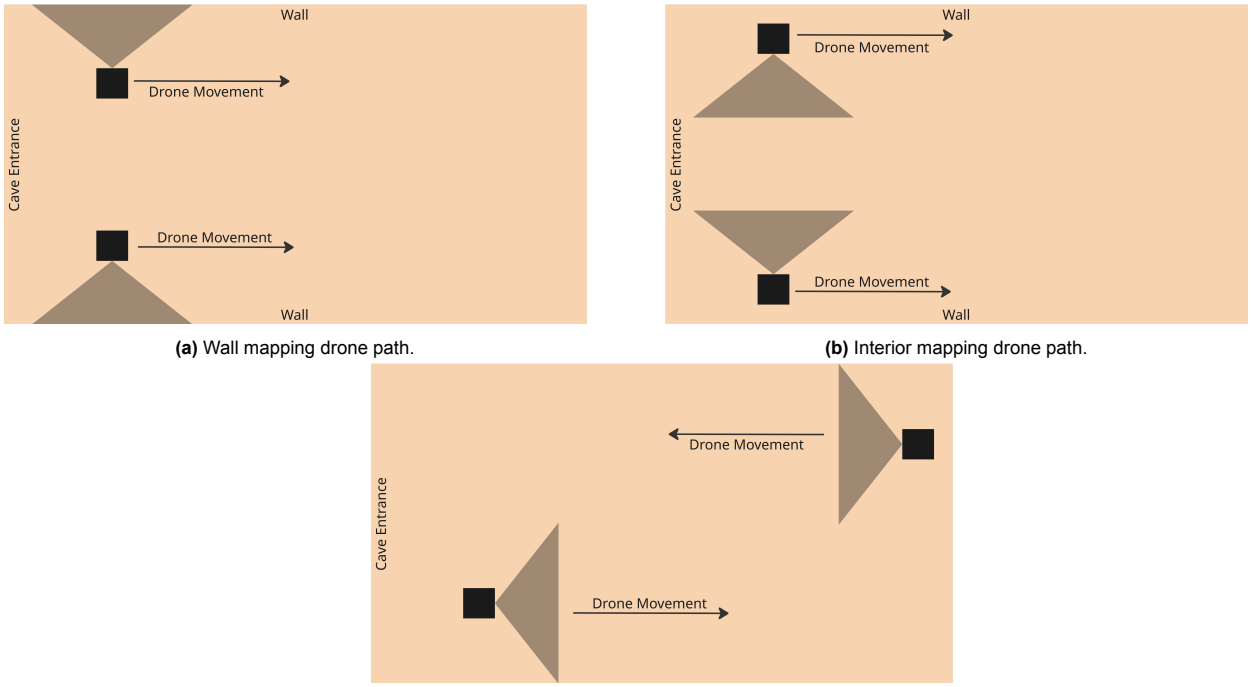

(a) Wall mapping drone path.

(b) Interior mapping drone path.

(c) Ceiling and floor drone path.

Figure 10.7: Top view of drone path visualization for mapping (not to scale).

Taking this information into account, the time needed for imaging is calculated as follows:

$$\text{time}_{\text{wall}} = \frac{\text{displacement}}{v_{\text{cov}} \cdot \text{rows}_w}, \qquad \text{time}_{\text{ceil}} = \frac{\text{displacement}}{v_{\text{cov}} \cdot \text{rows}_c} \tag{10.2}$$

Giving a total mapping time of 205 minutes for the highest mapping speed of 0.65 m/s. This calculation is expanded in order to cover the best-case and worst-case scenarios regarding the distance from the surface of the cave during mapping:

Table 10.5: Time to map the smallest possible cave estimated: 500 m (L) x 3 m (H) x 1 m (W), depending on distance from mapped surface.

Distance from Surface [m]	Corresponding Speed [m/s]	Time to Map [min]
5	0.652	77
1	0.131	1406

Table 10.6: Time to map the largest possible cave estimated: 500 m (L) x 10 m (H) x 3 m (W), depending on distance from mapped surface.

Distance from Surface [m]	Corresponding Speed [m/s]	Time to Map [min]
5	0.652	205
1	0.131	3837

With these calculations in mind, it is important to consider requirement MIS-DRN-1.2. The full cave system has to be mapped out within a 56 hour (equivalent to 3360 minutes) period from start to finish. As can be seen from the calculations, this requirements is met for all scenarios other than the instance where the drone is at a

distance of 1 meter from the cave in the 10m x 3m cave system. For this reason, throughout the operations it is key for the SpeleoDrone to keep the distance from the surface of the cave as close to 5 meters as possible.

It is also important to note the calculations and findings presented in the sensitivity analysis of the Flight Performance section, Section 7.4. It was found that a discrepancy of 10% in the mass or physical dimensions of the drone causes a change of 5% in the maximum attainable range of the drone. It is very important to note that the time to map the entire cave system depends on the endurance capabilities of the drone, and as such, it is very heavily affected by potential variations and differences in the attainable range. The longer the endurance of the drone, the longer the drone can map the cave during one mapping cycle.

10.3.2. Photogrammetry Reconstruction

A quick calculation shows that the number of images produced requires 12.2 TB of storage. After collating all images, the following steps are taken to reconstruct the cave map.

1. Image acquisition - 67% overlap to ensure atleast 3 images of any single cave feature, consistent lighting needed.
2. Camera calibration - pre-flight testing.
3. Feature detection and matching - algorithm based (SIFT, SURF, ORB).
4. Structure-from-motion (SFM) - computes camera's positions.
5. Dense reconstruction.
6. Meshing and texturing.

10.3.3. Field Clearance

In order to ensure that ceiling mapping is possible, some calculations are carried out to confirm that the drone structure does not hinder the payload's view.

First, the required angle is calculated using the following equation (chosen overlap is explained in Subsection 10.3.2):

$$\cos(\theta) \leq \frac{1}{1+(1-\text{overlap})} = \frac{1}{1+(1-0.67)}, \qquad \theta_{\min} = 41^\circ \tag{10.3}$$

This is the minimum angle needed to map the ceiling for future photo regeneration. Then, the actual angle between the payload normal and the propeller duct is calculated using trigonometry.

$$tan^{-1}\left(\frac{92}{104}\right) = 41.5^\circ \tag{10.4}$$

Since this angle is great than the minimum angle calculated previously, the payload is safe from the propellers. However, even if this margin is incorrect, future plans include noise removal from photos captured.

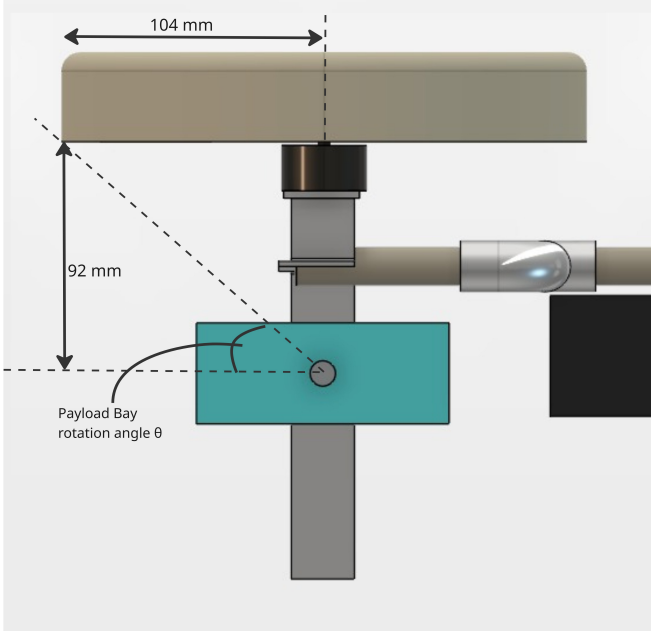

Figure 10.8: Payload Bay clearance angle

10.4. Power Generation

The drone is designed for a mission targeted at Isla de Mona, an uninhabited island in Puerto Rico. As no grid access is available there to charge the batteries and systems that allow the drone to operate, it was looked into what alternative power supply system would enable operation and battery charging.

One initial option considered was transporting a large pre-charged power bank to the island. However, this system would not comply with air transport requlations concerning battery transport, which permit only batteries with a capacity below 160 Wh to be brought on an airplane[14]. The larger batteries in the powerbank exceed this limit and therefore interfere with the stakeholder requirement STK-OPR-04 that makes transportability by air a obligatory aspect of the design.

Furthermore, various renewable energy options including charging stations on wind, wave, and solar energy were looked at. The target location was jugded to be suitable for solar panel use due to the significantly higher solar radiation at Isla de Mona compared to for example the Netherlands. On Isla de Mona this value lies on average around 5.8 kWh/m^2 per day, where at the Dutch coast this value is much lower: 2.7 kWh/m^2 per day[15]. Wind energy and wave energy were not looked into further, since they would require large systems to meet power demands, complicating the transport to the target location. Therefore, the option of a solar powered charging station was selected for the design.

For the design of the photovoltaic charging system, the following requirements were defined:

Table 10.7: Photovoltaic Charging System Requirements Definition

ID	Requirement	Parent
DRN-PG-01	The photovoltaic charging system shall not be heavier than 20 kg	STK-OPR-09
DRN-PG-02	The system shall be transportable within combined dimension of 158 cm (length + width + height)	STK-OPR-04
DRN-PG-03	The system shall be capable of simultaneously charging two 6s 7000 mAh batteries in 40 minutes, and one 1s 560 mAh and one 4S 350 mAh battery within 2 hours	MIS-OPR-10.3
DRN-PG-04	The system shall provide power to continuously charge a laptop and the NVIDIA Jetson Xavier NX computing module next to battery charging	MIS-OPR-10.3
DRN-PG-05	The system shall prevent batteries from overheating above 45 $^\circ C$ during charging and storage	MIS-DRN-1.5 & RSK-PP-003

Requirement DRN-PG-01 ensures the system is portable by the crew on site. DRN-PG-02 aligns with baggage regulations without extra costs on airplanes from KLM, used here as a reference airline[16]. DRN-PG-03 and DRN-PG-04 make sure sufficient energy is supplied to all systems needed on site. DRN-PG-05 stems from the charging temperature range specified for LiPo batteries[17].

A sizing method was established for the design process of the solar panel needed in the system. The following steps were taken to arrive at a preliminary solar panel design.

1. Compile data overview for components to be charged
2. Compile data for various solar cells
3. Compute how many cells needed in series and parallel and estimate size, weight and cost of the panel
4. Select best performer
5. Design cell layout for panel for operation and transportation

In Table 10.8 the components requiring power supply on site are listed together with their specifications. Since it was found that 2 separate solar panels would be needed to comply with the transport size constraint, the power requiring systems where split into two groups, each for one panel. This was done to end up at somewhat similar total power requirements for both panels. Two batteries are needed for one mission, during which 2 other batteries will be charging at the ground station, each at a different panel. Since the estimated time between the start of 2 missions is 40 min, the solar panel will be designed to charge a battery in 40 minutes as well, to have charged batteries available for the next mission. The flashlight used for imaging will also need charge, but due to their longer battery life (40 min - 1h), it was chosen to charge them less frequently, i.e., have a longer charging time of 2 hours. Lastly, the ground station laptop and Jetson module, a small embedded computer for

[14]URL: `https://www.faa.gov/hazmat/packsafe/lithium-batteries` [Accessed: 16 June 2025]
[15]URL: `https://solargis.com/resources/free-maps-and-gis-data` [Accessed: 16 June 2025]
[16]URL: `https://www.klm.nl/information/baggage/checked-baggage-allowance` [Accessed: 16 June 2025]
[17]URL: `https://www.lipobattery.us/understanding-the-importance-of-temperature-management-in-lipo-batteries/` [Accessed: 16 June 2025]

AI and data processing tasks[18], are continuously connected to the power supply system. This to ensure that if charging conditions not optimal the computer still has reserve battery charge left. For the specifications of the laptop, the mid-range model from the TU Delft Laptopproject was used as reference[19]. To maintain battery life and prevent damage, the batteries will only be discharged till 20% charge, and the charging itself will thus start from this percentage. To simplify manufacturing, only one type of panel will be produced. Since Panel 1 has slightly higher power requirements, the solar panels were sized accordingly.

Table 10.8: Electric specifications for all systems requiring charge from the solar panel charging system

Components		Voltage [V]	Current [A]	80% Capacity [Wh]	Charging time [min]	Charging power [W]
Panel 1	Main battery 1	22.2	8.5	124.3	40	188.4
	Laptop	20	3.3	-	cont.	65
	Total / max	*22.2*	*11.7*	-	-	*253.4*
Panel 2	Main battery 2	22.2	8.5	124.3	40	188.4
	Flashlight VIS	14.8	0.14	4.1	120	2.1
	Flashlight IR	3.7	0.22	1.7	120	0.83
	Jetson module	19	0.88	-	cont.	20
	Total / max	*22.2*	*9.7*	-	-	*211.3*

A monocrystalline silicon solar cell was selected due to its higher efficiency compared to polycrystalline silicon and thin film, which are other material commonly used for the production of PV cells. Higher performance cells such as GaAs cells are also available on the market and normally used in space applications. For the drone under design choosing such high-end solar cells does not fit within the budget[20]. Multiple commercially available monocrystalline silicon solar cells were compared with the main focus on their corresponding total cost and weight for the under design solar panel.

A solar panel consists of a certain number of cells in series to reach the required voltage, which form a string. Multiple of these strings are connected in parallel to increase the current the panel delivers [13]. The total voltage and current values from Table 10.8 were used together with the data from different solar cells, for estimating how many cell are needed in series and in parallel to deliver enough voltage and current. 20% contingency was added onto the required voltage and the numbers for required cells in series and parallel were rounded up. The FIT0601 solar cell from DFRobot[21] was selected as the most suitable for the solar panel design, when comparing cost and weight between the options. Table 10.9 provides a summary of the solar cell specifications and the corresponding panel design data.

Table 10.9: Specifications of selected solar cell and designed panel

Part	Cells in series	Cells in parallel	Avg. Voltage [V]	Avg. Current [I]	Max power [W]	Mass [kg]	Price [€]	Size [cm]
Cell	1	1	5	1	6	0.09	8	27.5x16x0.2
Panel	6	12	30	12	432	6.48	576	354.4x97.2x0.6

Two panels are needed to fulfill the total power generation required for all on site systems. These panels are designed in a foldable configuration to ensure air transport is possible. The 12 strings in each panel are separated into boards, thus each panel consist of 12 boards with 6 cells in series. The 12 boards are connected in parallel and mounted together with the use of hinges that allow for 180 °of motion when folding of the panel. As a whole, the panel can be extended and contracted in an accordion-like motion. This allows the whole panel to be folded within a footprint of 97.2x28.7 cm. This included hinges, estimated at 2 cm, and a 2 mm clearance per solar cell. A sketch of the solar panel design can be seen in Figure 10.9. For the structural integrity of the panel and mounting of the cells, a backing material is needed. A polyethylene panel[22] was selected, due to its UV-resistance, recyclability and appropriate temperature resistance. The panel thickness is chosen at 0.4 cm.

[18]URL: `https://www.nvidia.com/en-us/autonomous-machines/embedded-systems/jetson-xavier-series/` [Accessed: 16 June 2025]

[19]URL: `https://www.tudelft.nl/studenten/mijn-studie-ik/studietools/laptopproject/modellen-2024-2025` [Accessed: 16 June 2025]

[20]URL: `https://energyeducation.ca/encyclopedia/Types_of_photovoltaic_cells` [Accessed: 16 June 2025]

[21]URL: `https://www.digikey.nl/en/products/detail/dfrobot/FIT0601/9608218` [Accessed: 16 June 2025]

[22]URL: `https://www.s-polytec.nl/pe-platen-zwart.html` [Accessed: 16 June 2025]

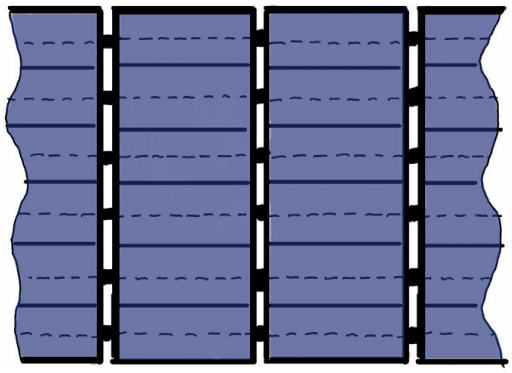

(a) Solar panel detailed view

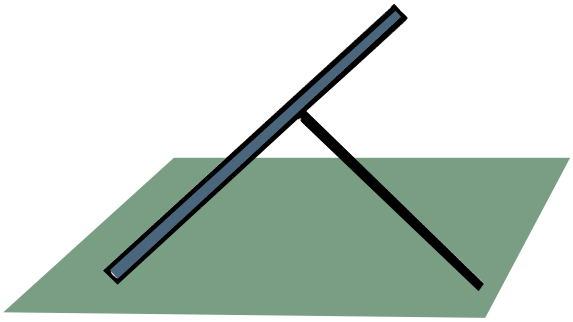

(b) Solar panel side view

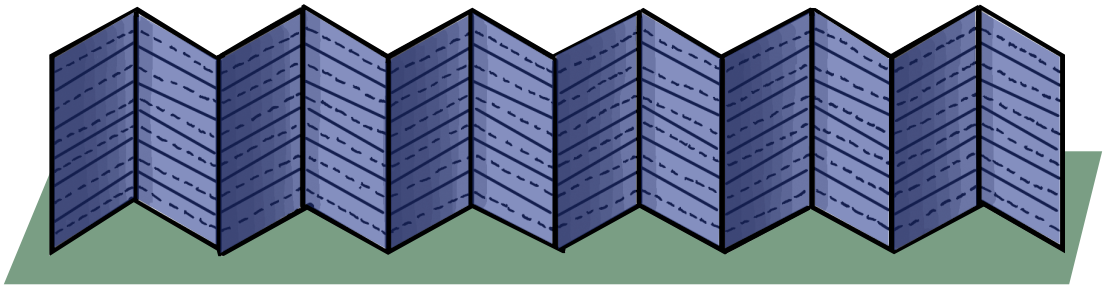

(c) Accordion-like folding of solar panel

Figure 10.9: Sketches of solar panel design for illustration purposes only

To estimate the depth of panel in folded stage, a space of 0.4 cm was assigned for potential protection material to prevent scratching between the panels. This results in a total estimate thickness of 12 x 1 cm = 12 cm, when folded. This 1 cm includes backing material and the solar cells next to the protective material. In total the length, width, and height add up to 137.9 cm, leaving 20 cm of room for air transport packaging and protection.

The solar charging system will also require additional components. Sicne this is a preliminary design, reference components are used to estimate cost. For the shunt diodes, blockage diodes, wiring, hinges and legs, their cost is estimate as 10% of the total cost. This is to be revised in a later stage of the project.

Table 10.10: Components of solar energy charging station

Component	**Function**	**Amount**	**Price [€]**
Cells	Energy supply	144	8
Backing material	Structural integrity and mounting	4	55
Maximum power point tracker[23]	Charge controller	1	92
Shunt diodes	Prevent open circuit failure	144	-
Blockage diodes	Prevent short circuit failure	12	-
Wiring, hinges, legs	Connection, folding and positioning	-	-
DC/AC converter[24]	Charge laptop	1	47
Total			1662

As mentioned earlier, the solar irradiation at Isla de Mona has a daily average of 5.8 kWh/m^2, meaning 5.8 peak sun hours per day. A peak sun hour is defined as the time where the solar intensity is equal to 1000 W/m^2. Since many solar cells are normally tested and rated at this intensity, it can be assumed that per day approximately 6 maximum power point charging hours will be available. Daily, 9 charging cycles of 40 minutes each for 2 batteries would be possible with the designed solar panel system. In the operational perspective, a limit of 8 mission per day was selected to ensure batteries can be charged for the next day. Also, 6 additional charged batteries will be brought to site, to allow for charge in non-optimal solar conditions or serve as reserves in case of battery failure. To comply with DRN-PG-05 that specifies overheating above 45 °C should be prevented, the system will include special LiPo battery storage and charging bags[23]. Also, a tarp will accompany the equipment to provide shade.

Looking ahead, the discussed solar energy charging system should be further developed in the future. The

[23]URL: `https://www.getfpv.com/batteries/battery-accessories/lumenier-lipo-safe-bag.html` [Accessed: 16 June 2025]

current panel is estimated to be able to meet the requirements, but a more detailed design could verify this and also allow for modifications when the panels under- or over-perfoms.

10.5. Ground Control Station

The Ground Control Station (GCS) serves as the central hub for human operators to monitor and control unmanned systems during missions. Designed with portability and flexibility in mind, the GCS integrates specialized hardware and software into a compact, laptop-based platform. This lightweight configuration ensures rapid deployment and ease of transportation, aligning with mission requirements that demand mobility and adaptability in diverse operational environments.

Hardware

To enable seamless communication between the SpeleoDrone and the laptop-based GCS, several critical components are required. The mission architecture is designed to offload computationally intensive tasks from the drone to a ground-based processing unit, ensuring the airborne system remains lightweight and power-efficient. A fiber optic cable (detailed in Section 10.2) transmits high-bandwidth optical data from the drone to the GCS. However, standard laptops lack support for optical signals, necessitating a media converter to bridge this gap. The converter transforms the optical signal into a USB-compatible data stream, enabling compatibility with the GCS hardware.

Given the need for real-time data processing and AI inference in resource-constrained environments, an NVIDIA Jetson Xavier NX module was selected as the ground-based computing unit. This high-performance embedded system excels in AI applications and handles the parsing, filtering, and preprocessing of raw sensor data from the drone. By centralizing these tasks on the ground, the system significantly reduces the computational burden on both the drone and the operator's laptop. To ensure stable operation under heavy workloads and varying environmental conditions, the Jetson module is equipped with active cooling[24]. This design choice eliminates the need for the drone to carry additional onboard processing hardware or larger batteries, preserving its maneuverability and flight endurance.

Finally, the processed data is relayed from the Jetson module to the operator's laptop, where the GCS interface displays real-time mission information. Further details on the GCS software and user interface are provided in the following section.

Software

The proposed ground control station interface, visualized in Figure 10.10, was designed with a user-centered philosophy. It adheres to standard aviation color codes [12] while prioritizing accessibility for operators unfamiliar with conventional systems. The interface integrates real-time data displays, visual representations and interactive controls to ensure efficient drone mission monitoring and management.

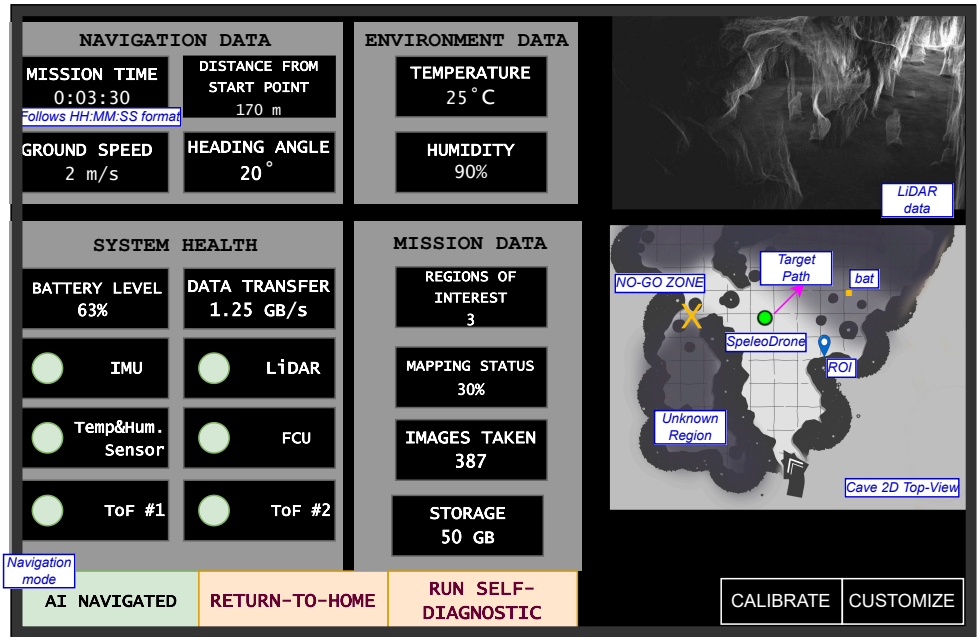

Figure 10.10: Ground Control Station Interface

[24] URL: `https://www.antratek.nl/heatsink-with-fan-for-jetson-xavier-nx-module` [Accessed: 14 June 2025]

The interface uses intuitive color conventions:

- **Red:** warnings requiring immediate action, e.g. critical battery level.
- **Amber:** cautionary alerts, e.g., no-go zones, battery 10% from critical.
- **White:** normal operation
- **Green:** active modes, e.g., AI Navigated
- **Magenta:** targets or selected items, e.g., target path.

Displayed data is grouped into four main categories: Navigation, System Health, Environmental, and Mission Data. Navigation Data displays critical flight metrics, like mission time or ground speed. System Health monitors vital components and includes status indicators for subsystems. Environment Data provides ambient conditions and it can alert the operator if temperatures approach the drone's maximum operating limit. Lastly, Mission Data presents the progress on the information collection.

On the right-hand side of the interface, visual displays provide situational awareness: a 2D top-down cave view and real-time LiDAR data. These update dynamically as the drone maps the cave topology. With onboard cameras and LiDAR, the drone detects obstacles (like bats), marks restricted "no-go" zones due to size constraints, and identifies Regions of Interest (ROIs) for later analysis. ROIs and their functionality was discussed in detail in Section 8.4. Operators can also see the path currently planned by the autonomous system and step in if intervention is needed.

While the interface is optimized for mid-flight decision-making, its interactive features allow operators to access deeper layers of information. For instance, clicking on "Regions of Interest" opens a detailed list including locations, confidence levels, and any collected data. Operators can command the system to revisit a specific ROI and re-collect data if necessary. At the bottom of the interface, several action buttons simplify control. In Figure 10.10, the drone is operating in "AI Navigated" mode (see Section 8.4 for more details), but this can be switched to "User Navigated" mode on the fly. Switching requires a secure transmitter connection and calibration, during which the AI Safety Feature keeps the drone hovering safely. Another key button, "Return-To-Home," immediately commands the drone to return to its starting position.

10.6. Transport

To make sure the system is safely transported to the site, appropriate protection and casing must be provided for all components; the drone, its batteries, and the solar panels. However, as can be expected, this is limited by airline regulations for baggage size and mass. The constraints set and considered are listed in Table 10.11 as per KLM regulations.

Table 10.11: Transport baggage limitations according to KLM [1].

Dimension	Regulatory Constraint
Size (Carry on)	55 cm x 35 cm x 25 cm
Mass (Carry on)	12 kg
Size (Check in)	L + W + H = 158 cm
Mass (Check in)	30 kg

The drone is packed in overhead cabins to ensure its safety and soft-handling throughout the trip, especially since multiple flight connections might be needed to get to the final site destination. So, a drone case chosen based on the maximum possible size allowed, this was the PeliProducts 1506 Air [28]. To protect the drone inside this case, compatible foam was chosen, namely the PeliProducts FUll 1506 Foam Set [29]. Specifications for the previous products are presented in the following table.

Table 10.12: Drone Case Specifications.

Specification	Value
External Dimensions [mm x mm x mm]	511 x 305 x 217
Internal Dimensions [mm x mm x mm]	475 x 239 x 198
Empty Weight [kg]	2.4
Weight with Foam [kg]	2.9

[27] URL: `https://www.klm.nl/en/information/baggage` [Accessed: 10 June 2025]

[28] URL: `https://peliproducts.co.uk/collections/cases/products/1506-air-case?_pos=3&_fid=08a72a26a&_ss=c` [Accessed: 13 June 2025]

[29] URL: `https://peliproducts.co.uk/products/full-1506-foam-set?_pos=2&_sid=0f245974c&_ss=r` [Accessed: 13 June 2025]

The internal dimensions of this case allow only for the drone body to be placed. So, the detachability of the noise ducts and propellers is taken advantage of here.

The batteries can only be packed 2 at a time according to air transport regulations [30] so ideally, each crew member would travel with a battery case to maximize the number of batteries available on site. This allows for an easy choice of battery casing, namely the Lumenier LiPo Safe Bag [31].

The solar panels which provide power to all drone batteries as well as any other battery-powered components should also be transported via air with the on-site team. However, due to the irregular package dimensions, it is difficult to find off-the-shelf packaging for such a component. So, a customized container is designed instead. Some features it should include are packaging materials and cushioning techniques to minimize shock and vibration, sturdy pallets, protective cushioning elements, cardboard/plastic sheets, and edge and corner protectors. This will be finalized in the next phase of the project, but will follow the structure outlined below:

- **Front Cover:** This is typically made of tempered glass and protects the photovoltaic cells from rough weather conditions while simultaneously allowing maximum light transmission. It should be impact resistant, scratch resistant, and UV stable.
- **Encapsulant:** This is usually produced from Ethylene Vinyl Acetate (EVA) or Polyolefin Elastomer (POE) and placed on front and back layers around cells to protect PV cells and maintain adhesion between glass, cells, and backsheet.
- **Backsheet:** A polymer-based sheet (PET, PVF, or a combination) needed to insulate and protect the panel's backside from moisture and UV radiation.
- **Frame:** The main structure (made of an aluminum alloy) which provides support, allows mounting, and protects edges. This is designed to be lightweight, corrosion-resistant, and most importantly, mechanically strong.
- **Junction Box:** A thermoplastic housing needed to store electrical connections and bypass diodes. The container should be weatherproof, heat-resistant, and UV stable.

10.7. Repairability

Part of repair analysis was carried out in Subsection 14.2.3, with the RAMS analysis, but some additional factors were addressed here. As discussed, making the drone repairable helps fulfill the sustainability goals and increases the probability of the success of the mission that is carried out by the archaeologists. Being able to address small issues on site was deemed an important part of the design and the plan for operations of the SpeleoDrone. In principle the repairs that can be carried out on site can be divided into two groups; mechanical and electrical repairs.

Starting with electrical repairs, as this is a smaller group, the archaeologists should be able to carry out small electrical repairs, such as replacing broken sensors or resoldering loose connections. Small soldering jobs can be carried out by almost anyone with relative ease, especially with the help of a wiring diagram (see Section 10.8). Additionally, backup batteries should be packed, such that if failure occurs, enough batteries are still present for the mission to be carried out successfully. Anything beyond these two types of failure cannot be reasonably repaired on site by non-technical personnel.

Mechanical repairs involve more cases. Replacement of a broken landing gear can be carried out by the team on-site. The landing gear itself is bolted into place, meaning the connection can be undone quickly and a new gear can be swapped in. Replacing one propeller can also be done with relative ease. The propeller is threaded onto the motor shaft and kept in place with a self-locking nut, meaning replacing it is also quite easy and doesn't require many tools. Any other replacement would be too involved to be carried out on site by non-qualified personnel.

Below is a list of tools and components required on site. This list is not yet complete and lacks numeric quantities. In the future the list of components can be expanded by conducting mock repairs with a prototype or a model of the drone, where the engineers can see what tools they need to carry out each repair. The amount of backup parts needed can be estimated by finding the probability of failure of singular components (for example the battery) and estimating how many failures are probable to occur throughout the duration of one expedition (so a week). Based on that number, the initial estimate for the quantity of backup components can be obtained and later adjusted based on the actual failure rates of different components in the field.

- Backup batteries

[30] URL: https://www.tsa.gov/travel/security-screening/whatcanibring/items/lithium-batteries-more-100-watt-hours [Accessed: 10 June 2025]

[31] URL: https://www.getfpv.com/batteries/battery-accessories/lumenier-lipo-safe-bag.html [Accessed: 10 June 2025]

- Backup wires
- Spare landing gear
- Bolts & nuts for the landing gear
- Self-locking nuts for propeller
- Spare propellers
- Soldering kit
- Set of wrenches
- Set of alan keys
- Small screwdrivers (for electronics)
- Multimeter

10.8. Operational User Manual

Operational user manual is a critical part of the finished product, as it outlines how the user should treat it and how to exploit it best to avoid failure. Below an initial list of things to be included in it can be found, containing a short description of each.

INTRODUCTION AND IMPORTANT INFORMATION OVERVIEW

- **System Description:** an introduction to the SpeleoDrone and an overview of all systems
- **Usage Conditions:** weather constraints, maximum mass that can be attached to the drone in case of changes in payload etc
- **Safety Warnings:** most important safety warnings, hazard information about LiPo batteries, user PPE and precautions
- **Transport:** how to pack the drone to avoid damage, permissions needed to transport by air etc

NOMINAL OPERATIONS

- **Ground station:** how to use the ground station, interface with the drone, explanation of the display
- **Pre-Flight Checks:** checklist of steps to be carried out and things to be checked before flight
- **Fiber Optic:** how to of the fiber optic cable, replacement guidelines, small troubleshooting sections etc
- **Charging:** how often to charge the batteries, charging conditions and voltage & power required

REPAIRS

- **Troubleshooting**: Most common issues found during operations and solutions for them
- **Common Repairs:** how to carry out repairs that were deemed to be needed often, such as replacing propellers or landing gear

MAINTENANCE

- **Recommended maintenance schedule:** recommended frequency of maintenance
- **Maintenance steps:** actions to be taken during maintenance sessions

DESIGN DETAILS

- **Wiring diagram:** wiring diagram of the drone to ease electronics repairs
- **Components specifications:** specifications for different components, for example battery discharge voltage or power draw required by the camera
- **Contact list for commercial parts:** contacts for commercial parts for further user support
- **End of Life Activities:** guidelines on disposal, recyclable parts and where to return them, how to utilize the batteries properly

11. Manufacturing, Assembly, Integration

The following chapter presents the manufacturing and assembly plans for the SpeleoDrone. These outline the steps and equipment needed to turn the SpeleoDrone design into a deliverable physical product. With the individual subsystems being designed and the individual components of the SpeleoDrone manufactured, in order for the drone to operate as intended, the subsystems need to be integrated accurately and in the correct order. For this reason, an Assembly Plan for the mechanical and electrical assemblies is created to provide the user with a detailed manual of how to proceed with the assembly of the drone.

11.1. Manufacturing Plan

This section outlines the manufacturing plan for the SpeleoDrone. All SpeleoDrone components that are not commercial off the shelf (COTS) products, have to be manufactured prior to assembly. This includes the composite frame beams, beam connections propeller ducts, and the bio-degradable fiber optic cover.

11.1.1. Composite Beams

As the cross-section of the composite beams is circular, filament-winding proves efficient. In filament winding, pre-impregnated (prepreg) unidirectional carbon fiber tape is deposited onto a rotating cylindrical mandrel. Currently, no ABS prepreg exists as a COTS solution, hence the appropriate tape has to be manufactured in-house. The composite beams have a total length of 638 mm, and can be manufactured as a continuous tube before being cut into the individual beams later on. A mechanical hacksaw is preferred for this to deliver perfectly straight cuts, although the beams could also be cut by hand depending on equipment available.

The production of unidirectional prepreg is commonly done through a process called wet impregnation, depicted below in Figure 11.1. In this process, unidirectional carbon fiber tape is guided through a bath of molten polymer, which acts as the composite matrix, before moving through a die where excess matrix is removed. The wet tape then cools, allowing the thermoplastic polymer matrix to cool as solidify, producing a thermoplastic prepreg tape. The cooled tape is then wound onto a reel for storage.

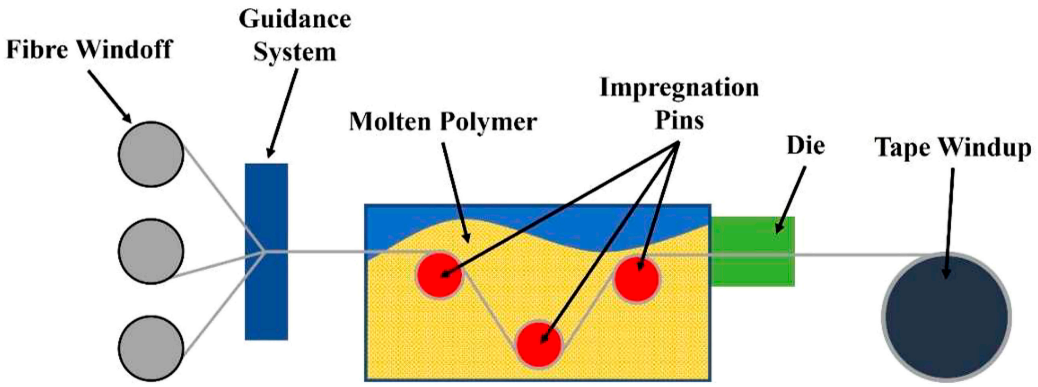

Figure 11.1: Wet Impregnation Manufacturing Process[1].

The design of the composite beams uses 100 g/m^2 plies for the three central 0° plies, and 50 g/m^2 plies for the outer +-45° plies. When filament winding is used, two 50 g/m^2 tape layers can be used in place of the 100 g/m^2 ply. However, no 50 g/m^2 unidirectional carbon fiber tape was found. Instead, 65 g/m^2 unidirectional tape[2] with a width of 25 mm comes closest to what is needed. To find the length of 65 g/m^2 unidirectional tape needed to manufacture the 638 mm composite tube, of diameter 1.5 cm, Equation 11.1 was first used to find the surface area of the tube:

$$S = l \cdot (2 \cdot \pi \cdot r) = 0.638 \cdot (2 \cdot \pi \cdot 0.0075) = 0.03m^2 \tag{11.1}$$

With a tube surface area obtained, Equation 11.2 was then used to find the length of unidirectional tape required. The circumferential area of the continuous beam was multiplied by 10 to get the total ply area. An additional

[1]URL: https://journals.sagepub.com/cms/10.1177/00219983221083841/asset/558eb562-f97d-4845-97aa-dcd95e9c980e/assets/images/large/10.1177_00219983221083841-fig1.jpg [Accessed: 18 June 2025]

[2]URL: https://gernitex.com/product/unidirectional-carbon-fiber-tape/ [Accessed: 18 June 2025]

factor n_{plies} was used to represent how much of the tape overlaps with other tape layers of same orientation. This factor being taken to be 1.5 to remain conservative. The resulting length of tape was rounded up to the nearest meter, as carbon fiber tape can only be purchased in meters.

$$l_{tape} = \frac{S \cdot n_{plies}}{w_{tape}} \cdot overlap = \frac{0.03 \cdot 10}{0.025} \cdot 1.5 = 15m \tag{11.2}$$

To find the mass of ABS needed for the manufacture of the prepreg tape , the mass of the entire continuous composite beam was calculated using Equation 11.3 and Equation 11.4:

$$V_{composite} = l \cdot (2 \cdot \pi \cdot r) \cdot t = 0.638 \cdot (2 \cdot \pi \cdot 0.0075) \cdot 0.00075 = 0.0000225m^3 \tag{11.3}$$

$$m_{composite} = V_{composite} \cdot \rho_{composite} = 0.0000225m^3 \cdot 1335kg/m^3 = 0.030kg \tag{11.4}$$

Since the mass fraction, FVF, of the matrix was 0.5 with respect to the entire composite laminate, 15 grams of ABS will be used in the composite tube. However, significantly more ABS than this is required for the resin bath during the manufacturing process for the unidirectional prepreg tape, as excess ABS is ”pressed” out of the impregnated tape by rollers.

This need for excess ABS proves of little inconvenience, as ABS can only be bought per kilo due to its cheap price and it is preferred to buy the ABS in filament spools used for 3D printing, as this filament can either be melted directly in the matrix bath or be used to 3D print various cosmetic components and lightly-loaded housing brackets for the SpeleoDrone.

11.1.2. Beam Connections

Two types of connections are used in SpeleoDrone to connect the composite beams: the elbow-shape connector and the T-shape connector. Both connectors consist of a solid piece of AZ31B magnesium alloy.

Two manufacturing methods are commonly used for manufacturing metal products: machining and casting. Machining proves beneficial when a low volume of parts has to be manufactured, as is the case with the SpeleoDrone. This is because machining equipment, such as CNC mills, is relatively widely available and has few to no tooling costs. However, casting allows for the manufacture of more complex shapes and allows for little material to be wasted, in comparison to machining which is a subtractive process. These advantages and disadvantages of each manufacturing process are presented in Table 11.1 below, with green representing positive aspects and red negative.

Table 11.1: Comparison of Machining and Casting Processes

Factor	Machining	Casting
Tooling Cost	Low to none	High
Part Complexity	Limited	High
Material Waste	High, recycling waste back into production cycle not an option at low production volume.	Very low, almost all material reaches mold.

The straight edges of the T-shape connector make it a good fit for CNC machining. For the elbow-shape connector, either process could be used. Casting would be a relatively straightforward process, while machining would first require the manufacture of a straight ”pipe”, with a profile characteristic of the elbow-shape connector thicknesses, using a CNC machine. This straight pipe would then have to be bent into the 90 degree elbow shape desired. Despite this more complicated process, as a CNC machine is already used for the T-shape connector, machining was chosen to manufacture the elbow-shape connector to reduce costs.

11.1.3. Propeller Ducts

The propeller ducts are solid pieces of styrodur (XPS) foam, and would be best cut using a hot wire CNC foam cutter. This would be done out of solid blocks of XPS, which can be purchased[3] in thicknesses of 100mm.

The ducts have a diameter of 208mm, and are placed side-by-side at both the front and back rotors. Hence, a block of 250 mm width by 500 mm length could easily be used to manufacture each ”pair” of ducts as a

[3]URL: `https://www.easycomposites.co.uk/xps-extruded-polystyrene-foam` [Accessed: 14 June 2025]

continuous structure. If the CNC comes with product size constraints, or the SpeleoDrone comes with travel size constraints, the ducts could be manufactured individually and then glued together at their intersection.

11.1.4. Motor, Payload and Landing Gear Mounts

In addition to the elbow and t-shaped connectors, there are three more connective structures present. These are the motor mounts, the landing gear mounts, and the landing gear mounts with an integrated payload interface. These structures clamp onto the composite beams, and are all hollow structures that are made out of AZ31B magnesium alloy.

Since these structures are hollow, welding thin plates together would be the only way of manufacturing them, despite being a very time-consuming process. Additive manufacturing would be much more convenient, however metal manufacturing is restrictively expensive for metals. This motivates switching the material used for these connective structures from AZ31B to for example PEEK, a 3D printable stiff thermoplastic.

11.1.5. Fiber Optic Cover Tubing

This subsection preliminarily outlines the production process of the fiber optic cable and its skin. As discussed in Section 10.2, 56 readily wound spools will be necessary in order to complete a single, week long mission. Therefore, the same production process will be repeated many times, which makes it more efficient and cheaper.

An extrusion process for polymer tubing will be used to construct the sleeve for the fiber optic cable[4]. At the same rate as the extrusion, the fiber optic cable will be pulled through the extruding sleeve.

11.2. Assembly Plan

The assembly plan of the drone outlines all the steps that need to be taken to assemble the individual parts into the final end-product. The assembly plan of the SpeleoDrone is divided into 2 sections: Mechanical assembly and Electrical assembly. As the names suggest, the mechanical assembly section focuses on the assembly of the physical components which make up the drone, whilst the electrical assembly focuses on the set-up and assembly of the electrical components such as wiring and sensor integration. the flow diagrams for these 2 processes can be found below.

[4] URL: `https://www.ace-extrusions.com/custom-plastic-pipe-tubing.html` [Accessed: 18 June 2025]

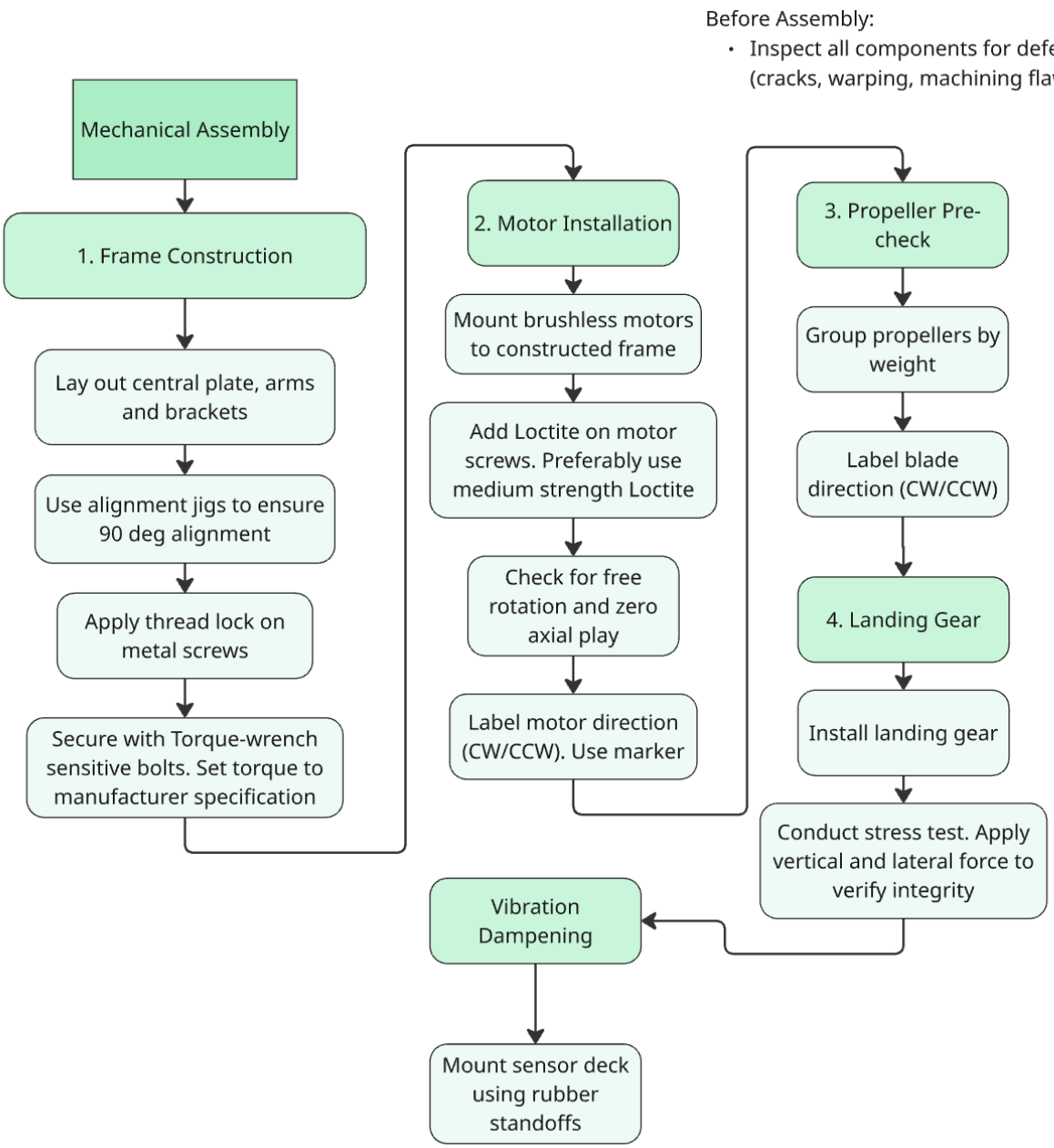

Figure 11.2: Mechanical Assembly Plan

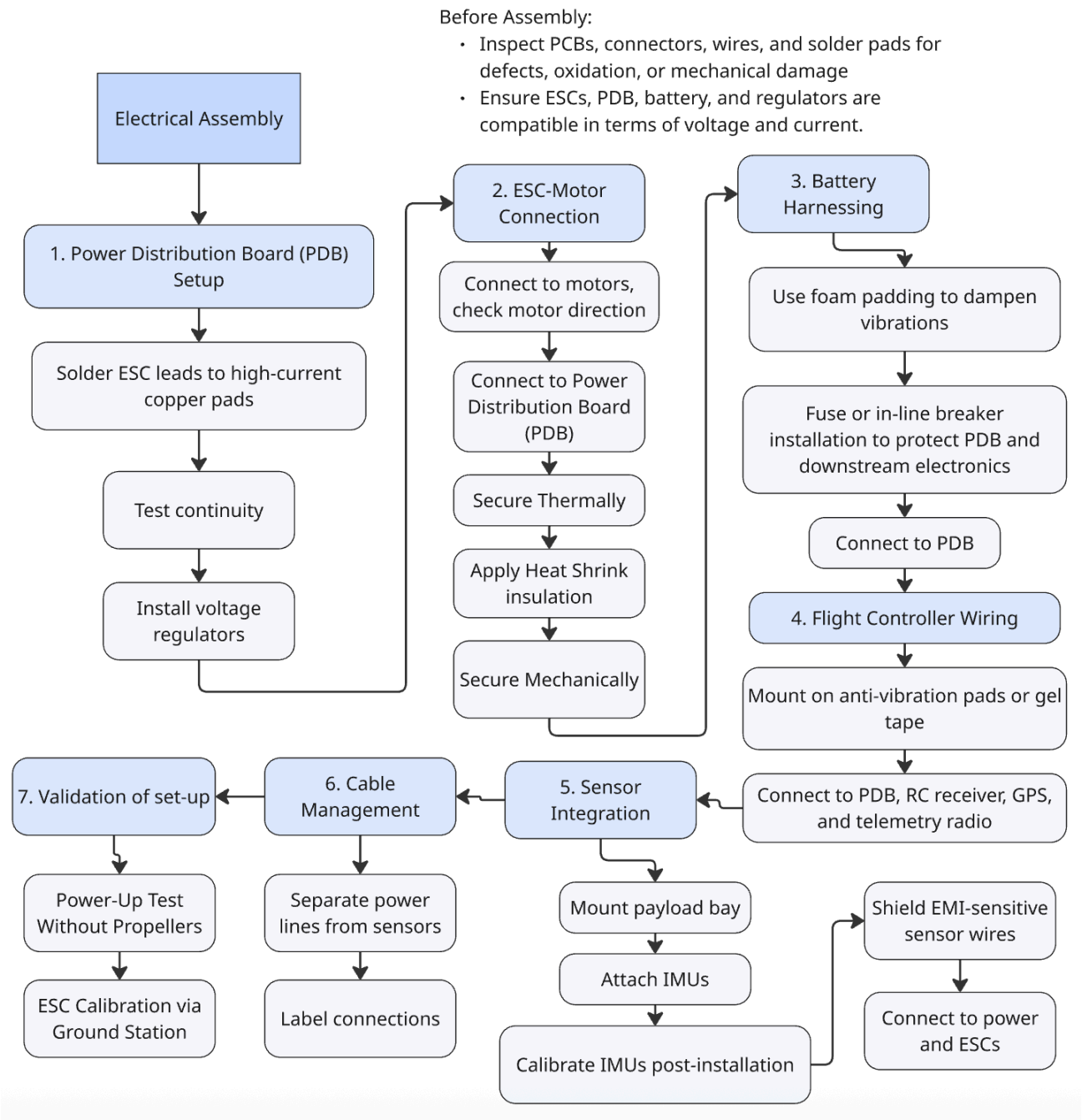

Figure 11.3: Electrical Assembly Plan

12. Life Cycle Assessment

This chapter will expend on the sustainability strategy implemented in the design. The end-of-life phase will be discussed in more detail with regard to recycling in Section 12.1. Also, the performed Life Cycle Assessment will be presented in Section 12.2.

12.1. End of Life

At end of life, at least 75% of the drone's total weight must be recyclable. Component selection was made with this requirement in mind. The drone structure is composed of magnesium alloy AZ31B, ABS, and carbon fiber-reinforced ABS—all materials recyclable through industrial or specialized recycling firms. While such firms typically do not process small-scale items individually, a potential SpeleoDrone company would implement a take-back system to collect drones in bulk for proper recycling. Alternatively, users may utilize services like Droneoptix[1], which offer free drone recycling and reuse of viable components. Solar panels can be dropped off at municipal recycling centers in the Netherlands[2], where they are processed by Stichting OPEN[3]. Similarly, ground station electronics can be recycled via Stichting OPEN, and casings through municipal waste centers[4]. The tarp is suitable for textile recycling or reuse[5]. The only non-recyclable component is the 170-gram LiPo safe bag, which is reusable but cannot be recycled through standard systems. Overall, the system meets the 75% recyclability requirement by weight.

12.2. Life Cycle Assessment

A Life Cycle Assessment (LCA) was performed to better understand emissions across the drone's life cycle phases. The Eco Audit Tool of the material database software Granta EduPack was used. This tool compiles so-called Eco Audits, which are bar charts that show, per life cycle phase, how much energy and CO_2 are consumed and emitted. The phases included are material production, product manufacturing, transport, product use, and disposal [3]. The tool expresses emissions in kilograms of CO_2 equivalent, accounting for emissions of various greenhouse gases [2]. Since various simplifications are made when using this tool, the software is used to get a rough assessment of the energy and CO_2 related to the whole life cycle of the designed product, but not a detailed analysis.

In the applied software, the user has to input the mass, material, and production method of all elements of the product, together with the choice of transport and end-of-life solution. The tool will extract the material's embodied energy and CO_2 footprint, together with information about the other phases from its database, and compile the Eco Audits. The inputs used for compiling Eco Audits for the drone under design are specified in Table 12.1. Here, only the structural components of the drone were considered, since all other components are mainly off-the-shelf, which limits the information available on the materials and manufacturing methods used. In the analysis presented, it was assumed that all materials used were 100% recyclable as defined by requirement **DRN-STRC-10**, except for the composite tubes, which, because of their selected material, can only be downcycled. For some manufacturing methods, the exact method was not available in the software, and thus, the most similar option was selected for the input of primary processes. The same goes for material types that were not available.

Table 12.1: Input parameters for LCA

Component name	Quantity	Material	Mass [kg]	Primary process	End-of-life
Motor mount	4	AZ31B	0.015	Roll forming	Recycle
Landing gear	4	AZ31B	0.039	Roll forming	Recycle
T connector	2	AZ31B	0.018	Extrusion	Recycle
Elbow connector	2	AZ31B	0.019	Extrusion	Recycle
Composite tubes	1	ABS w/ 40% carbon fibre	0.030	Extrusion	Downcycle
Duct	4	PS foam	0.080	Extrusion	Recycle

Other inputs include ones for joining and finishing, transport, and use of the product. Electric welding was done for the landing gear and motor mounts, which was estimated to span 2.8 m in total from the dimensions of the components. For transport, a conservative scenario was considered where the manufactured product is

[1] URL: https://www.droneoptix.repair/recycle-your-drone/ [Accessed: 17 June 2025]
[2] URL: https://tinyurl.com/3z9xamax (www.milieucentraal.nl) [Accessed: 17 June 2025]
[3] URL: https://www.stichting-open.org/2024/06/14/recyclen-van-end-of-live-zonnepanelen/ [Accessed: 17 June 2025]
[4] URL: https://tinyurl.com/2mmkcr6f (www.iamexpat.nl) [Accessed: 17 June 2025]
[5] URL: https://tinyurl.com/4rnevzzn (www.government.nl) [Accessed: 17 June 2025]

transported to the user over a distance of 7500 km by airplane, comparable to the distance between Asia and Europe. Also, the use phase covers energy during operation and includes transport from the user's location to the mission site. The end-of-life phase shows potential CO_2 savings from recycling materials after use.

Emissions and energy use are strongly related, as energy consumption is the main cause of CO_2 emissions. A significant part of the energy used globally is generated by burning fossil fuels, which produces greenhouse gas emissions [36]. For all Eco Audits compiled in this LCA, the graphs depicting energy use and CO_2 emissions showed similar trends, as expected due to their correlation. Since the designed system uses only solar energy during operation, which does not lead to CO_2 emissions as, for example, fossil fuel combustion does, the only major difference between the energy use and emissions appeared in the use phase. Since the difference was solely caused by the use of a renewable energy source that does not directly impact the system's environmental footprint, only CO_2 emissions were looked at in this chapter.

First, a scenario was considered where the transportation related to the use phase was only done once, i.e. back and forth to the mission site. This scenario is referred to as 'Case A'. Since the structure of the product is designed to sustain at least ten mission periods of 7 days, it was also looked at what the impact would be considering all of these missions and the transportation needed to and from these sites, assuming they are independent events. This scenario is referred to as 'Case B'. How these two considered scenarios compare can be seen in Figure 12.1a. Here, it is evident that the use phase has a dominant contribution to the total equivalent-CO_2 emissions when all ten missions are accounted for (Case B), due to the significant increase in air transport. This relatively high level can be reduced in trivial ways by simply choosing a different mode of transport or going to a mission site closer to home. It could also be possible to cluster far-away missions at sites that are close together, minimizing the number of times long-distance air transport is needed. For the rest of this analysis, it is most interesting to look at the Eco Audit considering only one mission (Case A), since this highlights the inter-phase differences more.

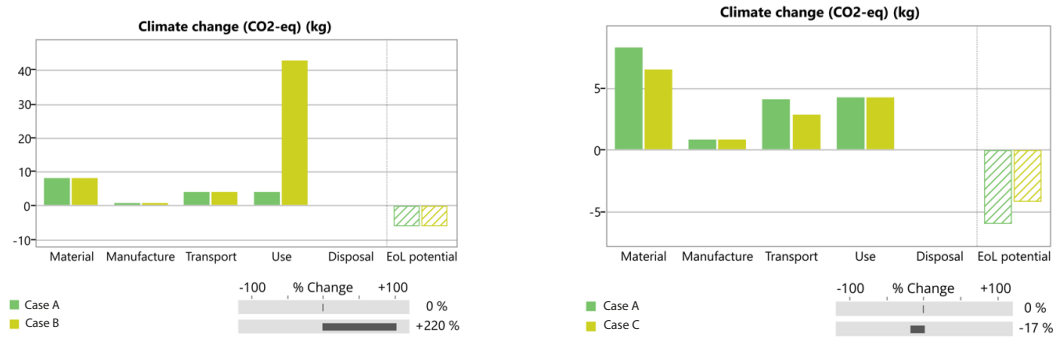

(a) Varying mission count **(b)** Recycling and transportation implementations

Figure 12.1: Comparison of Eco Audits

Case A, the conservative one-mission scenario in Figure 12.1a, was examined in more detail to establish the main contributing factors for each phase. It was found that in the material phase, the magnesium alloy used in the landing gear and motor mounts had the highest contribution to the emissions. For the manufacturing phase, the polymer extrusion used for manufacturing the ducts and the electric welding used for the landing gear and motor mounts contributed the most.

A second comparison was made between Case A from Figure 12.1a and a scenario where improvements were integrated to achieve lower emissions, referred to as 'Case C'. These improvements include using recycled material, whereas in Case A, new materials were selected. Additionally, a more environmentally friendly type of transport, such as a small truck, was selected for the transport between the manufacturer and client. How Case A and C compare can be seen in Figure 12.1b. Both implemented measures decreased the equivalent CO_2, as was expected, and are therefore important factors to consider in later design stages. Another measure that could be implemented to improve the carbon footprint is exploring other low-emission material choices.

The two scenarios covered in Figure 12.1b, Case A and C, have a total CO_2 emission of 17.5 kg and 14.5 kg, respectively, when only one mission is considered. This compares to the emissions of traveling 150 km by an average passenger car, which is approximately 16 kg CO_2[6]. In general, the CO_2 emissions of the life cycle of the structural components are relatively low due to their low weight and the exclusion of all other components integrated into the drone system, such as batteries, motors, payload, and other electronics in this analysis. Therefore, the total carbon footprint of the complete drone life cycle would be significantly higher. For the future project stages, it would be interesting to perform an LCA for all components, including the off-the-shelf ones, to gain insight into a more complete picture. This could then be used for establishing what phases contributed most to the overall carbon footprint of the system and what design changes have the largest beneficial impact.

[6]URL `https://www.eea.europa.eu/en/analysis/indicators/co2-performance-of-new-passenger` [Accessed: 24 June 2025]

13. Cost Analysis

This chapter presents a comprehensive cost analysis of the SpeleoDrone system, outlining the financial considerations related to its development, production, and operation. The objective is to assess the economic feasibility of the design. Section 13.1 details the cost breakdown, categorizing the expenses and explaining the methodology used to derive them. Subsequently, Section 13.2 establishes and justifies the purchase price, enabling a calculation of the expected return on investment.

13.1. Cost Breakdown

This section outlines the total cost of the SpeleoDrone project. A high-level overview is presented in Figure 13.1. The total cost was divided into three main categories: Research and Development Costs, Subsystem Costs, and Operational Costs. Since Subsystem and Operational Costs are primarily based on Commercial Off-The-Shelf (COTS) components, they could be calculated with reasonable accuracy and are detailed in Table 13.1 and Table 13.2, respectively. Development costs were estimated using methods presented in the literature [17].

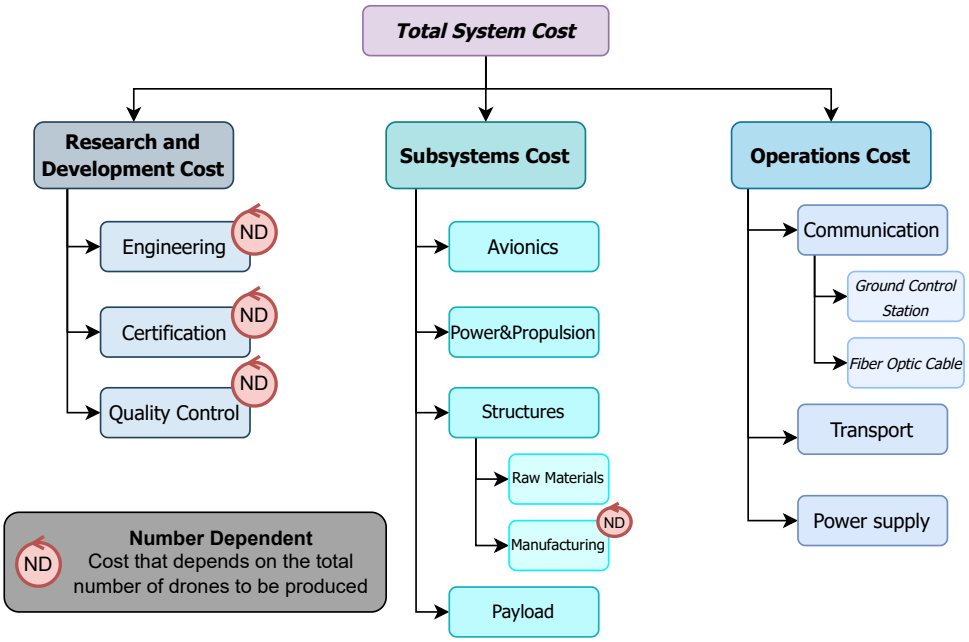

Figure 13.1: Cost Breakdown Diagram

13.1.1. Development costs

Engineering

The total engineering man-hours required for the design and RDT&E (Research, Development, Testing, and Evaluation) phases were estimated using the following empirical relation:

$$H_{ENG} = 10 \cdot 26 \text{ [days]} \cdot 8 \text{ [hrs/day]} \cdot N^{0.183} \tag{13.1}$$

In Equation 13.1, the factor of 10 corresponds to the number of engineers involved in the design effort, each contributing 8 hours of work per day. The total project duration was approximated as 26 full working days, based on the available design time while excluding non-engineering commitments such as review preparation, lectures, and miscellaneous delays (e.g., illness or technical issues like internet outages). The exponent term $N^{0.183}$ is derived from the Eastlake cost model [17], which captures the nonlinear relationship between engineering effort and the number of units produced. This reflects the pattern, where the engineering effort does not scale linearly with production quantity due to design reuse and process streamlining.

To estimate the cost of engineering labor, the average hourly labor cost within the European Union for the year 2024 was used, which stood at € 33.30 for the “Professional, Scientific, and Technical Activities” sector (NACE

Rev. 2 category M) [18]. This value was sourced from Eurostat [1]. To reflect inflation from 2024 to 2025, a Consumer Price Index (CPI) adjustment factor of 1.01 was applied[2].

Manufacturing, Certification and Quality Control

Costs for manufacturing, certification and quality control were calculated u an adapted Eastlake cost model [17]. Although originally intended for manned aircraft, the parametric nature of the Eastlake model allows for scaling down to smaller systems such as drones. The nonlinear exponents in the equations inherently accommodate size reductions, and drone-specific simplifications were made—for example, neglecting factors such as pressurization and control surfaces like flaps.

Firstly, the cost of tooling was found using Equation 13.2, which calculates the man-hours required to design and build tools, fixtures, jigs, molds, etc., and Equation 13.3

$$H_{TOOL} = 1.0032 \cdot W_{\text{airframe}}^{0.764} \cdot V_H^{0.899} \cdot N^{0.178} \cdot Q_m^{0.066} \quad (13.2) \qquad C_{\text{TOOL}} = 2.0969 \cdot H_{\text{TOOL}} \cdot R_{\text{TOOL}} \cdot \text{CPI}_{2012}^{2025} \quad (13.3)$$

$W_{airframe}$ is the weight of the system's structure in pounds, V_H is the maximum level airspeed in knots, N is the number of planned systems to be produced over a 5-year period, CPI_{2012}^{2025} is the adjustment factor for inflation relative to 2012 and R_{TOOL} represents rate of tooling labor in $/hour and Q_m is estimated production rate in number of aircraft per month over 5 years ($= N/60$). The manufacturing cost was computed similarly, with the change of R_{MFG} being the rate of manufacturing labor in $ per hour. The hours and cost were calculated using Equation 13.4 and Equation 13.5, respectively.

$$H_{MFG} = 9.6613 \cdot W_{\text{airframe}}^{0.74} \cdot V_H^{0.543} \cdot N^{0.524} \quad (13.4) \qquad C_{MFG} = 2.0969 \cdot H_{MFG} \cdot R_{MFG} \cdot CPI_{2012}^{2025} \quad (13.5)$$

Additionally, quality control costs during manufacturing-covering personnel and equipment to ensure compliance with standards - were included, as defined in Equation 13.6.

$$C_{QC} = 0.13 \cdot C_{MFG} \quad (13.6)$$

Certification costs, including the development of prototypes and associated flight-testing programs, were estimated using Equation 13.7.

$$C_{FT} = 0.009646 \cdot W_{\text{airframe}}^{1.16} \cdot V_H^{1.3718} \cdot N_P^{1.281} \cdot \text{CPI}_{2012}^{2025} \quad (13.7)$$

In the equation above, N_p is number of prototypes to be produced.

Labor costs were sourced from literature [17]: $61/hr for tooling, and $53/hr for manufacturing. These were adjusted for inflation using a CPI factor of 1.42[3] to reflect changes from 2012 to 2025. All development and manufacturing costs were calculated in U.S. dollars and then converted to euros using an exchange rate of 0.86 EUR/USD[4], based on current market data verified through Revolut. The airframe mass was extracted from the CAD model as 398.75 grams, and the maximum velocity (V_H) was identified as 29.8 m/s, as outlined in Chapter 7.

The cost of flight testing is inherently dependent on the number of prototypes. Since the system is largely composed of COTS components, it benefits from a relatively high Technology Readiness Level (TRL). Therefore, a conservative estimate of five prototypes was adopted. While evaluating certification cost, it was observed that due to the very low scaling factor in Equation 13.7 (0.009646), the final certification cost was almost negligible in comparison to the total project cost. Nevertheless, it has been included in the model for completeness and transparency.

Autonomy

One of the key factors affecting the cost of drone systems is the level of autonomy they are designed to operate with. In Midterm report[6], the safety factors to account for increased complexity depending on level of autonomy were derived based on the Advanced Mission Cost Model (AMCM)[5]. As the chosen level of autonomy corresponds to Level 3[48], the total cost excluding the cost of COTS components and materials, is multiplied by **1.5**. This accounts for the costs related to designing, training and validating AI, data acquisition, integration of AI with computer vision and certification.

[1] URL: https://ec.europa.eu/eurostat/statistics-explained/index.php?title=Hourly_labour_costs [Accessed: 22 June 2025]

[2] URL: https://www.in2013dollars.com/europe/inflation/2024?amount=1 [Accessed: 22 June 2025]

[3] URL: https://www.bls.gov/data/inflation_calculator.htm [Accessed: 15 May 2025]

[4] URL: https://www.revolut.com/currency-converter/convert-usd-to-eur-exchange-rate/ [Accessed: 18 June 2025]

[5] URL: https://www.globalsecurity.org/military/intro/reference/calc/AMCM.htm [Accessed: 15 May 2025]

13.1.2. COTS components

Costs for all COTS components were determined using market prices and then converted to euros. When prices were originally provided in U.S. dollars, the conversion rate of 0.86 EUR/USD was used. For components priced in British pounds, a conversion rate of 1.16 EUR/GBP - based on rates from Revolut bank - was used.

The subsystem-level cost breakdown, including details for Avionics, Power & Propulsion, Payload, and Structural Materials, is presented in Table 13.1. Each subsystem's total cost was computed by summing its individual COTS components. Additional technical specifications and context for these subsystems can be found in Chapter 9 (Avionics and Battery), Chapter 7 (Motors and Propellers), Chapter 5 (Payload), Chapter 6 (Materials).

Table 13.1: Subsystem Cost breakdown

Component	Product	Unit Cost [€]	Total Cost [€]
Avionics			**771.48**
Main IMU	*MicroStrain 3DM-CV5-IMU*	476	476
Redundant IMU	*Adafruit 9-DOF Absolute Orientation IMU Fusion Breakout - BNO055*	30.06	30.06
ToF sensor	*TFmini S LiDAR module - Short-Range ToF LIDAR Range Finder*	39	78
Buck Converter	*LTM8083*	20	40
ESC	*T-Motor F45A V2 4in1 ESC (3-6S)*	64.42	62.42
Temp&Hum Sensor	*HDC302x*	3	3
LDO	*ADM7160ACPZN3.3-R7*	3	3
Remote ID	*BlueMark DB152FPV RemoteID Module*	60	60
GPS	*Flywoo GOKU GM10 Nano V3.1 GPS Module*	17	17
Buzzer	*AT-2440-TWT-R*	2	2
Power & Propulsion			**1982.29**
Battery	*Spektrum 22.2V 7000mAh 6S 30C Smart G2 LiPo battery with IC5 connector*	190	1900
Motor	*EMAX ECO II Series 2807 Motor 1300kV*	18.57	74.29
Propellers	*HQProp 7x3.5x3 Propellers (4 stuks)*	4	8
Payload			**1473.53**
Camera	*Alvium 1800 C-320 VSWIR*[3]	517.91	517.91
Lens	*Kowa LM5NCL*	159	318
Infrared Flashlight	*D3060 IR Light*	76.89	230.67
Visible Light Flashlight	*Mini 5 / Avata & Avata 2 Tactical Light*	171.95	171.95
LiDAR	*Hesai ATX*[4]	190	190
Microchip	*Adafruit Controller Board for DRV2605L for Haptic Motor*	9	45
Structure			**60.04**
Styrofoam	*EasyComposites XPS Extruded Polystyrene Foam (Styrofoam) 100mm*	25.73	25.73
Unidirectional carbon fiber tape	*UD-25-T700-66 (cost of unit given per meter*	0.37	4.81
ABS	*AC Products Polymaker PolyLite ABS Filament Black 1.75mm 1Kg*	29.5	29.5

The last category to be considered is the operational cost, which further detailed can be found in Chapter 10.

The cost of the fiber optic cable with spool is discussed below. Since a custom made spool with a fiber optic

[6] Information obtained by contacting company

cable of 1000 m will be used for the mission, which is not readily available on the market. Therefore, the price of a 5 km spool and 30 km spool[6] has been extrapolated to find the approximate cost of a 1 km spool: € 51.

Table 13.2: Operations Cost Breakdown

Component	Product	Unit Cost [€]	Total Cost [€]
Communication			**4060.68**
Fiber Optic Cable	FPV Drone Fiber Optic Cable	51	2,983
Transmitter	*TBS Tango 2*	189	189
Media Converter	*Gigabit Ethernet Fiber Media Converter*	92	92
Embedded AI computing module	*NVIDIA Jetson Xavier NX-module*	768.91	768.91
Cooling for AI module	*Heatsink with Fan for Jetson Orin NX / Orin Nano / Xavier NX Module*	27.77	27.77
Transportation			**368.50**
Protective Case Speleo-Drone	*PeliProducts 1506 Air Case*	282.93	282.93
Foam for drone case	*PeliProducts Full 1506 Foam Set*	85.57	85.57
Power supply			**1726**
Cells	*Monocrystalline Solar Panel FIT0601*	8	1152
Backing material	*S-POLYTEC PE-HD sheets black custom cut (UV-stabilised)*	55	220
MPPT	*Bateria Power 20A/10A MPPT Solar Charge Controller*	92	92
Laptop adapter	*RS PRO Modified Sine Wave 100W Power Inverter*	47	47
Shunt diodes, blockage diodes, wiring, hinges, legs	*Taken as 10% of the cost*	150	150
Safe Bag	*Lumenier LiPo Safe Bag*	15	30
Tarp	*QUECHUA Tarp*	35	35

13.1.3. Final Cost Estimate

The final cost estimates, as shown in Table 13.3, were derived using the methodologies detailed in Subsection 13.1.1 and Subsection 13.1.2. Engineering costs were the most significant contributor, which aligns with expectations given the system's custom development. The table presents the cost evolution depending on production scale, incorporating both development-related expenses and per-unit COTS components.

Table 13.3: Final cost breakdown depending on the number of drones to be produced

N	C_{eng} [€]	C_{tool} [€]	C_{MFG} [€]	C_{QC} [€]	C_{FT}	Total cost per drone	With autonomy	With COTS
1	€ 69,956.64	€ 4,166.70	€ 10,801.98	€ 1,404.26	€ 20.89	€ 86,350.47	€ 129,525.71	€ 139,966.89
2	€ 79,417.72	€ 4,934.51	€ 15,532.57	€ 2,019.23		€ 50,962.46	€ 76,443.69	€ 86,884.87
3	€ 85,534.66	€ 5,447.66	€ 19,209.46	€ 2,497.23		€ 37,569.96	€ 56,354.95	€ 66,796.13
4	€ 90,158.34	€ 5,843.80	€ 22,334.85	€ 2,903.53		€ 30,315.35	€ 45,473.03	€ 55,914.21
5	€ 93,916.19	€ 6,170.79	€ 25,105.21	€ 3,263.68		€ 25,695.35	€ 38,543.03	€ 48,984.21
6	€ 97,102.55	€ 6,451.51	€ 27,621.98	€ 3,590.86		€ 22,464.63	€ 33,696.95	€ 44,138.12
7	€ 99,880.77	€ 6,698.79	€ 29,945.73	€ 3,892.94		€ 20,062.73	€ 30,094.10	€ 40,535.28
8	€ 102,351.55	€ 6,920.64	€ 32,116.09	€ 4,175.09		€ 18,198.03	€ 27,297.05	€ 37,738.23

Based on the customer analysis in Table 2.5, eight potential buyers — excluding the current client — were identified. Under an optimistic scenario where all proceed with procurement, the unit cost of production drops below € 38,000, demonstrating clear economies of scale.

[6] URL: `https://www.aixton.com/sale-52154373-5-30km-fpv-drone-fiber-optic-cable-ultra-lightweight-airborne-sky-fiber-optic-tra` `html` [Accessed: 18 June 2025]

13.2. Return on Investment

The Return on Investment (RoI) is calculated by comparing the total net profit to the total production cost:

$$\text{RoI} = \frac{\text{Revenue - Total Costs}}{\text{Total Costs}} \tag{13.8}$$

To estimate the RoI, the expected number of units sold must be determined. According to the market analysis (Section 2.5), approximately 50 potential customers were identified. To maintain a conservative forecast, only 8 customers were assumed as early adopters — institutions and companies likely to invest during the initial market phase, as shown in Table 2.5.

To estimate a realistic sales price, comparable products were analysed. The Elios 2 and Elios 3 were identified as suitable benchmarks due to their similar size and focus on indoor inspection in confined, GPS-denied environments. While both are well-established, SpeleoDrone offers clear advantages. With a flight endurance of 18 minutes - compared to 12.5 minutes for Elios 3 - SpeleoDrone provides 44% more airtime per mission, enabling longer operations with fewer interruptions. SpeleoDrone also supports modular payloads such as thermal cameras, LIDAR, and gas sensors, unlike the closed architecture of the Elios series. This flexibility makes it especially suitable for research and exploration. Additionally, onboard AI enables automatic detection of regions of interest, reducing operator workload —-particularly useful in fields like archaeology, where users may not have technical expertise. The purchase cost was set at € 45,000, despite the system not yet being flight-proven. This pricing is justified by the inclusion of all essential operational equipment: 56 kilometers of biodegradable fiber optic tether, a ground control station, charging unit, and a protective transport case. The package is designed for immediate deployment, removing the need for separate purchases. In contrast, the Elios 3 price includes only the drone itself. This all-in-one approach, combined with SpeleoDrone's longer endurance and modular adaptability, positions it as a more complete and higher-value solution within its niche.

Based on this assumption, the expected RoI is approximately 19.24% after the sale of 8 units. The break-even point occurs between the 5th and 6th unit. The RoI increases steadily with each additional sale beyond this point.

The Table 13.4 presents the cost per unit, total cost, total revenue, net profit, and RoI for production volumes ranging from 1 to 8 drones. The break-even point (6 units) is highlighted in blue. The forecasted RoI for the conservative 8-unit scenario is also indicated.

Table 13.4: Return on Investment analysis

N	Cost of 1 drone if produced N	N drones	Revenue	Profit	RoI
1	€ 139,966.89	€ 139,966.89	€ 45,000.00	-€ 94,966.89	-67.85%
2	€ 86,884.87	€ 173,769.74	€ 90,000.00	-€ 83,769.74	-48.21%
3	€ 66,796.13	€ 200,388.38	€ 135,000.00	-€ 65,388.38	-32.63%
4	€ 55,914.21	€ 223,656.82	€ 180,000.00	-€ 43,656.82	-19.52%
5	€ 48,984.21	€ 244,921.03	€ 225,000.00	-€ 19,921.03	-8.13%
6	€ 44,138.12	€ 264,828.74	€ 270,000.00	€ 5,171.26	1.95%
7	€ 40,535.28	€ 283,746.94	€ 315,000.00	€ 31,253.06	11.01%
8	€ 37,738.23	€ 301,905.82	€ 360,000.00	€ 58,094.18	19.24%

This analysis demonstrates that, under conservative assumptions, the project is expected to reach profitability with a small number of units sold. The RoI increases significantly beyond the break-even point, indicating strong economic potential for the SpeleoDrone once it enters the market.

14. Risk Assessment

This chapter discusses the risk analysis of the SpeleoDrone. The objective is to identify and mitigate possible threats to the project, increasing the probability of success. Section 14.1 will describe the risk assessment. Section 14.2 will detail the Reliability, Availability, Maintainability and Safety Characteristics of the product.

14.1. Risk Assessment

The Continuous Risk Management (CRM) process, used before for the Mideterm Report[6], has been continued in this phase of the project as well. Like discussed before (see [5] and [6]), CRM aims at responding to any possible risks, as soon as they are identified in the design. As such, when the team has moved into a more detailed design phase, many new risks were identified and some were removed. An overview of those changes can be found in Table 14.1.

An example of a risk that was removed is ***RSK-PL-003****: One of the payload instruments runs out of storage space*. As the design progressed, decision was made to stream the data over the fiber optic cable, rather than store it onboard. With enough information about the required and available data rates, this was deemed a better option than onboard data storage. As such, this risk was rendered obsolete and removed from the register.

An example of a risk that was added is ***RSK-PP-010****: Premature battery failure due to improper storage temperature*. Once the battery was chosen, a more detailed inspection of its properties and failure points was carried out. Because a LiPo battery was chosen, a serious risk of the battery degrading or even catching on fire was uncovered. To avoid that, a prevention strategy was implemented in the design- a fireproof, thermally isolated bag was found and included in the operations guidelines (see Chapter 10). This will protect the batteries from the unfavorable conditions of Puerto Rico and extend their lifespan.

The updated register can be found in Figure 14.1. As before, the severity of risks is rated on a scale from one to five, one being 'insignificant' and five being 'catastrophic'. Probability is also rated on such scale, going from 'very unlikely' to 'almost guaranteed to happen'.

Some risks have had a higher influence on the design than others. Certain risks were translated directly into requirements, for example ***RSK-FC-005****: Control sensor broken* was the parent to the requirement **DRN-AVIO-09**. That requirement was then satisfied by adding a backup sensor to each of the sensors needed for control, the design for which can be found in Section 9.2.

RSK-PP-008*: Motor failure due to bearing failure* is an example of a risk that determines the operations around the drone, more specifically the maintenance schedule (see Subsection 14.2.3). Bearing failure or the drying out of bearing grease is one of the most common failure modes of brushless DC motors. Ensuring regular maintenance of the part can prevent an accident from happening.

Finally, risks such as ***RSK-EL-009****: Data corruption* will only become significant in the future. It was identified during the Fault Tree Analysis carried out in Subsection 14.2.1, but the steps that have to be taken in order to prevent it from happening or mitigate it can only be implemented at a more detailed design phase- specifically when software architecture is designed and communication protocols are established. If the entire network is to be coded from the ground up, an error-detecting algorithm of choice (for example a checksum) can be implemented. Alternatively, if the risk of data loss remains too high, a local backup can be implemented. Either way, with the resolution of the software design at the time of writing, this risk could not have been directly adressed yet.

ID	Risk	Pre-Prob	Pre-Sev	Prob Prevention	Sev Mitigation	Post-Prob	Post-Sev
RSK-PL-001	One of the instruments is broken	2	5	Inspect instruments before use	Bring back up instruments that can be installed quickly	1	2
RSK-PL-004	One of the instruments is misalgined	5	3	Check alignement with a reference sheet/ manual before use		3	3
RSK-PL-005	One of the instruments is missing	3	5	Check with reference sheet / assembly manual before use	Redundant perofrmance critcial instruments if possible	2	3
RSK-PL-006	One of the instruments gets damaged	4	4	Protect delicate instruments	Redundant perofrmance critcial instruments if possible	2	3
RSK-PL-007	Payload sensors not calibrated	5	4	Pre-Flight checklist to include sensor calibration		2	4
RSK-PL-008	Payload cannot be integrated into the UAV	4	5	Mock integration test with a CAD model, integration test of the finished product		1	5
RSK-PL-010	Payload camera doesn't have enough light to operate	4	4	Add a light source		1	4
RSK-PL-011	UAV flies too fast for the camera to record well	4	4	Check camera specs before planning the mission flight speed	Get a camera capable of recording at high speeds	2	3
RSK-PL-012	Camera view obstructed by drone elements	5	4	Check camera FoV in a CAD mockup in advance		2	4
RSK-PL-013	Payload camera damaged	3	4		Have a backup camera on site	3	2
RSK-OP-001	UAV impacts a terrain obstacle (cave wall, cave ceiling, etc)	5	5	Experienced pilot / well trained and tested AI	Implement protection or crash zones where possible	2	4
RSK-OP-002	The team loses information about the location of the drone	4	5	Add a reliable tracking module	Add a return to base mode in case of loss of contact	2	5
RSK-OP-003	UAV flies into a member of the operating team	3	5	Avoid operating UAV around the team, evacuate non-essential personnel, have an experienced pilot / well trained and tested AI	Make sure the team wear appropriate PPE during drone operations	1	3
RSK-OP-004	UAV collides with a bat	2	5	Make sure the UAV is bat-detectible		1	5
RSK-OP-006	UAV experiences a hard landing	4	4	Experienced pilot / well trained and tested AI, practise landing in lab conditions	Design the landing gear to be extra sturdy	2	2
RSK-OP-007	UAV cannot be integrated together	4	5	Mock assembly test in CAD, assembly test before expedition		1	5
RSK-OP-008	Contamination of cave system	3	5	Limit the amount of potentially toxic substances used, make sure each is contained well	Discuss a contaimination plan with environemntal agencies in advance	2	4
RSK-OP-009	Bat chewing on the fiber optic cable	1	5			1	5
RSK-OP-010	Fiber optic cable getting stuck on a rock	5	5	Minimise amount of turns in one flight to avoid looping around obstacles on the ground	Implement cutting mechanism that can free the drone up	5	3
RSK-OP-011	Noise produced by the drone damaging to human hearing	3	5	Asses noise emission beforehand, ensure it's within an acceptable level	Hearing protection for the operating team	2	3
RSK-OP-012	Ground station can't generate sufficient power	4	4	Calculate power generation required for needed charging rate, add a sfaety margin		2	4
RSK-EL-001	Bad connector	4	4	Check all connectors before use		2	4
RSK-EL-002	Wiring damage due to humidity	3	4	Water-proof sensitive electronics		1	4
RSK-EL-003	Communication system fails due to cable damage	4	5	Test the communication system in advance, protect the fiber optic cable, change cable after each use	Aim at some degree of autonomousness, trigger emergency protocole (return to base) in case of loss of communication	3	4
RSK-EL-004	Damage to components due to ESD	2	4	Take care when handling electronics in dry conditions		1	4
RSK-EL-005	Damage to components due to power surge	3	4	Use fuses/LEDs before critcial hardware		1	4

RSK-EL-009	Data corruption	3	4	Change fiber optic before each use, implement data checks in firmware / software		2	4
RSK-EL-010	Loss of communication due to transmitter/receiver issue	3	5	Use reliable hardware, test in advance, test firmware / software in advance	Aim at some degree of autonomousness, trigger emergency protocole (return to base) in case of loss of communication	2	4
RSK-PP-002	Propeller blade damage due to impact	4	4	Use stronger material for the blades or cover blade tips and / or edges wioth stronger material	Ensure the drone can still operate with some amount of damage, bring backup propellers that can be easily installed (ensure ease of installation)	3	2
RSK-PP-003	Battery Fire	3	5	Don't use damaged batteries	Encase battery in fire resistant casing during storage	2	4
RSK-PP-005	Insufficient power generated	4	5	Put a safety margin on the required amount of power, test the power generation system in advance	Have the power distribution system prioritize critcial systems in case of insufficient amount of power	2	3
RSK-PP-006	Power system failure	3	5	Test in advance	Include emergency power system or an emergency protocole allowing for easier retrieval	2	4
RSK-PP-007	Propulsion system underperforms	4	4	Test the propulsion subsystem in advance	Make sure the UAV is still operational enough for retrieval	1	3
RSK-PP-008	Motor failure due to bearing failure	4	5	Lubricate bearings during maintenance breaks, replace motors every TBD cycles		2	5
RSK-PP-009	Motor failure due to overheating	3	5	Perform therman analysis, add insulation / cooling if deemed necessary		2	5
RSK-PP-010	Premature battery failure due to improper storage temperature	5	4	Store and charge batteries in a thermally-isolated casing	Bring more batteries than strictly necessary	2	3
RSK-FC-003	On-board software bug	5	5	Unit, system and integration test the code befofre use, ideally perform mock flights in lab conditions with the final code, make sure the code is clean and well documented	Try to avoid having code that if non-functional would completely destroy everything	1	4
RSK-FC-004	Control sensor not calibrated	5	4	Pre-Flight checklist to include sensor calibration	Redundant sensors	1	3
RSK-FC-005	Control sensor broken	4	4	Pre-flight checklist to include checking sensors	Redundant sensors	2	3
RSK-FC-009	Control board can't unpack and process user commands quickly enough	3	5	Enbsure enough prcoessing power, test in advance	Prioritize commands, have overload handling implemente	2	2
RSK-FC-010	AI navigation provides wrong input	4	4	Test the AI in advance in a mocked cave enviornment	User override	3	3
RSK-FC-011	AI navigation malfunction	4	4	Test the AI in advance in a mocked cave enviornment	Implement return to home algorith as backup	3	2
RSK-FC-012	Bad user input	3	4	Implement AI 'copilot' to correct user mistakes		2	4
RSK-STR-001	Strcutural failure due to flight load	4	5	Test the strucrue in advance, make sure there is a sufficient safety margin on the design	Introduce failure points that don't have a critical impact on the performance	1	4
RSK-STR-002	Failure due to preexsiting material impurities / fractures	4	5	Design with a sufficient margin to allow for imperfections, try to predict probable strength of production material based on statistical distrubiution	Introduce failure points that don't have a critical impact on the performance	2	4
RSK-STR-003	Fatigue failure	5	5	Inspect between uses, have a clearly defined design life time. Use as long-lasting materials as available	Introduce failure points that don't have a critical impact on the performance	2	4
RSK-STR-004	Undoing of connections due to vibrations	4	4	Use locktite or similar glue on nuts and bolts that can vibrate out of place, insepct between uses	Make sure only non-critcial connections can vibrate out of place	2	3
RSK-STR-005	Structure yields during handling	3	4	Include warning about fragile components in the user manual, suggest handling via elements that can be more easily repeaired / replaced	Attach a repair manual	1	3

Figure 14.1: Risk Register

Table 14.1: Risk Registry Changelog

Date	Added	Removed	Note
30/04/2025	RSK-PL-001, RSK-PL-009, RSK-OP-001, RSK-OP-008, RSK-EL-001, RSK-EL-007, RSK-PP-001, RSK-PP-007, RSK-FC-001, RSK-FC-007, RSK-STR-001, RSK-STR-004	RSK-PL-009, RSK-OP-005, RSK-EL-006, RSK-EL-007, RSK-PP-001, RSK-FC-001, RSK-FC-002, RSK-FC-006	Created
19/05/2025	RSK-PL-010, RSK-PL-011, RSK-FC-009, RSK-EL-008		After conclusion of trade-off
17/06/2025	RSK-PL-012, RSK-PL-013, RSK-OP-009 - RSK-OP-012, RSK-EL-009, RSK-EL-010, RSK-PP-008 - RSK-PP-010, RSK-FC-010 - RSK-FC-012, RSK-STR-005	RSK-EL-008, RSK-PL-002, RSK-PL-003, RSK-PP-004, RSK-FC-007, RSK-FC-008	Detailed Design Phases

Finally, to aid in visualising of the register, risk maps were once again constructed. Figure 14.2, shows the risks before mitigation. It can be seen in Figure 14.3 that most risks have moved in the direction of the left bottom corner. The few risks remaining in the yellow zone after mitigation will have to be observed with greater care and attention in the future.

The two risks with highest impact after mitigation remain

- **RSK-EL-003**: Communication system fails due to cable damage
- **RSK-OP-010**: Fiber optic cable getting stuck on a rock

They both pose unique challenges, which will have to be addressed in more detail in the future. Both, however, pertain to the communication system, meaning the fiber optic cable implementation will have to face more scrutiny in the final design phase. This is to be expected, as this is a relatively uncommon way of communicating with quadcopter. The hardships caused by the fiber optic cable were partially addressed in Chapter 10, with a more detailed solution still being worked on.

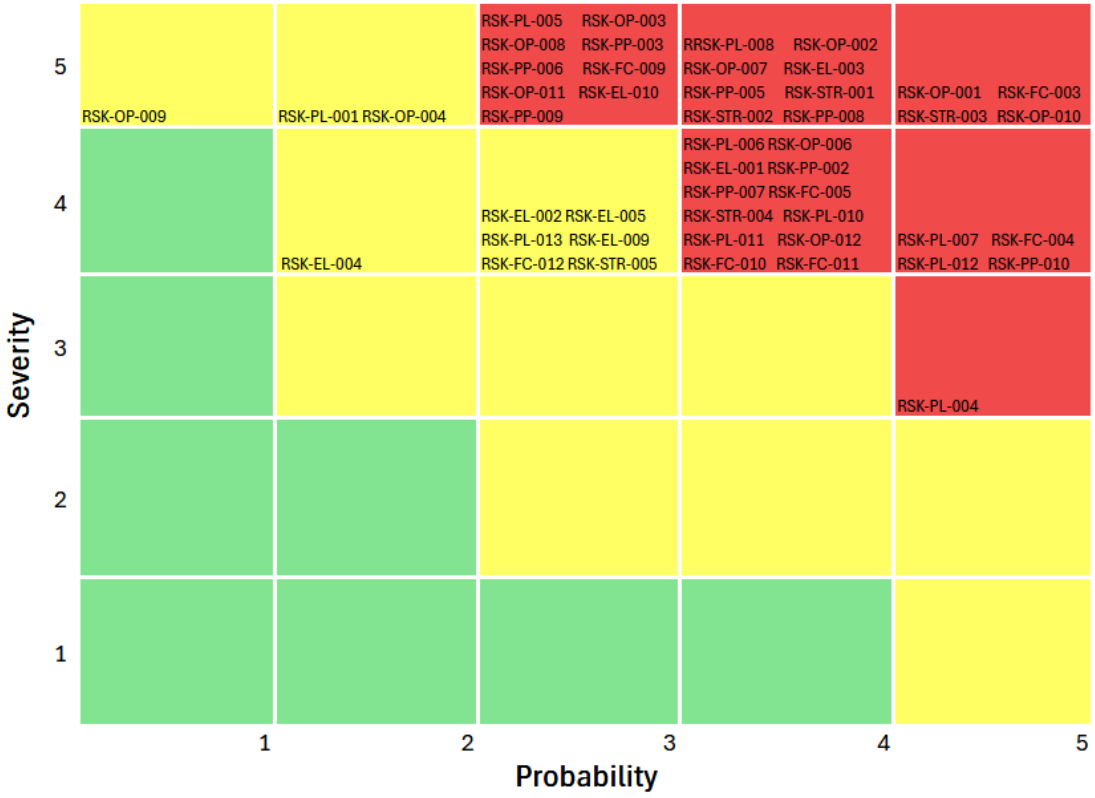

Figure 14.2: Risk Map Before Mitigation

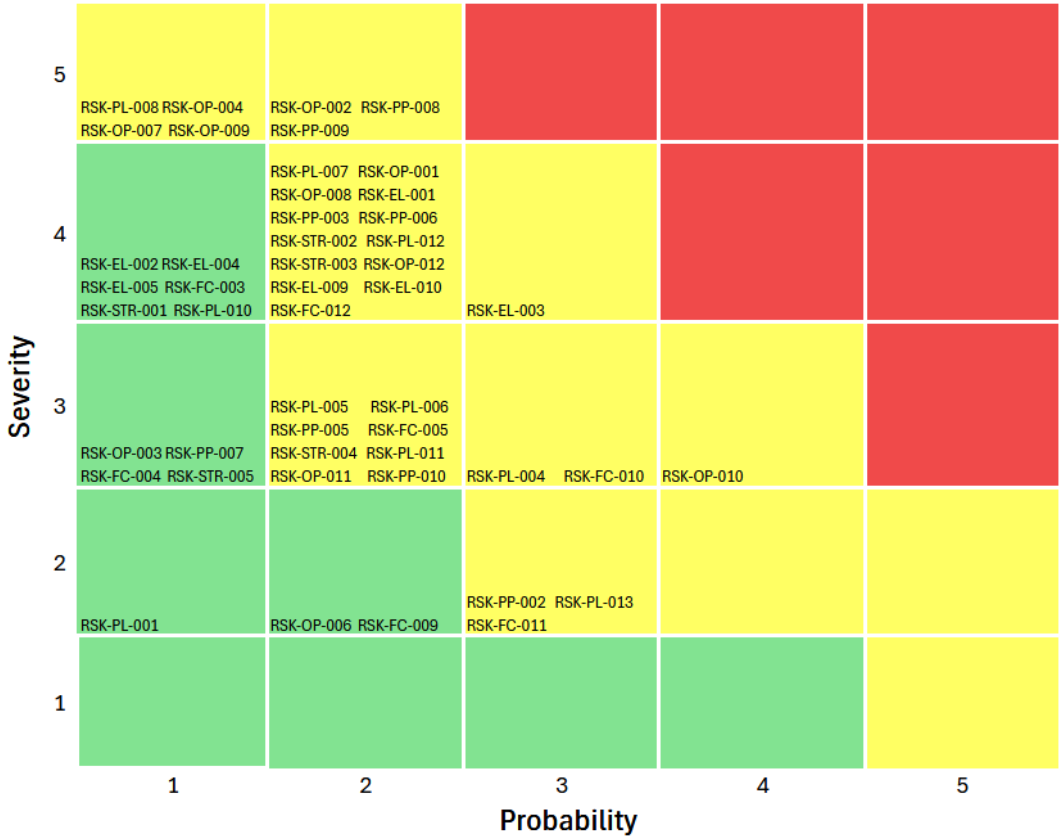

Figure 14.3: Risk Map After Mitigation

14.2. Reliability, Availability, Maintainability, and Safety

This section will discuss the Reliability, Availability, Maintainability (RAMS) characteristics of the drone. Subsection 14.2.1 will dsicuss the reliability of the drone. Subsection 14.2.2 will discuss the availability of the drone. Subsection 14.2.3 will discuss the maintainability and Subsection 14.2.4 will discuss the safety aspects of the design and operations.

14.2.1. Reliability

Reliability is a measure of the ability of the system to perform a given function. It's usually expressed in terms of failure rate or the Mean Time Between Failures (MTBF). In order to obtain this number, the probability of failure has to be calculated.

Because the UAVs are a relatively new development in the field of aerospace, there is no reliable way of estimating the probability of failure with a degree of certainty that would make it useful. Literature values were considered, but they are sparse and mostly touch upon fixed wing UAVs. Additionally, these studies themselves highlight the uncertainty of the values obtained[50]. Thus decision was made to not try to obtain a numeric value for reliability of the SpeloDrone, as it would be unfeasible and unreliable.

Instead, the most common failure modes were analyzed instead. For that a tool called a Fault Tree Analysis was used. The Fault Tree is a tree which depicts all possible failures, going from the mission failure all the way down to singular points of failure. The goal of constructing such a tree is identifying those singular failure points.

Figure 14.4 is the fault tree for the entire mission. It can be seen that the mission will fail if at least one of the main components fails- the drone itself, the payload or the ground station. Because the drone is the main component of the mission, its fault tree was constructed on a separate graph to improve readability (see Figure 14.5). In both trees all connections between different levels are OR gates, meaning that at least one of the conditions below has to occur for failure.

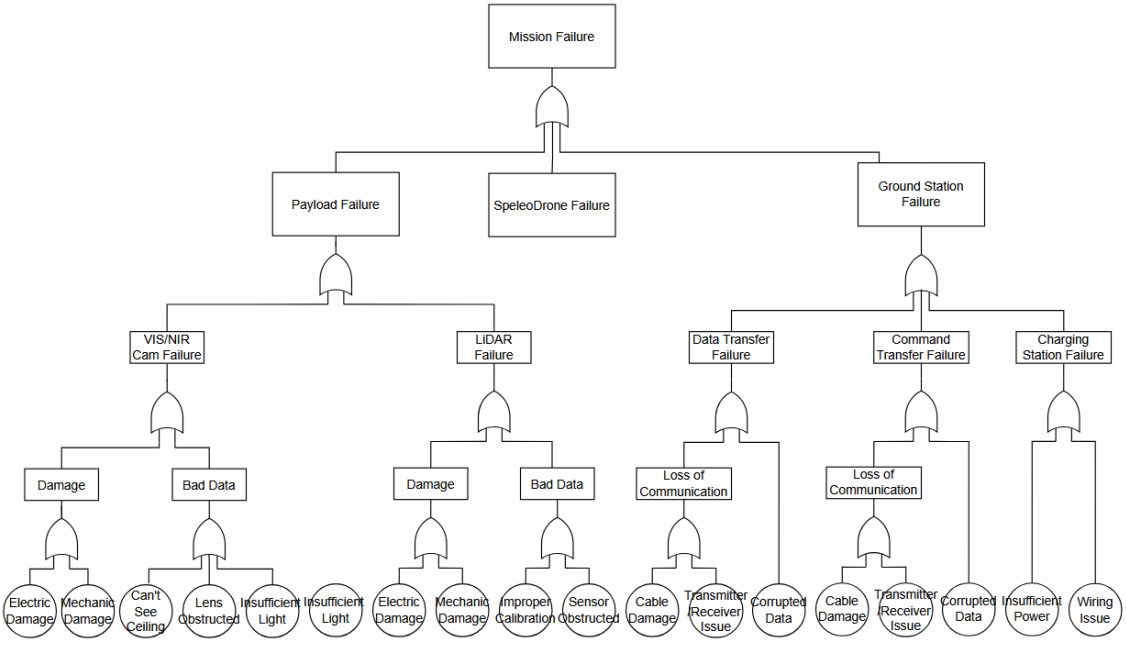

Figure 14.4: Mission Fault Tree

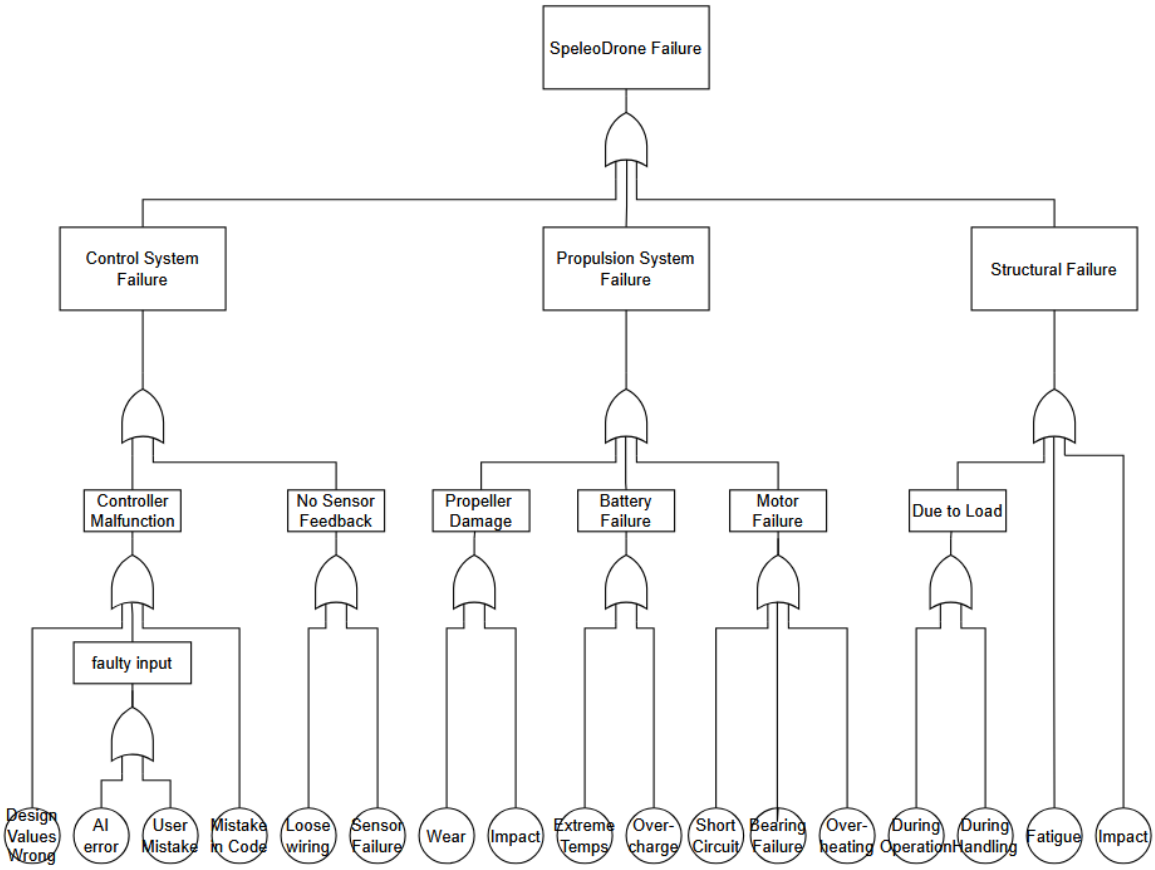

Figure 14.5: Drone Fault Tree

The fault tree provided a number of possible failure causes. Out of all of them, the following were identified as the most significant:

- Errorous AI input
- Control sensor failure
- Fatigue failure of the drone
- Battery failure due to extreme temperatures
- Obstruction of camera lens
- Loss of communication due to fiber optic cable damage

In the next design step, more attention will have to be directed to these aspects of the design, to ensure the possibility of failure can be minimized. Additionally, the risk register has been updated with risks pertaining to these failure points.

14.2.2. Availability

Availability is defined as the probability that the system can function at the desired time. The system is not counted as functional during maintenance, repairs or during the downtime caused by failures. Because, as discussed in Subsection 14.2.1, it's hard to predict the exact frequency of failures, this part of RAMS will deal with only scheduled downtime, divided into two categories- between missions and maintenance.

First, a limiting factor for availability will be all operations that have to be carried out between the missions. After retrieval of the drone, the batteries will have to be swapped for new ones, old batteries will have to be put on a charger, the fiber optic cable will have to be reeled out of cave, while a new reel of fiber optic will have to be placed on the drone. Additionally, a small inspection will have to be figured out before the drone can be deployed again, to ensure that it's flight worthy. The operations taken and time needed per operation can be found in Table 14.2

Table 14.2: Downtime Between Mission

Name	Time [min]
Battery removal	5
Fiber optic cable retrieval	15
Drone inspection	10
New reel installation	5
New battery installation	5
Total	40

One noteworthy thing regarding Table 14.2, is that it assumes all operations are carried out by one person, which in reality will not be the case. That means that one of the members of the operating team can begin reeling the fiber optic back in, while other members inspect the drone and swap the batteries. Then, assuming that the operations will still take the same amount of time, the total downtime between missions becomes **25 min**.

The second type of downtime to be considered here is the scheduled maintenance. It is currently still unclear how often this maintenance will have to be carried out, but realistically it will be somewhere between each full day of exploitation or after the full week of the expedition. Either way, the time needed to carry out this maintenance can be estimated like before by knowing the actions that have to be carried out and predicting the time they consume. The actions currently identified as crucial for maintenance and the time estimate assigned to them can be found in Table 14.3

Table 14.3: Downtime For Maintenance

Name	Time [min]
Detailed visual inspection	30
Change of propellers	30
Change of landing gear	20
Camera lens cleaning	5
Sensor re-calibration	15
General Cleaning	20
Total	120

Table 14.3 implies that the total downtime for the regular maintenance is equal to two hours. Applying a 20% contingency margin results in a total time of **144 min**. While this number is a very preliminary estimate and should be treated as a guideline, rather than an exact value, it illustrates the difference between the maintenance inspections and the activities need to be carried out between each flight. The latter is significantly shorter, highlight the design philosophy of ensuring the maximum possible availability of the drone during the operating time. This stems directly from the stakeholder requirement **STK-DRN-1** (see Section 2.3), which details the maximum mission time as one week.

14.2.3. Maintainability

Maintainability pertains to system's ability to be easily maintained, inspected and repaired. The SpeleoDrone was designed with maintainability in mind, as one of the principles of the design philosophy used was modularity. Two reasons driving the modularity of the design was the payload layout and the possible market expansion. Originally, it was discussed to have two cameras, a UV camera and a visible spectrum/NIR camera that would be swapped between runs. This idea has been abandoned (see Chapter 5 for more details), but the modular approach to the design continued.

That modularity has improved the maintenance activities significantly. An example of an unscheduled maintenance that has been made easier, is landing gear replacement. The landing gear of the quadcopter has been designed to absorb the shock of impact- in case of hard landing it would act as a crush zone and prevent the load from affecting the main airframe. Because of that the gear will have to be replaced more often than other elements, so it has been designed to be detachable with relative ease.

Like it was discussed in Subsection 14.2.1, a more detailed maintenance schedule hasn't been created yet, but it will be addressed in the future design phase. Additionally, decision was already made to include a repair kit with some spare parts and required tools with the SpeleoDrone.

14.2.4. Safety

Finally, safety encompasses many aspects, but most importantly, the ability of the system not to harm people, the environment or any assets. Each of these was discussed in detail in the following three sub-subsections.

Assets
Beginning with harm to assets, this has been decided to be a relatively insignificant aspect for the SpeleoDrone, as it operates in a remote cave, meaning no private assets can be endangered by its operations.

Environment
The harm to the environment was partially discussed in Chapter 3, but the main points are reiterated here. While the entire ecosystem of the caves is at risk due to operations of the SpeleoDrone, the most endangered group are the bats that live in the cave. As such the safety precautions regarding the environment were divided into precautions for the ecosystem and precautions needed for the bats specifically.

For the ecosystem as a whole, the main important safety aspect is not bribing potentially toxic or erosive materials into the cave. Care was taken that all elements of the SpeleoDrone are as non-harmful as possible. The only potentially toxic material is the acid inside the LiPo batteries, but for it to be exposed to the environment a lot would have to go wrong. It was still advised to the future development team to investigate a mitigation strategy for this, such as placing the batteries in an additional casing or similar.

Regarding the bats, they are the most exposed to the SpeleoDrone as they live in the cave and prefer quiet and dark environments. While a collision with a bat is incredibly unlikely, considering that bats have evolved to be quite good at avoiding obstacles, other ways of harming them are possible. Bats have incredibly sensitive hearing, as they use it to navigate their way around. Additionally, their eyes are quite weak and unused to sunlight. As such, extra care had to be taken to ensure no light or noise pollution would have an adverse effect on their quality of life.

For the light pollution, while a flashlight is needed to take pictures in the cave, a solution was found to prevent the bats from being exposed to a sudden source of unnaturally bright light. Namely, each time the drone enters a new 'room' in the cave, it first does a NIR sweep to detect if any bats have remained in the area, and only then turns on the flashlight. This measure, while excessive since the bats would most likely escape the area upon detecting the presence of the drone, was deemed necessary.

The bats are likely to avoid the SpeleoDrone due to noise emissions. While propeller frequencies won't harm them directly, the high-pitched sound from the ESCs may be unpleasant at close range. Though bats are unlikely to approach closely, foam or sound-absorbing material will be added around the ESCs to further reduce noise as a precaution.

People
Finally, for the members of the operating team, a few major safety considerations were addressed.

Firstly, the noise emissions of the drone was deemed unharmful towards humans. The maximum noise the drone produces during operations is equal to 67 dB (see Subsection 7.3.1. This is equivalent to a regular conversation[1] and is considered perfectly safe to work around. That means no hearing protection will have to be used by the operating team. A different type of PPE that will be strongly recommended to be used are helmets. While the drone is outfitted with an obstacle detection system and a manual override, which means a collision with a member of the operating team is incredibly unlikely, it is still advised to wear a helmet in case something fails. More specifically, the helmets will be required during the retrieval and the deployment of the SpeleoDrone.

Potentially the most dangerous element of the drone is its LiPo battery pack. These batteries are known for being a fire risk[2]. As such, certain precautions have to be taken, which was addressed in Section 14.1 and Chapter 10. The batteries have to be stored and charged in a special fire proof bag and kept cooler than the outside temperature- LiPo batteries operate in the range of 20-25°, while temperatures in Puerto Rico reach 30°. A specialized bag was chosen for this purpose and included in the list of components required to operate the drone.

Finally, a need for a safety manual was discussed. To ensure the operating team would follow all safety precautions, it was advised to create a safety overview manual in the next phase of the project, that would contain an overview of all actions needed for safe operations of the SpeleoDrone. Additionally, it was recommended to include safety steps in the operation procedures, for example include the need for PPE at the beginning of the pre-flight checklist.

[1] https://www.gcaudio.com/tips-tricks/decibel-loudness-comparison-chart/,[Accessed: 22 June 2025]
[2] https://hobbyking.com/nl_nl/blog/LiPoBatteryExplosionRiskPreventionGuide/?___store=nl_nl,[Accessed: 21 June 2025]

15. Verification and Validation

This chapter covers the verification and validation procedures that were and will be used throughout the design. First, Section 15.1 covers the verification and validation of the product, ensuring all requirements are met. Next, Section 15.2 goes over the model verification & validation, which ensures the output of models and equations is reliable. Finally, Section 15.3 summarizes whether the current design meets all user requirements.

15.1. Product Verification & Validation

Verifying and validating the product implies demonstrating that both the requirements and customer needs are met. To do this, criteria were assigned that the requirement formulation must meet, and the different verification methods were laid out and assigned to each of the requirements.

15.1.1. Requirement Validation

The requirements were validated in two stages. First, they were checked to see if they were formulated according to the VALID (Verifiable, Achievable, Logical, Integrable, Definitive) criteria. The exception is the stakeholder requirements, which were translated into VALID system-level requirements.

Next, the coverage of the requirements was validated. The requirements should cover the complete design to avoid missing functionality. To guarantee this, each identified function the UAV must perform was analyzed to discern whether there were matching requirements.

15.1.2. Requirement Verification

There are four main methods for verifying the requirements: inspection, analysis, demonstration, and testing:

- **Inspection** Inspecting the design to show the requirements are met.
- **Analysis** Perform mathematical analysis to establish compliance with the requirements.
- **Demonstrate** Establish by operation that the requirements are met.
- **Testing** Perform tests under similar conditions to the mission operations.

Testing procedures for the most important requirements are described in Table 15.1. Furthermore, testing procedures for every subsystem requirement were defined in Table 15.2. The method chosen is based on the accuracy of results, cost-effectiveness and the ease of execution. If all verification tests are performed once the design is finished, all customer needs should be adequately validated.

15.1.3. Testing Cost

The cost for verification & validation is limited, since almost no specialized test setups are required in the mentioned procedures, and the tests only have to be executed a single time to validate all products. Consequently, the primary costs stem from two sources: man-hours and travel costs. The actual costs will depend on how much confidence is desired in the design.

Table 15.1: High-level requirement verification procedures

Requirement ID	Description	Method	Procedure
STK-DRN-1	The system shall be able to fully map a cave system distance of up to 500 m from the entrance, within 1 week	Analysis	Analyze the endurance and mapping capabilities to see whether the requirement can be achieved
STK-DRN-2	The system shall be able to visually map the cave system with a resolution of 1 cm	Testing	Take an image in a dark room with the payload at a distance similar to that in cave conditions
STK-DRN-3	The system shall be able to georeference a location on the map with a resolution of 1 cm.	Testing	Take measurements in conditions similar to the mission and check the georeferencing resolution
STK-DRN-4	The system shall be able to pass through any opening an adult human can pass	Demonstrate	Move the system through a 40 cm by 40 cm hole

Table 15.1: Requirement verification procedures

Requirement ID	Description	Method	Procedure
STK-OPR-01	The system shall comply with EASA requirements for safe operation of drones.	Demonstrate	Demonstrate through operation that all EASA requirements are met
STK-OPR-02	The system shall be 75% by weight recyclable, excluding the payload	Inspection	Inspect the materials the structure is made from for recyclability
STK-OPR-03	The system shall have a purchase cost of no more than €25,000	Analysis	Analyze the total cost of the system
STK-OPR-04	The system shall be suitable for transportation as air cargo	Inspection	Compare features of the design to airport regulations
STK-OPR-05	The system shall be able to operate in a remote location (i.e. no access to grid power or cellular telephone networks)	Testing	Test operations in a remote location without access to grid power and cellular telephone networks
STK-OPR-06	The system shall not produce any emissions inside the cave system	Inspection	Inspect the design for any sources of emissions
STK-OPR-07	The system shall minimize disturbance to the site being investigated	Testing	Test in a similar environment to the mission to show there are minimal disturbances
STK-OPR-08	The system shall be designed to be operable with minimal training	Demonstrate	Let an inexperienced pilot operate it
STK-OPR-09	The system shall be easily portable	Demonstrate	Demonstrate by physically transporting to another location that the system can easily be relocated
STK-OPR-10	The system shall incorporate sustainable policies as defined by the European Union	Analysis	Analyze the complete design to assess the sustainability policies incorporated.
STK-OPR-11	The system shall be adaptable to other missions	Demonstrate	Demonstrate the system functioning in other applications
STK-OPR-12	The system shall be designed within 10 weeks	Inspection	Inspect the time used for the design of the system
MIS-DRN-1.2	The system shall be capable of mapping accessible area within a total of 56 operational hours	Analysis	Analyze the endurance, velocity and mapping capabilities to determine how fast the site can be mapped
MIS-DRN-1.3	The system shall successfully complete its primary mission objectives in at least 95% of deployments under nominal environmental and operational conditions	Demonstrate	Demonstrate the mapping of an archaeological site under mission conditions
MIS-DRN-1.4	The system shall detect and localize physical collision risks with at least 95% accuracy from a minimum distance of 1 meters	Testing	Test the system when flying at maximum speed, navigating around a variety of obstacles
MIS-OPR-2.1	The system shall be designed such that at least 90% of its total weight can be separated into dissimilar material types using standard disassembly tools at End-Of-Life	Analysis	Analyze the design to determine the fraction of separable materials
MIS-OPR-2.2	65% of the standard components used in the system — including fasteners, wiring, and structural elements — shall be designed for direct reuse in other products without requiring any mechanical, chemical, or thermal reprocessing	Analysis	Analyze material properties of components used, ensuring they do not require additional reprocessing

Table 15.1: Requirement verification procedures

Requirement ID	Description	Method	Procedure
MIS-OPR-5.1	The system shall operate without reliance on any non-portable infrastructure or services not provided by the mission crew	Demonstrate	Demonstrate all parts are portable by transporting them between two locations
MIS-OPR-7.1	The peak noise levels produced by the system during operation shall not be higher than 120 dB	Testing	Measure the noise level while all scientific equipment is active and the drone is operating at full power
MIS-OPR-7.2	The average noise levels produced by the system during operation shall not be higher than 85 dB	Testing	Measure the average noise level during navigation around obstacles mimicking cave obstacles
MIS-OPR-7.3	All components of the system shall be retrievable from the environment after operation within 1 week since the beginning of the mission	Demonstrate	Demonstrate that no components are left behind during operation
MIS-OPR-7.5	The wavelength of the light levels produced by the system during operation shall not be in the range of 310-510 [nm]	Analysis	Compare the payload specifications to the wavelength range
MIS-OPR-8.1	The system shall be provided together with a guidelines document for on-site inspection before flight of UAV	Inspection	Inspect whether the guidelines document is present in addition to the design
MIS-OPR-8.2	The components of the system that are critical failure points (electrical wiring, fiber optic, landing gear) shall be repairable on site by no more two people from the crew without special training using portable manual tools	Analysis	Analyze the critical failure points and determine whether the required action can be performed by two inexperienced crew members
MIS-OPR-8.3	Replacements of components of the system that are critical failure points (landing gear, fiber optic, propellers) shall be provided with the product	Inspection	Inspect whether the replacement components are provided
MIS-OPR-10.1	The energy used over the full life-cycle of the system (e.g., material production, product manufacturing, transport, product use, and disposal) shall not exceed 2000 MJ	Analysis	Perform a life cycle analysis to determine the total energy consumed
MIS-OPR-10.2	The CO2 emitted over the full life-cycle of the system (e.g., material production, product manufacturing, transport, product use, and disposal) shall not exceed 60 kg	Analysis	Perform a life cycle analysis to determine the total CO2 emissions
MIS-OPR-10.3	The system shall be capable of utilizing a renewable energy source on-site to recharge its power supply system	Demonstrate	Demonstrate the use of a renewable energy source to recharge the power supply used by the system
SYS-DRN-1.2.1	The system shall maintain an attitude positioning accuracy of less than 2 degrees on each of the three principal axes (roll, pitch, and yaw) during nominal flight conditions	Analysis	Analyze post-flight data to determine the angular accuracy
SYS-DRN-4.2.1	The system shall maintain its position with an accuracy of less than 15 cm per axis during hover or groundspeeds lower than 25 m/s, under nominal conditions	Analysis	Analyze post-flight data to determine the positional accuracy

Table 15.1: Requirement verification procedures

Requirement ID	Description	Method	Procedure
SYS-DRN-4.2.2	The system shall be capable of providing translation acceleration along each axis up to 1.5*g [m/s^2] during nominal flight conditions	Testing	Measure the maximum achievable translational accelerations under in a controlled test
SYS-DRN-4.2.4	The system shall allow for angular acceleration of 380 rad/s^2 or less in each axis during nominal flight conditions	Testing	Measure the maximum achievable angular accelerations under in a controlled test

Table 15.2: Subsystem requirement verification procedures

Requirement ID	Description	Method	Procedure
PL-DRN-01	The maximum speed of the drone when visually mapping shall be below 0.7 m/s.	Testing	Analyze the control scheme to see whether it does not overshoot the velocity limit during visual mapping maneuvers
PL-DRN-02	The maximum speed of the drone when 3D Mapping shall be below 0.7 m/s.	Analysis	Analyze the control scheme to see whether it does not overshoot the velocity limit during 3D mapping maneuvers
PL-DRN-03	The payload components shall be fully operable in temperatures up to 30 degrees Celsius.	Demonstrate	Demonstrate that the payload can still obtain data at extreme temperatures
PL-DRN-04	The resolution of the camera shall be higher than 1 cm.	Inspection	Inspect the camera specifications to check whether the resolution is sufficient
PL-OPR-01	All payload components shall be retrievable within 1 week from the beginning of the mission.	Demonstrate	Demonstrate that no payload components are left behind during operation
PL-OPR-02	The payload shall be fully operable in light conditions under 6000 lumen	Testing	Light up a room as close to the lumen value as possible and assess the payload performance at those conditions
PL-OPR-03	The light emission of the payload shall be below 10000 lumen	Testing	Test whether the light source required for sufficient mapping resolution remains below the lux level with a meter
PL-OPR-04	The payload shall require no more than 30 Wh per mission	Analysis	Determine the fraction of the mission spent mapping and the power required while mapping and when idle
PL-DRN-05	The payload shall have a minimum data rate of 9000 bit/s to ensure complete cave mapping within total mission time	Analysis	Analyze the data rate based on the payload frequency and resolution
PL-DRN-06	The payload shall have a maximum data rate of 9000 bit/s to ensure complete data transfer	Analysis	Analyze the data rate based on the payload frequency and resolution
PL-OPR-05	The combined size of the payload shall be below 18 x 10 x 4 cm^3	Inspection	Inspect the payload specifications and measure the delivered product
PL-OPR-06	The mass of the payload shall be below 750 g	Inspection	Inspect the specifications of the payload components chosen and weigh the delivered components on a scale
PL-OPR-07	The noise emission of the payload shall be below 85 dB	Testing	Operate the payload at maximum mapping rate for an extended period of time and measure the noise

Table 15.2: Subsystem requirement verification procedures

Requirement ID	Description	Method	Procedure
DRN-STRC-01	The structure of SpeleoDrone shall have a mass of less than 0.9 kg	Testing	Put all the structural elements on a scale to measure the mass
DRN-STRC-02	The direction of the thrust vector shall not vary more than 2° during flight	Analysis	Analyze the rigidity of the propeller, motor and structural arm to determine the deflection maximum deflection of the thrust vector during operation
DRN-STRC-03	During operation, deformation of the structure shall not offset the payload orientation by more than 0.1°	Analysis	Analyze the loads and resulting vibrations through equations of motion to determine the offset they would cause
DRN-STRC-04	The structure shall not yield or permanently deform during operation or handling	Analysis	Analyze the expected loads and stresses and see whether these are lower than the yield stress
DRN-STRC-05	The drone structure shall withstand a fall from 1 meters, onto the cave floor	Analysis	Analyze the impact a fall from 1 meter will have on each component of the drone and check whether this is tolerable.
DRN-STRC-06	The structure shall have a fatigue lifespan of 1680 operational cycles	Analysis	Determine fatigue behaviour, simulate the loads and compare initial and final properties
DRN-STRC-07	Oscillations of the structure shall not hinder the function of the payload	Analysis	Analyze the vibrations the payload will experience due to the structure and mathematically analyze that this does not degrade performance
DRN-STRC-08	The structure must not lose more than 10% mechanical performance over its lifespan	Analysis	Determine fatigue, creep and aging behaviour and simulate the loads the drone may experience. Then compare the initial and final properties
DRN-STRC-09	All frame and fastener materials shall be corrosion-resistant and non-reactive in high-humidity environments	Analysis	Analyze the corrosion resistance and reactivity of the materials used in each structural component
DRN-STRC-10	All structural elements shall be 100% recyclable	Analysis	Perform a recyclability analysis on the structural elements
DRN-STRC-11	The structural elements & fasteners must be easily switched out or assembled within 10 minutes in the field	Demonstrate	Demonstrate the ease of swapping out each structural elements and the fasteners
DRN-STRC-12	The structure of the SpeleoDrone must provide access to switch out the battery	Demonstrate	Demonstrate that the batteries can be swapped out
DRN-STRC-13	All structural interfaces housing electronics or other water-sensitive components shall support sealing against particulate and moisture ingress	Analysis	Analyze each component for regions sensitive to moisture and the corresponding impact
DRN-AERO-01	The propulsion system shall have a mass of no more than 0.25 kg	Testing	Before assembly, put the individual components on a scale
DRN-AERO-02	The propellers' diameter shall not exceed 18 cm	Inspection	Inspect the model dimensions and measure the diameter of the propellers
DRN-AERO-03	The minimum thrust provided by the rotors shall be at least 40N	Testing	Fix the rotors to a thrust stand and measure the maximum force exerted
DRN-AERO-04	Maximum cost of the rotors and motors shall be below 100EUR	Inspection	Inspect the cost of the combination of motors and rotors

Table 15.2: Subsystem requirement verification procedures

Requirement ID	Description	Method	Procedure
DRN-AERO-05	The clearance between rotors shall be at least 1cm	Inspection	Inspect the finished design by measuring the clearance
DRN-AERO-06	The propulsion system shall use less than 5000W of power at all times	Analysis	Analyze the component draw from each component to determine the maximum power draw
DRN-AERO-07	The drone shall have at least 15 minutes of flight time in hovering flight	Demonstrate	Demonstrate that the drone can hover for more than 15 minutes
DRN-AERO-08	The combined noise emitted by the rotors shall be less than 85 dB	Testing	Fix the drone to the ground, turn the throttle to maximum and use a sound level meter to measure the noise levels
CTRL-DRN-01	The system shall allow for angular acceleration of up to 380 rad/s^2 or less in each axis during nominal flight conditions	Analysis	Mathematically analyze the maximum achievable accelerations based on the equations of motion
CTRL-DRN-02	The system shall limit the overshoot of each state variable to less than 10% of the commanded value during step-response tests, measured under nominal flight conditions	Analysis	Analyze the states after inducing a step input in a simulation
CTRL-DRN-03	The system shall autonomously reduce speed when nearing physical boundaries within 50 cm, based on onboard sensors	Analysis	Analyze how close to an object the AI algorithm gets before the system reduces the speed of the system through with the use of test data
CTRL-DRN-04	The control system shall support soft constraints to limit roll and pitch angles to less than 70 degrees during tight maneuvering	Inspection	Inspect whether the flight controller limits the roll and pitch rates of the controller between a certain range
CTRL-DRN-05	The system shall compensate for minor disturbances (<30 N impact force) without catastrophic loss of stability	Analysis	Analyze the disturbance forces at which the quadcopter is able to return to a stable position through simulation
CTRL-DRN-06	The system shall include a Return-to-Home function that automatically activates upon signal loss, battery levels below 30%, or user instruction	Testing	Test the return to home function in a condition similar to a cave environment and observe whether it works
DRN-AVIO-01	The batteries shall not have a capacity larger than 160 Wh	Inspection	Inspect the specifications of the used batteries and compare to the energy stored
DRN-AVIO-02	The batteries shall be possible to separate from the drone in less than ten minutes	Demonstrate	Demonstrate the ease of replacing the batteries by letting an experienced person replace them within ten minutes
DRN-AVIO-03	The batteries shall be rechargeable	Inspection	Inspect the specifications of the chosen batteries to ensure they are rechargeable
DRN-AVIO-04	The batteries shall have a minimum voltage of 22.2 V	Testing	Test with a voltmeter that sufficient voltage is being supplied
DRN-AVIO-05	The batteries shall be able to provide a minimum total current of 50 A	Testing	Test with an ammeter that sufficient current is being supplied
DRN-AVIO-06	The batteries shall have a total capacity large enough to power the drone in hovering conditions for at least 10 minutes	Demonstrate	Demonstrate that the drone can hover for more than 15 minutes

Table 15.2: Subsystem requirement verification procedures

Requirement ID	Description	Method	Procedure
DRN-AVIO-07	Voltage converters shall be included in the electronic circuit for components that draw less than 22.2 V	Inspection	Check that voltage converters are integrated for each component
DRN-AVIO-08	The system shall be supplied with a total of 10 batteries: 4 batteries designated for the flight and charging loop, and 6 additional spare batteries	Inspection	Inspect the part list to ensure the correct amount of batteries is supplied
DRN-AVIO-09	Sensors used for control shall have a main and redundant variant	Inspection	Inspect the design for redundancy of every sensor
DRN-AVIO-10	The avionics subsystem shall be able to measure acceleration with 0.05 mg resolution	Analysis	Analyze the predicted error in the accelerations through sensor accuracy and simulation error
DRN-AVIO-11	The avionics subsystem shall be able to measure rotational rate with 0.003°/sec resolution	Analysis	Analyze the predicted error in the rotational rates through sensor accuracy and simulation error
DRN-AVIO-12	The avionics subsystem shall be able to measure the distance between the drone and the ceiling of the cave with 1% accuracy	Testing	Compare the distance measurements with the actual distance measured from the ceiling
DRN-AVIO-13	The avionics subsystem shall be able to measure the distance between the drone and the floor of the cave with 1% accuracy	Testing	Compare the distance measurements with the actual distance measured from the ground
DRN-AVIO-14	The avionics subsystem shall be able to measure the relative humidity in the vicinity of the drone with 0.5%RH accuracy	Testing	Compare the measurement data of the drone with that of an external validated hygrometer
DRN-AVIO-15	The avionics subsystem shall be able to measure the ambient temperature in the vicinity of the drone with 0.1°C accuracy	Testing	Compare the measurement data of the drone with that of external validated thermometers
DRN-AVIO-16	The avionics subsystem shall be equipped with a remote identification transmitter	Inspection	Inspect the system to see if the component is present
DRN-PG-01	The photovoltaic charging system shall not be heavier than 20 kg	Testing	Put the photovoltaic charging system on a scale and compare to the 20 kg
DRN-PG-02	The system shall be transportable within combined dimension of 158 cm (length + width + height)	Inspection	Measure whether the system fits within the size constraint
DRN-PG-03	The system shall be capable of simultaneously charging two 6s 7000 mAh batteries in 40 minutes, and one 1s 560 mAh and one 4S 350 mAh battery within 2 hours	Demonstration	Demonstrate the system charging empty batteries
DRN-PG-04	The system shall provide power to continuously charge a laptop and the NVIDIA Jetson Xavier NX computing module next to battery charging	Inspection	Inspect the design for a connection between a laptop and the computing module
DRN-PG-05	The system shall prevent batteries from overheating above 45 $^{\circ}C$ during charging and storage	Analysis	Analyze the heat generated by the system and the resulting maximum temperatures which the batteries may experience during operation

15.2. Model Verification & Validation

This section covers the methodology for model verification & validation, which was carried out and presented in the sections where models were used. In addition, it covers tests that were not carried out, but may be carried out during future development. The purpose of verifying the models is to ensure that it is error-free and that its outputs match the underlying equations. Similarly, model validation aims to determine whether the model outputs match the real world. To achieve this, several types of tests were executed: unit tests, system tests, and, where applicable, a sensitivity analysis. The extent of these tests is proportional to the size of the model. With more complex models being tested more thoroughly, to compensate for them being more error-prone. Moreover, unit and system tests have unique IDs associated with them to make them traceable and referenceable. The test IDs are of the form `{Program-ID}-{Test-Type}-{Test#}`, where the program ID differentiates between models and the test-type is either UT or ST for unit test and system test, respectively.

15.2.1. Unit Testing

Unit tests are the lowest-level form of testing performed on the models. Their primary function is to check whether smaller blocks of the model perform their function as intended. The tests come in a wide range of forms, including comparison to exact solutions for simplified structures, checks for correct matrix dimensions and terms, and tests related to appropriate error handling.

The aim while performing unit tests is to provide as much coverage of the model as possible, to the point where there is sufficient confidence that the part of the model functions as intended. However, this does not guarantee that the interfacing between blocks functions correctly. Thus, system tests are carried out as well.

15.2.2. System Testing

System tests evaluate whether the blocks are integrated correctly by testing the interfaces and the complete model. Four types of system tests will be used: deterministic tests, extreme value tests, convergence tests, and coverage tests.

The different tests serve the following purposes: deterministic tests aim to verify that the output to a fixed input remains identical across multiple simulations. Extreme value tests ensure that the model does not fail under extreme input conditions. Convergence tests determine whether the model converges to a solution within a sufficiently small margin when the step size decreases. Finally, coverage tests are run across the unit tests to ensure the unit tests cover the complete model.

15.2.3. Sensitivity Analysis

The purpose of performing a sensitivity analysis on used models is to quantify the effect that approximations of key parameters may have on the output. This comes in two steps: determining the range of values the key parameters can take on, and comparing the outputs across multiple simulations with unique input parameters.

Where feasible, Monte Carlo simulations will be used to provide a more complete range of output values. However, for pre-existing models, where this may prove difficult due to a lack of access to the underlying code or long run times, a subset of extreme input values will be used instead.

15.2.4. Model Validation

To validate the models, the inputs and outputs were compared to values found in literature. For example, the thrust and moment coefficients that were used in the Simulink model were compared to typical values used in simulation. This is to avoid unrealistic values being used, which are not reproducible in reality.

Furthermore, should similar models exist, the outputs will be compared to determine whether similar values are obtained, improving the credibility of the model. However, discrepancies between the assumptions made in the different models should be carefully tracked and quantified to determine whether the comparison is valid.

15.3. Requirement Compliance

Each design must be thoroughly verified to confirm compliance with all user requirements, providing clear evidence of whether the proposed solution meets the specified performance criteria. As shown in Table 15.3, every requirement is systematically evaluated and labeled with a ”PASS” (marked in green) for compliance or ”FAIL” (marked in red) for non-compliance, along with a reference in the ”Remarks” column directing readers to the relevant section for detailed justification. For completeness, the table includes STK-OPR-03, though this requirement has since been renegotiated and superseded by the updated cost requirement STK-OPR-3.1. This structured approach ensures transparency in the verification process and facilitates traceability between design decisions and stakeholder expectations.

Table 15.3: Compliance Matrix

ID	Description	Compliance	Remarks
STK-DRN-1	The system shall be able to fully map a cave system distance of up to 500 m from the entrance, within 1 week	PASS	See Chapter 5
STK-DRN-2	The system shall be able to visually map the cave system with a resolution of 1 cm.	PASS	Successfully mapping with resolution of 0.471 cm/px, see Chapter 5
STK-DRN-3	The system shall be able to georeference a location on the map with a resolution of 1 cm.	PASS	See Chapter 5
STK-DRN-4	The system shall be able to pass through any opening an adult human can pass	FAIL	The drone is 40.4 cm, see Chapter 4
STK-OPR-01	The system shall comply with EASA requirements for safe operation of drones.	PASS	See Section 2.3
STK-OPR-02	The system shall be 75% by weight recyclable, excluding the payload	PASS	See Chapter 12
STK-OPR-03	The system shall have a purchase cost of no more than €25,000	N/A	Requirement renegotiated, see requirement **STK-OPR-3.1**
STK-OPR-3.1	The system shall have a purchase cost of no more than € 50,000	PASS	The purchase cost was set at € 45,000, see Chapter 13
STK-OPR-04	The system shall be suitable for transportation as air cargo	PASS	See Section 2.3 for further specifications, see Section 10.6 where designed casing was discussed
STK-OPR-05	The system shall be able to operate in a remote location (i.e. no access to grid power or cellular telephone networks)	PASS	Charging station provides power, see Section 10.4; System does not use cellular networks
STK-OPR-06	The system shall not produce any emissions inside the cave system.	PASS	Chosen battery will not produce any emissions while in nominal conditions, see Chapter 3
STK-OPR-07	The system shall minimize disturbance to the site being investigated	PASS	Fiber optic cable itself is small enough that disturbance is minimal, additionally biodegradable sleeve was integrated, see Section 10.2
STK-OPR-08	The system shall be designed to be operable with minimal training	PASS	Implemented AI for navigation (see Section 8.4) and user-friendly interface in ground control (Section 10.5)

The system demonstrates strong compliance, successfully meeting 11 out of 12 defined requirements. The only exception is **STK-DRN-4**, which addresses the drone's dimensional constraint. The current design marginally exceeds the specified 40 cm limit by less than 1%, a deviation primarily driven by functional necessity rather than oversight. The 40 cm threshold was set arbitrarily, and the minimal excess—just 2 mm on either side—was essential to accommodate 7-inch propellers, which were selected to achieve sufficient thrust-to-weight ratio and ensure extended endurance. Reducing the propeller size to, for example, 6 inches would significantly impact flight time, compromising mission viability and eliminating the system's competitive edge over platforms like the Elios 2 and 3. Additionally, larger propellers operating at lower RPMs are inherently more efficient and generate less noise, which aligns with the need to minimize acoustic disturbance in sensitive environments. The expanded frame also provides necessary clearance for the integrated payload bay, supporting key mission functionalities. To further mitigate environmental impact, ducted propellers have been employed to reduce noise levels during operation. Overall, the slight deviation in size is a well-justified trade-off that enables enhanced performance without meaningfully compromising system compatibility or deployability.

16. Post DSE Activities

This chapter covers all the post DSE activities to be performed should development continue. First, Section 16.1 presents a gantt chart describing the timeline of future activities. Then, Section 16.2 provides an overview of the design and development logic describing the further development of the design.

16.1. Project Gantt Chart

A Gantt chart was created to determine the timeline of activities should the design continue post DSE. The Gantt chart covers the final design iterations required and all the verification & validation procedures required before arriving at a market-ready design. The gantt chart is displayed Figure 16.1.

The first phase displays the final iterations of the design before arriving at the final configuration. This implies the development of each subsystem until the design converges to an optimal solution.

After that, the first prototypes are made and the software is finalized based on the final characteristics. After successful prototype tests, the final integration and assembly are done before the verification and testing phase can start.

The testing will begin with basic off-site tests and move into more complex and extreme tests as time goes on until the design is verified appropriately. If all tests are passed, the design is ready to go onto the market.

16.2. Project Design and Development

Since the final design can be further developed and improved, a project design and development was created in which the next steps are laid out. It is shown in Figure 16.2, in which the arrow pointing downwards on the right side is the overall timeline to which all the modules are connected to. The chronological order can be determined by following the inputs and converging the subsystems into each other and into the overall timeline.

SpeleoDrone

Read-only view, generated on 18 Jun 2025

Instagantt

	ACTIVITIES	ASSIGNEE	EH	START	DUE	STATUS	%
	Design Iteration:		-	30/Jun	20/Jul		0%
1	Payload Reconsideration	Unassigned	-	30/Jun	04/Jul	Not started	0%
2	Structures Iteration	Unassigned	-	02/Jul	18/Jul	Not started	0%
3	Aerodynamics Iteration	Unassigned	-	02/Jul	11/Jul	Not started	0%
4	Avionics Iteration	Unassigned	-	07/Jul	11/Jul	Not started	0%
5	Operations Iteration	Unassigned	-	11/Jul	15/Jul	Not started	0%
6	Final Design Configuration	Unassigned	-	14/Jul	20/Jul	Not started	0%
	Simulation and Modelling:		-	21/Jul	08/Aug		0%
8	Develop 3D model	Unassigned	-	21/Jul	25/Jul	Not started	0%
9	Simulate drone navigation	Unassigned	-	25/Jul	31/Jul	Not started	0%
10	Model environmental factors	Unassigned	-	25/Jul	31/Jul	Not started	0%
11	Risk analysis for environme...	Unassigned	-	30/Jul	31/Jul	Not started	0%
12	Simulate communication si...	Unassigned	-	31/Jul	07/Aug	Not started	0%
13	Test autonomy algorithms	Unassigned	-	31/Jul	07/Aug	Not started	0%
14	Verify and validate algorith...	Unassigned	-	04/Aug	08/Aug	Not started	0%
	Prototyping:		-	05/Aug	28/Aug		0%
16	3D print/manufacture airfra...	Unassigned	-	05/Aug	12/Aug	Not started	0%
17	Assemble a basic working p...	Unassigned	-	12/Aug	18/Aug	Not started	0%
18	Mount essential component...	Unassigned	-	18/Aug	22/Aug	Not started	0%
19	Prototype swappable paylo...	Unassigned	-	22/Aug	28/Aug	Not started	0%
	Software Development:		-	05/Aug	06/Oct		0%
21	Integrate flight control soft...	Unassigned	-	05/Aug	25/Aug	Not started	0%
22	Implement SLAM for mappi...	Unassigned	-	05/Aug	29/Aug	Not started	0%
23	Integrate sensor drivers	Unassigned	-	25/Aug	05/Sep	Not started	0%
24	Develop autonomous navig...	Unassigned	-	01/Sep	29/Sep	Not started	0%
25	Build ground control interfa...	Unassigned	-	15/Sep	06/Oct	Not started	0%
	Integration and Assembly:		-	29/Aug	10/Sep		0%
27	Mount electronics	Unassigned	-	29/Aug	02/Sep	Not started	0%
28	Wire and secure all compon...	Unassigned	-	01/Sep	03/Sep	Not started	0%
29	Calibrate sensors	Unassigned	-	04/Sep	05/Sep	Not started	0%
30	Upload and configure softw...	Unassigned	-	04/Sep	09/Sep	Not started	0%
31	Conduct dry-run power-on t...	Unassigned	-	08/Sep	10/Sep	Not started	0%
	Ground Testing:		-	11/Sep	19/Sep		0%
33	Power-on tests for all comp...	Unassigned	-	11/Sep	15/Sep	Not started	0%
34	Validate sensor readings in ...	Unassigned	-	15/Sep	18/Sep	Not started	0%
35	Run motors without lift to en...	Unassigned	-	15/Sep	18/Sep	Not started	0%
36	Test communication betwe...	Unassigned	-	15/Sep	18/Sep	Not started	0%
37	Simulate sensor failures to t...	Unassigned	-	17/Sep	19/Sep	Not started	0%
38	Develop list of required fixe...	Unassigned	-	19/Sep	19/Sep	Not started	0%
	Flight Testing (Indoor):		-	22/Sep	06/Oct		0%
40	Conduct basic hover and m...	Unassigned	-	22/Sep	23/Sep	Not started	0%
41	Tune PID flight control para...	Unassigned	-	23/Sep	26/Sep	Not started	0%
42	Test obstacle avoidance in i...	Unassigned	-	24/Sep	26/Sep	Not started	0%
43	Record SLAM map generati...	Unassigned	-	26/Sep	02/Oct	Not started	0%
44	Evaluate stability and endur...	Unassigned	-	29/Sep	02/Oct	Not started	0%
45	Map accuracy and error an...	Unassigned	-	01/Oct	06/Oct	Not started	0%
	Field Testing (Simulated Cave):		-	07/Oct	28/Oct		0%
47	Deploy in a real or mock cave	Unassigned	-	07/Oct	10/Oct	Not started	0%
48	Fly complete missions auto...	Unassigned	-	09/Oct	16/Oct	Not started	0%
49	Evaluate communications p...	Unassigned	-	13/Oct	17/Oct	Not started	0%
50	Measure real-time SLAM/m...	Unassigned	-	14/Oct	20/Oct	Not started	0%
51	Monitor battery performanc...	Unassigned	-	14/Oct	24/Oct	Not started	0%
52	Final tuning of hardware/sof...	Unassigned	-	24/Oct	28/Oct	Not started	0%
	Evaluation and Troubleshooting:		-	29/Oct	21/Nov		0%
54	Analyze flight logs and sens...	Unassigned	-	29/Oct	31/Oct	Not started	0%
55	Identify system bottlenecks	Unassigned	-	31/Oct	03/Nov	Not started	0%
56	Re-calibrate and re-test co...	Unassigned	-	03/Nov	06/Nov	Not started	0%
57	Patch bugs in flight softwar...	Unassigned	-	06/Nov	10/Nov	Not started	0%
58	Conduct targeted re-tests o...	Unassigned	-	07/Nov	12/Nov	Not started	0%
59	Validate all performance cri...	Unassigned	-	10/Nov	14/Nov	Not started	0%
60	Final Buffering/Polishing	Unassigned	-	17/Nov	21/Nov	Not started	0%

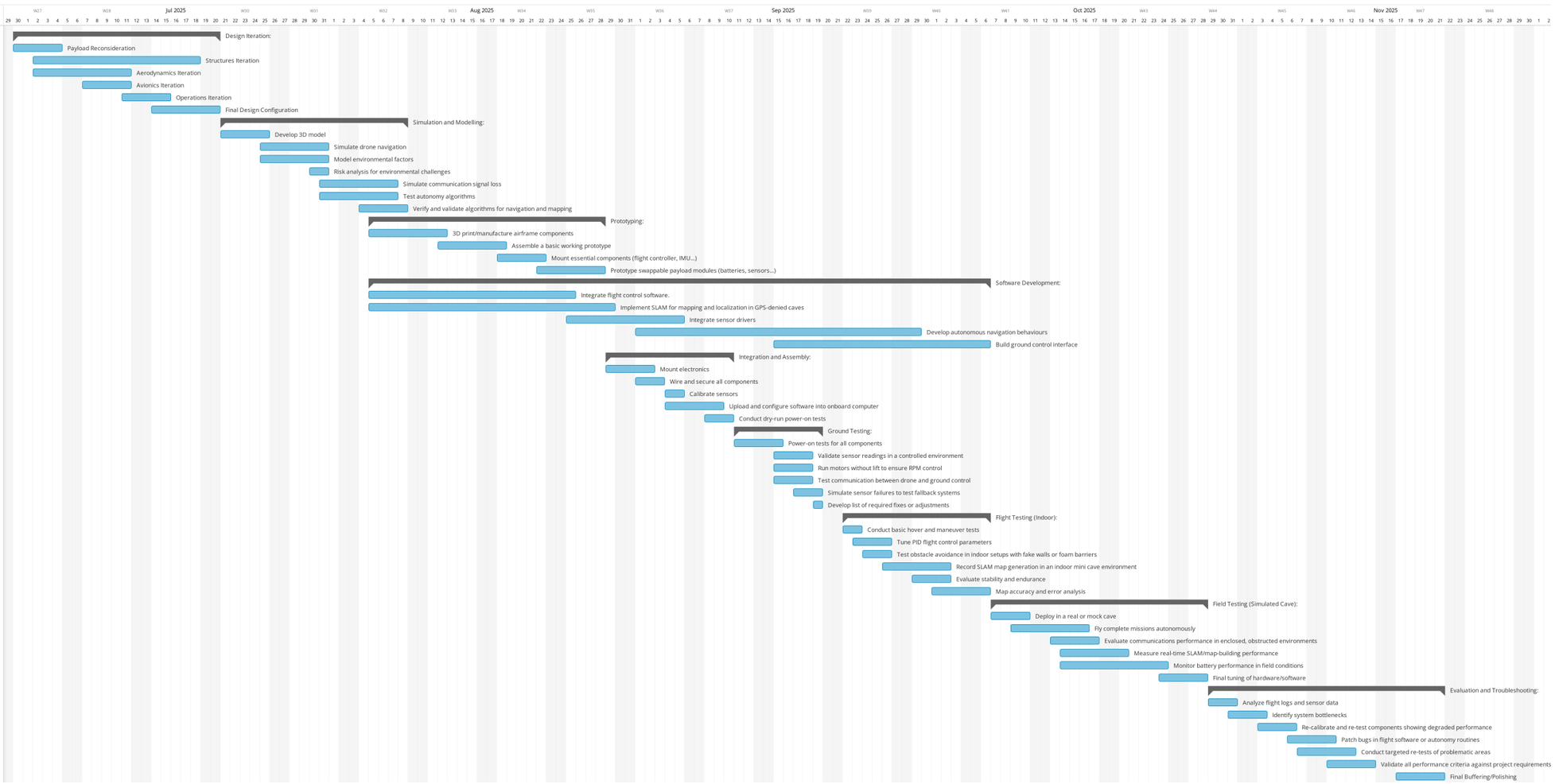

Figure 16.1: Post DSE gantt chart

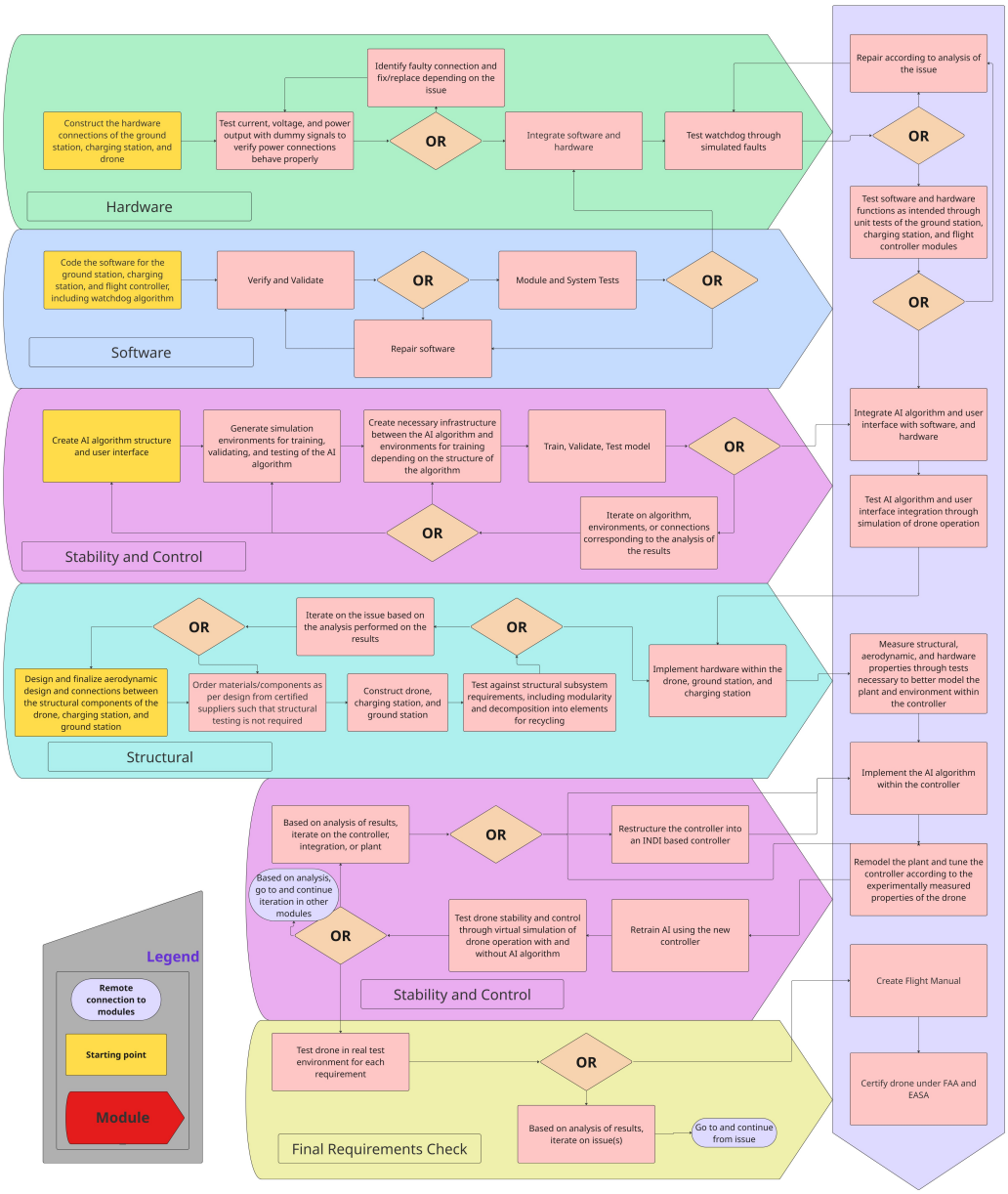

Figure 16.2: Project Design and Development Diagram

17. Conclusion

The objective of this report was to document the design of an innovative unmanned aerial system (UAS) to be remotely operated by an archeologist, capable of visually mapping a cave system while maintaining site integrity, within 10 weeks by 10 students. The design is vital to avoiding unsafe working conditions from toxic environments and opens up opportunities to explore inaccessible caves.

After a trade-off between several promising configurations was performed, a quadcopter design with switchable batteries that is largely AI-controlled came out on top. This design was further developed with a focus on payload, structures, aerodynamics, avionics, control and operations and logistics. Since each subsystem is closely related to each other, this was an iterative design procedure that slowly converged to a final configuration.

This led to a final mass of 3174 grams with a power usage at maximum range of 1073 Watts, including contingencies. The maximum endurance while continuously hovering was determined to be 18.7 minutes. Furthermore, the design is over 75% recyclable and produces minimal disturbance to the site.

To navigate the cave, a control system was implemented that allows for fully autonomous control, combining payload data, sensor readings, AI processing and simulation outputs into a prediction of the position, orientation and velocity. The operator can also manually provide the quadcopter with commands through a fiber optic cable connection link, which does not disturb the site long-term. The cable connects to a ground station, where data is processed and the cave is mapped the moment data is collected. Additionally, a solar-powered charging station is present that is capable of continuously charging spare batteries to maximize operation time.

From the design iterations, a CAD model was constructed that is displayed in Figure 17.1. Here, the blue, green, orange and red elements represent the fiber optic reel, batteries, payload and propellers, respectively. Additionally, the rotors have ducts around them serving to reduce noise, increase efficiency and provide collision protection. The final design is capable of mapping and georeferencing caves within 500m from the entrance within a week time, fitting through any holes smaller than 41cm. This barely violates the requirement of 40cm, but it comes at greatly improved performance, required for successful completion of the mission.

Figure 17.1: CAD model of the final design of the SpeleoDrone

Should the design be further developed, the connections, casings and wiring should be defined in more detail. Furthermore, the controller should be tuned with a developed AI model and experimental sensor readings from prototypes. After the design is complete, extensive verification testing of the design should be executed to guarantee that the design meets all requirements and satisfies the user's needs. Finally, if all tests are passed successfully, the design can be made available to the public and revolutionize cave exploration in a safe and efficient manner, while maintaining site integrity.

References

[1] Ali Akturk and Cengiz Camci. “Tip Clearance Investigation of a Ducted Fan Used in VTOL Unmanned Aerial Vehicles—Part I: Baseline Experiments and Computational Validation”. In: *Journal of Turbomachinery* 136.2 (Sept. 2013). DOI: 10.1115/1.4023468. URL: https://doi.org/10.1115/1.4023468.

[2] M. Ashby, H. Shercliff, and D. Cebon. *Materials: engineering, science, processing and design*. 4th ed. Oxford, United Kingdom: Butterworth-Heinemann, 2019.

[3] M. Ashby et al. *Granta EduPack Eco Audit Tool-A White Paper*. Tech. rep. ANSYS, Inc., 2021.

[4] Vicente Bayarri et al. “Integration of Remote-Sensing Techniques for the Preventive Conservation of Paleolithic Cave Art in the Karst of the Altamira Cave”. In: *Remote Sensing* 15.4 (Feb. 2023), p. 1087. DOI: 10.3390/rs15041087.

[5] M. Beisert et al. *SpeleoDrone - Baseline Report - Group 24*. Tech. rep. TU Delft, 2025.

[6] M. Beisert et al. *SpeleoDrone - Midterm Report - Group 24*. Tech. rep. TU Delft, 2025.

[7] M. Beisert et al. *SpeleoDrone - Project Plan - Group 24*. Tech. rep. TU Delft, 2025.

[8] Herman de Beukelaer et al. “Overview of the mechanical, thermal and barrier properties of biobased and/or biodegradable thermoplastic materials”. In: *Polymer Testing* 116 (Dec. 2022). DOI: https://doi.org/10.1016/j.polymertesting.2022.107803.

[9] Bhawna et al. “Advancements and challenges in lithium-ion and lithium-polymer batteries: towards sustainable energy storage solutions”. In: *Ionics* (2025). ISSN: 18620760. DOI: 10.1007/s11581-025-06309-x.

[10] F Binz and Dieter Moormann. “Actuator modelling for attitude control using incremental nonlinear dynamic inversion”. In: *International Journal of Micro Air Vehicles* 12 (Dec. 2020), p. 175682932096192. DOI: 10.1177/1756829320961925.

[11] F. Broekhuizen et al. *SpeleoDrone - Baseline Report Plan - Group 24*. Tech. rep. TU Delft, 2025.

[12] Kim Cardosi and Dan Hannon. *Guidelines for the Use of Color in ATC Displays*. Technical Report DOT/FAA/AR-99/52. Report No. DOT-VNTSC-FAA-98-5. Washington, DC: U.S. Department of Transportation, Federal Aviation Administration, June 1999. URL: https://rosap.ntl.bts.gov/view/dot/34408.

[13] A. Cervone and B.T.C. Zandbergen. *Reader Electrical Power Systems for Aerospace Vehicles*. Tech. rep. TU Delft, 2017.

[14] Deborah D. L. Chung. “Properties of Carbon Fibers”. In: *Carbon Fiber Composites*. Ed. by Deborah D. L. Chung. http://nguyen.hong.hai.free.fr/EBOOKS/…/91697_04.pdf. Elsevier (reprinted), 1987. Chap. 4, pp. 70–89.

[15] R. J. Clarke and D. A. Miller. “Computational Micromechanics for the Optimization of Compression Strength of Unidirectional Carbon Fiber Composites for Use in Wind Turbine Blades”. In: *Journal of Energy and Power Technology* 2.2 (2020), p. 010. DOI: 10.21926/jept.2002010.

[16] Izzat Al-Darraji, Morched Derbali, and Georgios Tsaramirsis. “Tilting-rotors Quadcopters: A New Dynamics Modelling and Simulation based on the Newton-Euler Method with Lead Compensator Control”. In: *2021 8th International Conference on Computing for Sustainable Global Development (INDIACom)*. 2021, pp. 363–369.

[17] Charles N. Eastlake. “Aircraft Cost Analysis”. In: *General Aviation Aircraft Design*. Elsevier, 2014, pp. 33–53. DOI: 10.1016/B978-0-12-397308-5.00002-7.

[18] Eurostat. *NACE Rev. 2: Statistical Classification of Economic Activities in the European Community*. Methodologies and Working Papers. Catalog No. KS-RA-07-015-EN-N. European Commission. Dec. 2008. URL: https://ec.europa.eu/eurostat/web/products-manuals-and-guidelines/-/KS-RA-07-015.

[19] Amir Feizollahi and Rene V Mayorga. “Optimized motion planning of manipulators in partially-known environment using modified D* Lite algorithm”. In: *WSEAS TRANSACTIONS on SYSTEMS* 16 (2017), pp. 69–75. ISSN: 2224-2678.

[20] Edward Frank et al. “Geology of Isla de Mona, Puerto Rico”. In: *Journal of Cave and Karst Studies* 69 (July 1998), pp. 69–72. URL: https://caves.org/wp-content/uploads/Publications/JCKS/v60/V60N2-Frank-Geology.pdf.

[21] Daniel Garcia-Pozuelo et al. “Bump Modeling and Vehicle Vertical Dynamics Prediction”. In: *Advances in Mechanical Engineering* 6 (2014), pp. 1–10. DOI: 10.1155/2014/736576. URL: https://www.academia.edu/104448426/Bump_Modeling_and_Vehicle_Vertical_Dynamics_Prediction.

[22] P J Gibson, P Lyle, and D M George. “Application of Resistivity and Magnetometry Geophysical Techniques for Near-Surface Investigations in Karstic Terranes in Ireland”. In: *Journal of Cave and Karst Studies* 66 (2 2004), pp. 35–38.

[23] Charles S. Chiau Graham Hawkes Glen Sussman. “Ocean Deployable Biodegradable Optical Fiber Cable”. US 20110299819 A1. U.S. Patent. Dec. 2011. URL: https://patents.google.com/patent/US20110299819A1/en.

[24] H. A. Hashim. “Advances in UAV avionics systems architecture, classification and integration: A comprehensive review and future perspectives”. In: *Results in Engineering* 25 (Mar. 2025). ISSN: 25901230. DOI: 10.1016/j.rineng.2024.103786.

[25] Zheng-Ming Huang. “Micromechanical Failure Analysis of Unidirectional Composites”. In: *Failure Analysis*. Ed. by Zheng-Ming Huang and Sayed Hemeda. Submitted: 24 May 2018; Reviewed: 08 August 2018; Published: 05 November 2018. IntechOpen, 2018. DOI: 10.5772/intechopen.80807. URL: https://doi.org/10.5772/intechopen.80807.

[26] I. N. Ibrahim, M. A. A. Akkad, and I. V. Abramov. “UAV efficient PID and LQR controllers design based on its stochastic state space dynamics model including disturbances”. In: *2018 Moscow Workshop on Electronic and Networking Technologies (MWENT)*. 2018, pp. 1–9. DOI: 10.1109/MWENT.2018.8337171.

[27] Dmitry Ivanov. *AENGM0091 Composites Design, Manufacture and Product Development – Coursework Assignment*. Bristol Composites Institute, University of Bristol. 2025.

[28] Peiyuan Jiang et al. “A Review of Yolo Algorithm Developments”. In: *Procedia Computer Science* 199 (2022). The 8th International Conference on Information Technology and Quantitative Management (ITQM 2020 & 2021), pp. 1066–1073. DOI: 10.1016/j.procs.2022.01.135. URL: https://www.sciencedirect.com/science/article/pii/S1877050922001363.

[29] Hatem Kandeel, Ebrahim Abdelmaksod, and Abdelrady Elnady. “Modeling and Control of X-Shape Quadcopter”. In: *IOSR Journal of Mechanical and Civil Engineering* 19 (Feb. 2022), pp. 46–57. DOI: 10.9790/1684-1901034657.

[30] Larisa Kapustina et al. “The global drone market: main development trends”. In: *SHS Web of Conferences* 129 (Jan. 2021), p. 2. DOI: 10.1051/shsconf/202112911004.

[31] D. W. Kurtz and J. E. Made. *A Review of Aerodynamic Noise From Propellers, Rofors, and Lift Fans*. Technical Report 32-7462. National Aeronautics and Space Administration, Jan. 1970.

[32] Curtis E. Larsen and Ivatury S. Raju. *Moving Aerospace Structural Design Practice to a Load and Resistance Factor Approach*. Tech. rep. 20160007733. NASA Langley Research Center, 2016. URL: https://ntrs.nasa.gov/api/citations/20160007733/downloads/20160007733.pdf.

[33] Jonathan Last. *The Archaeology of English Caves and Rock-Shelters: A Strategy Document*. Tech. rep. Accessed: 2025-05-07. Fort Cumberland Road, Eastney, Portsmouth PO4 9LD: English Heritage Centre for Archaeology, 2002. URL: https://historicengland.org.uk/research/results/reports/5231/TheArchaeologyofEnglishCavesandRock-Shelters_AStrategyDocument.

[34] B. D. Lawrence and J. A. Simmons. “Measurements of atmospheric attenuation at ultrasonic frequencies and the significance for echolocation by bats”. In: *The Journal of the Acoustical Society of America* 71.3 (1982), pp. 585–590. DOI: 10.1121/1.387529.

[35] David Lennström, Thomas Lindbom, and Arne Nykänen. “Prominence of tones in electric vehicle interior noise”. In: *Internoise 2013: Noise Control for Quality of Life*. ÖAL Österreichischer Arbeitsring für Lärmbekämpfung, 2013, pp. 508–515. ISBN: 9781632662675.

[36] X. Liu et al. “The role of energy consumption in global carbon intensity change: A meta-frontier-based production-theoretical decomposition analysis”. In: *Energy Economics* 109 (May 2022), p. 105968. ISSN: 01409883. DOI: 10.1016/j.eneco.2022.105968.

[37] Teppo Luukkonen. *Modelling and control of Quadcopter*. Aug. 2011. URL: https://sal.aalto.fi/publications/pdf-files/eluu11_public.pdf.

[38] Teppo Luukkonen. “Modelling and control of quadcopter”. In: *Independent research project in applied mathematics, Espoo* 22.22 (2011), pp. 1–24.

[39] D. Mackay. *Path Planning with D*Lite: Implementation and Adaptation of the D*Lite Algorithm*. Technical Memorandum DRDC Suffield TM 2005-242. Medicine Hat, Alberta, Canada: Defence R&D Canada – Suffield, Dec. 2005.

[40] Anwar M.N. Malgoezar et al. “Experimental characterization of noise radiation from a ducted propeller of an unmanned aerial vehicle”. In: *International Journal of Aeroacoustics* 18 (4-5 July 2019), pp. 372–391. ISSN: 20484003. DOI: 10.1177/1475472X19852952.

[41] Adrien Michez, Stéphane Broset, and Philippe Lejeune. “Ears in the Sky: Potential of Drones for the Bioacoustic Monitoring of Birds and Bats”. In: *Drones* 5.1 (Jan. 2021), p. 9. DOI: 10.3390/drones5010009. URL: https://doi.org/10.3390/drones5010009.

[42] JE Mylroie. “Cave surveys, cave size, and flank margin caves”. In: *Compass Tape* 17.4 (2007), pp. 8–16.

[43] Aws Abdulsalam Najm and Ibraheem Kasim Ibraheem. “Nonlinear PID controller design for a 6-DOF UAV quadrotor system”. In: *Engineering Science and Technology, an International Journal* 22.4 (2019), pp. 1087–1097. ISSN: 2215-0986. DOI: https://doi.org/10.1016/j.jestch.2019.02.005. URL: https://www.sciencedirect.com/science/article/pii/S2215098618318846.

[44] C. Negrato. “Prediction of the performance of ducted propellers with BEM and hybrid RANS-BEM methods”. In: *Marin* (Jan. 2015). URL: https://repository.tudelft.nl/islandora/object/uuid%3A5dbf8251-33a8-41f8-a454-2b1b55cbf1c7.

[45] A.T. Nettles. *Basic Mechanics of Laminated Composite Plates*. NASA Reference Publication NASA-RP-1351. 103 pages. Huntsville, AL: NASA, Marshall Space Flight Center, 1994.

[46] Ryusuke Noda et al. “Characterization of the low-noise drone propeller with serrated Gurney flap”. In: *Frontiers in Aerospace Engineering* 1 (2022). ISSN: 2813-2831. DOI: 10.3389/fpace.2022.1004828. URL: https://www.frontiersin.org/journals/aerospace-engineering/articles/10.3389/fpace.2022.1004828.

[47] Sergi Palleja-Cabre et al. “Reduction of Shrouded Propeller Noise With Over-Tip-Rotor Liners”. In: *28th AIAA/CEAS Aeroacoustics 2022 Conference* (May 2024). DOI: 10.2514/6.2024-3407. URL: https://doi.org/10.2514/6.2024-3407.

[48] Bizhao Pang, C. H. John Wang, and Kin Huat Low. “Framework of Level-of-Autonomy-based Concept of Operations: UAS Capabilities”. In: *2020 IEEE International Conference on Unmanned Aircraft Systems (ICUAS)*. IEEE. 2020, pp. 1–10. DOI: 10.1109/ICUAS48674.2020.9213937. URL: https://ieeexplore.ieee.org/document/9213937.

[49] S. B Peck and J. Kukalova-Peck. “The Subterranean Fauna and Conservation of Mona Island (Puerto Rico): A Caribbean Karst Environment”. In: *NSS Bulletin* 43 (1981), pp. 59–68.

[50] Enrico Petritoli, Fabio Leccese, and Lorenzo Ciani. “Reliability and Maintenance Analysis of Unmanned Aerial Vehicles”. In: *Sensors* 18.9 (2018). DOI: 10.3390/s18093171. URL: https://www.mdpi.com/1424-8220/18/9/3171.

[51] Hao Qin et al. “Evaluation of tensile strength variability in fiber reinforced composite rods using statistical distributions”. In: *Frontiers in Built Environment* 10 (Jan. 2025). DOI: 10.3389/fbuil.2024.1506743. URL: https://www.frontiersin.org/journals/built-environment/articles/10.3389/fbuil.2024.1506743.

[52] Borrdephong Rattanagraikanakorn et al. “Multibody system modelling of unmanned aircraft system collisions with the human head”. In: *International Journal of Crashworthiness* 25.6 (2019), pp. 689–707. DOI: 10.1080/13588265.2019.1633818.

[53] Eiad Saif and İlyas Eminoğlu. “Modelling of quad-rotor dynamics and Hardware-in-the-Loop simulation”. In: *The Journal of Engineering* 2022.10 (2022), pp. 937–950. DOI: https://doi.org/10.1049/tje2.12152. eprint: https://ietresearch.onlinelibrary.wiley.com/doi/pdf/10.1049/tje2.12152. URL: https://ietresearch.onlinelibrary.wiley.com/doi/abs/10.1049/tje2.12152.

[54] Hossain Sakhawat et al. “Effect of Fiber Orientation and Volume Fraction on Young’s Modulus for Unidirectional Carbon Fiber Reinforced Composites: A Numerical Investigation”. In: *Malaysian Journal on Composites Science and Manufacturing* 13.1 (2024), pp. 45–54. DOI: 10.37934/mjcsm.13.1.4554.

[55] Sumit. Sharma. *Drone Development from Concept to Flight : Design, Assemble, and Discover the Applications of Unmanned Aerial Vehicles*. 1st. Packt Publishing Ltd., 2024.

[56] Donald L. Simon et al. *Adaptive Augmented Reality Display Concepts for Unmanned Aircraft Systems in Emergency Response Operations*. Tech. rep. NASA/TM–20220006288. https://ntrs.nasa.gov/api/citations/20220006288/downloads/simon_v4.pdf. NASA Glenn Research Center, 2022.

[57] Wennie Tabib et al. “Autonomous Cave Surveying With an Aerial Robot”. In: *IEEE Transactions on Robotics* 38.2 (Sept. 2021), pp. 1016–1032. DOI: 10.1109/tro.2021.3104459.

[58] Zaid Tahir et al. “Design and Development of Optimal Control System for Quad Copter UAV”. In: *Indian Journal of Science and Technology* 9 (July 2016). DOI: 10.17485/ijst/2016/v9i25/96611.

[59] Hao Tian et al. “DIMA: Distributed cooperative microservice caching for internet of things in edge computing by deep reinforcement learning”. In: *World Wide Web* 25 (Aug. 2021), pp. 1–24. DOI: 10.1007/s11280-021-00939-7.

[60] Rolf Vieten et al. “Seasonal temperature variations controlling cave ventilation processes in Cueva Larga, Puerto Rico”. In: *International Journal of Speleology* 45.3 (2016), pp. 259–273. DOI: 10.5038/1827-806X.45.3.1983. URL: https://doi.org/10.5038/1827-806X.45.3.1983.

[61] H.P. Wallin, H. Bodén U. Carlsson M. Åbom, and R. Glav. *Sound and vibration*. 2nd ed. Stockholm: Institutionen för farkostteknik, Tekniska högskolan, 2010.

[62] H. Wang et al. “Study on the Transverse Properties of T800-Grade Unidirectional Carbon Fiber-Reinforced Polymers”. In: *Materials* 18.4 (2025), p. 816. DOI: 10.3390/ma18040816. URL: https://doi.org/10.3390/ma18040816.

[63] Pengcheng Wang et al. “Dynamics modelling and linear control of quadcopter”. In: *2016 International Conference on Advanced Mechatronic Systems (ICAMechS)*. 2016, pp. 498–503. DOI: 10.1109/ICAMechS.2016.7813499.

[64] K.K. Yeung and K. Rao. “Mechanical Properties of Kevlar-49 Fibre Reinforced Thermoplastic Composites”. In: *Polymers and Polymer Composites* 20 (June 2012), pp. 411–424. DOI: 10.1177/096739111202000501.

[65] Jingbo Zhao et al. “The Effects of Visual and Control Latency on Piloting a Quadcopter Using a Head-Mounted Display”. In: *2018 IEEE International Conference on Systems, Man, and Cybernetics (SMC)*. 2018, pp. 2972–2979. DOI: 10.1109/SMC.2018.00505.

A. Requirements

The requirements set in previous design phases are restated in this chapter to ensure ease of accessibility. These requirements are used to invent subsystem requirements for each of the drone subsystems; payload, structure, aerodynamics, avionics, and operations.

A.1. Missions Requirements

This section includes all missions requirements.

Table A.1: Mission requirements

ID	Description	Upstream requirement ID	Definition
MIS-DRN-1.1	The system shall be capable of mapping all accessible areas of a cave system within a 500 m displacement from the entrance	*STK-DRN-1*	
MIS-DRN-1.2	The system shall be capable of mapping accessible area within a total of 56 operational hours	*STK-DRN-1*	Key
MIS-DRN-1.3	The system shall successfully complete its primary mission objectives in at least 95% of deployments under nominal environmental and operational conditions.	*STK-DRN-1*	Key
MIS-DRN-1.4	The system shall detect and localize physical collision risks with at least 90% accuracy from a minimum distance of 10 meters.	*STK-DRN-1*	Key
MIS-DRN-1.5	The system shall remain fully operational without component failure when continuously exposed to ambient temperatures up to 310 K (37°C) throughout the duration of its mission.	*STK-DRN-1*	
MIS-DRN-1.6	The system shall remain fully operational without component failure when continuously exposed to maximum relative humidity of 100% throughout the duration of its mission.	*STK-DRN-1*	
MIS-DRN-1.7	The system shall include an onboard navigation solution capable of maintaining continuous 3D position and orientation estimates with a maximum drift of 1% relative to distance traveled	*STK-DRN-1*	
MIS-DRN-1.8	The system shall remain fully operational and structurally intact when subject to to impacts up to 2137 [Ns] in all 3 axis.	*STK-DRN-1*	
MIS-DRN-1.11	The system shall implement power management controls to limit input voltage to a safe operating range of 22 V throughout mission duration	*STK-DRN-1*	
MIS-DRN-2.1	The system shall generate a 3D visual map of all accesible areas of the cave with a spatial resolution of at least 1 cm	*STK-DRN-2*	Key
MIS-DRN-2.2	The system shall take informative pictures of specified areas with a resolution of at least 1 cm.	*STK-DRN-2*	Key
MIS-DRN-2.3	The system shall be capable of 3D mapping the cave walls from a maximum distance of 5 meters	*STK-DRN-2*	Key
MIS-DRN-2.4	The system shall be capable of photographing the cave walls from a maximum distance of 5 meters	*STK-DRN-2*	Key

Table A.1: Mission requirements (continued)

Identifier	Description	Upstream requirement ID	Definition
MIS-DRN-3.1	The system shall georeference the generated cave map with a positional accuracy of at least 1 cm relative to a fixed reference point at the cave entrance	*STK-DRN-3*	Key
MIS-DRN-4.2	The system shall be capable of safely navigating through horizontal and vertical openings of 41 dimensions with a minimum clearance of 0.5 cm during flight, without contact with surrounding surfaces.	*STK-DRN-4*	Key
MIS-DRN-4.3	The system's dimensions shall not exceed 40 cm in lateral and vertical directions.	*STK-DRN-4*	Key
MIS-OPR-1.1	The system operator shall be registered to operate the system.	*STK-OPR-01*	Key
MIS-OPR-1.2	The system shall be equipped with a remote identification system.	*STK-OPR-01*	Key
MIS-OPR-2.1	The system shall be designed such that at least 90% of its total weight can be separated into dissimilar material types using standard disassembly tools at End-Of-Life	*STK-OPR-02*	Driving
MIS-OPR-2.2	65% of the standard components used in the system — including fasteners, wiring, and structural elements — shall be designed for direct reuse in other products without requiring any mechanical, chemical, or thermal reprocessing.	*STK-OPR-O2*	Key/Driving
MIS-OPR-4.1	The system shall remain fully operational and structurally intact after withstanding vibrations of up to 2g in all 3 axis during up to 3 [hrs].	*STK-OPR-04*	
MIS-OPR-4.2	The system shall remain fully operational and structurally intact after experiencing pressure variations of 650 hPa at 12000 m altitudes of up to 10 hours of air transport.	*STK-OPR-04*	
MIS-OPR-5.1	The system shall operate without reliance on any non-portable infrastructure or services not provided by the mission crew.	*STK-OPR-05*	Key
MIS-OPR-7.1	The peak noise levels produced by the system during operation shall not be higher than 120 [dB].	*STK-OPR-O7*	Key/Driving
MIS-OPR-7.2	The average noise levels produced by the system during operation shall not be higher than 85 [dB].	*STK-OPR-O7*	Key
MIS-OPR-7.3	All components of the system shall be retrievable from the environment after operation within 1 week since the beginning of the mission	*STK-OPR-O7*	Driving/Killer
MIS-OPR-7.4	The noise frequency produced by the system during nominal operation shall not exceed 6000 [Hz], measured at a distance of 1 meter from the system	*STK-OPR-O7*	
MIS-OPR-7.6	The peak light levels produced by the system during operation shall not be higher than 12000 [lux].	*STK-OPR-7*	
MIS-OPR-7.7	The average light levels produced by the system during operation shall not be higher than 10000 [lux].	*STK-OPR-07*	
MIS-OPR-7.8	The system shall not directly expose bats and other cave fauna to light of wavelength in the range of 310-510 nm	*STK-OPR-07*	Key

Table A.1: Mission requirements (continued)

Identifier	Description	Upstream requirement ID	Definition
MIS-OPR-8.1	The system shall be provided together with a guidelines document for on-site inspection before flight of UAV.	*STK-OPR-08*	Key
MIS-OPR-8.2	The components of the system that are critical failure points (electrical wiring, landing gear, fiber optic) shall be repairable on site by no more two people from the crew without special training using portable manual tools	*STK-OPR-O8*	Key
MIS-OPR-8.3	Replacements of components of the system that are critical failure points (landing gear, fiber otpic, propellers) shall be provided with the product.	*STK-OPR-O8*	Key
MIS-OPR-9.1	The system shall not exceed a mass of 20 kg	*STK-OPR-09*	
MIS-OPR-10.1	The energy used over the full life-cycle of the system (e.g., material production, product manufacturing, transport, product use, and disposal) shall not exceed 2000 [MJ].	*STK-OPR-10*	Driving
MIS-OPR-10.2	The CO2 emitted over the full life-cycle of the system (e.g., material production, product manufacturing, transport, product use, and disposal) shall not exceed 60 [kg].	*STK-OPR-10*	Driving
MIS-OPR-10.3	The system shall be capable of utilizing a renewable energy source on-site to recharge its power supply system.	*STK-OPR-10*	Key
MIS-OPR-11.1	The system shall allow for replacement of the payload module without requiring disassembly of the core airframe or reconfiguration of flight control systems.	*STK-OPR-11*	
MIS-OPR-11.2	The system shall be capable of operation using equipment with varying power supply requirements, with the maximum power consumption per component not crossing 30 [W]	*STK-OPR-11*	
MIS-OPR-11.3	The system shall be capable of operation using equipment with varying voltages, with the maximum voltage used per component not crossing 22 [V]	*STK-OPR-11*	

A.2. System Requirements

This section includes all system requirements.

Table A.2: System Requirements

ID	Description	Upstream requirement ID	Definition
SYS-DRN-1.11.1	The system shall be capable of providing power to all electronics throughout the whole mission duration.	MIS-DRN-1.11	
SYS-DRN-1.11.2	The system shall be capable of managing voltage distribution to all electronics throughout the duration of the whole mission.	MIS-DRN-1.11	
SYS-DRN-1.2.1	The system shall maintain an attitude positioning accuracy of less than 0.1 degrees on each of the three principal axes (roll, pitch, and yaw) during nominal flight conditions.	MIS-DRN-1.2	Key

Table A.2: System Requirements (continued)

ID	Description	Upstream requirement ID	Definition
SYS-DRN-1.3.2	The system shall be able to process data at a rate over 9000 [bit/s] bits with 90% accuracy.	MIS-DRN-1.3	
SYS-DRN-1.6.1	No part of the system shall experience critical corrosion within 100 [days] days of operation under nominal mission conditions.	MIS-DRN-1.6	
SYS-DRN-1.8.1	The system shall protect the exposed components from structural failure when subjected to impacts up to 2137 [Ns].	MIS-DRN-1.8	
SYS-DRN-4.2.1	The system shall maintain its position with an accuracy of less than 1 cm per axis during hover or groundspeeds lower than 0.7 [m/s], under nominal conditions.	MIS-DRN-4.2	Key
SYS-DRN-4.2.2	The system shall be capable of providing translation acceleration along each axis up to 1 m/s^2 during nominal flight conditions.	MIS-DRN-4.2	Key
SYS-DRN-4.2.4	The system shall allow for angular acceleration of 380 rad/s^2 or less in each axis during nominal flight conditions.	MIS-DRN-4.2	Key
SYS-OPR-1.2.1	The system shall operate continuously for no less than 15 min on a single full charge or energy cycle under nominal mission conditions, including payload operation, navigation, and communication.	MIS-DRN-1.2	
SYS-OPR-4.1.1	The system shall remain fully operational and structurally intact in flight during vibrations of up to 10 g in all 3 axis up to 1000 hrs of each component individually.	MIS-OPR-4.1	
SYS-OPR-5.1.1	The system shall be capable of being transported without any physical damage, through a handheld case of dimensions 55cm x 25cm x 35cm.	MIS-OPR-5.1	
SYS-OPR-5.1.2	The system during transportation shall weigh no more than 20 kg.	MIS-OPR-5.1	
SYS-OPR-7.3.1	The system shall have designed points of failure such that all post-failure system parts are at least 30% of their initial dimension.	MIS-OPR-7.3	
SYS-OPR-7.3.2	The system shall include a Return-to-Home function that automatically activates upon signal loss, battery levels below 30%, or user instruction.	MIS-OPR-7.3	

B. Technical Drawing

The Figure B.1 below shows the technical drawing of the SpeleoDrone, constructed via 3DExperience. Some of the main dimensions are showed.

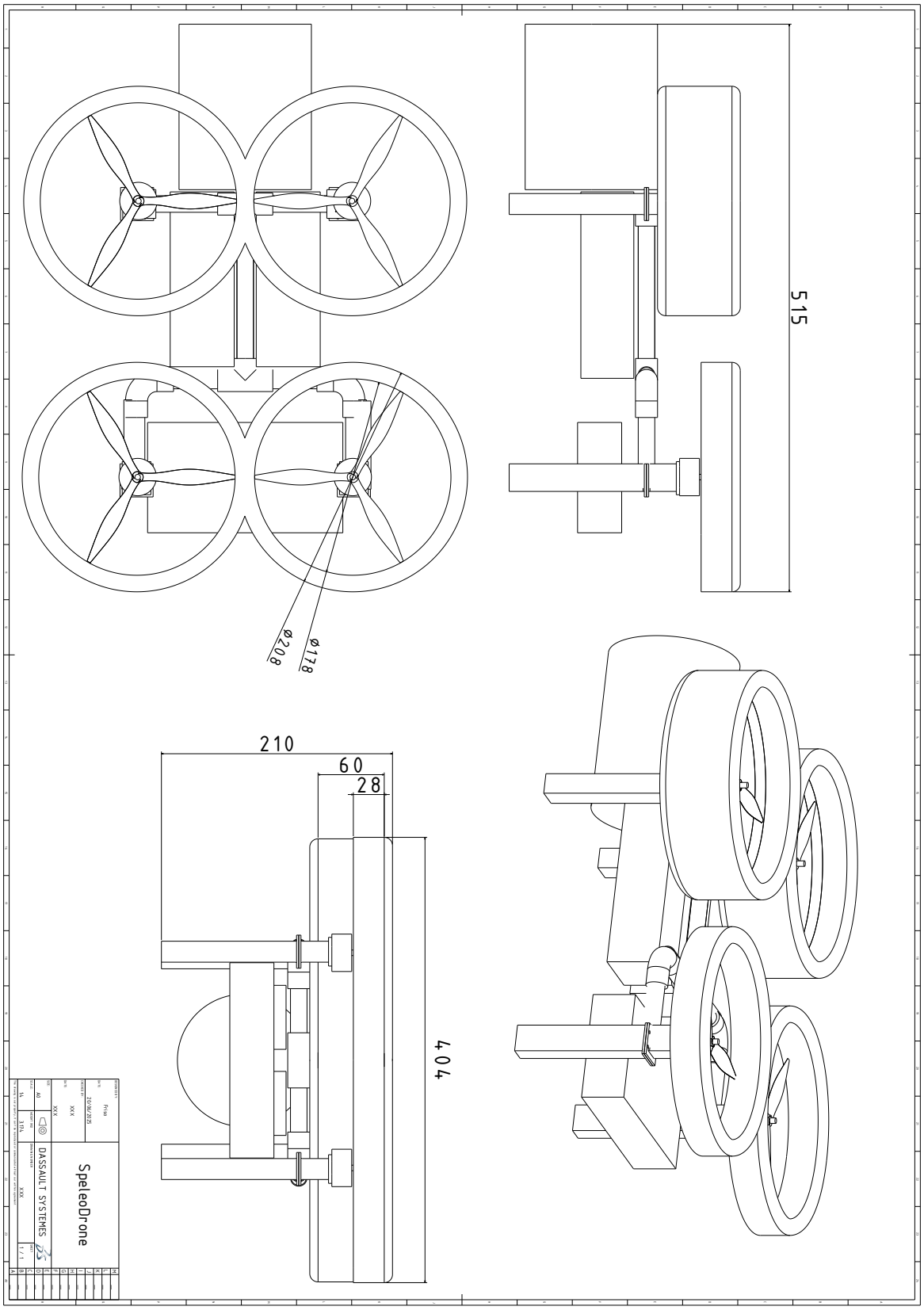

Figure B.1: technical Drawing